Institut für Biologie und Biochemie

Arbeitsgruppe Molekulare Enzymologie

Reconstitution of Molybdenum Cofactor Biosynthesis in Giant Vesicles

Dissertation

zur Erlangung des akademischen Grades

"doctor rerum naturalium" (Dr. rer. nat.)

in der Wissenschaftsdisziplin " Biochemie "

eingereicht an der

Mathematisch-Naturwissenschaftlichen Fakultät
der
Universität Potsdam

International Max Planck Research School (IMPRS)
on Multiscale Bio-Systems

Von

Akanksha Moga

Potsdam, September 2020

Published online on the
Publication Server of the University of Potsdam:
https://doi.org/10.25932/publishup-51016
https://nbn-resolving.org/urn:nbn:de:kobv:517-opus4-510167

I. Abstract

Bottom-up synthetic biology is used for the understanding of how a cell works. It is achieved through developing techniques to produce lipid-based vesicular structures as cellular mimics. The most common techniques used to produce cellular mimics or synthetic cells is through electroformation and swelling method. However, the above-mentioned techniques cannot efficiently encapsulate macromolecules such as proteins, enzymes, DNA and even liposomes as synthetic organelles. This urges the need to develop new techniques that can circumvent this issue and make the artificial cell a reality where it is possible to imitate a eukaryotic cell through encapsulating macromolecules. In this thesis, the aim to construct a cell system using giant unilamellar vesicles (GUVs) to reconstitute the mitochondrial molybdenum cofactor biosynthetic pathway. This pathway is highly conserved among all life forms, and therefore is known for its biological significance in disorders induced through its malfunctioning. Furthermore, the pathway itself is a multi-step enzymatic reaction that takes place in different compartments. Initially, GTP in the mitochondrial matrix is converted to cPMP in the presence of cPMP synthase. Further, produced cPMP is transported across the membrane to the cytosol, to be converted by MPT synthase into MPT. This pathway provides a possibility to address the general challenges faced in the development of a synthetic cell, to encapsulate large biomolecules with good efficiency and greater control and to evaluate the enzymatic reactions involved in the process.

For this purpose, the emulsion-based technique was developed and optimised to allow rapid production of GUVs (~18 min) with high encapsulation efficiency (80%). This was made possible by optimizing various parameters such as density, type of oil, the impact of centrifugation speed/time, lipid concentration, pH, temperature, and emulsion droplet volume. Furthermore, the method was optimised in microtiter plates for direct experimentation and visualization after the GUV formation. Using this technique, the two steps - formation of cPMP from GTP and the formation of MPT from cPMP were encapsulated in different sets of GUVs to mimic the two compartments. Two independent fluorescence-based detection systems were established to confirm the successful encapsulation and conversion of the reactants. Alternatively, the enzymes produced using bacterial expression and measured. Following the successful encapsulation and evaluation of enzymatic reactions, cPMP transport across mitochondrial membrane has been mimicked using GUVs using a complex mitochondrial lipid composition. It was found that the cPMP interaction with the lipid bilayer results in transient pore-formation and leakage of internal contents.

Overall, it can be concluded that in this thesis a novel technique has been optimised for fast production of functional synthetic cells. The individual enzymatic steps of the Moco biosynthetic pathway have successfully implemented and quantified within these cellular mimics.

I. Zusammenfassung

Die synthetische Biologie wird in der von unten-nach-oben-Methode eingesetzt, um zu verstehen, wie eine Zelle funktioniert. Dafür werden Techniken zur Herstellung lipidbasierter vesikulärer Strukturen als zelluläre Nachahmungen entwickelt. Die gebräuchlichste Technik zur Herstellung von Zellnachahmungen oder synthetischen Zellen ist die Elektroformations- und Schwellmethode. Diese Techniken können jedoch Makromoleküle wie Proteine, Enzyme, DNA und sogar Liposomen nicht effizient als synthetische Organellen einkapseln. Daher ist es dringend erforderlich, neue Techniken zu entwickeln, die dieses Problem umgehen und die künstliche Zelle zu einer Realität machen, in der es möglich ist, eine eukaryotische Zelle durch Einkapselung von Makromolekülen zu imitieren. Das Ziel dieser Arbeit war es, ein komplexes Zellensystemmodel zu konstruieren, bei dem riesige unilamellare Vesikel (GUVs) zur Rekonstruktion des mitochondrialen Molybdän-Kofaktor-Biosynthesewegs verwendet werden. Dieser Stoffwechselweg ist bei allen Lebensformen hoch konserviert und daher aufgrund von Störungen, die durch Fehlfunktionen hervorgerufen werden, für seine biologische Bedeutung relevant. Darüber hinaus ist die Biosynthese selbst eine mehrstufige enzymatische Reaktion, die in verschiedenen Kompartimenten abläuft. Zunächst wird GTP in der mitochondrialen Matrix in Gegenwart von cPMP-Synthase zu cPMP umgewandelt. Anschließend wird das produzierte cPMP über die Membran zum Zytosol transportiert, wo es von der MPT-Synthase in MPT umgewandelt wird. Dieser Biosyntheseweg bietet eine Möglichkeit, den allgemeinen Herausforderungen bei der Entwicklung einer synthetischen Zelle zu begegnen, um große Biomoleküle mit guter Effizienz und Kontrolle zu verkapseln und die am Prozess beteiligten enzymatischen Reaktionen zu bewerten.

Zu diesem Zweck wurde die emulsionsbasierte Technik entwickelt und optimiert, die eine schnelle Produktion von GUVs (~18 min) mit hoher Verkapselungseffizienz (80%) ermöglicht. Möglich wurde dies durch die Optimierung verschiedener Parameter wie Dichte, Öltyp, Einfluss von Zentrifugationsgeschwindigkeit/-zeit, Lipidkonzentration, pH-Wert, Temperatur und Emulsionstropfenvolumen. Darüber hinaus wurde die Methode in Mikrotiterplatten für das direkte Experimentieren und die Visualisierung nach der GUV-Bildung optimiert. Mit dieser Technik wurden die beiden Schritte, die Bildung von cPMP aus GTP und die Bildung von MPT aus cPMP, in verschiedenen GUVs eingekapselt, um die beiden Kompartimente nachzuahmen. Zwei unabhängige fluoreszenzbasierte Detektionssysteme wurden eingerichtet, um die erfolgreiche Einkapselung und Umwandlung der Reaktanten zu bestätigen. Alternativ wurden die Enzyme mittels bakterieller Expression produziert und gemessen. Nach der erfolgreichen Einkapselung und Auswertung der enzymatischen Reaktionen wurde der cPMP-Transport durch die mitochondriale Membran mit Hilfe von GUVs unter Verwendung einer komplexen mitochondrialen Lipidzusammensetzung nachgeahmt. Es wurde festgestellt, dass die cPMP-Wechselwirkung mit der Lipiddoppelschicht zu einer transienten Porenbildung und zum Auslaufen des inneren Inhalts führt.

Insgesamt kann der Schluss gezogen werden, dass in dieser Arbeit eine neuartige Technik für die schnelle Herstellung funktioneller synthetischer Zellen optimiert wurde. Einzelne enzymatische Schritte des Moco-Biosynthesewegs wurden in diesen zellulären Mimiken erfolgreich implementiert und quantifiziert.

II. Declaration of Authorship

I hereby declare that I am the sole author and composer of my thesis and that no other sources or help than those listed have been used. Wherever contributions of others are involved, this contribution is indicated, clearly acknowledged and due reference is given to the author and source. Furthermore, I declare that I have not submitted this thesis, either in its entirety or in excerpts thereof, at any other institution

(Date, place) (Signature)

III. Publication and Manuscript

Published: Optimisation of the inverted emulsion-based method for high-throughput production of giant unilamellar vesicles

[Akanksha Moga, Dr. Naresh Yandrapalli, Dr. Rumiana Dimova, and Dr. Tom Robinson 2019 ChemBioChem, 2019 - Wiley Online Library]
doi/full/10.1002/cbic.201900529

Reconstitution of molybdenum cofactor biosynthesis within GUVs *(in preparation)*

[Akanksha Moga, Silke Leimkühler, Tom Robinson]
In vitro biosynthesis of Moco was reconstituted in the GUVs for the first time and detected under a novel fluorescent-based assay

IV. List of abbreviation

Å	Ångström = 10^{-10} m
°C	Degree Celsius = x + 273.15 K
λ	Wavelength
µ	Micro = 10^{-6}
AC	Alternating current
AGE	Agarose gel electrophoresis
AMP	Adenosine 5'-monophosphate
ATP	Adenosine triphosphate,
BSA	Bovine serum albumin
Chol	Cholesterol
CV	Column volume
DIlC18	1-1 dioctadecyl 3-3-3-3-tetramethylindocarbocyanine perchlorate
DMSO	dimethyl sulfoxide
DNA	deoxyribonucleic acid
ds	double-stranded
DTT	1,4-dithio-D-threitol, 1,4-disulfanylbutane-2,3-diol
E. coli	*Escherichia coli*
FeS	Iron sulfur
Fig.	Figure
cPMP	cytosolic pyranopterin monophosphate
EDTA	ethylenediamine-tetra-acetic acid
eGFP	enhanced green fluorescent protein
g	centripetal acceleration = 9.80665 m/s^2
Glc	Glucose
GTP	Guanosine triphosphate
GUV(s)	Giant unilamellar vesicle(s)
Hz	Hertz = s^{-1}

HPLC	High-pressure liquid chromatography
i.e	that is
IPTG	Isopropyl-D-thiogalactopyranoside
ITO	Indium thin oxide
J	kilo-Joule = 103 kg m^2/s^2
K	kilo- = 103
KCl	Potassium Chloride
LB	Lysogenic broth
LU	Light units = artificial unit
LUV(s)	Large unilamellar vesicle(s)
m	Meter, milli- = 10^{-3}
MES	2-(morpholin-4-yl) ethane-1-sulfonate
Min	Minute = 60 s
Mo	Molybdenum
Moco	Molybdenum cofactor
MOCS	Molybdenum cofactor synthesis
MPT	Molybdopterin
n	nano = 10^{-9}
NA	Numerical aperture
NaCl	Sodium Chloride
Ni-NTA	Nickel-Nitrilo Triacetic Acid
PAGE	polyacrylamide-gel electrophoresis
PCR	polymerase chain reaction
PC	Phosphatidylcholine
PDMS	Polydimethylsiloxane
PE	Phosphatidylethanolamine
PI	Phosphatidylinositol
PL	Phospholipid
PMF	Potential of mean force

PS	Phosphatidylserine
pH	decimal cologarithm of proton concentration
pKa	decimal cologarithm of acid dissociation constant
RNA	Ribonucleic acid
rpm	Revolutions per minute
RT	Room temperature
ROI	Region of interest
NR	Nitrate reductase
SAM	S-adenosylmethionine
SDS	sodium dodecyl sulfate
SM	Sphingomyelin(s)
SO	Sulfite oxidase
T	Temperature
Tab.	Table
Tris	tris-(hydroxymethyl) aminomethane
U	Unit = 1 µmol/min
UV-VIS	Ultraviolet-visible
V	Volt = 1 kg m^2/A s^3
XDH/ XDH	Xanthine dehydrogenase
XO/ XO	Xanthine oxidase
XOR/ XOR	Xanthine oxidoreductase

V. List of Figures

VI. List of Tables

VII. Table of Content

1 Introduction

In the process of bottom-up construction of a synthetic cell, lipid membrane compartments are considered a key component. Lipid membranes are critical for many cellular processes and also to maintain cell morphology. They provide a physical barrier from the outer environment that enables a cell to contain biochemical reactions that are essential for life. This thesis aims to provide a synthetic cell model in the form of giant liposomes and utilise them as bioreactors to process Moco biosynthesis *in vitro*. Hence, this introduction chapter includes an understanding of the different biological aspects that are relevant to this thesis, which is hereby discussed in three main sections. In the first section, the fundamentals of cells, and the organelles are outlined. In the second section, current methods for the construction of model membranes *de novo* using chemical building blocks, and in the third section of this chapter, Moco biosynthesis together with the main intermediate steps are discussed. Finally, the aims of this thesis are discussed in the last section of this introductory chapter.

1.1 Protocells

Our planet is inhabited by a myriad of living organisms that can be thought of as biochemical factories that can grow and create copies of themselves. These cellular factories can interact with their environment and utilise the surrounding materials (and energy) to create new molecules. The simplest structured life form was proposed by A.O. and JBS H. in the 1920s which was termed the protocell (see Figure 1).[1,2] The given theoretical protocell consists of a lipid fatty acid bilayer, which is self-organised into a spherical entity under the prebiotic conditions, and with the capability to grow and divide into daughter cells. Lipid membranes surrounding these cellular systems ensure efficient compartmentalization. This makes them critical for many biochemical processes and to maintain cell morphology. A characteristic feature in the early protocell evolution was the ability to compartmentalise basic biomolecules (e.g., dsRNA and nucleotides) within the inner aqueous environment.[3,4]

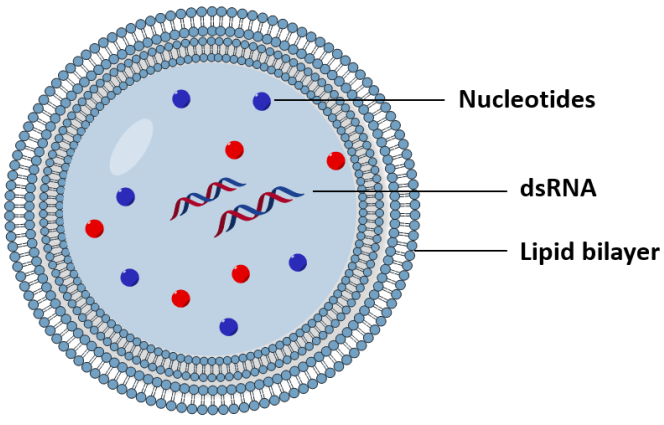

Figure 1. Schematic representation of a protocell.
The protocell surrounded by multiple fatty acid lipid membrane composed of simple amphiphilic molecules. The cell contained functional RNA (helical structures) and nucleotides within the inner aqueous environment

In theory, a protocell is described as a fast-changing and straightforward structure with a concentrated aqueous solution surrounded by a membrane.[5] While living systems include multi-cellular organisms or colonies, the fundamental unit of life is the cell, as illustrated in Figure 2 (a-c). Cells first evolved from the primordial soup, and are thought to have been simple self-sustaining chemical systems capable of Darwinian evolution.[1] Later on, protocells evolved to a modern cell by forming subcellular organelle each enclosed by an independent membrane. As for now, more than 100 billion different biological living forms inhabitant the Earth, each self-replicating which yield progeny that are composed of the same types of chemical molecules at the cellular level. All these different species composed of many of cells (multicellular) or single cell (unicellular) consistently respond to the progressive surrounding environment.[1,5]

1.2 Modern Biological Cells: Prokaryotes and Eukaryotes

The modern cell has evolved into two major cellular classes: prokaryotes and eukaryotes.[2] Prokaryotes are rather small compared to eukaryotes, varying between 0.1 nanometres and few micrometres. Prokaryotes are nucleus-free and organised into a single compartment with a simple internal organisation (see Figure 2). In contrast, the modern eukaryotic cells maintain complex biological reactions within different internal compartments, shown in Figure 3.[1,6] These cell shows an astonishing mixture of sizes and shapes ranging from 10 - 100 µm diameter with a membrane-bound nucleus.[6]

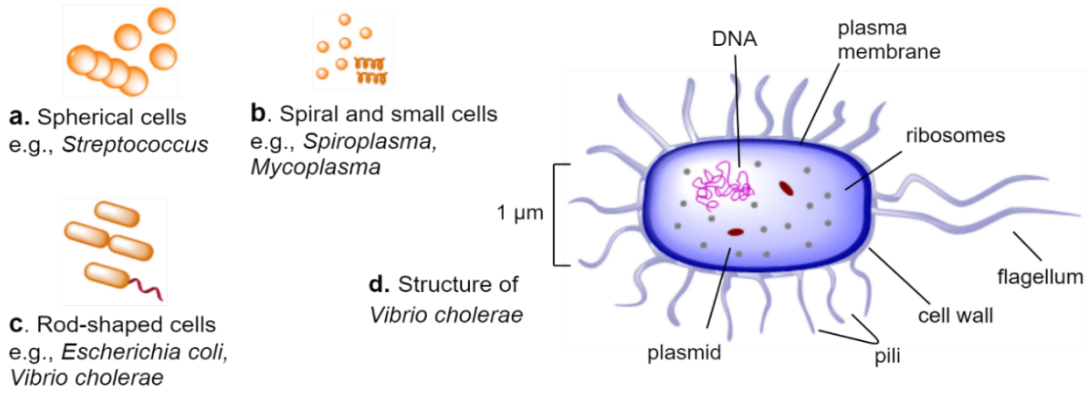

Figure 2. Basic shapes and sizes of prokaryotes.
a-c) Micrometre-sized cells can appear as spiral, rod-shaped, and spherical. (d) The bacterium Vibrio cholerae that is about 1 µm in diameter, exhibits a simple internal organization with a circular DNA, a plasma membrane, and a helical tail at one end called a flagellum, that propels the cell forward.

A functional cell membrane is a common feature in both the cellular classes, which imports molecules such as ions, water, and small organic molecules to produce three main macromolecules: polysaccharides, proteins, and nucleic acids.[7] These macromolecules are considered vital for the series of biochemical processes in the cell such as structural integrity, energy metabolism, and cell signalling etc. The fluidic membrane mainly serves as a physical boundary, forming a selective barrier to control diffusion to and from the cell. In addition to the external membrane, eukaryotic cells contain a comprehensive internal membrane system enclosing very organised subcellular compartments,[1,7] as shown in Figure 3, known as cell organelles. Examples

include the nucleus, mitochondria, and Golgi apparatus etc. These individual organelles further maintain a specific internal environment (varying pH, oxidation state etc.), supported by lipid membranes for various biochemical processes and collectively responsible for cell functioning.[2,6] There are processes in the cell that are known for the synthesis of lipids and other membrane macromolecules.[1]

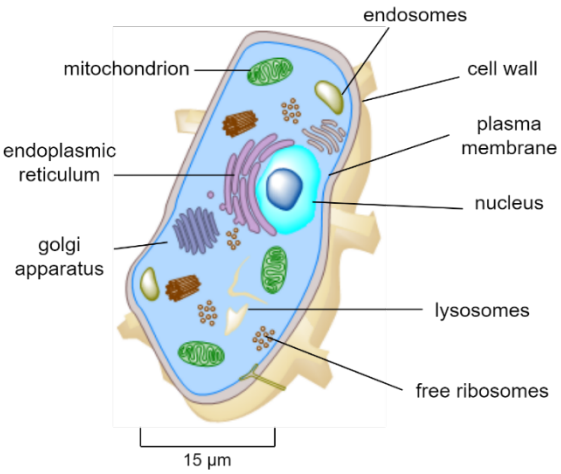

Figure 3. The structure of a typical Eukaryotic cell.
The cell showing the principal intracellular organization of eukaryotic cells, with distinct compartments such as cytosol, endoplasmic reticulum, Golgi apparatus, nucleus, mitochondrion, endosome, lysosome, and peroxisome confined within the physical boundaries of their bilayered membranes.

In general, proteins are responsible for a variety of functions in the cell, mainly as enzymes, in chemical reactions and in synthesising macromolecules such as DNA, RNA and the other proteins.[2,6] An essential organelle is the mitochondria, which is a unique organelle with its own circular DNA, and two bilayer membranes which constitute 25 % of the total cell volume.[1,6] The two mitochondrial membranes differ in composition and generally termed as; 1) the outer mitochondrial membrane, 2) inner mitochondrial membrane. Since mitochondria also provide energy to the cell via adenosine triphosphate (ATP) production, it is an essential organelle and often named as powerhouse of the cell.

1.2.1 The Structure of Eukaryotic Cellular Membranes

Lipid membranes are very thin, ~4-6 nm in thickness, and primarily composed of two phospholipid monolayers 'leaflets' making a bilayer structure (see Figure 4).[4,8] As been said, it provides a physical barrier and separates the cytoplasm from the outer environment, while maintaining the cell's morphology. The cytoplasm is an aqueous interior to the cell which contains water, ions, proteins and other macromolecules required for the cellular activities.[1,9] The cytosol contains a mesh of crisscrossing fibrous proteins forming a filamentous system, known as the cytoskeleton.[1,6,9] The transport across the membrane take place via noncovalent interactions between protein-phospholipids and with phospholipids. This structure of the cell membrane was first elaborated in 1972 by Jonathan Singer and Garth Nicolson using a classic Fluid mosaic model of the cell membrane,[10] as shown in Figure 4. The membrane proteins are categories on their orientation in the membrane such as-

1) Integral membrane proteins or transmembrane proteins, which span the bilayer and often form dimers.
2) Lipid-anchored proteins, which are covalently bound to one leaflet of the membrane through a hydrocarbon chain.
3) The peripheral proteins are framed onto the membrane by specific noncovalent interactions with integral membrane proteins or the membrane lipids.

The phospholipids are amphiphilic molecules, with a hydrophilic (water-soluble) "head" which either points towards the cytoplasm or the outside environment, and a hydrophobic (water-insoluble) "tail". This simple physicochemical property of amphiphilic molecules allows them to aggregate and self-assemble spontaneously in an aqueous environment into a bilayer. Details of the molecular structure of lipids are further discussed in later section 1.3.[11,12] Overall, as shown in Figure 4, the plasma membrane (bilayer coded in red) is a heterogeneous, asymmetric, and dynamically cell component studded with proteins (coded in blue) to selectively perform a variety of function not only in the transport of small metabolites but also for cell-cell interaction, signalling and binding to form tissues.[6]

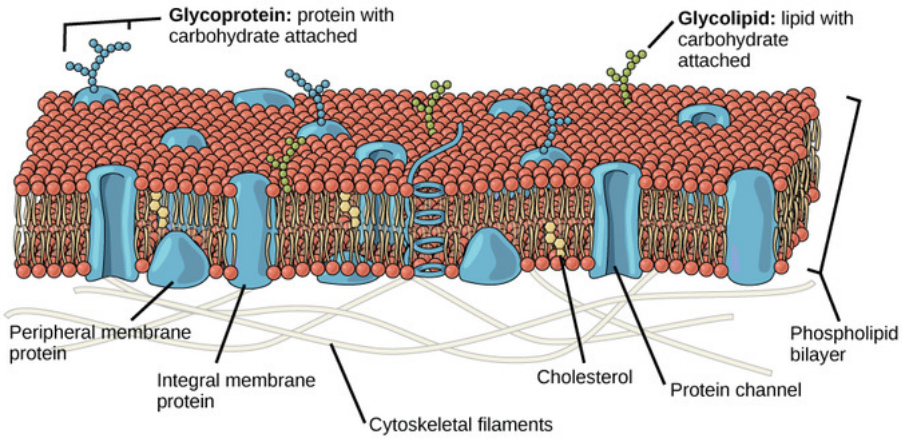

Figure 4. Schematic representation of the fluid mosaic model.
A phospholipid bilayer has thickness of about 3 nm, here presenting the underlying architecture of a membrane and other embedded elements of the membrane. The lipid molecules can move via lateral translocation or spinning within the same plane of the membrane, providing a fluid-like consistency. The hydrophobic core of the bilayer restricts the movement of hydrophilic molecules to and from the membrane. There are different proteins attached on the membrane via noncovalent interactions, between protein-phospholipids, and between phospholipids. These interactions provide strength and flexibility to the membrane, in some cases make a widespread connection with the cytoskeleton. *Image taken from Wikipedia-Fluid mosaic model of a cell membrane.*

1.2.2 Composition and Dynamics of Organelle Specific Membranes

Since a functional cell involves membrane heterogeneity in shape and chemical properties with its lipid composition. Likewise, every cellular organelle maintains a unique membrane, presented in Figure 5 a, essentially to regulate organelle-specific membrane-based functions such as signalling, intracellular protein sorting, and molecule transport via fusion-fission of vesicles, etc. In mitochondria, the powerhouse of the cell,

the synthesis of ATP occurs with the transport of H^+ during oxidative phosphorylation and photosynthesis.[6,13,14] As said earlier, mitochondria are responsible for ATP production on its well-known complex and dynamic membranes. First described in 1914, the mitochondrial membrane contains two major membranes (Figure 5 b) and different lipid composition, shape, and chemical properties including various transporters. The two mitochondrial membranes, in contrast to the composition of membranes of other cell organelles, are characterised by the high content of phospholipids, and a lower amount of sterols or sphingolipids.[1,6,15]

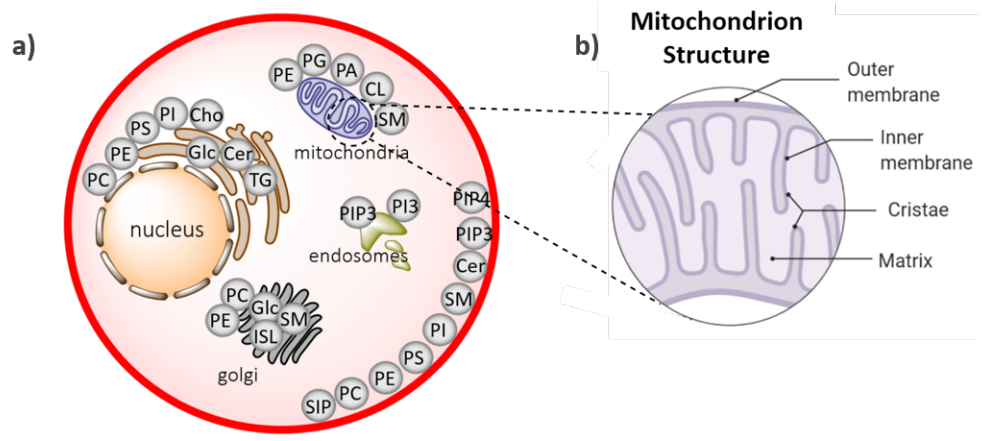

c) **Lipid Composition**

Plasma membrane	Golgi	Mitochondria	Endo. Reticulum
PC 21%, PI 6%, SM 12%, Chol. 17%, PE+PS 24%	PC 42%, PI 10%, SM 8%, Chol. 16%, PE+PS 22%	PC 46%, PI 5%, SM 3%, CL 20%, PE+PS 35%	PC 51%, PI 5%, SM 3%, Chol. 7%, PE+PS 25%

Figure 5. Illustration of the lipid compositions in different cell organelles.
(a) The lipid composition varies among every organelle in the cell, as this figure represents, their significant sites for the synthesis. The lipids are further distributed within the cells to their destinations based on their surface modification using budding vesicles. Regardless of their structural differences, all the lipids are synthesised inside the cell and distributed, respectively. For example, the phosphoglycerides are synthesised in the endoplasmic reticulum (ER), and sphingolipids in the Golgi complex. (b) Most organelles have a single bilayer, whereas only mitochondria contain two bilayers i.e., inner, and outer membrane. (c) The data taken on the lipid composition in different biological membranes present inside animal cells, from *Gallet et at., 1999*.[16]

Mitochondria and its membrane have been attractive organelle for its dynamic nature. This membrane reflects a unique composition (the mitochondrial membrane along with other organelles, are shown in Figure 5 c) mostly cardiolipin, sphingomyelin, cholesterol, phosphatidyl/ lysophosphatidylcholine, phosphatidylinositol, phosphatidylserine, phosphatidyl/ lysophosphatidylethanolamine, with varying consistency on each leaflet.[1,15,16] The inner mitochondrial membrane also has highly compressed lipid density due to cristae formation with almost 40 % negatively charged lipids. The two membranes have quick and continuous bidirectional lipid trafficking (to, within, and out of the mitochondria) to maintain the defined composition. Following through the similarities between prokaryotes and mitochondria, due to the ancient symbiotic events, the inner mitochondrial membrane contains similar electron transport proteins as the plasma membrane of prokaryotes.

1.3 Lipids and their Physiochemical Properties

The cell consists of about ~1000 different types of lipids, and the lipid molecules constitute 50% of the total cell mass, while the remaining mass is known to be contributed mostly by the proteins.[1] In 1920, two Dutch scientists Evert Gorter and François Grendel, for the first time, proposed the bilayer nature of biological membranes using red blood cells. As later modified, to the fluid mosaic model of Jonathan Singer and Garth Nicolson in 1972, stating that lipids and proteins form the building blocks of cellular systems, Figure 4.[1,6,8] Regardless of their functional differences, all the biological membranes have a thin structure of lipid and protein molecules, held together by noncovalent interactions. Lipids are amphiphilic chemical entities insoluble in water or aqueous solution while soluble in organic solvents such as ethanol, ether and chloroform etc. Majority of the lipids are phospholipids, and they are amphiphilic with a hydrophilic head and the hydrophobic tails containing two fatty acyl chains, represented in Figure 6. Therefore, phospholipids self-assemble into the bilayer in an aqueous environment and readily forms a hydrophobic core. These assemblies result in various structures of the lipid bilayer, depending on the nature of the head group modification and length of the fatty acyl chains, Figure 8.

1.3.1 Types of Lipids and their Head-group Modification

The length of fatty acids, the nature of the head group, and the backbone diversity result in a diverse range of lipids. Therefore, both the composition and structural differences affect the physicochemical properties of the lipid membrane.[8] There are three main groups of membrane lipids named- phosphoglycerolipids, sphingolipids, and sterols. The former of which is the most abundant lipid present in the cell, mostly phospholipids classified as followed (their structural details in is represented Figure 6, 7).[1]

1. **Phosphoglycerolipids**, are the derivatives of glycerol 3-phosphate and consists of a hydrophobic tail comprised of two fatty acids (acyl) chains and a polar head group attached to the phosphate group. The two-acyl chains are esterified to the three-carbon glycerol backbone, where the third carbon atom of the glycerol is attached to a phosphate group. The two acyl chains may vary in length depending on the number of carbons and their degree of saturation, as shown in Figure 6 a. The length of the acyl chain (number of hydrocarbons, usually between 16 and 24) and the degree of unsaturation (presence of *cis*-double bonds, usually 1 or 2) determine the packaging of lipid molecules in the membrane. Phosphoglycerides are typically named according to the nature of their head group, for example, phosphatidylcholine (PC) with a head group choline, followed by phosphatidylserine (PS) with a head group serine, phosphatidylethanolamine (PE) with a head group ethanolamine, phosphatidylinositol (PI) with a head group inositol.

2. **Sphingolipids** are compounds that are derived from sphingosine, are a long-chain fatty acid with an amino group and two hydroxyl groups. The most common sphingolipid is sphingomyelin (SM), with an acyl tail attached to the amino group, and a phosphocholine group attached to the terminal hydroxyl group. As seen in Figure 6 b, glucose-containing sphingosine, glycolipids contain 2–10% of the total lipid content of plasma membranes and are most abundant in nervous tissue.

3. **Sterols** are another important class of membrane lipid, with a rigid steroid ring structure attached to a single polar hydroxyl group and a nonpolar hydrocarbon chain, Figure 7. The major sterols present in animals is called cholesterol, in fungi is ergosterol, and in plants is stigmasterol. Although the structures of these principal sterols differ slightly, they all serve as crucial components of the membranes.

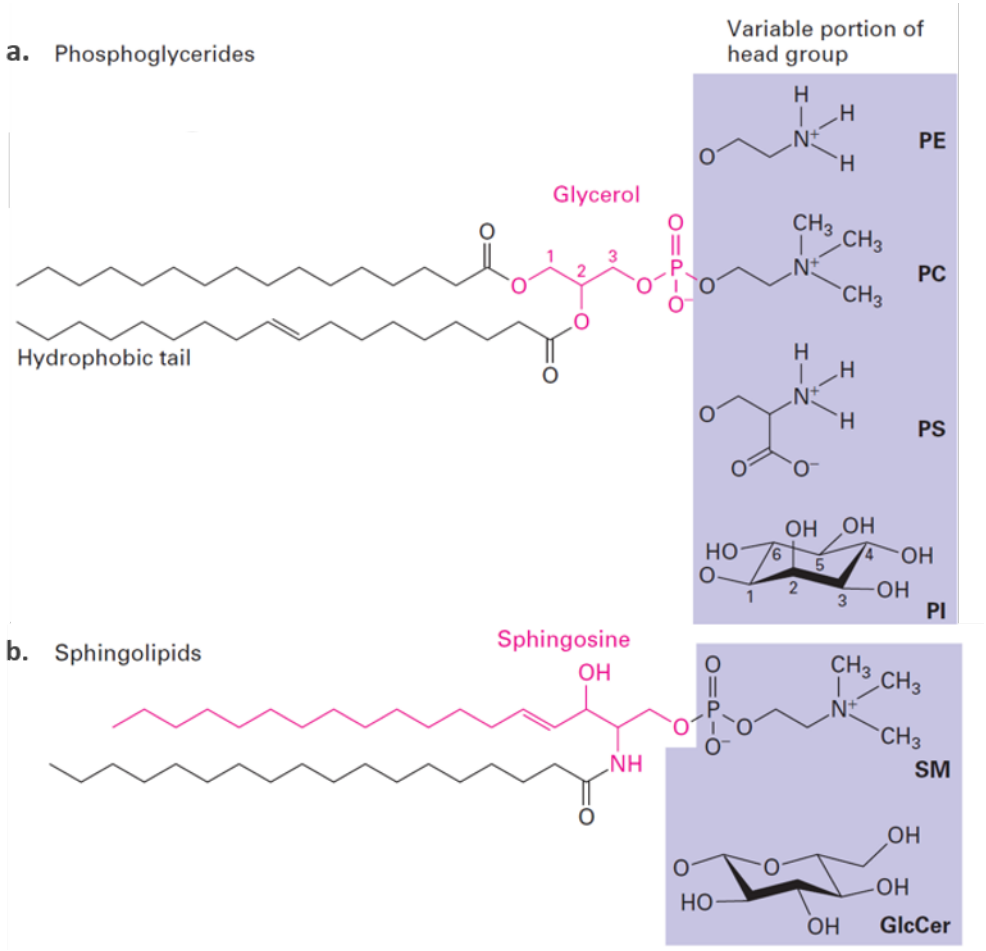

Figure 6. Major Classes of Phospholipids.
There are in principle three major class of phospholipids phosphoglycerides, sphingolipids, sterols (not shown here). a) Phosphoglycerides contains glycerol 3-phosphate (pink) with two esterified fatty acyl chains that compose of a hydrophobic tail and a polar head. Most common examples are, phosphatidylcholine (PC), phosphatidylethanolamine (PE), phosphatidylserine (PS), and phosphatidylinositol (PI). The fatty acids vary in chain length and are saturated (no double bonds) or unsaturated (with double bonds). (b) Sphingolipids contain sphingosine (pink), amino alcohol with a long hydrocarbon chain and the common are sphingomyelins (SM), containing a phosphocholine head group. Other sphingolipids containing a single sugar residue, or a branched oligosaccharide are called glycolipids. For example, a glycolipid glucosylcerebroside (GlcCer). *Image adapted from Lodish et al, 2016.*[1]

Lipids such as phosphatidylcholine, phosphatidylethanolamine, phosphatidylserine and sphingomyelin constitute more than half the lipid mass in most mammalian cell membranes. Whereas, the presence of the phosphocholine group in sphingomyelin, make the overall structure of sphingomyelin is similar to phosphatidylcholine that allows it to form a mixed-bilayer with other phospholipids, Figure 7 b.[1] Phosphatidylcholines are the most abundant phospholipid with a choline headgroup, where a positively charged alcohol ester-bonded to a negatively charged phosphate, which represents a zwitterionic structure.[17,18]

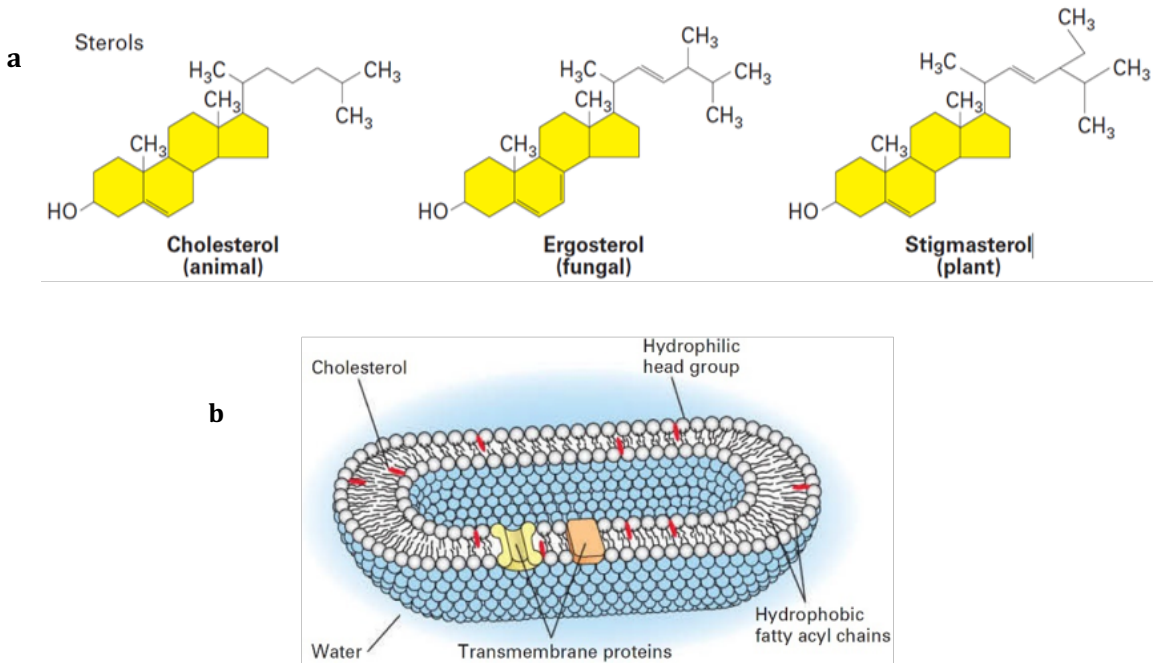

Figure 7. Third major class of lipids, sterols.
(a) The basic structure of sterols is a four-ring hydrocarbon, image showing the major sterols in animals (cholesterol), fungi (ergosterol), and plants (stigmasterol). (b) A simple construction of the phospholipid-based cell with cholesterol impeded in the membrane. *Image from Lodish et al, 2016.*[1]

Sterols, such as cholesterols, are often amphipathic and hydrophobic, and hence they are often intercalated between phospholipid molecules in the membrane as seen in Figure 7 b. Therefore, cholesterol and triglycerides are stored easily in the cell, and they are an essential component in structuring the cell where they also serve as a source of fuel. Additionally, while present in the membrane cholesterol interacts with phospholipids and provide stability to the membrane.[1,6,19]

1.3.1.1 Lipid Assembly in Aqueous Environments

The amphiphilic nature and the shape of the lipid molecules induce the bilayer formation in an aqueous environment under the energetically favourable condition. The Van der Waals interactions between lipid tails and the fundamental amphiphilic nature allow lipid molecules to self-assemble and provide stability to the biological membranes.[1,8,20] For instance, phospholipid suspension dispersed in an aqueous environment would spontaneously re-arrange their hydrophobic tails into a shielded core while exposing the hydrophilic heads to the aqueous environment. Hence, the driving forces, and the geometry of lipids results in the lateral pressure that induces different monolayer curvature which follows typically four structures: 1) spherical micelles, 2) bilayered vesicles, 3) planar or sheet-like bilayers, 4) inverted micelles as explained in Figure 8 with geometric profiles.[21] The formation of these structures depends on various factors, including the nature and concentration of lipid molecules, hydration, temperature and pH of the system etc. The sheet-like structure, either symmetric or asymmetric, phospholipid bilayers are found most in nature (most energetically favourable system).[8,21]

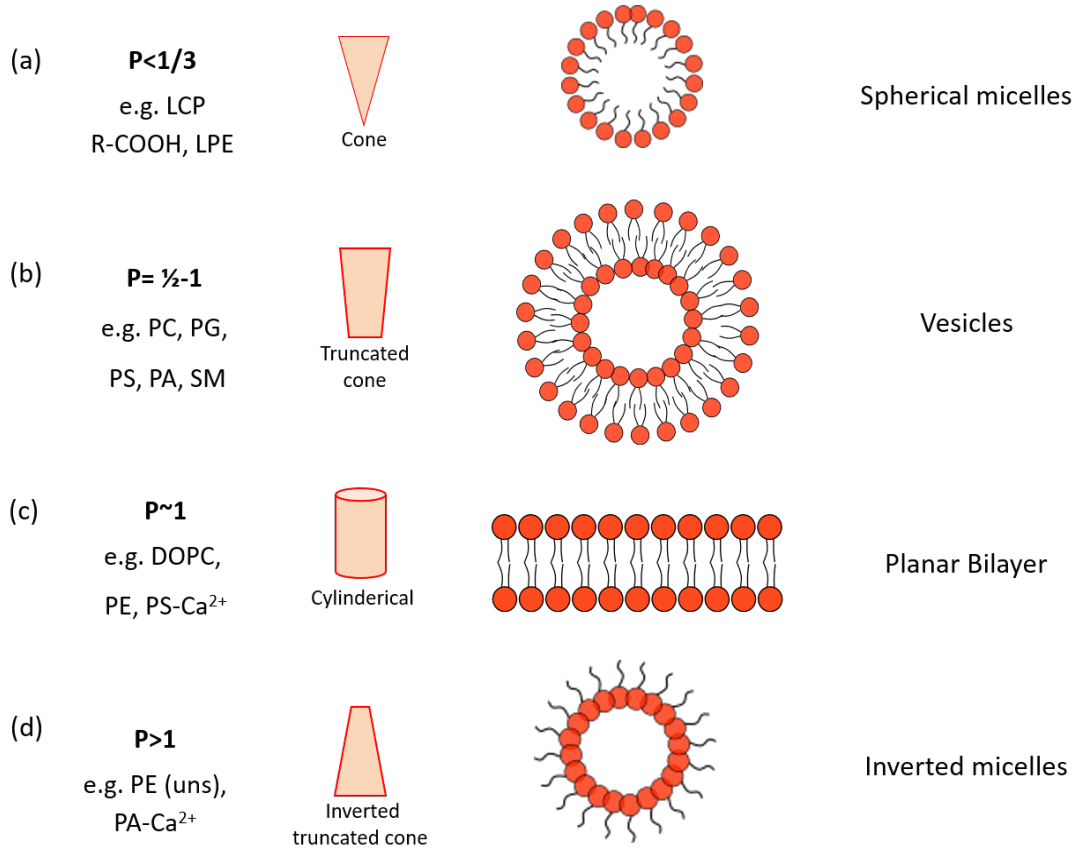

Figure 8. Schematic representation of the phospholipid bilayer assembly.
There are four different shapes that lipids can render naturally depending on the *P* factor such as, a) A spherical micelle to shield the hydrophobic fatty acyl tails from the aqueous environment. b) A spherical liposome composed of a phospholipid bilayer enveloping an aqueous core within. c) The hydrophobic effect and van der Waals interactions between the fatty acyl tails induce a planar bilayer assembly, and d) the inverted micelle.

Whereas, micelles are the spherical aggregates with bulky fatty acyl chains into the interior that are considered as the rarest form of the phospholipid structure.[3,22] The packing of lipids in these shapes can be explained with Israelachvili-Mitchell-Ninham packing parameter (P), using a simple geometric property of the lipid molecule.

$$P = \frac{v}{al} \qquad (1)$$

where *v* is the lipid volume, *a* is the cross-section area of the head group, and *l* is the length of the lipid molecule. The P-value is useful to predict the structure of the lipid assemblies, as shown in Figure 8. If the P-value is close to 1, the structure is bilayer as represented in equation 1. These are usually cylindrical (Figure 8 c) or truncated cone (Figure 8 b) phase that packs tightly whereas the non-bilayer phase is among the packing parameter value far from 1.[19] For example, lipids with P-value less than 1 induces positive curvature and form micelles, while the value is higher than 1 induce negative curvature and form inverted micelles.

1.3.1.2 Semi-Permeability of the Lipid Bilayer

The bilayer is selectively permeable only to ions, small molecules hence require the integrated mesh of transporter proteins to import and export the specific metabolites, as suggested in the fluid mosaic model (Figure 4) of the membrane.[1,6] Small, hydrophobic, and nonpolar molecules can diffuse immediately through a pure lipid (protein-free) bilayer, Figure 9. Although, the passage of most polar or large molecules is limited due to the hydrophobic core of the lipid bilayer.[23] The large uncharged or ionic molecules can cross the membrane but in considerably more time than small uncharged molecule or gases.[6]

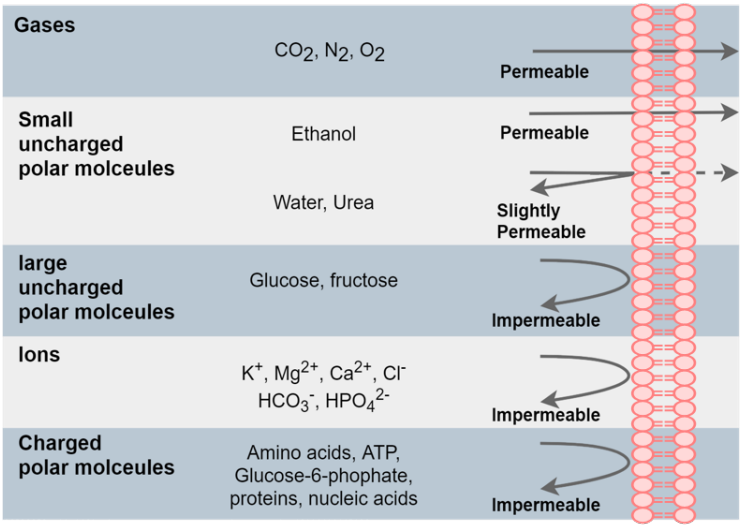

Figure 9. Schematic Representation of a Relative Permeability of a lipid bilayer. Permeability of a lipid bilayer to different classes of molecules such as small molecules. A phospholipid bilayer is selectively permeable to gases and small, uncharged, and polar molecules. Whereas, impermeable to ions, charged or uncharged and large polar molecules.

Integral transmembrane proteins selectively transport molecules and ions from one side to the other, under a thermodynamically unfavourable process that can occur only when external energy is applied. These are the modes of ATP driven transport, known as active transport where membrane proteins are involved.[1,6,8,20] The movement of nearly all the large molecules is favoured by membrane transport proteins. Whereas, only gases such as O_2 and CO_2, and small uncharged nonpolar such as water, urea, and ethanol, can cross the membrane through bilayers via simple diffusion. However, the pore formation in membranes can also induce transport of molecule.[24,25]

1.4 Construction of a Synthetic Cell

There have been many attempts to mimic the cell, with a functional cell-like structure known as a synthetic cell. The field of synthetic biology involves the construction of artificial biological systems, which is different from the fundamental biological research where the investigations are performed to identify the natural phenomena in natural cells.[7,26] Synthetic cells are designed for engineering a minimal cell-like entity to address the basic research into cell functioning. Besides, the designed cells are used as bioreactors, drug delivery vehicles in therapies, immunological vaccinations, signal carriers in diagnostics and biofuels. Synthetic biologists aim to go above and beyond to engineer biological models and to build a highly functional artificial cell with its own genomes, Figure 10.[8,26,27] In the past, two main engineering approaches have been thoroughly studied to produce a novel synthetic system with desirable properties, namely Top-down, and Bottom-up.

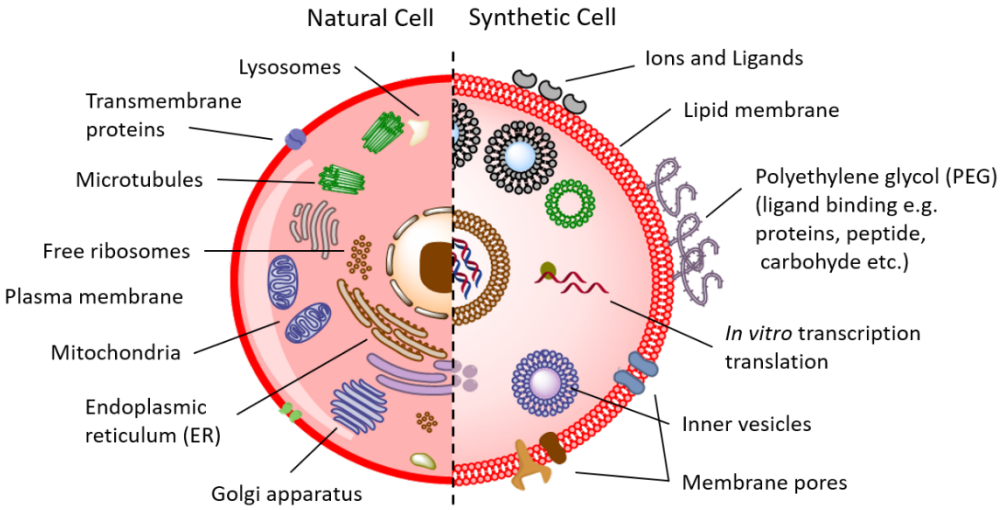

Figure 10. Construction of an artificial cell that mimics a natural one.
Modelling a synthetic cell by engineering the plasma membrane with phospholipids bilayer or decorated with Poly (ethylene glycol) (PEG)-ylated lipids, embedded protein-pores as gateways, and targeting ligands for stimuli-response. This also includes subcellular compartments within the future artificial cell and a biomimetic nucleus with distinct functions, such as *in vitro* transcription–translation.

1.4.1 Top-down Approach

A top-down approach involves a host cell with an additional foreign element or module. The host cell already contains machinery to use the cofactors, metabolites, for general functioning from its surroundings.[28] A modification can be introduced with an enzyme-encoding gene that incorporates into the host cell and produces a molecule of interest. Thus, the new modified model will be responsible to perform the given function utilising the additional gene. For example, a metabolic or signalling pathway of a cell can be transformed with a pathway from different species, resulting in a new pathway. The top-down method also includes *in silico* modelling of the systems, which has been remarkably valuable only by using the genome data including whole-system analysis. The first genomic description using the bioinformatics analysis was provided in 1996 by

Mushegian and Koonin by comparing three fully sequenced bacterial genome.[29] Top-down models have the advantage of using the host cell (known as the chassis), to utilise the existing biochemical machinery of the host. These models can be either prokaryotes or eukaryotes, where the cofactors, metabolites, and transcription pathways are modified for the synthetic system.[30] However, there is a disadvantage of potential crosstalk within the chassis between two modified synthetic systems.[31,32]

1.4.2 Bottom-up Approach

In the past decades, bottom-up synthetic biology has developed towards the goal of building a minimal system using non-living components. The approach uses cellular components such as lipids, nucleic acids and enzymes reconstituted enzymes to form a minimal living cell *de novo*.[26,28] A minimal cell is defined as a cell-like structure composed of a basic set of building blocks essential for the biochemical characteristics of a living cell such as ATP production.[13] As discussed in chapter 1.3.1.2, the semipermeable nature of the lipid bilayer membrane constitutes a selective barrier, which allows the controlled diffusion of molecules. The diffusion across the membrane generates the exchange of hydrophilic molecules on the membrane, which thereby allows the passage for many signalling pathways and metabolic activities.[1,6,27] In contrast with the top-down approach, which aims to reach this goal by modifying and reducing the genome of the pre-existing organisms. In the bottom-up approach, biological cells are mimicked in a simplified and controlled manner, primarily by creating the enclosed biomembrane.[33–35] There are alternative compartments available such as water-in-oil droplets, liquid-phase droplets, and polymersomes, however, GUVs are considered as the gold standard due to their natural biocompatibilities.

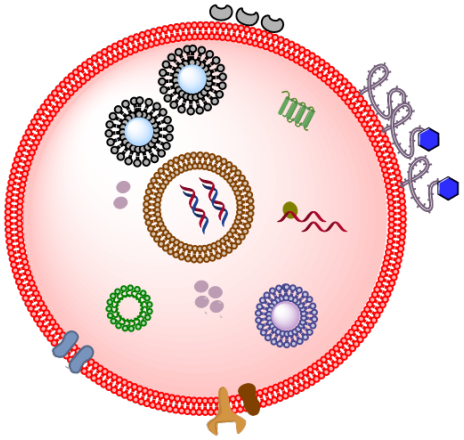

Figure 11. Simple construction for the lipid-based synthetic cell system.
The bottom-up approach can use a lipid-rich bilayer membrane forming a liposome or vesicle as a compartment. The membrane is studded with proteins, i.e. transmembrane transporters, or with pore-forming protein such haemolysin, or other ligand-receptor units. The lipid bilayer can be further modified to be asymmetric (across the bilayer) using a variety of lipids. They can also contain internal synthetic organelles composed of small lipid vesicles to process various biochemical reactions. These multi-compartment lipid vesicles are sometimes referred to as vesosomes.

Recent progress towards creating a synthetic cell, ranging from minimal protocells to multi-compartment synthetic cells demonstrate that the synthesis of life is realistic but in contrast to the top-down method, it requires a large amount of work.[7,23,35,36] The main

advantage of the bottom-up is its minimal system that does not possess the natural complexity of the existing biological system, Figure 11. Synthetic cells are the potential basis of a new generation synthetic analogues that will eventually be capable of self-repair, responding to their environment and interacting within biological cells. The growth in bottom-up synthetic biology towards constructing cell-like structures has opened potential ways across a range of applications.[37–40]

Theoretically, the construction of a minimal cell from the bottom-up is possible by mimicking and redesigning the natural structure from individual components, such as sugars, lipids, proteins, and genetic material.[3,41] Systems with highly controlled size, molecular organisation, and compartmentalisation are advantageous, in the case of an individual reaction traversing from reactant to product through the neighboring compartments with or without transmembrane protein or pores within two or more compartments. In a work by Elani *et al*., a three-step glucose oxidation reaction was performed in a multicompartment liposome.[42] The reaction includes three steps 1) formation of glucose from lactose by lactase 2) Glucose oxidation by glucose oxidase resulting in the hydrogen peroxide production. These two steps take place in the same compartment whereas, the hydrogen peroxide permeate through the bilayer to an adjacent compartment to 3) oxidise Amplex Red, in the presence of horseradish peroxidase (HRP) as a resultant resorufin, a fluorescent molecule, is produced and detected using fluorescence microscopy.[31,43] Hereby, the multistep enzymatic pathways are established in a two or more synthetic compartment vesicle. To provide communication between the compartments using membrane-impermeable molecules, transmembrane pores can be introduced such as alpha-hemolysin, a membrane pore protein.

1.4.3 Liposomal Model for Synthetic Cells

Liposomes or the lipid-based membrane systems are widely used as a framework for synthetic cells to host a range of biological processes, and to study various membranes properties such as cell-cell communication, cargo transport, intercellular molecular synthesis, and cell-protein interactions.[8] These are fully enclosed lipid bilayer-based structures with both interior and exterior aqueous environments composed mainly of phospholipids which serve as a simple micro-compartment (Figure 11).[44–46] They are mainly characterised based on their sizes, as seen in Figure 12, such as small unilamellar vesicles (SUVs) below 100 nm diameter, large unilamellar vesicles (LUVs) 100-1000 nm, and giant unilamellar vesicles (GUVs) >1 μm.[8] The unilamellarity of the liposomes indicates a single bilayer sheet as represented in Figure 12.

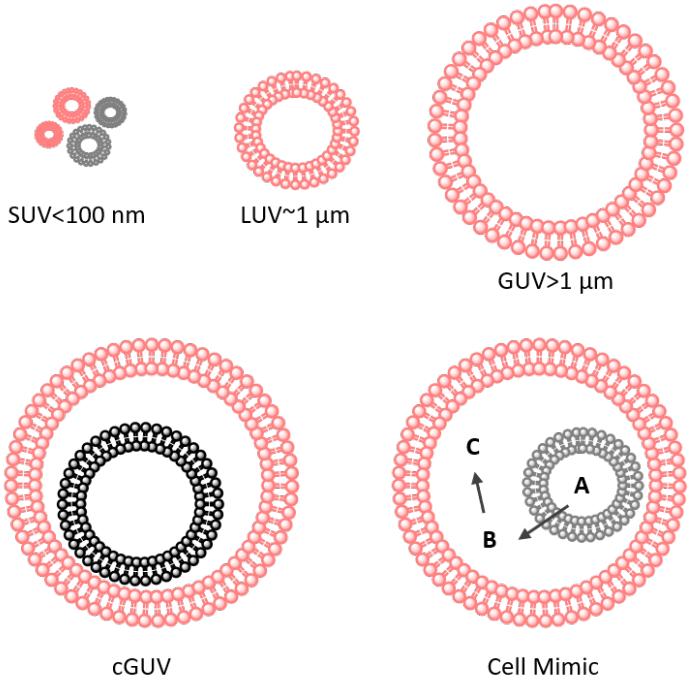

Figure 12. Main classes of liposomes.
Small unilamellar vesicles (SUVs) are less than 100 nm in diameter; large unilamellar vesicle (LUVs) is between 100-1000 nm; giant unilamellar vesicle (GUVs) are larger than 1 μm in diameter, and with these existing systems the modern goal is to develop compartmentalised GUVs (cGUVs), and the end application will be to establish reaction within and across the compartments. Not to scale.

GUVs are the preferred candidate due to their membrane's similarity (size and curvature) to that of a mammalian cell. Moreover, they are giant and visible by optical microscopy unveiling the biological events.[3,47] With advances in technologies, such as microfluidics for their production and handling, GUVs are becoming increasingly more biocompatible.[36,48,49] These model membranes are being increasingly used to comprehend biological processes on the membranal level. Other potential biomimetic GUVs are compartmentalised GUVs (cGUV) with small vesicle inside as a distinct compartment, and other more innovative models with more than one compartment are known as eukaryotic cell mimic. However, using conventional techniques to form them still remains challenging; i.e. encapsulating large or charged biomolecules inside giant vesicles.[50–53]

Microfluidic systems have been demonstrated as excellent platforms for the preparation of monodisperse liposomes with high precision lossless encapsulation of biomolecules.[51,54] Conventional techniques do not readily yield the encapsulation of large biomolecules or offer control over size or yield.[3,55,56] However, the production of GUVs employing microfluidic systems involve complex, time-consuming setups and intense instrumental manipulation.[50,57] Whereas, the emulsion-based method (explained below) have shown great promise in encapsulating macromolecules such as polymers,[58] DNA,[59] enzymes,[60] cells[61] and even micron-sized particles.[62] This GUV preparation method is acknowledged for the notably high encapsulation efficiency of macromolecules compared to swelling-based methods. In the context of a subsequent application as micro-reactors, GUVs produced by the emulsion-based methods are readily compatible with biological reactions.[63–66] Finally, multi-compartment liposomes are being developed using surfactant-assisted microfluidics systems with water-in-oil-in-water (W/O/W) double emulsion droplets as hierarchical assemblies towards the goal of the synthetic cell.[67]

1.4.4 GUV Production Techniques

Several platforms have developed many conventional techniques to create GUVs, such as electroformation of dried lipid membranes, gentle hydration or swelling, and freeze-drying, represented in Figure 13. Additionally, modern techniques such as the emulsion-based method and microfluidic devices have the ability to produce multi-compartment GUVs,[43,68] symmetric/ asymmetric liposomes, polymersomes,[69,70] proteasomes,[52] and additional application in producing coacervates.[22]

1.4.4.1 Gentle Hydration

Since a phospholipid bilayer spontaneously seals and forms and closed liposomal structure without applied electric field, represented in Figure 13 a. The method requires no external field while the liposomes are gradually formed upon hydration with an aqueous solution. The method is well known for the interaction studies such as membrane-protein, membrane-particles, membrane curvature and nanotube within vesicles. Liposomes can be produced using a variable range of temperature, a variety of solutions with varying osmolarities/physiological buffers, and lipid mixtures. The method can assist the encapsulation, as opposed to electroformation, but the process is often time-consuming.[3,71,72] Often the liposomes are small (in order of SUVs to LUVs) heterogeneous distributed and categorised from unilamellar to having multiple lamellae.[36] However, there have been attempts to expand the application of the method as seen in a recent study: a highly advanced synthetic photosynthetic organelle was demonstrated with a controlled ATP-dependent cytoskeleton formation (actin polymerisation) within the GUVs, using the hydration method in the combination with the electroformation method.[14]

1.4.4.2 Electroformation

Electroformation is one of the conventional swelling techniques known for the GUV preparation using an applied electric field, shown in Figure 13 b. Electroformation increases the vesicle production by enhancing the electrostatic repulsion between the bilayers with electric fields in a few hours. Although, the method still fails to efficiently encapsulate large quantities of water-soluble molecules such as enzymes, and charged molecules, other macromolecules, the method is well known for membrane studies. It

produces single-bilayer liposomes under relatively high voltages, and mainly results in multi-layered membranes under lower voltages.[55,73] However, the method is better suited to liposome production at relatively low osmolarities compared to other methods, with possibilities of modifications for specific applications and efficiently produce high volumes of GUV samples for bulk experiments.

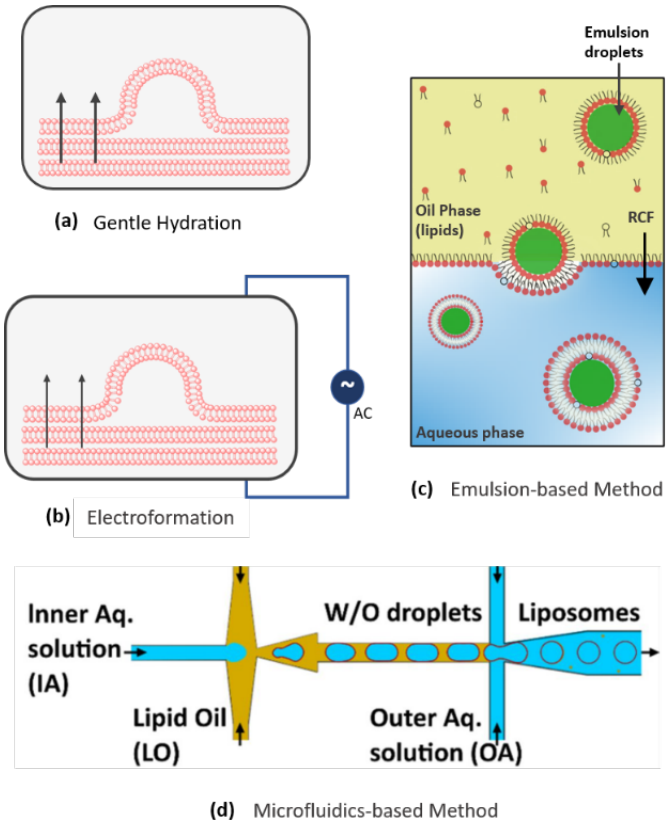

Figure 13. Overview of some of the frequently used methods for the GUV formation. (a) Gentle hydration b) Electroformation; (c) Emulsion-based method; (d) Microfluidic *(microfluidic scheme from Yandrapalli et. al 2020).*[79]

1.4.4.3 Emulsion-based Method

The emulsion-based technique shows great promise in encapsulating various macromolecules (at high concentrations). The method is also used to produce GUVs with complex lipid mixtures providing diverse symmetric/asymmetric membrane systems. The method's name implies two-phases; oil phase and aqueous phase, that when combined segregates, Figure 13 c. The amphiphilic lipid molecule, therefore, assembles as monolayers at the interfaces of the aqueous phase. The emulsion is further added on the oil phase, where emulsion droplets transverse the monolayer and form bilayered GUVs. Moreover, to generalize the applications towards a minimal cell, a method must readily provide encapsulation of the varying range of salt concentrations, pH, and charged/uncharged macromolecules.[59,65] The method can be modified with the possibility to harvest the GUVs upon formation. For this GUV production is performed inside an Eppendorf Tube, and by pricking a hole using a needle-tip into the bottom of the reaction chamber (Eppendorf Tube).

For the harvesting, closing the lid back produces an air pressure within the tube which causes the GUV solution to flow out.[74] Despite this, the method suffers from a few drawbacks such as poor yields or polydisperse sized GUVs. For this reason, very few groups have adapted the method and often prefer more established techniques such as electro- or gentle-hydration, even if these choices limit the range of experimental possibilities.[67,75] Moreover, since a typical procedure needs the lipid-oil mixture in the oil phase, added on top of an aqueous solution to form an oil-water interface, there are possible chances of oil contamination in the membrane.[42,76] This could be a major setback for the widespread acceptance and usage of this method, even though a couple of studies have shown no significant changes in the membrane mechanics of GUVs prepared from the emulsion-based method.[77,78]

1.4.4.4 Microfluidic Methods

GUV formation using microfluidic-based techniques such as droplet phase-transfer, pulsed jetting, and double-emulsion methods is becoming widely popular.[79] These techniques are advantageous for direct control over the sizes, high-throughput production and for the encapsulation study, merely using small volumes.[22] Microfluidic devices are also able to apply different types of lipid compositions and can produce symmetric and asymmetric GUVs. Moreover, many microfluidic-systems has applied organic solvents (n-alkanes) for the production of monodisperse GUVs and further encapsulation.[23,80] As stated, the emulsion-based method can result in membranes having unwanted oil residues, and microfluidics offers to eliminate the risk of this contamination. As reported, surfactant-assisted dewetting phenomena of double-emulsion, leading the formation of oil-free multicompartment liposomes, achieving complete dewetting. The unilamellar and oil-free nature of the bilayer was confirmed by reconstituting the melittin and α-HL into liposomal bilayers and quantifying the fluorescence transport over time.[37] These model systems have been extremely beneficial for the direct encapsulation of the different aqueous solutions, including enzymatic cascades and receptor-ligand based suspensions.

In a study, microfluidics-based encapsulation of liquid-liquid phase separation systems and unpolymerised FtsZ, active protein into microdroplets was presented.[81] Asymmetry in the lipid membrane is also essential to fully replicate the functions of the cellular membrane. A microfluidic system using a pulse jet flow on a planar lipid bilayer has been shown to produce cell-sized asymmetric GUVs.[82] The asymmetry was investigated with various processes associated with biological membranes such as phospholipid translocations (i.e. flip-flop), and lipid–membrane protein interaction using *in vitro* synthesis of CX43-eGFP.[80] Although microfluidic systems have been demonstrated as excellent platforms for the preparation of monodisperse GUVs with high precision lossless encapsulation of biomolecules, their practice involves complex time-consuming instrumental setups, which are not always convenient for the particular application.

1.4.5 Techniques to visualise GUVs

Microscopes are universally applied over the fields of biology to produce images of the structures and internal features in nature. These magnified images of the micron size objects are often known as micrographs. The microscopes are classified with the number and the nature of magnifying glasses combined with the instrument. However, the current microscopes are divided into three major classes, 1) optical microscope, 2) electron microscopes, and 3) scanning probe microscopes.[83] In this thesis, optical microscopy was utilised to visualise GUVs, with the mode of illumination as light. A typical optical instrument consists of one or more biconvex lenses providing an enlarged image of the sample, Figure 14.[84] The most commonly exercised optical microscopes in this study are phase-contrast and fluorescence microscopy. The phase-contrast microscopy is an illumination technique that does not require labelling of the sample, whereas, in fluorescence microscopy, labelling with fluorophores is essential.

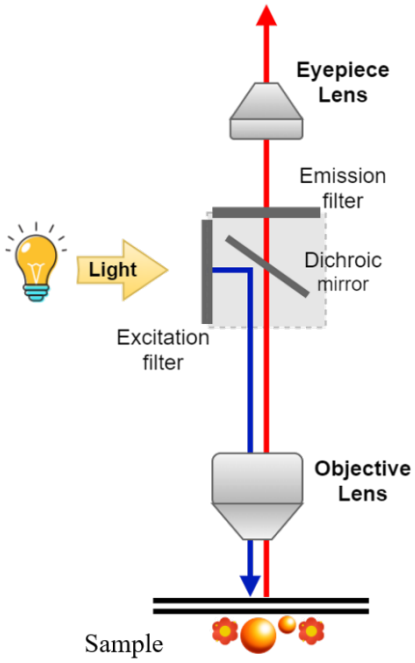

Figure 14. The optical settings for an epifluorescence microscope.
A simplified representation of the optical pathway and the principal component utilised in the epifluorescence microscope.

1.4.5.1 Fluorescence Microscopy

In 1911, Oskar Heimstädt developed the first fully functional fluorescence microscope to study autofluorescence within organic and inorganic compounds. Fluorescence microscopy is a highly sensitive technique that provides an efficient way to study a variety of biological systems.[84] The basic principle of fluorescence in a biological context involves the irradiation of a fluorescently-labelled molecule in a sample with a certain wavelength, and to collect images with the emitted fluorescence. The emission is at a longer wavelength and hence it has specificity and better signal to noise ratio compared to other optical microscopic techniques. Molecules that exhibit fluorescence properties are commonly known as fluorescent probes, dyes, or fluorophore.

In this thesis, various fluorescent probes were utilised; eGFP labelled enzymes, calcein dye, fluorescamine, and lipid membrane labels such as DiI and NBD-PE.

1.4.5.2 Theoretical Background to Fluorescence

The physical phenomenon of fluorescence, as explained in the Jabloński energy diagram, follows a series of steps where electromagnetic radiation at a specific wavelength is absorbed, with the emission of photons with a longer wavelength.[85] The Jablonski energy diagram explains the physics behind the fluorescence event inside the fluorophore (see Figure 15).

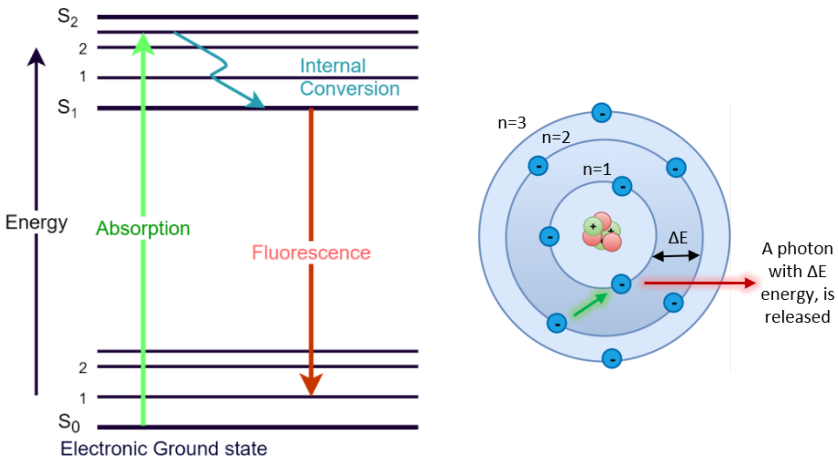

Figure 15. Jablonski diagram presenting the phenomenon of fluorescence. with the aid of energy absorption from the light source, including vibrational levels for absorbance, non-internal conversion, and fluorescence. Along with a schematic of the classic Bohr model of an atom representing the principle of fluorescence.

The diagram representing the electronic (energy) states, with S_0 indicating the lowest energy state or ground state, S_1 indicating the first excited energy state, and S_2 is the second excited energy state. There are many sublevels within these energy states of the electrons representing different vibrational or rotational sub-states. Electrons typically reside in their lowest energy state or ground state S_0, unless irradiated with a beam of a photon. When a beam of light with one wavelength reaches a fluorescent sample, the sample absorbs a quantum of light in the form of energy. Once the fluorescent molecules gain the energy, it pushes the valence electron out of the ground state into a higher energy state S_n in femtoseconds with energy $\Delta E = E_{sn} - E_{so}$. However, not all the incident photons get absorbed, the whole process completes within the femtosecond range, and the energy of the photons involved in fluorescence is given by Planck's law in equation 2,

$$E = h.v = h\frac{c}{\lambda} \qquad (2)$$

where E is the quantum's energy, h is Planck's constant, ν the frequency, λ is the wavelength of the photon, and c is the speed of light. There can be many sublevels of the excited state (vibrational levels) which varies sample to sample depending on their fluorescent properties. The excited electron in the higher energy level Sn immediately (in the picosecond range) jumps into the lowest level in the excited state (S_n) after losing its energy to vibrational energy, this phenomenon is called an internal conversion. The excited electron eventually befalls into the ground state with the release of energy

equivalent to transition energy, as shown in Figure 16.[85,86] After this phenomenon, the emitted photon has lower energy than the absorbed photon and therefore a longer wavelength, which is detected in fluorescence microscopy.

1.4.5.2.1 Confocal Microscope

Confocal microscopy is an advanced optical imaging technique and frequently known as confocal laser scanning microscopy (CLSM). It is widely recognised for its enhanced optical resolution, particularly in the z-plane. The basic principle of a confocal microscope includes two simultaneous processes; first is the scanning of the illumination, where the irradiated beam of light focused into the specimen and scans the individual section of the specimen in a sequence. Second, scanning of the detected signal, the illuminated signals from the specimen simultaneously enters the detector while the specimen being scanned while passing through the pinhole (discussed later in detail) with an additional subtraction of out-of-focus signals. This means that CLSM can generate high-resolution images (using an objective lens) with small structures in a selective depth (optical section) and produce 3-D images after reconstruction from data. The objective lens is a central component in the quality and the resolution of optical images. Generally, a microscope consists of 3, 4 or more objective lens with 10x, 20x and 40x magnifications that gathers light from the object.

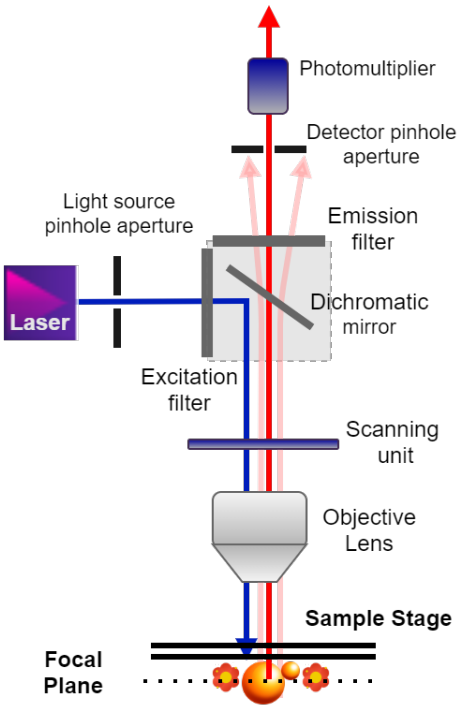

Figure 16. The optical settings for a confocal microscope.
A simplified representation of the optical pathway and principal component of the confocal laser-scanning microscope. A coherent tightly focused laser beam directs onto the sample by a dichromatic mirror, as the light source and causes the excitation. The pinholes filter the out-focus light, where only the in-focus light reaches photomultiplier and are detected.

The lens has a complex and multi-element design that collects light from the specimen and generates a real optical image. In CLSM a laser beam is employed as the source of

light, where the intensity of the laser can be adjusted with neutral density filters. The laser illumination takes place through two oscillating mirrors, that can be tuned precisely and very quickly onto the back focal plane of the objective, and further focusing on the specimen as shown in Figure 16.[86–88] The advantage that the confocal microscope provides over conventional fluorescence microscope is the spatial pinhole aperture which provides 3-D sectioning of the samples. A pinhole installed in front of highly sensitive detectors, which enables the elimination of all the out-of-focus signals. Since the signal emerging from CSLM vary in their intensity, the highly sensitive detectors such as photomultiplier tube (PMT) are employed to amplify the signal intensity. The pinhole is a circular hole with a diameter in micrometres range that acts as a physical barrier to blocks out-of-focus light from the acquired optical image. The pinhole size can vary to allow more or less light through depending on the size, where the usual size is one Airy unit (A.U.) resulting in the best signal to noise ratio and can be defined with the given equation 3-

$$d_A = \frac{1.21\,\lambda}{NA} = 1\ Airy\ Unit \qquad (3)$$

d_A is the size of a pinhole, λ is the wavelength of the emitted light from the specimen and NA is the numeric aperture of the objective lens. The size of the pinhole is inversely proportional to the numeric aperture of the lens, meaning that by employing an objective with higher NA such as 63x magnification or higher, or emulsion objectives, the out-of-focus light can be better blocked.[88]

1.5 The Biological role of Molybdenum

Molybdenum is an essential component for metalloproteins that is present in trace amounts amongst all the living forms. The first evidence of molybdenum being essential was described in 1932 by a Dutch scientist Prof. Ir. H. ter Meulen, from experimental studies on the everyday plants and organic materials.[89] Following decades of work, it is now universally recognised that molybdenum plays a vital role in prokaryotic and eukaryotic cells.[90,91] The biologically active state of molybdenum is an oxyanion molybdate (MoO_4^{-2}) which is introduced to cells via specific (as represented in Figure 17), and unspecific transport systems (sulfate carrier superfamily and phosphate uptake system, not shown here).[92] The molybdenum is a 4d transition metal with varying oxidation states ranging between VI and IV, which make it an excellent catalyst for redox reactions in global carbon, nitrogen and sulfur cycle.[90,93] In almost all the molybdenum-containing enzymes, a mononuclear molybdate is found in a bound state with a tricyclic structured pterin molecule through dithiolene moiety.[93] Molybdenum is an essential element for the basic functioning of various biological processes, with catalytic reactions such as oxidation of sulfite, hydroxylation of purines and pyrimidines, oxidation of purines, pyrimidines and pteridines.[94] In a recent study, Moco-dependent anaerobic enzymes were found to have a significant role in the inflammation-associated bloom of the gut microbiome.[95]

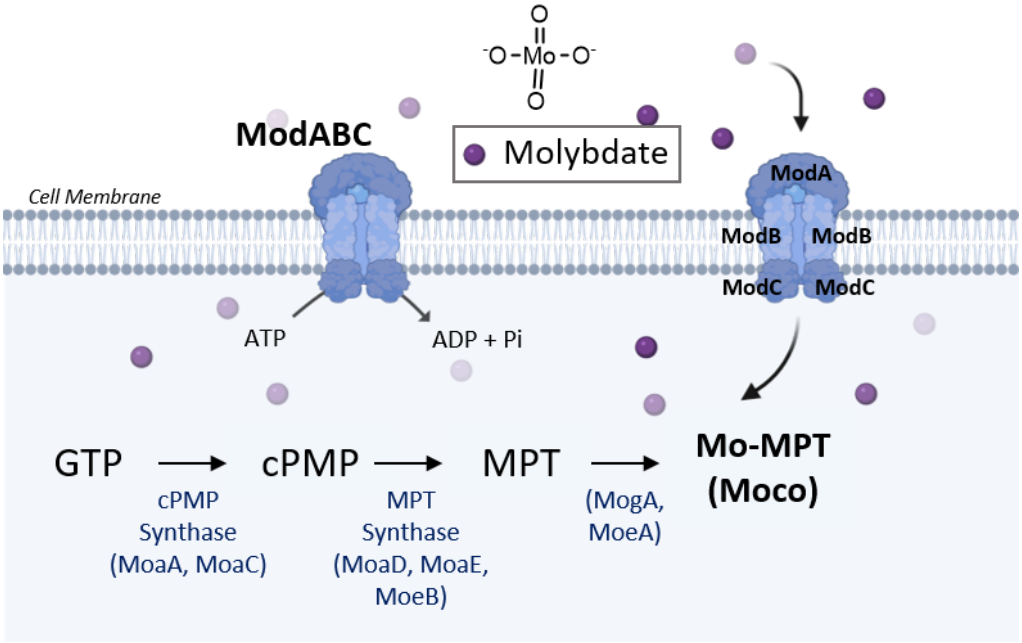

Figure 17. Overview on Moco Biosynthesis.
The oxyanions transport system indicated in the schematics representing, the high-affinity ModABC molybdate transporter, regulated by ModA (the molybdate-binding protein), ModB (the membrane protein), and ModC (the ATPase). The molybdate once transported to the cells, it further binds to molybdopterin (MPT) to finally form molybdenum cofactor (Moco).

1.5.1 The Structure of Molybdenum Cofactor

The molybdate (molybdenum anion) in the cell upon binding with the MPT molecule, produces an active entity known as molybdenum cofactor (Moco). The free molybdenum atom is coordinated on the dithiolene group on the 6-alkyl side chain on MPT molecule to form an active Moco molecule (represented with Figure 18).[96,97] Moco is an essential organometallic cofactor, responsible for the catalytic activity of the entire molybdenum-containing enzyme (molybdoenzymes) family. Like many other organic cofactors, Moco is not accessible as nutrition and must be synthesised de novo.[97] The basic structure of Moco is highly conserved, as shown in Figure 18 demonstrating a heterocyclic-pyrano connected with a pterin ring with two sulfur atoms acting as the ligated to the mononuclear molybdenum.

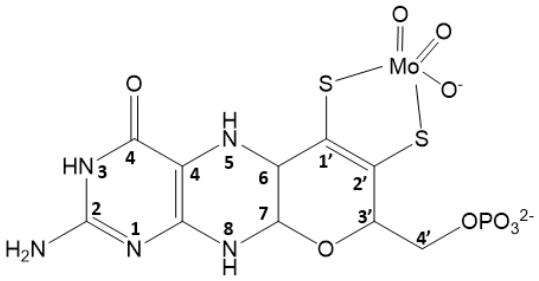

Figure 18. Structure of Molybdenum cofactor.
The structure includes the basic form of a 5,6,7,8-tetrahydropyranopterin (MPT) with a dithiolene group and a heterocyclic-pyrano-pterin ring, coordinated to the molybdenum ion, naming it metal-containing pterin (MPT).

While the first few shreds of evidence from genetic studies confirm the existence of the Moco, the later incorporation studies confirm instability of the free-Moco with a lifetime of only a few minutes. However, the structural characterisation of Moco was made possible using two distinct stable degradation products, Form A and Form B.[98,99] There have been more than 50 molybdenum-containing enzymes identified in bacteria (majorly), and archaea, whereas only four and five in animals and plants. The molybdenum-containing enzymes or molybdoenzymes are categories based on the structural coordination of their central molybdenum atom and are divided into three main families in bacteria, 1) sulfite oxidase (SO) family, 2) xanthine oxidase (XO) family, and 3) dimethyl sulfoxide (DMSO) reductase family.[100]

1.5.2 The Biosynthesis of the Molybdenum Cofactor

As seen in Figure 17, the molybdenum made available to the cells mainly either specific via the high-affinity ModABC molybdate transporter, which is known to be regulated by ModA (the molybdate-binding protein), ModB (the membrane protein), and ModC (the ATPase). Additionally, with low-affinity with the CysPTWA sulfate-thiosulfate permease and unspecific transport systems that include sulfate carrier superfamily and phosphate uptake system.[92] The Moco is synthesised inside the cell *de novo*, under a highly conserved pathway that has been studied extensively over the past decades. The pathway in eukaryotes, represented in Figure 19, is mainly separated into three steps (1) starting with the rearrangement of guanosine 5'-triphosphate (5'GTP) to cyclic pyranopterin monophosphate (cPMP), (2) the conversion of cPMP to form MPT, (3) insertion of

molybdenum atom to transform the MPT molecule to Moco. And (4) additionally, the modification of Moco with different nucleotides such as CMP to generate molybdopterin cytosine dinucleotide cofactor (MCD) or GMP to generate molybdopterin guanosine dinucleotide cofactor (MGD).[94]

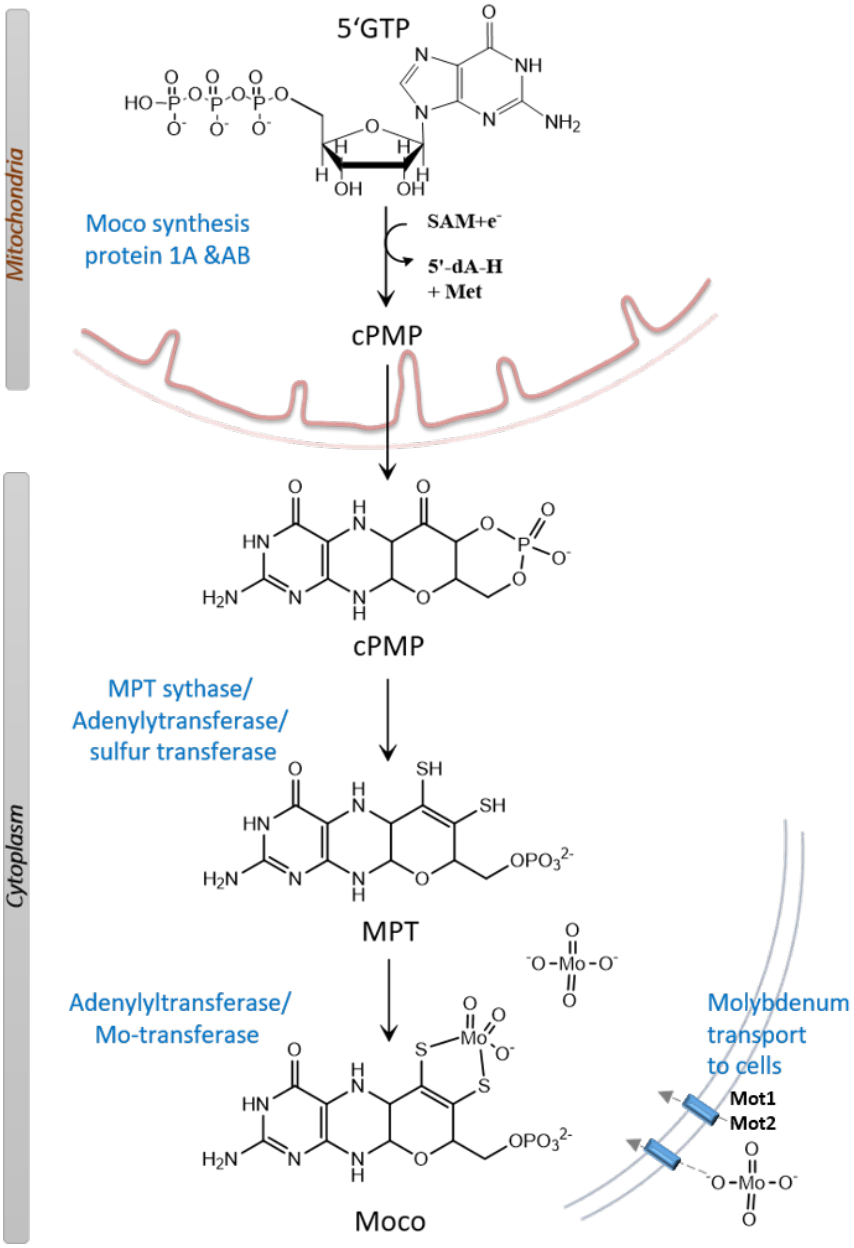

Figure 19. Schematics of Moco biosynthesis in Eukaryotes.
The pathway starts with the conversion of 5'GTP to cPMP in the presence of Moco synthesis proteins inside mitochondria, followed by translocation of cPMP into cytosol. In cytosol MPT synthase transfer the sulfur which enables the conversion of cPMP into MPT, and thereby the formation of Moco occurs on the insertion of molybdate. Whereas, in case of bacteria, this biosynthesis occurs in a single compartment.

The pathway starts in the mitochondrial matrix, for eukaryotes where every step of the biosynthesis is specifically regulated and catalysed by the combination of enzymes. The biosynthesis is ubiquitous in all biological kingdoms, and the bacterial system will be

studied in this thesis. However, it is not compartmentalised in bacteria and found in its single compartment. The first three steps in the pathway are identical for all Moco-containing proteins in all the microorganisms, besides the final Moco modification, which varies among the different organisms.[90] The individual steps in the pathway are described in the chapter below with details using bacterial enzymes, whereas the corresponding humans' enzymes are discussed in Figure 20.[94] There are 13 genes combined into six loci that are directly involved in the biosynthesis. They are named respectively *moa (moaABCDE), mob (mobAB), moc (mocA), moe (moeAB), mog (mogA)* and *modAB*, for high-affinity molybdate transport.[100] Six essential proteins are directly responsible for the biosynthesis in humans that are: MOCS1A, MOCS1B, MOCS2A, MOCS2B, MOCS3, the enzymes are named as MOCS (Molybdenum Cofactor biosynthesis), and GEPHYRIN. The gephyrin gene expresses 11 alternatively spliced exons and possesses the 2 domains, essential for the MPT binding, conversion to Moco, and Moco stabilization. It has two domains named G-domain (homologous to MogA), and E-domain (homologous to MoeA) which bind to the MPT molecule with high affinity.[101,102]

Bacteria	Humans	Reaction catalyzed
MoaA	MOCS1A	Formation of (3′,8-cH$_2$GTP) from 5′GTP
MoaC	MOCS1B	Formation of cPMP from (3′,8-cH$_2$GTP)
MoaD	MOCS2A	Sulfurtransfer to cPMP, formation of MPT
MoaE	MOCS2B	Binding of cPMP, formation of MPT
MoeB	MOCS3	Adenylation of MPT synthase small subunit
MogA	GEPHYRIN-G	Formation of MPT–AMP
MoeA	GEPHYRIN-E	Molybdate insertion into MPT–AMP, Mo–MPT formation
MobA	–	Formation of bis-Mo–MPT, GMP transfer to bis-Mo–MPT,
MocA	–	CMP transfer to Mo–MPT, formation of MCD

Figure 20. The list of enzymes responsible for catalysing Moco biosynthesis.
The respective enzymes involved in the Moco biosynthesis in bacteria, and humans, from GTP to molybdenum cofactor. *Image adapted from Leimkühler and Mendel, 2015.*[94]

1.5.2.1 Step 1: Production of cyclic Pyranopterin Monophosphate

The biosynthesis starts with the conversion of 5'GTP to cyclic pyranopterin monophosphate (cPMP), the first stable intermediate. In humans, the first step is localised in the mitochondrial matrix and catalysed by MOCS1A/MOC1B, in bacteria with corresponding homologous enzyme MoaA/MoaC, Figure 21.[94] In eukaryotes, the newly produced cPMP transverse the mitochondrial matrix and enters the cytosol for the later modification. The transport of cPMP from the mitochondria to the cytosol is not well understood, yet there is a hypothesis that ABC transporters play an essential role in the transport.[103] This hypothesis of cPMP transport had not accepted through the research community, where there have been contradictory speculations in the study. It is also believed that cPMP is transported through unspecific transporter or merely via simple diffusion through the membrane, being the key for the therapeutic application.[104] Whereas, this transport is a subject to establish more understanding, as described in many further publication.[105–107]

However, the mechanism of cPMP production from GTP has been thoroughly investigated in bacteria.[90,108] The bacterial enzyme, MoaA is a homodimer with each monomer comprising of two oxygen-sensitive [4Fe-4S] clusters, which belongs to radical S-adenosyl methionine (SAM)-dependent enzyme superfamily. Almost all the SAM radical enzymes hold one or more Fe-S clusters, the SAM undergoes cleavage with the aid of an electron derived from the Fe-S clusters. This cleavage leads form L-methionine, and a high-energy substrate radicle, 5' deoxyadenosyl radical (5'-dA). Consequently, this highly reactive 5'-dA eliminates an H-atom from the substrate to initiate the chemical reaction. Whereas, a conserved Fe-S cluster from the radical enzymes provides the first necessary electron for the cleavage.[109] In the first step of the Moco biosynthesis, SAM binds to [4Fe-4S] present on the N-terminal of MoaA and the 5'-GTP on the C-terminal, to readily initiates the reaction.

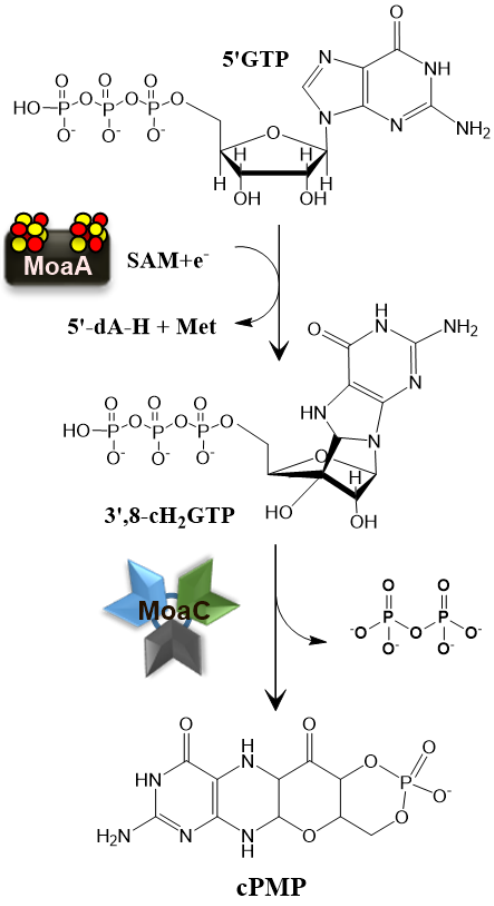

Figure 21. The transformation of GTP to cPMP.
The GTP form cPMP through intermediate 3',8-cH$_2$GTP, with SAM as co-substrate, in presence of MoaC and MoaA with a release of one PPi molecule. Note: The formation of cPMP form GTP, includes numerous intermediate steps which are neither addressed nor discussed in this thesis.

The reaction involves several intermediate steps, starting with the opening of the guanine imidazole ring to result in a 3',8-cyclo-7,8-dihydro guanosine 5'tri-phosphate (3',8-cH$_2$GTP) intermediate. The guanine C-8 formyl group is then inserted between C-2' and C-3' on the ribose ring, results in forming a 3',8-cH$_2$GTP intermediate, Figure 21. 3',8-cH$_2$GTP is an acid-labile with a half-life of approximately 10 minutes and extremely oxygen-sensitive with a half-life of approximately 60 minutes.[110,111] Further, the

intermediate 3',8-cH$_2$GTP act as the substrate for MoaC and results in the elimination of a pyrophosphate molecule from the GTP backbone. Unlike MoaA, MoaC is not an oxygen-sensitive enzyme with a hexameric structure of three homodimers, and six conserved essential amino acids for its catalytic activity.[94,110,112] This later step results in the generation of the cyclic monophosphate and thus a pyran ring through 3'hydroxyl on the pterin is formed i.e the first stable intermediate of the reaction. cPMP is the first stable intermediate in the Moco biosynthesis, but it is a highly oxygen-sensitive molecule with 6-alkyl pterin and a cyclic phosphate at the C2′ and C4′ atoms, which are later modified in the reaction. The mechanistic formation of cPMP remarkably interests the investigators due to its unique pyranopterin backbone formation.[94,96,98] The cPMP molecules are transported out of the mitochondria to the cytosol for further transformations towards the Moco formation. However, it is clear that bacterial Moco biosynthesis is not compartmentalised and would only occur in its single compartment.

1.5.2.2 Step 2: Formation of Molybdopterin

Once the cPMP reached the cytosol, the next step of the biosynthesis occurs, starting with the transformation of cPMP to MPT, the second stable intermediate. Both the stable intermediates, cPMP and MPT, are structurally identical, except the two dithiol groups present on the MPT molecule. Therefore, two sulfur atoms providing two dithiols are required for this step. The insertion of two sulfur atoms takes place at the C'1 and C'2 positions of the cPMP molecule catalysed by MPT synthase. MPT synthase is a heterodimeric protein (a tetramer) constituting two small and two larger protein domains, naming MoaD and MoaE (in bacteria), MOCS2B and MOCS2A (in humans) respectively.[94,113]

The next step in the biosynthesis occurs in the cytosol, starting with the transformation of cPMP to produce the second stable intermediate MPT. Both the stable intermediates, cPMP and MPT, are structurally identical, except the two dithiol groups present on the MPT molecule. Therefore, two sulfur atoms providing two dithiols are required for this step. The insertion of two sulfur atoms takes place at the C'1 and C'2 positions of the cPMP molecule catalysed by MPT synthase. MPT synthase is a heterodimeric protein (a tetramer) constituting two small and two larger protein domains, naming MoaD and MoaE (in bacteria), MOCS2B and MOCS2A (in humans) respectively.[97,98,114]

The crystal structure of the tetrameric bacterial analogue MPT synthase confirms the two large MoaE subunits are present at the centre, while the two small MoaD subunits reside on the opposite edges, Figure 22. In this reaction, cPMP molecules present in the keto state binds to a highly conserved active site at MoaE subunit, while being converted to MPT. Whereas, the C-terminal of MoaD domain carries the sulfur atoms needed for the cPMP modification, in the form of thiocarboxylate.[94,115] MoaD introduces the first thiocarboxylate sulfur at C'2 position to form a Hemi-sulfurated intermediate, coupled with the hydrolysis of the cyclic phosphate group of cPMP. The MoaD subunit dissociates from the MPT synthase complex upon transferring the sulfur atom, and a new thiocarboxylated-MoaD subunit (MoaD-SH) combines to renew the active enzyme complex.[97] This sulfur addition is coupled with the hydrolysis of the cyclic phosphate group of cPMP followed by the location shift of the intermediate molecule. The shifted cyclic phosphate within the enzyme complex makes the C'1 position more convenient choice for MoaD-SH to attack, Figure 22.

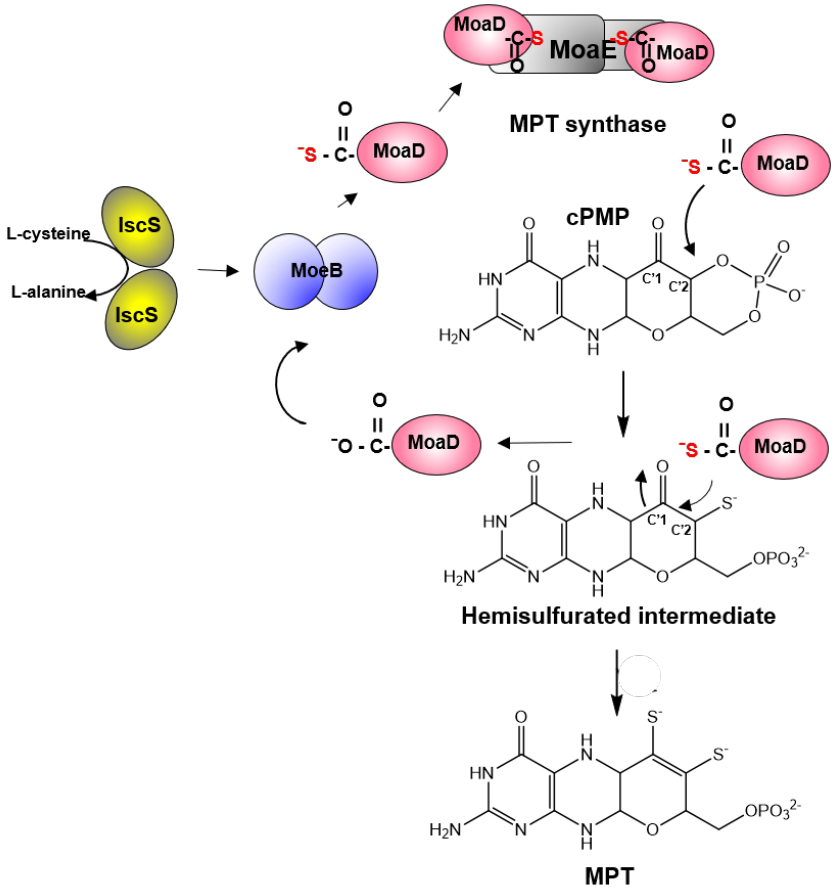

Figure 22. The second step of Moco biosynthesis, MPT formation.
cPMP in its keto state binds to MPT synthase complex, at a highly conserved active site at MoaE subunit while the MoaD domain carries the sulfur. The cPMP conversion to MPT through the incorporation of two sulphur atoms is catalysed via hemi-sulfurated intermediate. This intermediate formation is coupled with the hydrolysis of the cyclic phosphate group of cPMP. The hemi-sulfurated intermediate remains covalently attached to the MoaD subunit at the C-terminal via thioester bond and further hydrolysed with a water molecule. This MoaD subunit dissociate upon transferring the sulfur atom to form the final product of this reaction step, MPT.

Hence, the C'1 is now sulfurated, the addition of this second sulfur atom results in another sulfurated intermediate and inactive MPT synthase, forming the MPT. This exchange of carboxylated and thio-carboxylated of MoaD subunits, re-sulfuration and sulfur transfer continues until an equilibrium is achieved.[90,94] The continuous resulfuration of the MPT synthase complex is originated by L-cysteine, assembled against IscS protein and further transported to MoaD by MoeB. MoeB is known as MPT synthase sulfurase where it adenylates the MoaD at its C-terminal glycine residue (G81) forming MoaD-AMP, transferring the sulfur to produce MoaD-SH.[90,116] After the reaction of sulfur transfer, the MoaD-SH release MoeB, and AMP to re-associate with MoaE subunits to form active MPT synthase.[117]

1.5.2.3 Step-3: Insertion of Molybdate to Molybdopterin

The third and the final step of Moco Biosynthesis is the insertion of molybdenum into the MPT backbone to form the Moco. Molybdenum is introduced to cells as a soluble oxyanion molybdate, via high-affinity transporter.[92] The transformation takes place under the catalytic effect of GEPHYRIN (in human), or MogA/MoeA (in bacteria) to Moco, followed by MPT-AMP intermediate with the consumption of an ATP molecule as shown in Figure 23.[116–118] MogA and MoeA both play a significant role in the specific insertion of molybdenum into the cofactor, in multi-step reaction. MogA was the first protein in Moco biosynthesis to have elucidated its crystal structure. MogA exhibits a trimeric structure in solution, having each monomer folded into a single domain. Whereas, MoeA has a dimeric structure exhibiting an elongated monomer and four distinct domains, with one structurally analogous to MogA.[90,101] Though these enzymes are recognised to have different functions, they perform the steps in sequence. Initially, MogA forms high-affinity binding with newly synthesised MPT molecules and participates in the adenylation of the molecule forming an adenylated MPT intermediate (MPT-AMP) under Mg-depended incorporation.[100,116]

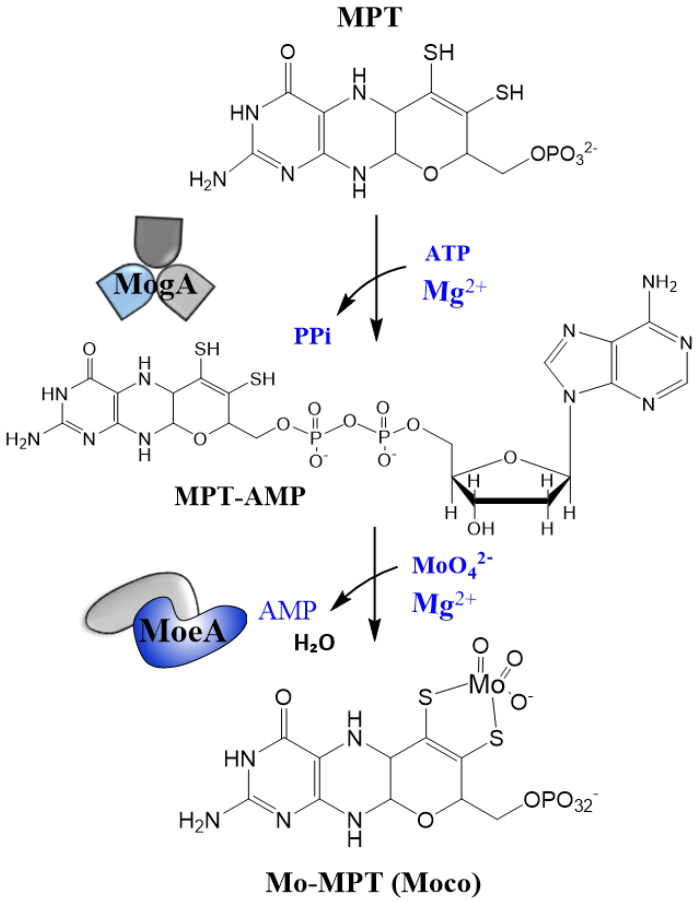

Figure 23. The third step in biosynthesis is formation of Moco.
The MPT is converted to Moco through the incorporation of Molybdenum. The reaction is catalysed by the action of MogA, and MoeA in coordination with ATP and Mg^{2+}. This step was not studied in the thesis.

Further, a molybdate atom is inserted into this intermediate under the catalytic effect of MoeA under physiological conditions, forming Mo-MPT. The end-product of the MoeA

and MogA modification is found to be attached to MoeA in a tri-oxo form, the primary form of the molybdenum cofactor. The ATP-dependent enzymatic incorporation of molybdenum and MPT is exclusive for Moco formation under physiological conditions.[108] However, it is well known that Moco can be synthesised *in vitro* by merely incorporating the pure MPT with molybdate without any additional enzyme.[93]

1.5.3 Moco-dependent Essential Enzymes

The Moco-depended enzymes are divided into three families in bacteria and two in humans. These families are identified with different modifications on the molybdenum atom coordinated in the centre, termed as coordination sphere. For example, XO reductase family consist of MPT-$Mo^{VI}OS(O^{-})$ core in the oxidised state, with the MPT bound to the molybdenum atom, one oxo-group, one sulfido-group, Figure 24. The member of SO family contains an MPT-$Mo^{VI}O_2$Cys core, while DMSO family exclusive to archaea and bacteria, contains MGD_2-Mo^{VI}X core; X, being a selenido, hydroxo or amino acid ligand (Ser, Cys, Sec or Asp).

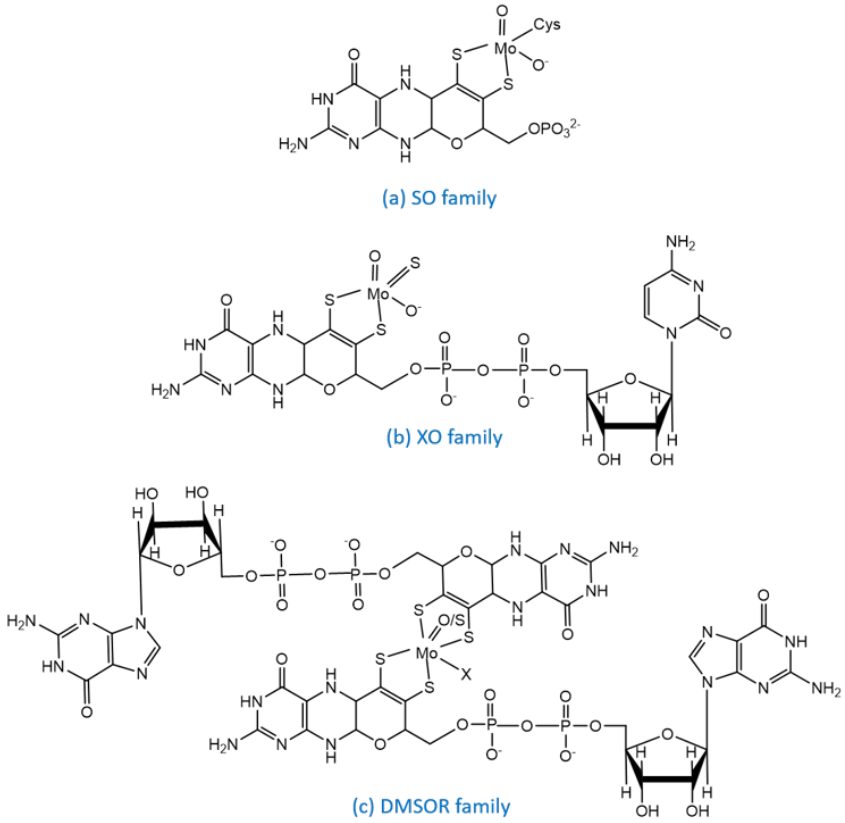

Figure 24. Molybdenum dependent enzymes in Bacteria.
As previously described three main Moco dependent families in bacteria, presenting the detailed structure of a) Xanthine Oxidase family consisting of a molybdenum core modified with one-oxo (mono), one-sulfido, and one-hydroxo group, b) Sulfite Oxidase family consisting of a molybdenum core modified with di-oxo, and proteinogenic cysteine ligand, c) DMSO family consisting of a molybdenum core modified GMP to form bis-MGD variant with one-oxo.

Whereas, in eukaryotic molybdoenzymes have been classified into two families, 1) Sulfite oxidase family, which consist of sulfite oxidase (SO), nitrate reductase (NR), and amidoxime-reducing (mARC) component the mitochondrial. And, 2) Xanthine oxidase

family, which consist of xanthine dehydrogenase (XDH) and aldehyde oxidase (AO).[117,118] Molybdoenzymes are ubiquitous among organisms except for yeast, where the complete Moco biosynthesis does not take place, with Uba4 is part of the Moco.[94] The mitochondrial proteins, sulfite oxidase and mARC are both very crucial to humans and have a cysteine ligand attached to the molybdenum core. The XDH and AO are both cytosolic enzymes, with additional sulfuration (third terminal sulfur) attached to the molybdenum centre, resulting in non-covalent binding with the cofactor. The loss of these molybdoenzymes progresses further to neurological disorders and death at an early age in humans, specifically, the sulfite oxidase (SO), which belong to SO family. The mitochondrial SO is the most crucial molybdoenzyme in humans, it is located in the mitochondrial intermembrane space (IMS) and abundantly found in the liver, kidney and the heart cells.[119] However, the loss of SO results in sulfite accumulation in the blood, causing neurological disorders.[109] Another essential enzyme is XOR, a homodimer with N-terminal domain binding two [2Fe-2S], a central FAD domain and Moco-binding domain for dimerization on C-terminal.[104,117,118] XDH is also considered necessary in human kidney development, whereas the loss of XDH activity generates a high concentration of xanthine in the blood leading renal failures.[114,118]

1.5.4 The Molybdenum Cofactor Deficiency

The insufficient supply of the molybdenum into the cell or any mutation in the biosynthesis of the molybdenum cofactor develops into a disease called molybdenum cofactor deficiency (MoCD). First reported in 1978, it is an autosomal recessive disease which was predicted to be caused by genetic mutations in proteins directly associated with the Moco biosynthesis or any of their cofactor SO, XDH, AO and mARC.[118,120] Primary symptoms involve neurological abnormalities, including mental retardation, dislocated ocular lenses, and dysmorphic features. As shown in Figure 25, the representative images of axial T2-weighted MRI brain of a 4-year-old patient showing the dislocated ocular lenses and abnormal bilateral basal ganglia. The symptoms start to appear within days after birth and typically resulting in death at early childhood.[121]

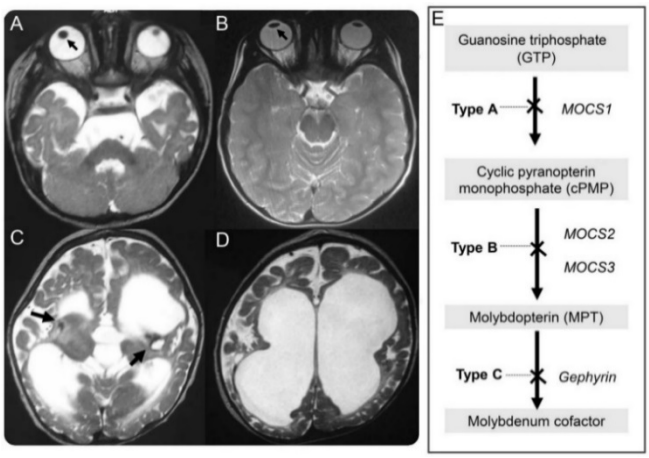

Figure 25. Axial T2-weighted MRI of a normal brain (B) and MoCD patients (A, C, D). The normal biconvex shaped ocular lenses (B) are visibly dislocated (A), along with abnormal bilateral basal ganglia (C, indicated), and cortical and subcortical atrophy (D) in a 4-year-old MoCD patient. (E) The schematic of the three different types of MoCD with the respective enzymes. *Image taken from Bindu et al 2015, adapted from Scriver, C. R. at al., McGraw-Hill, NY, 2001.*[121]

There are three different types of MoCD identified so far- 1) Failure of the reaction step 1 is Type A, caused by mutations in the MOCS1 gene, 2) Failure of the reaction step 2 is Type B, in the MOCS2 and MOCS3 gene and 3) Failure of the reaction step-3 is Type C, in the gephyrin gene.[120,122] The mutations in MOCS1 genes or Type A are most commonly administered in the reported patients, lack of cPMP. The patients with type A deficiency, which are not able to generate cPMP from GTP, can be treated with cPMP doses. The treatment includes periodic injection of pure cPMP directly to fulfil the primary function of the MOCS1 enzymes.[123,124] Although it is apparent that the intravenous supply of Moco would heal any MoCD, with the high instability of the free-Moco (not protein-bound), this would be rather highly unlikely in the near future.[93,125]

The patients with type C, mutations in the gephyrin gene shows severe classes of MoCD such as impaired synaptic inhibition, an essential function of gephyrin is also indispensable. Mutations in the gene of SO enzyme (SOUX) leads to a disease called the SO-deficiency, resulting in similar neuropathological dysfunctions.[119,126] Sulfite is toxic to humans if present in excess, and accumulate in the liver or brain.[94,104] Another significant disease in Moco deficiency is XOR deficiency, leading in the hypoxanthine and xanthine accumulation in the blood, as well as the xanthine in the urine leading to disease termed as xanthinuria.[114,125]

1.6 Aim and Outline

Major aims of this work are to develop a synthetic cell incorporated with Moco biosynthesis pathway. To achieve this goal, it is important to detect a suitable technique that not only allows us to construct a lipid-based synthetic cell, but also provides the possibility to encapsulate the enzymatic pathway. Like discussed earlier in the introduction, it is not possible to produce such a synthetic cell using existing techniques such as electroformation or swelling techniques. The emulsion-based method is highly suitable for this purpose, owing to their feasibility to incorporate large molecules inside the cells without requiring using large volumes of the encapsulates. However, the emulsion-based method needs to be optimised for faster and easy production and detection of the synthetic cells produced and the enzymatic activity encapsulated.

Following this understanding, it is required to develop and optimise the synthetic cell production technique itself, before encapsulating required enzymes for the Moco Biosynthesis. The first major aim would be to develop and optimise synthetic cell production-

- Studying and optimising various parameters for high yield of synthetic cells using the emulsion-based method
- Studying the effect of pH and temperature on the production process
- Optimizing the entire technique for fast and easy handling, to perform in a microtiter plate for high throughput and analyses
- Studying encapsulation efficiency and even the stability of the synthetic cells produced using this technique

After the production technique, the second major aim would be is to produce required enzymes for the Moco Biosynthesis and encapsulate them within the synthetic cells along with a fluorescent-based detection system.

To fulfil the objective of encapsulating Moco Biosynthesis within synthetic cells

- Bacterial expression and activity studies of cPMP synthase and MPT synthase
- *In vitro* bulk studies of the reaction systems and optimisation steps at various pH and temperature conditions.
- Encapsulation and fluorescence-based detection of cPMP synthase in the synthetic cells to produce cPMP.
- Encapsulation and fluorescence-based detection of MPT synthase in the synthetic cells to produce MPT.

In this thesis, GUVs were the chosen model to encapsulate the Moco biosynthesis machinery with high reproducibility and efficiency. For this, the biosynthesis was divided into two major steps, 1) GTP conversion to cPMP and 2) cPMP to MPT formation. A fluorescence-based detection was developed to assay the individual reaction steps separately. As explained previously, Moco biosynthesis starts in the mitochondria, but the mechanism for how the intermediate cPMP transports into the cell's cytosol is unclear. Here a mitochondrial mimicking GUV will be used to study cPMP transport across the membrane. Finally, the investigation on the passive transport of cPMP with mitochondrial mimicking membranes was approached.

2 Materials

2.1 Chemicals

The chemicals utilised in the thesis are enlisted below with their respective producers.

Name		Company
ß-mercaptoethanol		Duchefa Biochemie B.V
1,1'-dioctadecyl-3,3,3 ', 3'-tetramethylindocarbocyanine perchlorate	(DilC18)	Invitrogen- Thermo Fisher Scientific Inc
1H,1H,2H,2H-perfluoro-decyl trichlorosilane		abcr GmbH
1-palmitoyl-2-oleoyl-sn-glycero-3-phosphocholine	(POPC)	Avanti Lipids Polar, Inc. AL
1-palmitoyl-2-oleoyl-sn-glycero-3-phosphoethanolamine	(POPE)	Avanti Lipids Polar, Inc. AL
1-palmitoyl-2-oleoyl-sn-glycero-3-phospho-L-serin	(PI)	Avanti Lipids Polar, Inc. AL
2-(N-morpholino) ethane sulfonic acid	(MES)	Sigma-Aldrich Corporation,
4-(2-Hydroxyethyl)-1-piperazine ethane sulfonic acid	(HEPES)	Carl Roth GmbH & Co. KG
Acetic acid		Sigma-Aldrich Corporation
Acetone solution		Sigma-Aldrich Corporation
Agar-agar		Carl Roth GmbH & Co. KG
Alpha-haemolysin		Sigma-Aldrich Corporation
Ammonium acetate		Carl Roth GmbH & Co. KG
Ammoniumperoxodisulfat	(APS)	Carl Roth GmbH & Co. KG
Ampicillin		Carl Roth GmbH & Co. KG
Ammonium sulphate		VWR International GmbH
Ascorbic acid		Carl Roth GmbH & Co. KG
Bovine serum albumin	(BSA)	Sigma-Aldrich Corporation
Bromophenol blue		Sigma-Aldrich Corporation
Calcein Molecular Probe		Thermo Fisher Scientific Inc
Calcium chloride dihydrate		VWR International GmbH
Casein (from bovine milk)		Sigma-Aldrich Corporation
Cardiolipin Lipids		Avanti Lipids Polar, Inc. AL
Chloroform		Sigma-Aldrich Corporation
Coomassie R250 brilliant blue		Ferak Berlin GmbH
Cytochrome C		Carl Roth GmbH & Co. KG
Dimethyl sulfoxide	(DMSO)	Sigma-Aldrich Corporation
Dithiothreitol	(DTT)	AppliChem GmbH
D-(+)-Glucose		Sigma-Aldrich Corporation
D-(+)-Sucrose		Sigma-Aldrich Corporation
Ethanol		VWR International GmbH
Ethylenediaminetetraacetic acid	(EDTA)	Carl Roth GmbH & Co. KG
Fluorescamine		Thermo Fisher Scientific Inc
Glycerol (98%)		Sigma-Aldrich Corporation
Glycine		Sigma-Aldrich Corporation
Guanosine 5′-triphosphate sodium salt hydrate	(GTP)	Sigma-Aldrich Corporation
Hydrochloric acid, 37%	HCl	Sigma-Aldrich Corporation
Imidazole		Sigma-Aldrich Corporation
Isopropyl β-D-1-thiogalactopyranoside	(IPTG)	Carl Roth GmbH & Co. KG
Isopropanol		Carl Roth GmbH & Co. KG

L-ascorbic acid		Carl Roth GmbH & Co. KG
L-α-phosphatidylinositol Lipids		Avanti Lipids Polar, Inc. AL
Magnesium chloride hexahydrate		Sigma-Aldrich Corporation
Methanol, HPLC grade		Duchefa Biochemie B.V
Mineral oil		Sigma-Aldrich Corporation
Nickel (II)-chloride hexahydrate		Carl Roth GmbH & Co. KG
Peptone		Duchefa Biochemie B.V
Phenol		Carl Roth GmbH & Co. KG
Phosphate buffered saline	(PBS)	Sigma-Aldrich Corporation
Polydimethylsiloxane	(PDMS)	Dow Corning
Polyethylene glycol 4000 (PEG4000)		Sigma-Aldrich Corporation
Potassium chloride	KCl	VWR International GmbH
Potassium dihydrogen phosphate	KH_2PO_4	VWR International GmbH
Potassium iodide	KI	VWR International GmbH
Sphingomyelin Lipids		Avanti Lipids Polar, Inc. AL
S-(5′-Adenosyl)-*L*-methionine chloride dihydrochloride	(SAM)	Sigma-Aldrich Corporation
Sodium molybdate dihydrate		Carl Roth GmbH & Co. KG
Sodium acetate		Duchefa Biochemie B.V
Sodium chloride		Duchefa Biochemie B.V
Sodium dithionite		Sigma-Aldrich Corporation
Sodium dodecyl sulfate	(SDS)	AppliChem GmbH
Sodium hydroxide	NaOH	Carl Roth GmbH & Co. KG
Sodium hydrogen carbonate		Carl Roth GmbH & Co. KG
Sodium sulfide		Sigma-Aldrich Corporation
Streptomycin sulphate		Duchefa Biochemie B.V
Sulfuric Acid		Carl Roth GmbH & Co. KG
Tetrahydrofuran		Duchefa Biochemie B.V
N,*N*,*N*′,*N*′-Tetramethylethylendiamin	(TEMED)	Carl Roth GmbH & Co. KG
Trichloroacetic acid		Carl Roth GmbH & Co. KG
Tris(hydroxymethyl)aminomethane	(Tris)	Duchefa Biochemie B.V
Tris(2-carboxyethyl) phosphine	(TCEP)	Sigma-Aldrich Corporation
Tryptone		Duchefa Biochemie B.V
Yeast Extract		Duchefa Biochemie B.V

2.2 Enzyme and plasmids

Name	Company
Fast alkaline phosphatase	Carl Roth GmbH & Co. KG
DNase	Sigma-Aldrich Corporation
pET-15a	Merck-Sigma Karlsruhe
pJET1.2	Merck-Sigma Karlsruhe
pEGFP-N2	Merck-Sigma Karlsruhe

2.3 Buffers and solutions

All the solutions were prepared using deionized Millipore® MilliQ water with a conductivity lower than 0.055 µS/cm (Merck EMD Millipore Corporation, Billerica) unless otherwise specified. All the buffers were filtered (0.2 µm pore size) and if required degassed under the vacuum pressure. The buffers were stored up to one week at 4°C, and re-filtrated prior to the usage. Lysogenic broth (LB) was autoclaved for 20 minutes at 1 bar and 121°C, or if heat-sensitive, filtered (0.2 µm pore size) to sterilize.

Buffers	Composition
A1	TE + 1:100 RNase premix, pH 8
A2	200 mM NaOH, 1.25% w/v SDS
AGE-loading buffer	50% v/v glycerol, 40 mM Tris Ac, 1 mM Na_2H_2EDTA, pH 8
Competent cells preparation buffer	9.8 % (v/v) Glycerol, 10 mM MES-NaOH, 38 mM CaCl2, 45.5 mM MnCl2
Coomassie (de-) staining solution	40% v/v MeOH, 10 % v/v acetic acid, 0.25 Coomassie
K-MES	500 mM KOH x 2-(N-morpholino)-ethanosulfonic acid, pH 6.3
Lysis buffer	300 mM NaCl, 50 mM NaH2PO4, pH 8
Lysogeny Broth	10 g Tryptone/ peptone, 5 g Yeast extract, 10 g NaCl, pH 7, if needed 20 g Agar
MES-buffer	12% w/v glycerol, 50 mM CaCl2, 45 mM MnCl2, 2% v/v K MES, pH 6.3
Native-/(SDS)-PAGE loading	250 mM Tris-HCl, 30% w/v glycerol, 0.25% w/v brom-phenyl-blue, (10% v/v β- mercaptoethanol, 3% w/v SDS), pH 6.8
Native-/ (SDS)- PAGE running	192 mM glycine, 25 mM Tris, (0.1 % w/v SDS), pH 8.2
NTA elution buffer	50 mM NaH2PO4, 300 mM NaCl, 250 mM imidazole, pH 8
NTA washing buffer I	50 mM NaH2PO4, 300 mM NaCl, 10 mM imidazole, pH 8
NTA washing buffer II	50 mM NaH2PO4, 300 mM NaCl, 20 mM imidazole, pH 8
Phosphate-buffered saline (PBS)	137 mM NaCl, 2.7 mM KCl, 10 mM Na2HPO4, 1.8 mM KH2PO4
Size-exclusion chromatography	50-100 mM Tris-HCl, 200 mM NaCl, pH 8

2.4 Kits and other material

Name	Company
96 well plate, clear flat bottom	Dow Corning
Glass slides	Präzisions Glas & Optik GmbH
IMAC Profinity™ IMAC Resin	Qiagen NV, Hilden
PD-10 Desalting Columns containing Sephadex G-25	GE Healthcare USA
PPi Detection Assay Kit	Sigma-Aldrich Corporation
Superdex™ pg	GE Healthcare USA
Superose12	GE Healthcare USA

Table 1. Bacterial strains with the respective genotype and antibiotic resistance.

Strains	Genotype	Reference	Application
DH5α	F^-, endA1, gln V44, th-1, recA1, relA1, gyrA96, deoR, nupG, ϕ80lacZΔM15, Δ(lacZYA-argF)U169, hsdR17, λ^-	Hanahan 1985, Woodcock et al. 1989	Cloning
BL21 (DE3)	F^-, ompT, gal, dcm, lon, $hsdS_B(r_{B-}m_{B-})$, λ(DE3[lacI lacUV5-T7 gene 1 ind1 sam7 nin5])	Studier and Moffatt 1986	Protein Expression
RK5200	DE(argF-lac), 169 DE(fimB-fimE)632(::IS1), DE(fruK-yeiR)725(fruA25), F^-, λ^- , $[araD139]_{B/r}$, deoC1, e14-flhD5301, gyrA219, non-9, rbsR22, relA1, rpsL, 150(strR), chlA200::Muc(ts)	Stewart, V & MacGregor 1982	Protein Expression
TP1000	F^-, $[araD]_{B/r}$, Δ(lacZYA-argF)U169, λ^-, $e14^-$, Δ(fruK-yeiR)725, (fruA25)‡, rpsL150(strS), relA1, flb5301, ptsF, devC, rbsR22, Δ(fim B-fimE)632(::IS1), deoC1, mobAB::kan	Palmer et al. 1996	Protein Expression
DL41	F^-, λ^-, *met A28*, Δ moaE-pREP4	Hendrickson et al. 1990	Protein Expression

3 Methods

The chapter is divided into four main sections based on the various techniques utilised for enzymes and GUV preparation. The first section over-expression and protein purification were based on the *Escherichia coli* (*E. coli*) expression, and it requires the techniques in molecular biology, expression and purification of the proteins. The purified proteins are the essential enzymes for the Moco biosynthesis, and therefore the final biochemical analysis for the enzymatic activity was performed. The second section is dedicated to the synthetic liposomal production, e.g., GUVs, followed by the section on fluorescent-based detection of the reaction mechanism. The final technique implied in this chapter is microfluidics manipulation of pre-formed GUVs, described in the fourth section.

3.1 Molecular Biology and Protein Biochemical Methods

3.1.1 *E. coli* strains, Cultivation and Storage

Cells were grown aerobically in LB medium (5 g Yeast extract, 10 g Trypton and 10 g NaCl) and induction chemical such as IPTG at 37°C and 200 rpm. The optimum growth media was necessarily supplemented with ampicillin (final concentration 150 µg/ml), or kanamycin (final concentration 25 µg/ml), or (final concentration 50 µg/ml) for the selection purposes, as shown in Table 1. The cells were stored in 80 % glycerol at -80°C with a one-to-one dilution of an overnight culture mixed with 87% (v/v) glycerol stock for prolonged usage.

3.1.2 Chemo-competent *E. coli* Cells

For *E. coli* cells to easily incorporate a foreign DNA from the environment, the cell membrane is made more permeable. There are two conventional techniques to make bacterial cell membrane permeable 1) chemical transformation and 2) electroporation. In this thesis, we utilised chemically transformed cells with easily altered membranes that are known as competent cells. A 1:500 inoculum of 50 ml of sterile LB medium containing 20 mM $MgSO_4$ was incubated at 37°C and 200 rpm until the OD_{550} was reached 0.9 (~4-5 hours). The cells were allowed to cool down while stirring gently on ice-cold water for 2 minutes, followed by a 30-minute incubation at 4°C. The cells were harvested and centrifuged for 12 minutes at 0°C and 2500 rpm to form cell pellet, which was resuspended in 16 ml MES buffer supplemented with 500 mM 2-(N-morpholino) ethane sulfonic acid, 30 mM $CaCl_2$*2 H_2O, 10% glycerol, pH 6.3. The suspension in MES buffer was incubated for 10 minutes at 4°C on ice and centrifuged again for 12 minutes at 0°C and 2500 rpm. The supernatant was removed, and the cell pellets were suspended in 2 ml MES buffer, the DH5α competent cells were aliquoted for 100 µL each and stored at -80°C using liquid nitrogen.

3.1.3 Transforming Competent Cells

Transformation is the process in which an exogenous DNA is incorporated into the competent cells; the cell then replicates and expresses the exogenous DNA. The chemically competent cells were transformed with a template plasmid DNA using the heat shock method. An aliquot of 100 µL competent cells were gradually thawed on ice and applied with 100 µg of template plasmid DNA. The cells and plasmid mixture were

incubated on ice for 30 minutes before heat shock at 42°C for 2 minutes and again cooling down on the ice for 2 minutes. Subsequently, the cells were fed with 600 µL fresh LB medium to recover for 1 hour at 37°C in a gentle shaker. The cells were spread on LB agar plates containing a suitable antibiotic and incubated overnight at 37°C.

3.1.4 Plasmid preparation using PCR

PCR is a technique where a specific DNA fragment is exponentially amplified to generate multiple copies in a considerable amount. For amplification of a specific DNA fragment, PCR employs a template DNA, nucleotides, specific primers and a heat-stable DNA polymerase enzyme, as shown in Table 2. The technique contains a series of thermal cycles where the first thermocycle leads a DNA double helix to denature at a high temperature to separate the two strands into a single-stranded DNA. Lower temperature allows the specific primers and DNA polymerases to attach the denatured single-stranded DNA, to further elongate the template DNA. Primers guide the DNA polymerases, through the template single-stranded DNA, adding the complementary nucleotides to generate new double-stranded DNA. The process of denaturation, annealing and elongation repeat for the series of thermal cycles resulting in an exponentially amplified DNA fragment.

Table 2. The reaction mixture and the thermal cycle of the Polymerase Chain Reaction.

Compounds	
dNTPs (10 mM)	1 µL
Primer FW (10 µM)	1 µL
Primer RV (10 µM)	1 µL
Herculase II	0.7 µL
Template (100 ng)	0.5 µL
Reaction buffer 5x	10 µL
dH_2O	35.8 µL
Total Volume	50 µL

Cycle	Temperature	Time
1	95°C	6 minutes
25-30	95°C	30 seconds
	PrimerTm-5°C	30 seconds
	68°C	1 min/kb
1	68°C	7 minutes
1	4°C	∞

In this thesis, peGFP-MOCS2A was used as the template DNA with suitably designed primer to amplify the gene of eGFP-MOCS2A using polymerase chain reaction. Therefore, the primers with restriction sites Ndel (5'-prime) and Xhol (3'-prime) was introduced as shown in Table 3.

Table 3. List of oligonucleotides (primers).

Oligonucleotides	Sequence (5'-3')
eGFP_FW_Ndel	CAT ATG GTG AGC AAG GGC GAG
MOCS2A_RV_Xhol	CTC GAG CTA TCC TCC ACT AAT GG

3.1.5 Plasmid DNA purification

Plasmid purification is the process of isolating purified plasmid DNA from bacterial cells that are composed of other components such as protein, lipids, and genomic DNA. To isolate the plasmid, 5 ml culture was prepared from glycerol stocks or a single colony from agar plates to grow overnight. The overnight culture was centrifuged to form a bacterial cell pellet, and the NucleoSpin plasmid mini preparation kit (Macherey-Nagel)

was applied to extract the plasmid DNA according to the instructions provided with the kit. The plasmid DNA was eluted using 50 µL MilliQ water and stored at -20°C for prolonged usage. Here, the template pEGFP-MOCS2A was purified from transformed DH5α prior to PCR reaction. The PCR product (flanking eGFP-MOCS2A) was also purified prior to the ligation into the pJET1.2 cloning vector. Every plasmid construct was analysed over agarose gel and therefore, purified on the NucleoSpin plasmid mini preparation kit.

3.1.6 Agarose Gel Electrophoresis

Agarose gel electrophoresis is an effective technique to separate nucleic acid molecules such as RNA and DNA fragments according to their sizes. This technique employs an agarose gel matrix, creating a porous network with agar molecule, and an electric field to separate the DNA through the agarose. The pore size in the gel depends on the concentration of agar in the solution; in this thesis 1% agarose gels were prepared in TAE buffer (Tris-acetate-EDTA) with 1% ethidium-bromide. The gel was left to solidify in the container, and subsequently, the DNA samples are prepared with 6x loading buffer and restriction enzymes. The gel was loaded with the samples along with a GeneRuler™ 1 kb DNA ladder (Fermentas-Thermo Fischer Scientific GmbH, Germany), to identify the size of corresponding DNA fragments. Once the fragments were separated using the electric field, the desired DNA fragments were cut off the gel and extracted via the Nucleospin Extract II (Machery-Nagel) kit. The DNA was eluted in 15 µL MilliQ water according to the extraction protocol provided with the kit. Therefore, the agarose gels were thoroughly utilised in the thesis to analyse the blunt-end dsDNA plasmids and the constructs from digested EGFP-MOCS2A gene to pJET1.2-EGFP-MOCS2A and the final pET-15b-EGFP-MOCS2A, Figure 26 b.

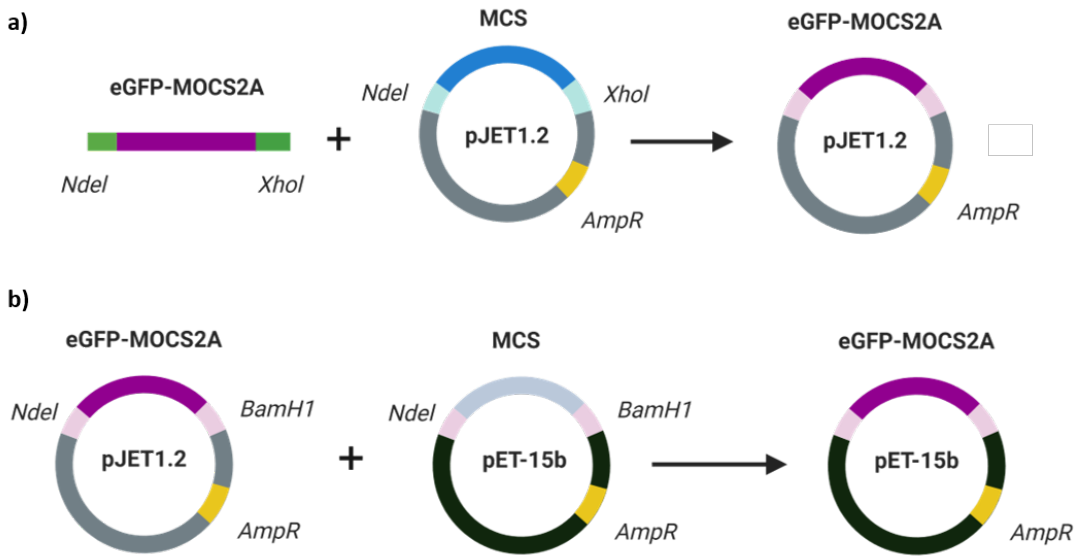

Figure 26. Recombinant Plasmid Construction.
a) the template DNA eGFP-MOCS2A with sites NdeI (5'-prime) and XhoI (3'-prime) introduced to the cloning vector pJET1.2. b) The eGFP-MOCS2A was further ligated to expression vector pET-15b with restriction sites NdeI and BamH1.

3.1.7 Recombinant Plasmid Construction

In this thesis, the fragments separated on an agarose gel and purified as described above were ligated to construct the expression plasmid. For the final expression plasmid pET-15b carrying eFGP-MOCS2A, the following restriction and ligation were performed, shown in Figure 26.

1. The restriction enzymes play a crucial role in plasmid construction. They have the DNA-cutting ability that recognises and cleave the specific DNA site or a few target sequences. Many restriction enzymes result in sequences with staggered ends, whereas some produce single-stranded overhangs or blunt ends. The digestion was performed in a 30 µL volume, containing 60-100 ng of purified DNA, 3 µL of restriction enzyme reaction buffer (10x), 1 or 2 µL of restriction enzyme and to the final volume of 30 µL filled with MilliQ water. The reaction mixture was incubated for 3 hours at 37°C, before loading on an agarose gel to have DNA fragments separated.

2. The DNA ligation is the final step in a recombinant plasmid construction to enable the incorporation of a DNA fragment (also known as inserts), into a compatible vector or the host plasmid. T4 DNA ligase enzyme catalyses the ligation reaction of two DNAs, covalently by ligating the two sugar backbones. The reaction mixture of 2 µL T4 DNA ligase, 2 µL 10x ligase buffer, 25 ng plasmid and 75 ng insert, filled up to 20 µL with MilliQ water was incubated preferably at 4°C overnight or for 2 hours at room temperature.

3.1.8 DNA sequencing

DNA sequencing is a method to determine the sequence of nucleotides (A, T, G, C) in the target template. The Sanger sequencing was performed by GATC to determine the sequence of template DNA. Aliquots of 50-100 ng plasmid or 20-50 ng of PCR fragments were utilised for the sequencing, collectively with the required primers (10 pmol/µL).

3.1.9 SDS-PAGE

Sodium dodecyl sulfate-polyacrylamide gel electrophoresis (SDS-PAGE) is an electrophoresis technique that separates the proteins based on their molecular mass irrespective of their charge. The acrylamide gel is a porous matrix with the pore size depends on the concentration of acrylamide. The SDS gel is composed of two-layers, stacking gel or the upper gel where the samples are loaded and separating gel or the lower gel that separates the proteins as described in Table 4. The protein sample or the cell lysate mixed with an SDS-loading dye contains 50% glycine, 3.5% SDS, 15% ß-mercaptoethanol, 0.02% bromophenol blue. The samples short spun, denatured at 95°C for 3 minutes and short spun before the loading. The acrylamide percentage was chosen according to the size of the proteins, for instance, the bigger the protein, the lower the percentage of acrylamide. The gels run in a Tris-glycine-SDS electrophoresis buffer at 120 Volt (PowerPac 300, Bio-Rad Laboratories, Inc.) for 1 hour, consequently, result in the smaller proteins to travel faster than the larger proteins and subsequently visualized with Coomassie blue stain.

Table 4. The solution utilised in SDS-PAGE preparation.

Compounds	15 % Running Gel	2 % Stacking Gel
Acrylamide/Bisacrylamid solution (30% (w/v); 0.8% (w/v))	2.5 mL	340 µL
4x Lower-Tris (1.5 M Tris/HCl, pH 8.8)	1.25 mL	-
4x Upper-Tris (0.5 M Tris/HCl, pH 6.8)	-	500 µL
Tetramethylethylendiamin (TEMED)	2.5 mL	2 µL
10% (w/v) Ammonium persulfate (APS)	25 mL	10 µL
H_2O	1.25 mL	1160 µL
Total Volume		2,012 µL

The SDS-Page incubated in the Coomassie staining solution that contains 40% methanol, 10% acetic acid, 50% H_2O and 0.25 g Coomassie brilliant blue R for 45 minutes. The dye soaked in the gel binds to proteins through ionic interactions to the positive protein amine groups. Finally, the excess dye stained out using a destaining solution that contains 40% methanol, 10% acetic acid and 50% H_2O. The destaining solutions allow a better visualisation by clearing the excess dye from the background that enables the sharp blue protein bands to appear.

3.1.10 Cultivation and Protein Purification

The competent cells were transformed with the desired constructs (given in section 3.1.11 for the individual protein) containing an N-terminal His_6-tag. The protein overexpressed using *E. coli* biomass was purified using immobilized metal affinity chromatography (IMAC) or ammonium precipitation method. A sub-culture prior to the main culture was prepared using the strains harbouring the over-expression plasmids (from Table1), containing codon-optimised sequences for the expression. The sub-culture was cultivated in LB medium supplemented with ampicillin 150 µg/ml, chloramphenicol 50 µg/ml or both, and incubated overnight (minimum 16 hours) at 37°C and 200 rpm. For the overexpression, 6-12 litres LB media (5 gm Yeast extract, 10 gm NaCl, 10 gm Tryptone) was prepared and autoclaved. Whereas the tryptone-containing LB medium was only used for 4-6 hours overexpression and the peptone medium was used for longer overexpression cultures (more than 24 hours).

The cells were grown using autoclaved LB with 2% (v/v) inoculum from the preculture and the corresponding antibiotics at 180 rpm and 30°C up to an approximate $OD_{600\ nm}$ of 0.6. Furthermore, the cells were induced with 0.1 mM IPTG and cultivated for another 4-6 hours at 30°C, with 180 rpm shaking. Subsequently, the cells were harvested at 8,000 g and 4°C for 30 minutes and resuspended gently in 50 ml of purification buffer-1 (50 mM NaH_2PO_4, 300 mM NaCl, 10 mM imidazole pH 8) and froze at -20°C. The cells were disrupted, using a continuous flow high-pressure cell disruptor (TS Benchtop Series 0.75 kW quipped with a 2.72 kbar head; Constant Systems, Northamptonshire, UK), twice at a pressure of 1.35 kbar at 12°C (Julabo ED/F25, Julabo Labortechnik GmbH, Germany). The cell lysate was further pelleted using a centrifuge at 4°C with 21,000 g for 1 hour and the supernatant was collected.

3.1.11 Immobilized Metal Affinity Chromatography Based Protein Purification

The His_6-tagged protein was purified using immobilized metal affinity chromatography (IMAC)-based purification technique over Ni^{2+}-nitriloacetic acid superflow, Figure 27. The IMAC Profinity™ IMAC Resin (Qiagen NV, Hilden, Germany) with 0.75 ml matrix/L of culture was equilibrated by washing with purification buffer 1. The purification of proteins was achieved by using standard IMAC protocols and recording of the 280 nm absorbance. The supernatant was poured onto the resin, and the column was then washed with 10 column volumes buffer-1 and 20-column volumes buffer-2. The protein was eluted in fractions with a visible change in colour (yellow-brownish) on Ni-NTA matrix, and the buffer was exchanged over PD 10 columns to respective protein and their assays. Throughout the protein purification process, the purity of the protein preparations was concluded from sodium dodecyl sulfate-polyacrylamide gel electrophoresis (SDS-PAGE).

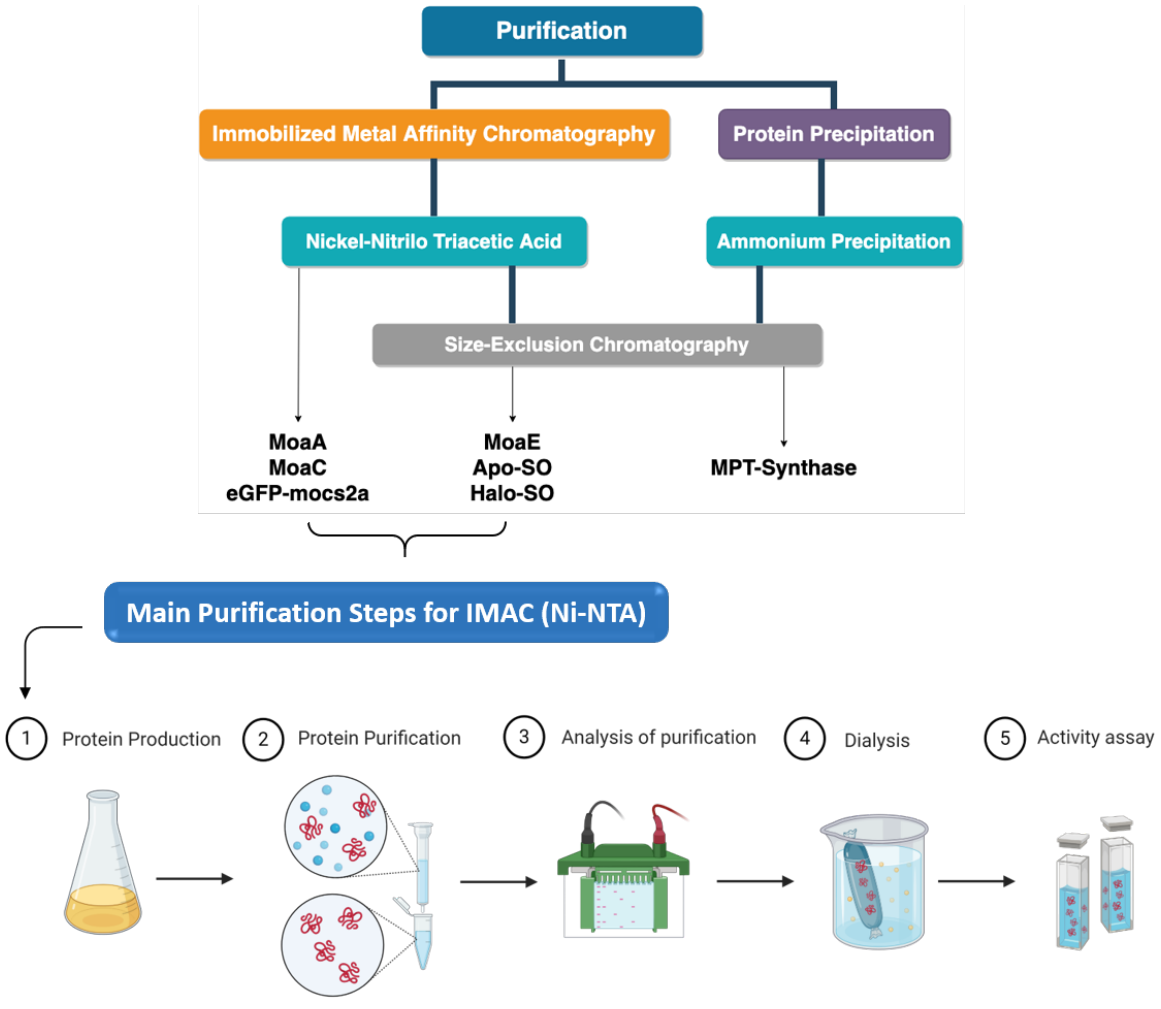

Figure 27. Techniques utilised in this thesis for the protein purification.
The proteins, namely MoaA, MoaC, eGFP-MOCS2A, MoaE and SO, were purified using mainly immobilized metal affinity chromatography and only MPT synthase was purified using ammonium precipitation. Further, the IMAC technique contains number of steps in the purification where some are listed in the schematics.

Please note that the flow-through from every IMAC run was collected and analysed along with the samples from every purification step over SDS-PAGE. Finally, by using Nanodrop Shimadzu Scientific and the extinction coefficient, the protein concentration was determined prior to the next purification steps, if needed. The final protein preparations exhibited homogeneities of more than 95 % with a yield of typically 20 - 35 mg (5.1 to 8.9 mg protein/ g cell wet weight).

- Ni^{2+}-nitriloacetic acid (Ni-NTA Superflow, Qiagen GmbH) Purification buffers:
  - Buffer-1: 50 mM NaH_2PO_4, 300 mM NaCl, 10 mM imidazole, pH 8
  - Buffer-2: 50 mM NaH_2PO_4, 300 mM NaCl, 20 mM imidazole, pH 8
  - Elution buffer: 50 mM NaH_2PO_4, 300 mM NaCl, 250 mM imidazole, pH 8

3.1.11.1 MoaA

An active MoaA with MoaC forms a complex with S-adenosyl-methionine and GTP, to produce cPMP, which is relevant for the thesis. Hereby, MoaA 35.81 kDa (*Staphylococcus aureus),* was expressed with sulfur operon from a glycerol stock (MoaA-Suf operon), ampicillin and chloramphenicol resistance. The purification was strictly performed under anaerobic condition; therefore, the preparation was started a day before purification by installing the following consumable in an anaerobic chamber (Coy Laboratory Products):

1. Filtered and degassed buffers

- IMAC Purification buffers
- 1 M Tris (unbuffered)
- 500 ml of 100 mM Tris, 300 mM NaCl, pH 9.0

2. The equipment required such as an icebox, de-gassed MilliQ water, 200 mM HCl, 270 mg $FeCl_3$ in 1 ml of 200 mM HCl (1 M), 2 centrifuge tube (Sarstedt AG & Co., Germany) with lid, parafilm, Pasteur pipettes, 4.5 ml of Ni-NTA column, 100x 1.5 ml Eppendorf, 2x 250 ml beaker, 5x 50 ml & 15 ml falcons, 8x PD 10 column (GE Healthcare Company, Germany), Branson Sonifier® SFX250 sonicator with a big stab, frozen MoaA cell pellet.

3. Prior to purification, the heat block was adjusted at 4°C (also inside the anaerobic chamber) to directly place the following substrates on at 4°C:

- 1 mg lysozyme in 1 ml (1 mg/ml)
- 1 mg DNase in 1 ml (1mg/ml)
- 154 mg DTT in 1 ml (1 M)
- 240 mg cysteine in 1 ml of 1 M Tris (1 M)
- 150 µM IscS
- 50 µM PLP

The resuspended cells in buffer-1 mixed with 1 µg/ml DNase and 1 µg/ml lysosomes, was lysed using Branson Sonifier® SFX250, 5-6 times for 10-15 seconds, with pulse ON/OFF sonication at 30 % amplitude for 5 minutes anaerobically. The cell lysate was carefully sealed using parafilm and brought out of the anaerobic chamber to centrifuge at 4°C with 21,000 g for 1 hour.

As explained His_6-tagged protein was purified using IMAC chromatography technique, therefore, the Fe-S clusters reconstitution was performed after the purification. The supernatant was collected anaerobically after centrifugation and purified using standard IMAC protocols. 50 µL of protein was brought out of the chamber to Nanodrop Shimadzu Scientific (extinction coefficient 28420 $M^{-1}cm^{-1}$) to determine the protein concentration for prior to Fe-S clusters reconstitution.

2[4Fe-4S] Reconstitution

100 µM of above-quantified proteins and 3 µM IscS was aliquoted where the reconstitution starts by incubation 435 µL MoaA, 5 µL of 1 M DTT in 1 ml vial for 30 minutes at 4°C. Further,7 µL IscS, 50 µL PLP, 10 µL $FeCl_3$-Cysteine (stock solution 1:1 of 1 M $FeCl_3$: 1M Cysteine) was mixed and filled up to 1 ml with 100 mM Tris buffer supplemented with 300 mM NaCl, pH 9. The reaction mixture was incubated for 4 hours at 4°C on a heat block for the final Fe-S reconstitution. The reaction mixture was centrifuged for 1 minute and the supernatant was poured on the PD10 column for the final cycle of buffer exchange with a buffer supplemented with 100 mM Tris, 300 mM NaCl pH 9. If required, the purified protein was concentrated using 30 kDa filter (Vivaspin®20), in a swing bucket rotor (Eppendorf 5804R, Eppendorf AG, Germany), aliquoted and frozen at -80°C.

3.1.11.2 eGFP-MOCS2A

MOCS2A is a cytosolic protein, fused with eGFP for encapsulation purpose towards constructing a synthetic model as a proof of principle (details in 4.1.7.4). For eGFP-MOCS2A, His_6-tagged protein of 36.20 kDa, the construct carrying the eGFP in frame with human MOCS2A was created as described above. The expression plasmid (eGFP-MOCS2A pET15b) was utilised to transform BL21 (DE3, Stratagene) to finally streak the colonies. The cells were grown in LB medium with Peptone, for 2-3 days in the dark to protect the fluorophore from light damage. As explained His_6-tagged protein was purified using IMAC chromatography technique, the cells were lysed using Branson Sonifier® SFX250, 5-6 times for 10-15 seconds, with pulse ON/OFF sonication at 30 % amplitude for 5 minutes. The supernatant was filtered through 0.25 µm filters and combined with the equilibrated Ni-NTA matrix (0.75 ml matrix/L of culture) and incubated at 4°C on a shaking plate for 1 hour until the matrix turns yellow, the colour indicates protein-matrix binding. The Ni-NTA matrix was washed with purification buffer-1 and 2, and subsequently, the protein was eluted in 1 ml fractions with a visible green colour using the elution buffer. The eluted protein suspension was dialysed overnight at 4°C against 2 litres 50 mM Tris buffer pH 7.5 and further concentrated by 30 kDa filter (Vivaspin®20), in a swing bucket rotor (Eppendorf 5804R, Eppendorf AG, Germany) at 4°C. The protein concentration from all the purification steps was determined using the Nanodrop Shimadzu Scientific and respective samples were applied to 15 % SDS-PAGE, the final protein concentrating was aliquoted and froze at -80°C.

Note: 1 ml cell culture was pelleted and resuspended in 1 ml phosphate buffer pH 8, to check the fluorophore using fluorimeter, and the cell suspension was used directly in the fluorimeter to obtain the fluorescence spectrum for eGFP, to make sure the presence.

3.1.11.3 MoaC

An active MoaC was utilised in regulation with MoaA to produce cPMP from GTP relevant for the study. The purification of MoaC 16.5 kDa, of *Staphylococcus aureus,* started with the transformation of the BL21 (DE3) competent cells with a plasmid pPH160 attached His_6-tag. The Ni-NTA purification steps were followed as aforementioned and the flow-through from every step was applied to 12 % SDS-PAGE. Additionally, the buffer exchange was performed with overnight dialysis against 2 litres 50 mM Tris, 300 mM NaCl, pH 8 at 4°C. Further, the protein was concentrated by 10 kDa filter (Vivaspin®20), in a swing bucket rotor (Eppendorf 5804R, Eppendorf AG, Germany) at 4°C, where the concentration was measured using the Nanodrop Shimadzu Scientific (extinction coefficient 6990 $M^{-1}cm^{-1}$) and froze the aliquots at -80°C.

3.1.11.4 MoaE

The glycerol stock of DL41 moaE-pREP4 was provided for MoaE 16.981 kDa (*E.coli*) His_6-tagged protein, for the preculture. The cultivated cells were purified under the IMAC purification steps and the flow-through from every step was applied to 12 % SDS-PAGE. The protein suspension was dialysed overnight at 4°C against 2 litres 50 mM Tris buffer 200 mM NaCl, 1 mM EDTA pH 7.5, and concentrated by 10 kDa filter (Vivaspin®20) at 4°C. Additionally, the second purification on a Superose12™ size-exclusion chromatography column (GE Healthcare Company, Germany) performed a better separate the protein species in the suspension. These columns are generally equilibrated using filtered and degassed solutions required for the flow such as degassed water degassed 20 % ethanol and filtered-degassed buffer. The dialysed protein suspension was concentrated to 2 ml, and the concentration (extinction coefficient 37470 $M^{-1}cm^{-1}$) was adjusted to load on the column. The concentrated protein suspension was carefully filtered through a 0.25 µm filter to avoid clumping on the HPLC column.

Simultaneously, the column was washed with 1 column-volume of degassed water, followed by 2 column-volume of the purification buffer, 50 mM Tris, 200 mM NaCl, 1 mM EDTA pH 7.5 while the temperature was maintained at 4°C. The sample was loaded for the Superose12™ equilibrated column for the second purification step and collected in 2 ml fractions. The proteins samples from the desirable HPLC fractions and the previous purification steps were analysed over 15 % SDS-PAGE. Fractions with the highest protein content were combined and concentrated, if required using (Vivaspin®20, 10 kDa cut-off at 4°C), finally aliquoted and hence store at -80°C.

3.1.11.5 MPT Synthase

MPT synthase is a heterodimer that catalyses the transformation of cPMP to MPT by providing the two sulfur atoms. The *E.coli* enzyme was purified using the precipitation method with ammonium sulphate. A complex of bacterial 2[MoaE-MoaD], 52 kDa is known as MPT synthase, and the glycerol stock of the complex, MoeA (DE3) pMW15aDaEeB was utilised to prepare the preculture. The cells were grown using the preculture 1:50 (20 ml) on 150 µg/ml ampicillin, up to $OD_{600\ nm}$ 0.6 at 130 rpm and 30°C. The cells were induced with 0.1 mM IPTG and overexpressed for 4-6 hours. Subsequently, harvested with 8,000g at 4°C, resuspended in 60 ml of 50 mM Tris buffer supplemented with 1 mM EDTA pH 7.5 and froze at -20°C until purification. The cells were brought to 4°C by thawing in the water bath, and 1 µg/ml DNase was added prior to cell lysis using

high-pressure cell disruptor twice at 1.35 kbar and 12°C. The cell lysate was centrifuged at 4°C with 21,000 g for 1 hour to get rid of debris and collect the supernatant (135 ml).

The purification of MPT synthase was performed using ammonium precipitation method with ammonium sulphate. In this method, the protein suspension was first mixed with (2% w/v) streptomycin sulphate solution slowly using a glass rod, 3 gm of streptomycin sulphate dissolved in 15 ml H_2O, while maintaining the temperature at 4°C. This streptomycin sulphate solution made the protein suspension appear milky cream in colour. This milky cream protein suspension was centrifuged for 30 minutes on 4°C with 20,000 g to collect the supernatant (150 ml). Whereas 36.3 gm of ammonium sulphate was gently added to the supernatant and incubated on the stirring disc (~10 g) for 1-2 hours at 4°C. Further, this ammonium sulphate-protein mixture was centrifuged for 30 minutes at 4°C with 20,000 g to collect the cell pellet. The pellet resuspended in 50 mM tris, 1 mM EDTA, pH 7.5 buffer was dialysed overnight against 2 litres of 50 mM, 1mM EDTA, pH 7.5 (the same buffer, to get rid of ammonium sulphate) at 4°C.

A second purification step was planned to use a 200-ml Superdex 200pg size exclusion chromatography column (General Electric Healthcare Company, Germany). The dialysed protein suspension was concentrated to 2 ml using Vivaspin®20, cut-off 30 kDa at 4°C, the concentration (extinction coefficient 85940 $M^{-1}cm^{-1}$) was measured for the column's protein capacity (maximum 100 mg/2ml). The final protein sample was filtered through the 0.45 µm syringe filters prior to loading on to the column. Simultaneously the HPLC column was washed with 1 column-volume of degassed water, followed by 2 column-volume of the purification buffer. The samples were loaded over the equilibrated HPLC column for the second purification step and collected with 1 ml fractions. The proteins samples from the HPLC fractions and the previous purification steps were analysed over 15 % SDS-PAGE. Fractions with the highest protein concentration were combined and concentrated using Vivaspin®20, cut-off 30 kD at 4°C and aliquoted to freeze at -80°C.

3.1.11.6 Moco Domain-Sulfite Oxidase

MPT-containing SO was utilised to purify the pure MPT. The plasmid, pTG818, was provided for His_6-tagged protein with human Moco Domain 44 kDa, and RK5202, MoaA knockout cells, were transformed using the plasmid. The protein was purified over Ni-NTA and every sample was analysed over 15 % SDS-PAGE. The buffer exchange was performed overnight in the cold room at 4°C by dialysing the protein against 2 litres of 100 mM Tris, 0.1 mM EDTA, pH 8.5. A second purification step was performed with gel filtration over a Superdex 200pg column, as stated in the above protocol with MPT synthase. The protein was further concentrated (extinction coefficient 82960 $M^{-1}cm^{-1}$) using 30 kDa filters at 4°C and aliquoted to freeze at -80°C.

3.1.11.7 apo-Sulfite Oxidase

The purification of human apo sulfite oxidase, 51 kDa, His_6-tagged protein extinction coefficient: 113000 $M^{-1}cm^{-1}$, from MoaA deficient RK5200 cells with a plasmid pTG718 was performed fresh for every experiment. The protein was purified anaerobically over Ni-NTA with a visible red colour and every sample was analysed over 15 % SDS-PAGE. The buffer exchange was performed over PD10 columns with 100 mM Tris, pH 7.2 and the protein was immediately reconstituted for further activity assay and studies.

3.1.12 IMAC Column Equilibration and Regeneration

The IMAC Profinity™ IMAC Resin (Qiagen NV, Hilden, Germany) were equilibrated with three column volumes (CV) of IMAC equilibration buffer before loading with three CV of 0.1 M $NiCl_2$. The solution was incubated on the resin overnight while the excess Ni-ions were washed with 3 CV IMAC equilibration buffer and 5 CV water. The resin was stored and equilibrated with IMAC purification buffer-1 for 3 CV, prior to samples loading. After the protein purification, Ni-ions were stripped with IMAC regeneration buffer and the material was stored at 4°C.

Note: The enzymatic activity of all the purified proteins was assayed under the well-established methods as described in the following section, with cPMP analysis, MPT analysis and sulfite oxidase activity assay.

3.1.13 cPMP Analysis using its Fluorescent Product

Moco biosynthesis starts with the conversion of guanine nucleotide (5'GTP) into the first stable intermediate, cyclic pyranopterin monophosphate (cPMP) in a series of intermediate reactions.[98] cPMP is an oxygen-sensitive molecule, whereupon oxidisation it results into a stable fluorescent product, known as compound Z, Figure 28. MoaA that belong to the S-adenosylmethionine dependent radical enzyme superfamily and depend on 2[4Fe-4S] clusters, in regulation with MoaC catalyse the conversion of GTP to cPMP.[96,127] Hence, the reaction requires a mildly basic pH ~9, under strictly anaerobic conditions. For the reaction, 2 µL of 100 mM GTP with 200 µM MoaA and 100 µM MoaC, and co-substrates such as 2 µL of 100 mM SAM, 8 µL of 100 mM DTT, 4 ml of 100 mM $MgCl_2$, 8 µL of 100 mM Na-dithionate were utilised to final volume 400 µL with 100 mM Tris-HCl buffer supplemented with 300 mM NaCl, pH 9. The reaction was incubated for 1 hour at room temperature in the anaerobic chamber to maintain the oxygen-free environment. This assay for the enzymatic activity via cPMP production was investigated over HPLC with compound Z.[96]

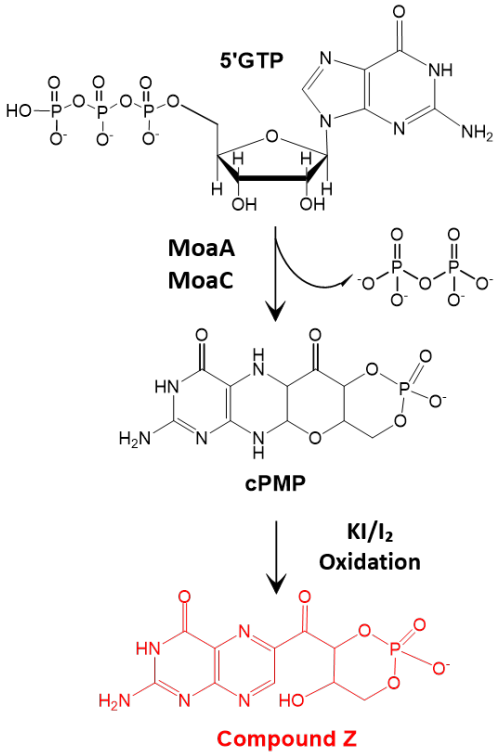

Figure 28. The first step Moco biosynthesis, 5'GTP, is converted to cPMP.
A reaction catalysed by MoaC, and a Fe-S cluster containing protein MoaA. cPMP is the first stable intermediate in the biosynthesis pathway, and can be detected as the oxidised stable fluorescent derivative, compound Z.

For the formation of compound Z, 50 µL of solution A (1063 µL KI and 100 µL 37% HCl) was added to 400 µL cPMP samples, followed by the addition of 150 µL of KI solution. The solution appears light brown in colour and further kept in the dark for overnight to achieve complete oxidation, which is subsequently centrifuged for 30 minutes at 16,200 g. 100 µL of 1% ascorbic acid was added to 400 µL supernatant, followed by the addition of 200 µL of 1 M Tris while adjusting the pH to 8.3, and finally, the samples were loaded on the QAE chromatography column. The sample on QAE column was washed with 10 ml

MilliQ water followed by 10 ml acetic acid wash and finally elution in four fractions of 1.5 ml each with 100 mM HCl. 200 µL of the samples eluted via QAE column was quantified over HPLC. The analysis was conducted at 1 mL/min with 1% (v/v) methanol in 10 mM potassium phosphate, pH 3.0, as mobile phase using a C18 reversed-phase column on HPLC system (Agilent Technologies, Germany) equipped with a fluorescence detector (ex 370 nm, em 450 nm).

3.1.14 MPT Assay based on its Fluorescent Product

The conversion of cPMP to MPT requires the opening of a cyclic phosphate to produce terminal monoester moiety and the transfer of two sulphur atoms, introducing a dithiolene group. MPT synthase, a heterodimer of MoaE and MoaD catalyse the conversion of cPMP to MPT. After transferring the two sulphur atoms to cPMP, MPT synthase must re-sulfurize by the MPT-synthase sulfurylase, thereby MPT synthase is also the limiting factor.[93,108] The total amount of MPT produced was detected via its stable fluorescent oxidation product, known as form A as shown in Figure 29.

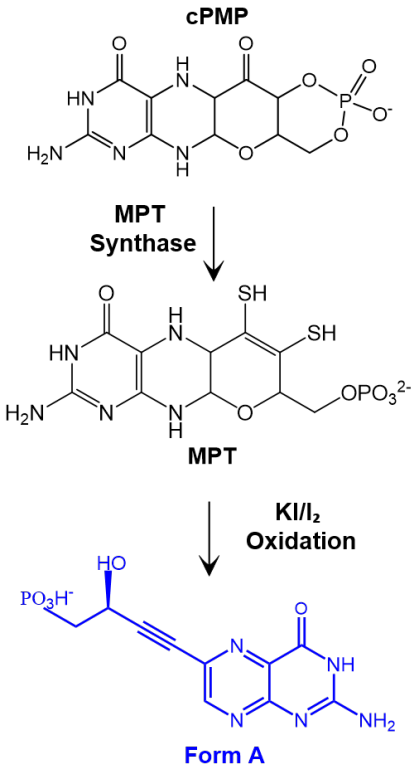

Figure 29. The second step of Moco biosynthesis.
cPMP is converted to MPT through the incorporation of two sulphur atoms catalysed by a complex protein MPT synthase. MPT is the second stable intermediate and can be detected as the oxidised stable derivative, form A.

Form A is obtained from all molybdenum cofactors when the protein was incubated at pH 2.5 in the presence of I_2/KI overnight.[91] An additional alkaline phosphatase help transform form A, into dephospho form A which can be further analyzed via fluorescence detector on HPLC.[99] For this, 100 µM *in vitro* produced cPMP was incubated with 40 µM active MPT synthase for 10 minutes in 400 µL of total volume with buffer 100 mM Tris-HCl pH 7.2 under aerobic condition. MPT was oxidised into its fluorescent degradation

product form A under the given protocol, 50 µL of solution A (1063 µL KI and 100 µL 37% HCl) was added to 400 µL samples, followed by the addition of 150 µL of KI solution turning the solution light brown. The samples were kept in the dark overnight and subsequently, centrifuged for 30 min at 16,200 g to collect the supernatant. 100 µL of 1% ascorbic acid was added to the 400 µL supernatant, followed by the addition of 200 µL of 1 M Tris to adjust the pH to 8.3. Further 30 µL 1 M $MgCl_2$ and 2 µL of fast alkaline phosphatase was added to obtain dephospho-formA. The reaction mixture incubated for two hours at room temperature, and the samples were loaded on the QAE column. The samples on the QAE column were washed with 10 ml MilliQ water followed by elution with 10 mM acetic acid in fraction of 1,3 ml each. HPLC analysis was conducted at 1 mL/min with 1% (v/v) methanol in 5 mM ammonium acetate, as mobile phase using a C18 reversed-phase column on HPLC system (Agilent Technologies, Waldbronn, Germany) equipped with a fluorescence detector.

3.1.15 Sulfite Oxidase Activity Assay

The activity assay of the Moco dependent enzyme sulphite oxidase (SO) was adapted from Leimkühler and Rajagopalan (2001),[93] to investigate the effect of TCEP on MPT stability. The goal of this assay was to examine whether Moco was better inserted into apo-sulfite oxidase in presence of TCEP. TCEP (tris(2-carboxyethyl) phosphine) is a reducing agent, selectively and completely reduces the stable water-soluble alkyl disulphides over a wide pH range. For this assay, a high molybdate concentration (>5 mM) was added to the pure MPT, which upon insertion forms Moco. This MPT-molybdate complex was inserted to Moco-free (apo) SO and assayed for sulfite oxidase activity. As molybdate combines with MPT to form Moco, and this complex inserts to apo SO resulting in the complete or halo SO. In addition to the Moco, the sulphite oxidase contains a cytochrome of the b5 type involved in electron transfer. The electrons are transferred to the Moco after the oxidation of the sulphate via the cytochrome b5 to the physiological electron acceptor cytochrome c, Figure 30. Therefore, the SO activity assay was measured utilising the reduction spectrum of cytochrome c to estimate the Moco/MPT insertion rate.[93,128]

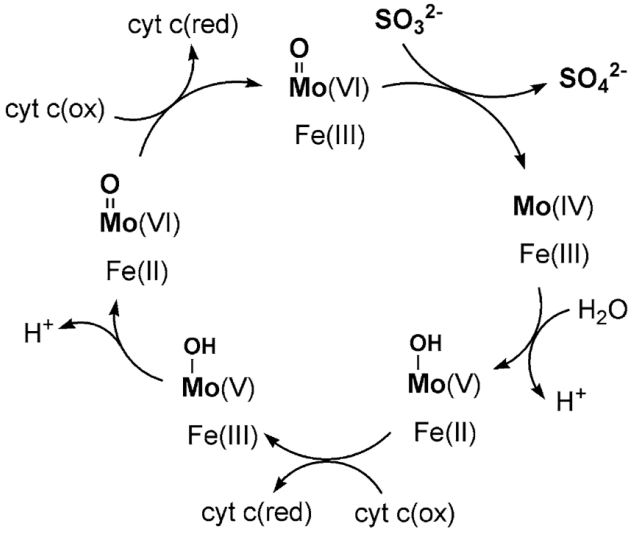

Figure 30. Schematic representation of the catalytic cycle of sulfite oxidase enzyme. The reaction that results in the oxidation of the cytochrome and involves sulfite oxidase for the activity. *Image taken from Marie-Celine van Severen et at., 2013.*[129]

To extract pure MPT from the Moco Domain-SO, the protein aliquots were heated for 5 minutes at 95°C. The denatured protein was centrifuged for 10 minutes at 13000 rpm, the supernatant containing the pure MPT was collected. Since MPT is very unstable, the extract must be immediately utilised for further experiments, while TCEP was provided to investigate the prolonged stability of the pure MPT. The SO characterized with UV-Vis spectrum shows a typical spectrum of heme-containing enzymes. While with the sulfite addition, a reduction spectrum should be seen and hence the activity of the SO can be measured through cytochrome c reduction at 550 nm.[129] An enzyme unit was defined as a reduced cytochrome c per minute and mg protein.

3.2 Liposome Production Techniques

In this thesis, a conventional technique of electroformation and an advanced emulsion-based technique were utilised depending on the application of the produced GUVs. For most of the methods, chloroform solubilised pure lipids labelled with DilC18 (0.01%) were employed, except in the case of NBD labelled lipids, to prepare a lipid stock solution and stored in -20°C. The various lipid compositions employed are given below in Table 5. Both preparation techniques are further discussed in this section.

Table 5. Types of lipid mixture utilised in the GUVs preparation with the molar percentage.

Lipids	DiIC18
POPC (99.99%)	0.01%
POPC (49.99%), DOPG (50%)	0.01%
POPC (89.99%), DOPG (10%)	0.01%
POPC (49.99%), DOTAP (50%)	0.01%
POPC (89.99%), DOTAP (10%)	0.01%
POPC (99.99%), NBD-PE (0.1%)	-
Cholestrol (50%), Sphygomylein (25%), DOPC (14.99%), DOPS (10%)	0.01%
Cholestrol (50%), Sphygomylein (25%), DOPC (24.99%),	0.01%
Cholestrol (20%), Sphygomylein (25%), DOPC (44.99%), DOPS (10%)	0.01%
Cholestrol (20%), Sphygomylein (25%), DOPC (44.99%),	0.01%
POPC (68%), Sphygomylein (1.99%), DOPE (30%)	0.01%
POPC (29.99%), Sphygomylein (5%), Cardiolipin (25%), NBD-PE (37%), PI (3%)	-

3.2.1 Electroformation

Electroformation started with a thorough cleaning of an indium tin oxidize coated (ITO) glass slides and Teflon spacers. First, the ITO-glasses and the Teflon spacers were washed twice, in a sequence with MilliQ water/soap/ethanol/chloroform/ethanol, and again with the MilliQ water. Next, the glasses were sprayed under high-pressure nitrogen flow followed by gentle wiping with a dried Kimtech tissue, followed by high-pressure nitrogen flow to remove any traces of moisture. These cleaning steps were performed in sequence, two times to remove any possible contamination. Finally, a thin lipid film was formed on the ITO-glasses by spreading 2 µL of 2 mM chloroform solubilised lipids (99.9%) and DilC18 (0.01%) stocks solution (see Table 5) with a glass syringe. Once the thin layer of the lipid was formed, the excess chloroform was evaporated first with high-pressure nitrogen flow and finally, the dried lipid film was vacuumed for 2 hours in a vacuum desiccator. After the lipid film was dehydrated, Teflon spacers were installed in between the two ITO-glasses to create a closed chamber, Figure 31. The chamber was carefully filled with a solvent (e.g., 100mM Sucrose) using a syringe (avoiding any bubbles). Then an electric field of 10 Hz, with 1.2 Vpp (peak-to-peak voltage) was applied and the vesicles were left to grow for 2-3 hours at room temperature. Finally, the GUVs were recovered after gently tapping the chambers and carefully opening with a scalpel.

The solution containing the GUVs was transferred to an Eppendorf tube and stored at 4°C until required for the experiments.

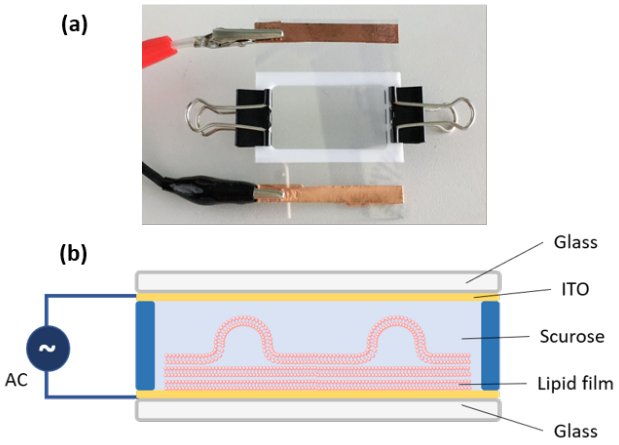

Figure 31. Representation of the electroformation process.
a) Photo of an electroformation chamber and b) schematic of a lipid film coated on the ITO glass within a closed chamber of sucrose-supplemented buffers. The closed chamber was created using Teflon spacers, this often referred as the electroformation chamber.

3.2.2 Emulsion Droplet Transfer Method

A standard emulsion droplet-based method involves a two-phase system comprising of oil and an aqueous phase, of which the oil phase contains dissolved lipids, and the aqueous phase contains inner and outer buffers respectively, see Figure 32. The oil phase was prepared by dissolving the lipids in mineral oil using a specific concentration of 200 µM for a chosen lipid mixture (seen in Table 5). For this, 50 µL of the 8 mM chloroform solubilised lipids was pipetted into a glass vial to evaporate the excess chloroform under argon flow, followed by vacuum drying for one hour. The dried lipid film was further rehydrated in mineral oil under low humidity (<10%) conditions using an AtmosBag (Sigma-Aldrich) filled with nitrogen gas and monitored with a humidity gauge (Klimalogg Pro, TFA Dostmann). Finally, this lipids-oil solution was sonicated for 1 hour at 37°C in a bath with a power of 160 W to obtain better solubilisation. The lipid-mineral oil solution was preferably incubated overnight at room temperature to assure that the lipids were thoroughly dissolved.

The oil-lipid solutions were used within a week while storing at 4°C throughout. All aqueous solutions in the phase were prepared using MilliQ Millipore® water, supplementing a density gradient between inner and outer solutions. The denser inner solutions contain either sucrose (50, 300, 600, and 900 mM) or PEG or PVA at 0.5, 1, 2.5, 5 w/v% along with the corresponding buffers for the reactants. Additionally, the inner solutions were buffered with NaOH or acetic acid for pH-dependent experiments. Inner solutions were also supplemented with HEPES (50, 100, 200, 400 mM) or Tris (50, 100, 200, 400 mM) or PBS and sucrose. A corresponding concentration of glucose solution was prepared as the outer solutions to maintain the isoosmotic conditions across the membrane. To achieve high throughput and parallelized experiments, the entire emulsion-based method has been performed in 96-well microtiter plate from Dow Corning. Surface treatment of the glass bottom was important to avoid surface adhesion and bursting of the GUVs. Wells within the plates are pre-coated by using aqueous solutions of β-casein (2 mg/mL). Typically, 30 mL of the coating solution was added to

each well and allowed to dry in the presence of vacuum for 1 hour. The wells were gently washed-out multiple times with the outer solution to remove any excess unbound traces of the protein before making the lipid interface. BSA at (2 mg/mL) was used as a coating material in experiments involving high (12) or low (4) pH where the β-casein coating was not stable. Figure 32 shows the main steps for the GUV formation using the emulsion-based method. Initially, 50 µL of glucose (outer) solution was added to the pre-coated well in a microtiter plate, followed by the addition of 20 µL of the lipid-oil solution on top of the glucose. The two layers were incubated for 30 minutes to form an interfacial lipid monolayer. Lipids, owing to their amphipathic nature, self-assemble at the interfaces with head groups towards the aqueous phase. In the meantime, 250 µL of the lipid-oil mixture was poured into a 1.5 ml Eppendorf® tube with 7 µL of the inner aqueous solution was added.

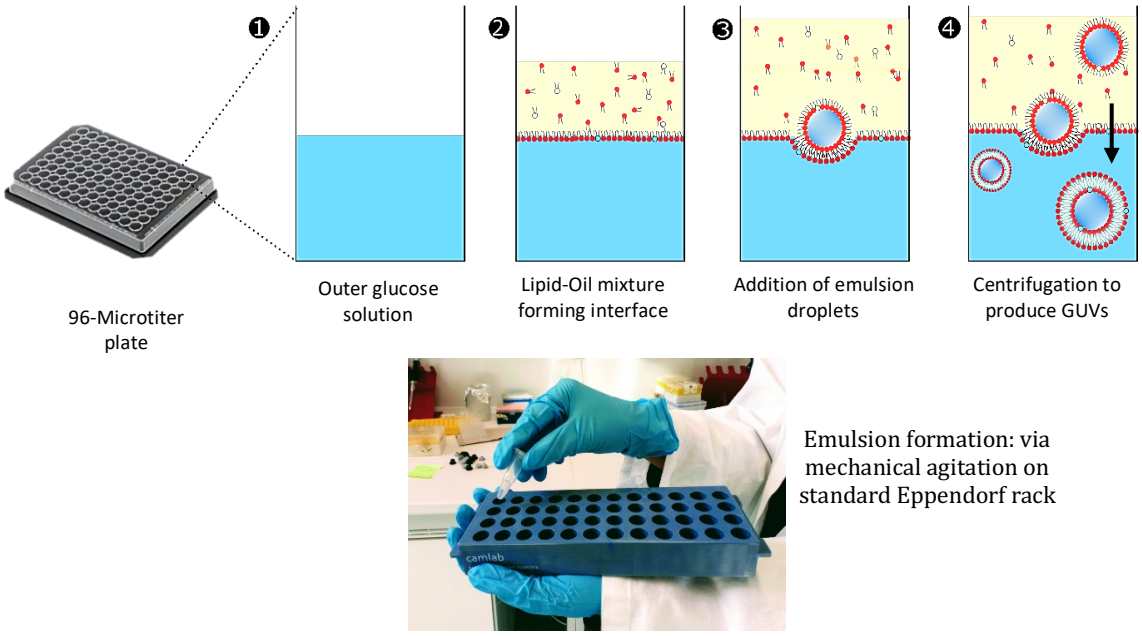

Figure 32. Schematic of the main steps in the emulsion-based method.
The method was performed within the microtiter well plates for the high-throughput production, where the main step involves 1) lipid monolayer interface formation, 2) emulsion-droplet addition, 3) Sedimentation of the droplets, mainly via centrifugation. The emulsion was formed using a 1.5 ml Eppendorf® with mechanical agitation on standard Eppendorf rack.

As seen in the photograph Figure 32, the Eppendorf was mechanically agitated along with a standard Eppendorf rack by hand to produce a water-in-oil emulsion and the 50 µL emulsion was gently pipetted over the two-layered system. Then immediately transferred to 'rotina 420R benchtop' centrifuge, to assist the movement of the droplets with centrifugal force through the interfacial lipid monolayer. Based on the experiment either 200, or 1200 x *g* force was applied for 3 minutes or 10 minutes. The GUVs formed after centrifugation settles down on the bottom of the well. Eventually, glucose becomes the outer environment of the GUVs, including the denser sucrose inside the vesicles, maintaining the density gradient. The GUVs formed were readily visualized on the plate with an inverted microscope.

3.3 Fluorescent Based GUV Imaging

The produced GUVs can be observed directly within the microtiter plate using an inverted microscope without any further sample preparation. Here the samples were observed using a confocal microscope (shown in Figure 33, Leica microsystems TCS SP8, Wetzler, DE)[130] equipped with a 63x/1.4 NA water immersion objective. In this thesis, Leica DMi8 series confocal laser microscope with motorised condenser and fluorescence, combined with all the transmitted light contrasts method (BF, PH, DF, DIC, and Pol), was utilised. The confocal microscope equipped with a transmitted light arm and a motorised stage. For the quantification of GUVs (sizes, numbers, etc.), sets of six confocal images were randomly taken in each well and with an identical field of view for comparable yield assessments. Note that multiple z-stacks were acquired at each position to ensure each vesicle was measured at the equatorial plane and those below the equator were excluded. DiIC18 fluorescence in the membrane was excited using a 552 nm diode laser with emission collected at 562-635 nm and calcein present inside the GUVs by a 488 nm diode laser with emission collected at 498-535 nm, and pyrophosphate in the UV region with 408 nm collected at 418-458 nm.

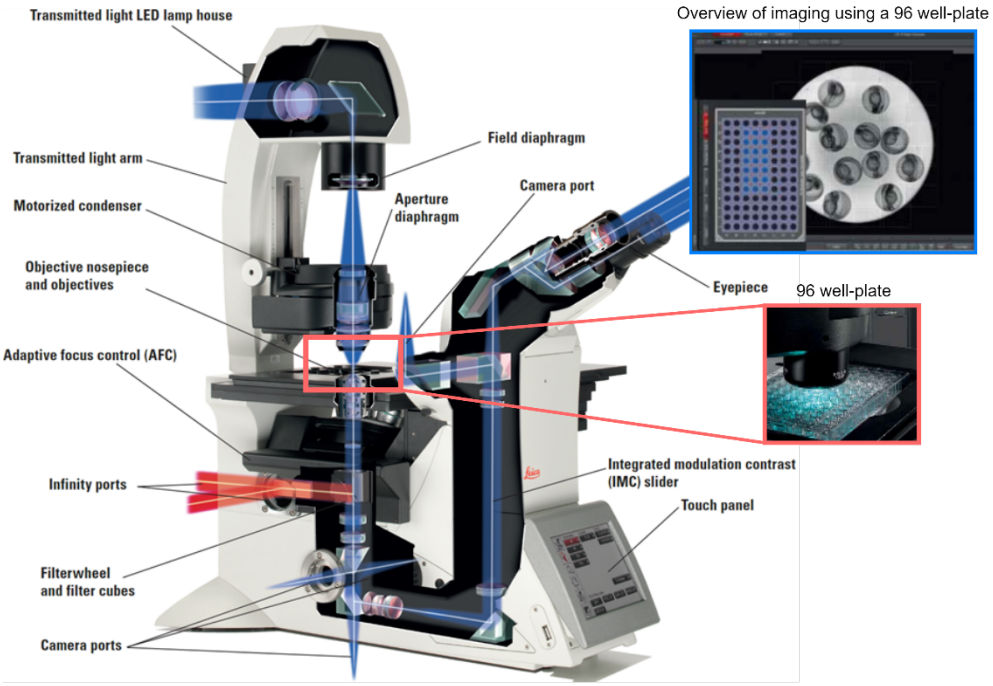

Figure 33. Leica DMi8 series confocal laser microscope.
The utilised confocal microscope, Leica microsystems TCS SP8, for the fluorescence detection. The samples were observed directly within 96-well microtiter plate as highlighted, with respective live view of a well. *Image adapted from Leica SP8 manual.*[130]

3.4 Microfluidic Chip Fabrication & Operation

3.4.1 Chip Fabrication

Fabrication of the microfluidic devices was performed using a procedure described previously by Robinson *et al.* in 2013.[131] In-house produced silicon wafer moulds to prepare chips, were salinized to prevent unwanted PDMS adhesion during chip fabrication. For salinization, the wafer was placed overnight inside a desiccator with 50 µL of 1H,1H,2H,2H-perfluoro-decyl trichlorosilane. PDMS was mixed with the curing agent in 10:1 ratio for the chip production and poured over the salinized wafer to a height of 5 mm, degassed for 30 minutes and cured at 90°C for 3 hours.[79] The chip designs were cut out from the PDMS, and fluidic inlet and outlet were made using a 1.5 mm biopsy puncher (Kai Europe GmbH). A sample reservoir with a capacity of approximately 150 µL was made with a 200 µL pipette tip above the inlet and sealed with PDMS at 90 °C for 30 minutes. The chip was bond to a glass coverslip by air plasma treatment (Plasma Cleaner PDC-002-CE, Harrick Plasma) at 0.6 mbar for 1 min, to seal the channels the device was heated for 2 hours at 60 °C to aid with the bonding. See Figure 34 for a photograph of the final assembled chip.[132]

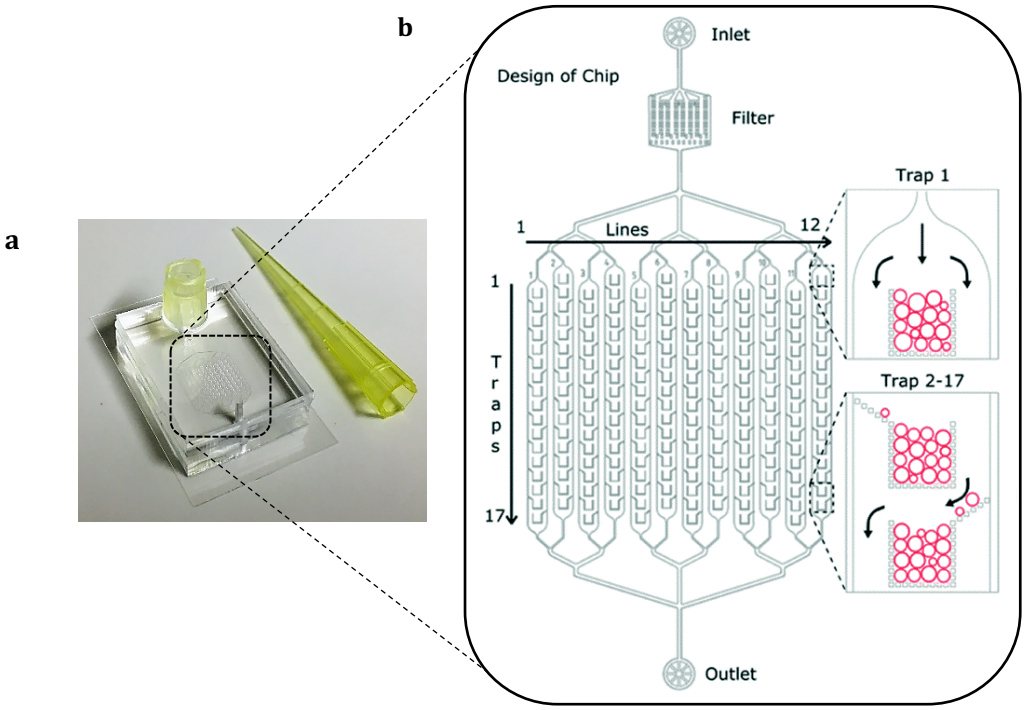

Figure 34. Schematic representation of a microfluidic chip design to trap GUVs. (a) Photograph of final assembled chip (b) The series of 12 separate lanes carrying 17 traps in each, with a total of 204 traps per device. Highlighted traps, showing the schematic representation of GUVs being filled with the flow. *Image adapted from N.Yandrapalli 2019, Lab on a chip.*[132]

3.4.2 Trapping and Buffer Exchange

The fabricated microfluidic chips were coated using 50 µL β-casein solution (2mg/ml) via centrifugation and incubating at room temperature for 30 minutes to prevent GUV adhesion and bursting in the device. The casein solution was further washed off with 100

µL of glucose solution of same the osmolality using negative pressure on the nemesis syringe pump (neMESYS, cetoni), connected onto the outlet of the chip. Subsequently, 100 µL of the electroformed GUVs were loaded in the reservoir and sucked into the chip via the reservoir. The introduced GUV suspension upon entering the inlet passes through a filter (see Fig. 34) to prevent any contamination from entering the reservoir. The GUVs flowed in using a negative pressure through the nemesis syringe pump, are expected to enter the series of traps in the 12 lanes of the chip. The chip was filled with GUVs solution using a continuous flow rate of 10 µL/min, where the smaller GUVs usually pass-through small openings. Hence, the trap only assembles GUVs ranging from the diameter of 20 µm & more. All the solutions utilised in this process were osmotically balanced to avoid any unwanted rupture and deflation upon entering the chip. The solutions in the chip were exchanged while keeping the flow 2 µL/min, and the reservoir was washed (at least 4 times) before introducing the flow again.

4 Results

Results are explained here in independent sections and divided into three main sections. The first section is entirely based on the optimisation technique utilised for GUV (our synthetic cells) production i.e., emulsion-based method. This optimisation study has been already published in Moga *et al.*, whereas the subsequent encapsulation study using this method is uniquely introduced in this thesis. The encapsulation of various fluorescent molecules was performed to validate the stability, and encapsulation efficiency of the produced GUVs. The second section is dedicated to *in vitro* Moco biosynthesis, which was studied using two intermediate steps. The study includes analytic assays, fluorescence-based assays, and the development of fluorescence methods to detect and visualise both reaction steps individually inside the GUVs. Finally, the last section describes the permeation study of cPMP molecule using calcein and fluorescamine dye, through the mitochondrial-like lipid membrane model. This permeation study was performed using two different membrane production approaches, including emulsion-based method and electroformation. Further, the microfluidics was used to analysis the permeation dynamically in real-time.

4.1 Optimisation of GUV formation using the Inverted Emulsion Method

The standard emulsion-based method involves multiple steps of a multi-phase system that can lead to unseen errors (Figure 35) and generally results in low or a variation in the number of GUVs produced. The literature on this method does not have any systematic optimisation on the method; hence, every step was individually optimised in this chapter.[45,76,133] The method optimisation was essential to the later application of using produced GUVs as bioreactors. The study focuses the parameters: lipid concentration (using POPC lipids), the incubation time for the formation of lipid monolayer at the interface, solution densities, and the type of the inner solutions in the GUV production. The whole method was performed in a 96-well glass-bottom microtiter plate for high throughput and easy reproducibility.

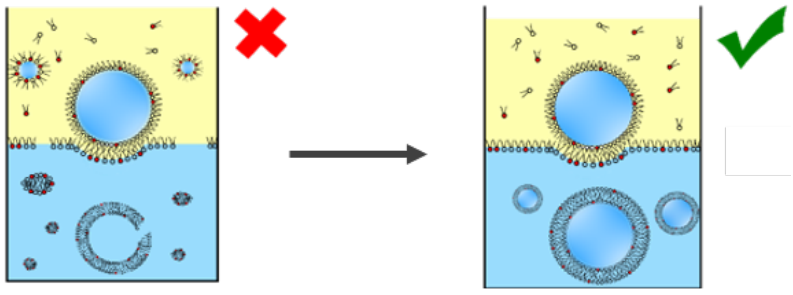

Figure 35. Schematic of the emulsion-based method with parameters optimised. The method involves various steps that can lead to many unseen errors which results in low yield and variation among GUV populations, as marked red on the representation. The parameters addressed in this study are as mentioned; lipid concentration, centrifugation speed/time, incubation time, emulsion volumes, and type of oil as described in the main text. An optimised case with the given parameters, marked green.

4.1.1 Preparation of Emulsion-droplets

The initial steps of the GUV formation included the droplet formation in an emulsion of mineral oil and buffer components. The size and yield of the droplets formed in these emulsions strongly determine the size and yield of the GUVs. Hence, an optimised droplet emulsion will yield a GUV population with the desired features. In this thesis, the sizes and dispersity of droplets were judged after sonication, pipetting, vortexing and mechanical agitation on the standard Eppendorf rack. The droplet sizes from these four techniques were compared with GUVs sizes to finalise the production method.

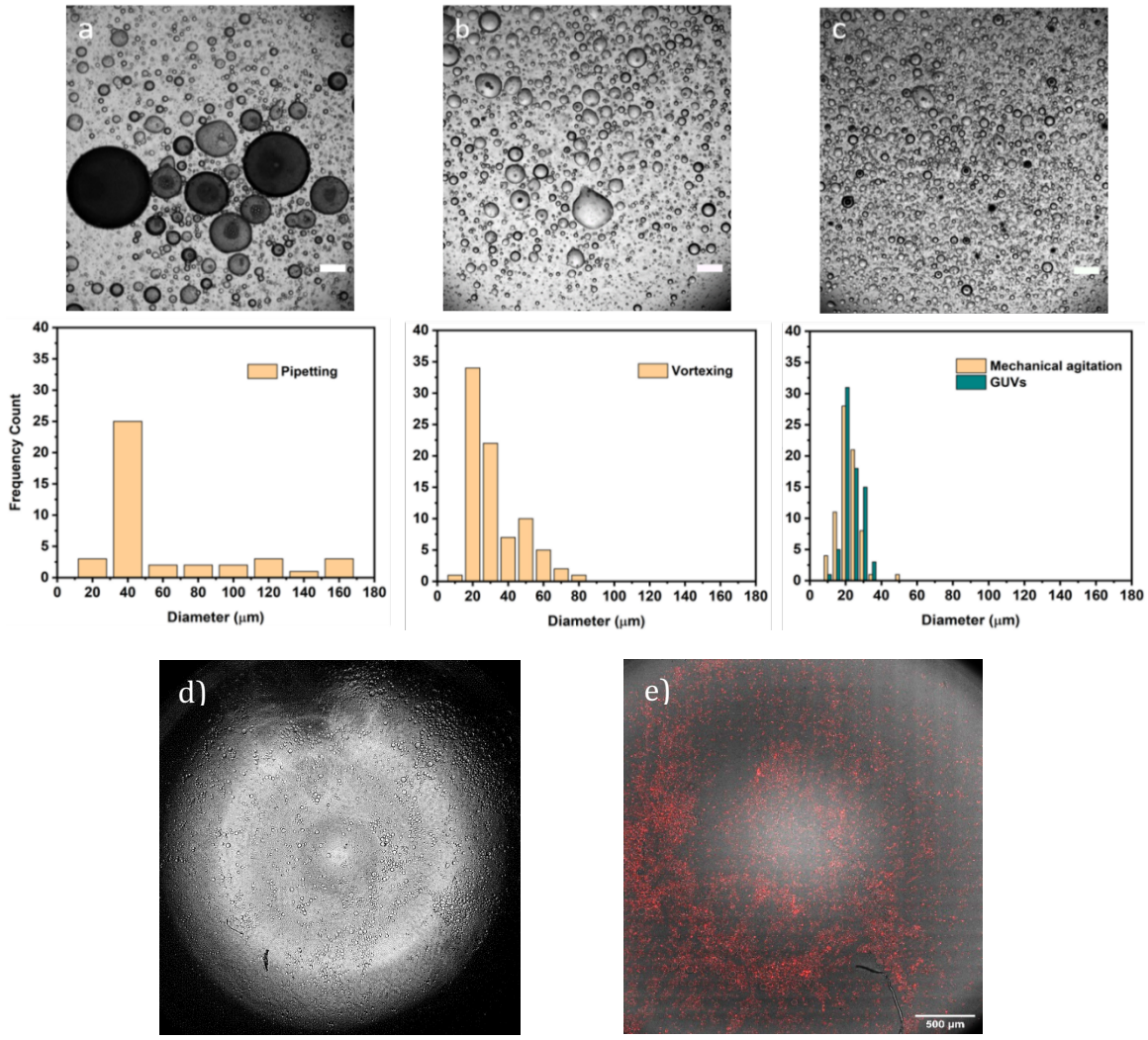

Figure 36. Comparison of emulsion preparation techniques.
a-c) Bright-field images of emulsion-droplets on a glass coverslip, compared to mechanical agitation, vortexing and hand pipetting yielded ~60% and ~44% droplets, respectively. The size distributions of the emulsions are included below. Scale bars: 50 μm. Final vesicle sizes for the mechanical agitation are also including to verify that the sizes are conserved from droplets to GUVs. d-e) Bright-field and merged (bright-field and fluorescence) stitched images of a well from 96-well plate showing final GUVs from mechanical agitation, where the GUVs are labelled with DiIC18 (red).

The size distributions of droplets produced with these methods are shown in Figure 36 (a-c), with the representative images of the emulsions. Sonication did not provide a suitable emulsion (therefore the data not shown) droplet yield compared to mechanical agitation. Whereas the vortexing yielded more polydisperse W/O droplets. However, pipetting and mechanical agitation both had more monodisperse size distributions, with a narrower size distribution for mechanical agitation from 10 to 40 μm. The sizes of the emulsion droplets resulted in similar sizes of the final GUVs (Fig. 36 c) and therefore, the mechanical agitation was preferred. Moreover, the yield of the droplets and the GUV produced was significantly lower in vortexing and hand pipetting (~60% and ~44% respectively) compared to mechanical agitation.

4.1.2 Influence of Sugar-based Density Gradients on GUV formation

The inclusion of a density gradient between the lipid-oil and the inner aqueous solution is an essential factor for the formation of GUVs for the emulsion-based method. Mainly for the successful transfer of the W/O droplets from the oil phase to the aqueous phase through the interface. Most natural oils contain a lower density than pure water, whereas mineral oil with a density of 0.87 g/cm^3 is lower and was therefore primarily utilised. There was another density gradient to be taken into consideration the density difference between the inner aqueous solution and the outer aqueous solution. GUVs need to settle at the well bottom not only for instant visualization but also to avoid aggregation at the interface. It was only possible if the outer aqueous solution was less dense compared to the inner aqueous solution present inside the droplets (and eventually inside the GUVs).

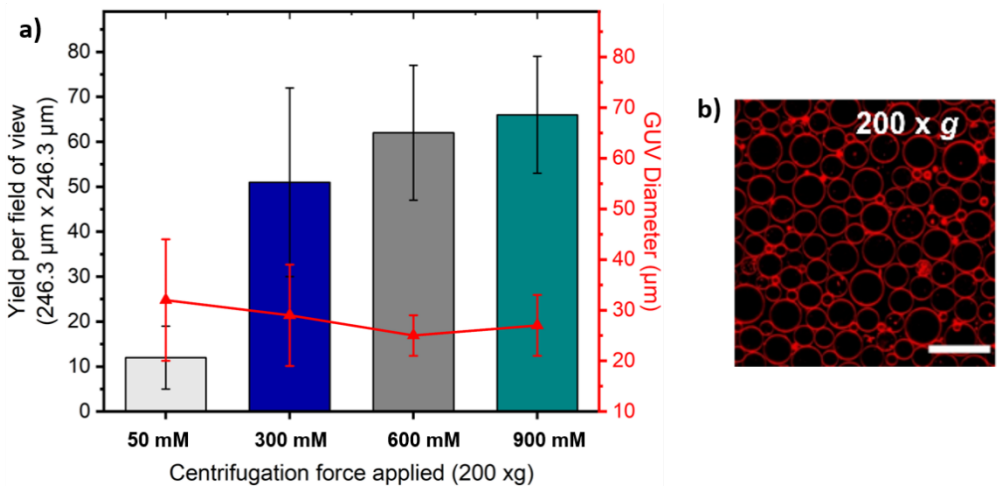

Figure 37. Yield and size distribution of GUVs with varying the inner solution density. The GUVs were produced using 1-palmitoyl-2-oleoyl-sn-glycero-3-phosphocholine (POPC) at different sugar concentrations. a) Yields obtained for each concentration of inner sucrose solution tested at 200 x g centrifugation speeds. Along with a line plot for the mean size of GUVs obtained at varied sugar concentrations and applied centrifugation speed, (n=3). b) Representative confocal images of GUVs containing 600 mM sucrose solution at various centrifugation speeds. Note that at 400 x g bursting occurs. Here, the inner volume was 5 mL and the incubation time for the interface formation was 30 min with a lipid concentration of 400 mm. Scale bars: 50 mm

This method of production not only requires a significant density gradient but also needs a sufficiently long enough time for all the droplets to cross through the lipid monolayer to obtain a good yield. From Figure 37 a, it was evident that there was a significant increase (at least ~5 fold) in the number of GUVs produced when the inner solution sucrose concentrations are equal to 300 mM or above compared to 50 mM at the given centrifugation (200 x g). Additionally, the GUV diameter was measurement from all the GUV population, as seen in Figure 37 a, line plot for the mean size of GUVs obtained at varying sugar concentrations. Figure 37 b confirms the average diameter of the GUVs remained ~20 µm, while varied between 50 mM - 300 mM. Please note that the glucose solution at an iso-osmolar concentration, with the inner solution, was utilised as the outer solution. Alternatively, this process was aid by applying a combination of the centrifugal speed with varying duration (next study).

4.1.3 Influence of the Centrifugation on the GUV formation

The centrifugation is required to assist the droplet to cross through lipid monolayer to form the GUVs. In this study, achieving a good yield at lower speeds but with longer time durations was aimed, as shown in Figure 38 a. As expected, the yield increased with increasing duration of centrifugal force applied, (see 1200 x *g* centrifugal speed for 10 min in Figure 38 a), that a longer applied force will increase the chances of the droplets crossing over the interface. Figure 38 a, also shows that the yield of GUVs remains highest with a minimum of 3 minutes and above 200 x *g*. Furthermore, as the yield of the GUVs remained the same for higher forces, it suggests that most of the droplets have passed through the interface (for this specific volume of emulsion droplets and solution density gradient).

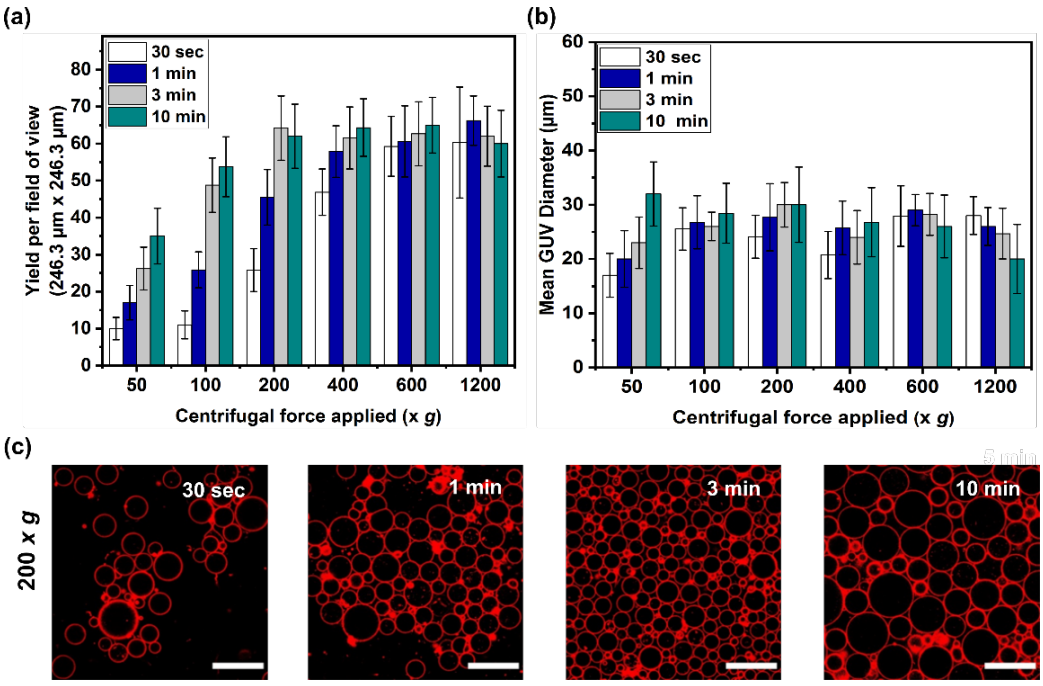

Figure 38. Plots of the produced GUV at different centrifugation time periods and speeds.
The graphs representing a-b) GUV yield and size, respectively. c) Confocal images of GUVs produced at 200 x g centrifugation speed at various times. DiIC18 was used as a membrane stain to visualize the GUVs. Note that error bars are taken from the standard deviations throughout, (n=3). These results were obtained for fixed 600 mm sugar solutions, 5 mL inner volume, incubation time for the interface formation of 30 min, and with a lipid concentration of 400 mm. Scale bars: 50 mm.

Considering this observation, at a centrifugation force of 200 x *g,* a maximum yield of GUVs was formed (~60 GUVs at 3 min centrifugation) which did not further increase even by an increased force applied or prolonged centrifugation time. Hence, the GUV formation for this thesis was performed under the latter conditions.

4.1.4 Influence of the Volume of Inner solution on GUV formation

It was hypothesized that the GUV yield depends on the initial number of water-in-oil droplets. Therefore, the volume used to produce the initial emulsion of the inner aqueous solution was varied. Note that all other volumes were kept constant and the same total of 50 µL volume of the emulsion was applied in the production. The inner solution volumes from 1 µL to 25 µL, was utilised, as shown in Figure 39 a, the yield increased with volumes between 5 µL and 10 µL. As shown in Figure 39 b, the GUV size peaked at 25 µL inner solution volume. It expected that the yield decreases with smaller volumes of the inner solution, but it was unexpected that it decreases again at higher volumes. Whereas, in the case of 10 µL and 25 µL conditions, the average diameter is 1.5-fold more than the other conditions. Consequentially, these results suggest a possibility to adapt the size of the GUVs by varying the volume of the inner solution to make the emulsion. For the next experiments, we selected 7 µL for the inner solution volume as it produces the highest number of GUVs with the least variation in GUV size.

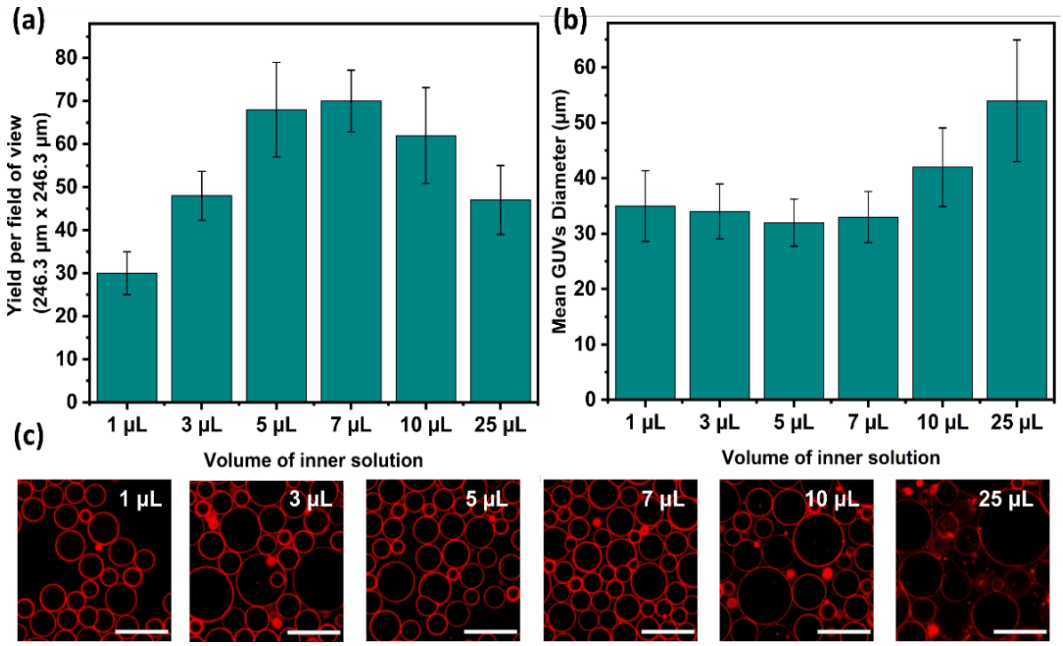

Figure 39. The effect of the inner solution volume on water-in-oil droplet emulsions. The plot representing the effect that inner solution has on the emulsion, a) the yield and b) the average size distribution of the GUVs, (n=3). c) Confocal images of GUVs with 600 mm sucrose produced at 200 x *g* speed for 3 min. Scale bars: 50 mm.

4.1.5 Lipid Concentration and Interface Incubation time

The concentration of solubilised lipids in the oil phase directly affects the time it takes to form the monolayers at the oil-water interfaces. Consequently, this puts a limit on the speed of the overall preparation time, which can be a disadvantage without optimisation. Moreover, an incomplete lipid monolayer at the interface can directly affect the yield of the GUVs produced. An incomplete lipid monolayer at the interface can directly affect the yield of the GUVs produced. Since incomplete monolayer would allow the droplets to fall through without encircling the second monolayer around, thus, the droplets would end-up in the outer solution. In Figure 40, the minimal required total concentration of lipids in the oil phase to help form a complete interfacial monolayer at the shortest possible time while still providing good GUV yield was investigated. For the various lipid concentrations tested (50, 100, 200,

400 and 800 µM), the GUV yield increases with lipid concentration with any given period of incubation (Figure 40 a). Confocal image for 200 µM in Figure 40 c, also shows that a more extended period of incubation results in better yield. However, the data also reveals that if the lipid concentration was too low (<200 µM), it was not possible to increase the overall yield with longer incubation time. Presumably due to the unavailability of lipids needed to cover the interfacial area of the well entirely. For higher lipid concentrations (200, 400 and 800 µM), the yield was similar and reached a plateau with a minimum of 30 minutes incubation time. Likewise, the diameters were similar and only varied between 20-30 µm with all the given condition. Considering this finding, for the next optimisation, we fixed the interfacial incubation time at 30 minutes and the lipid concentrations at 200 µM.

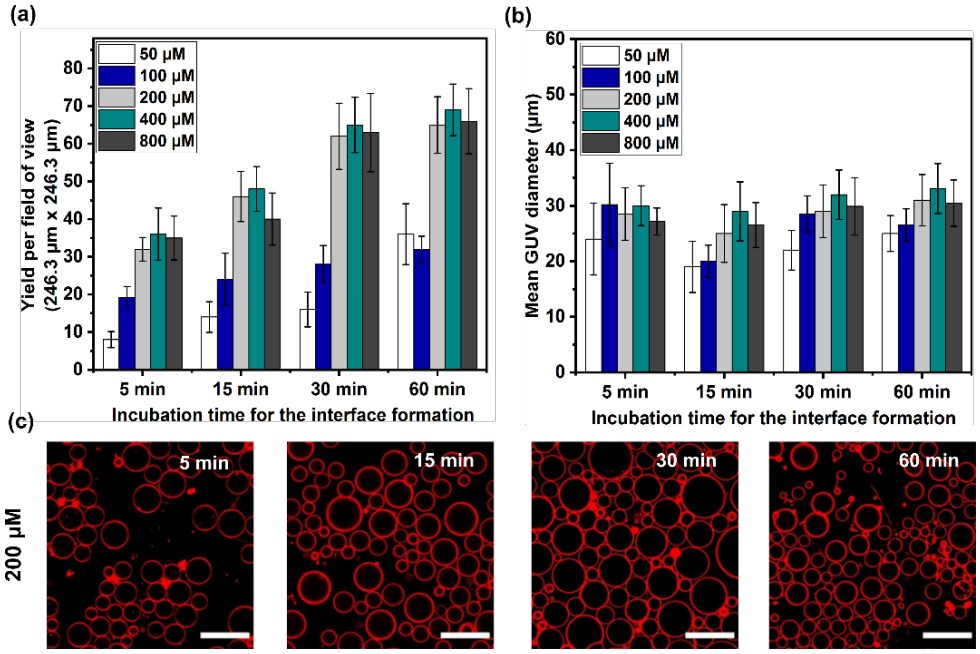

Figure 40. Plots of the GUVs produced with various lipid concentrations.
Lipid concentration and different incubation time periods are studied here with yield and size of GUVs, (n=3). c) Confocal images of GUVs with 600 mm sucrose solution produced at 200 x g for 3 min with 200 mm lipid concentration in mineral oil. Scale bars: 50 mm.

4.1.6 Effects of pH and Temperature on GUV formation

pH and temperature play a significant role in the functionality of the biological processes.[134,135] The giant vesicles have been shown to be robust at various physiologically relevant pH and temperature ranges.[44] Since this emulsion-based method has the advantage of encapsulating large biomolecules such as enzymes, it is, therefore, possible to study the enzymatic activity of biologically relevant chemical reactions encapsulated within. To determine if it is possible to produce GUVs at such conditions, GUVs were prepared at various pH (inside and outside) and temperature conditions. Figure 41 shows the change in yield and size with varied temperatures and pH conditions. Yields moderately increased from pH 4 to 9 and decreased significantly at pH 12 (Figure 41 a). Moreover, at a higher pH such as pH 12, the vesicles were observed to be larger with clustering and aggregation (Figure 41 c). In a further experiment to ascertain the greater applicability of the method for producing

biomimetic compartments, we used the buffering agents HEPES, Tris and PBS within the inner solution only, section 4.1.7.1.

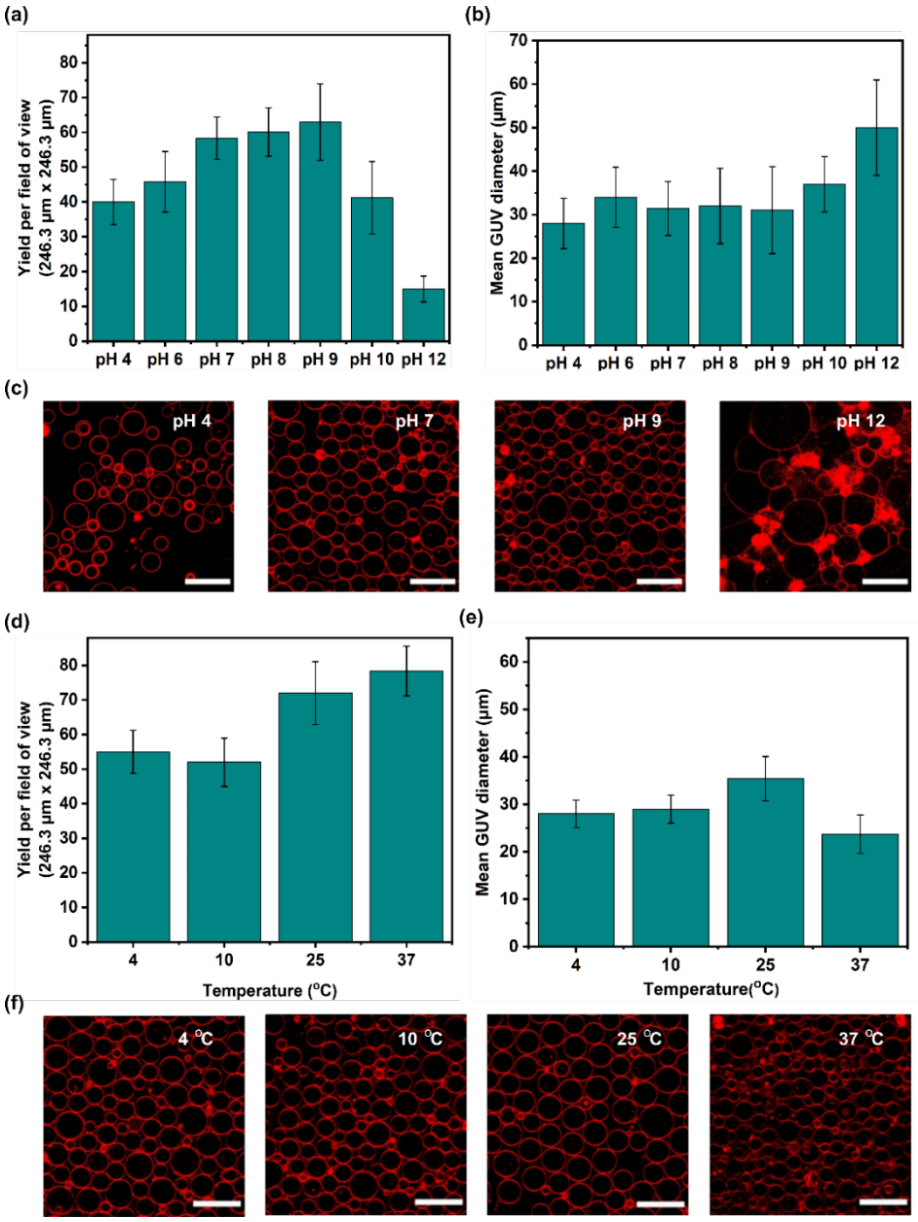

Figure 41. The yields and sizes of the GUVs produced at different pH and temperature. a,b) pH and d,e) temperature conditions, (n=3). Confocal images of these GUVs acquired for c) pH 4, 7, 9 and 12 and f) temperatures 4°C, 10°C, 25°C and 37°C. Scale bars: 50 mm.

Unlike pH, the temperature does not show a drastic influence on the overall yield of the GUVs (Figure 41d). The yield appears to increase marginally with temperature, at least for the one component POPC lipid composition implemented here. While the maximum temperature used in this study (37°C) yielded a higher number of GUVs, the average size of the GUVs (23 ± 4 µm) was smaller than the average size of the GUVs (30 ± 4 µm) produced at rest of the temperature conditions (Figure 41 e). Visually, the GUVs produced at all the temperatures tested were without defects or aggregations and large size variations except at 37°C where some small lipid clumps were seen (observed as bright red spots in Figure 41 f).

4.1.7 Encapsulation of Macromolecules in the GUVs

In this thesis, a high encapsulation of proteins from the biosynthesis was essential for the *in vitro* study. Hence, a technique providing efficient and rapid encapsulation of low sample volumes (µL-mL), with varying salts buffers, and charged molecules, was required. Hereby, in this section, we took the above-optimised emulsion-based method of GUV production and investigated for the encapsulation efficiency of different macromolecules. The emulsion-based method has been previously reported to have a few drawbacks as bioreactors such as reduced yields or insufficiently large GUVs with heterogeneities. Thus, very few groups have employed the method resulting in the alternative limitation with the range of experimental possibilities.[25,71,136]

4.1.7.1 GUVs prepared under different Physiological buffers

Prior to the encapsulation of different macromolecules from the pathway, GUVs were produced using different buffers with varying concentrations. This study ascertains the greater applicability of the method for producing further biomimetic compartments within given physiological conditions. For this study, buffering agents such as 4-(2-hydroxyethyl)-1-piperazineethanesulfonic acid (HEPES), Tris and phosphate-buffered saline (PBS) within the inner solution only were utilised.

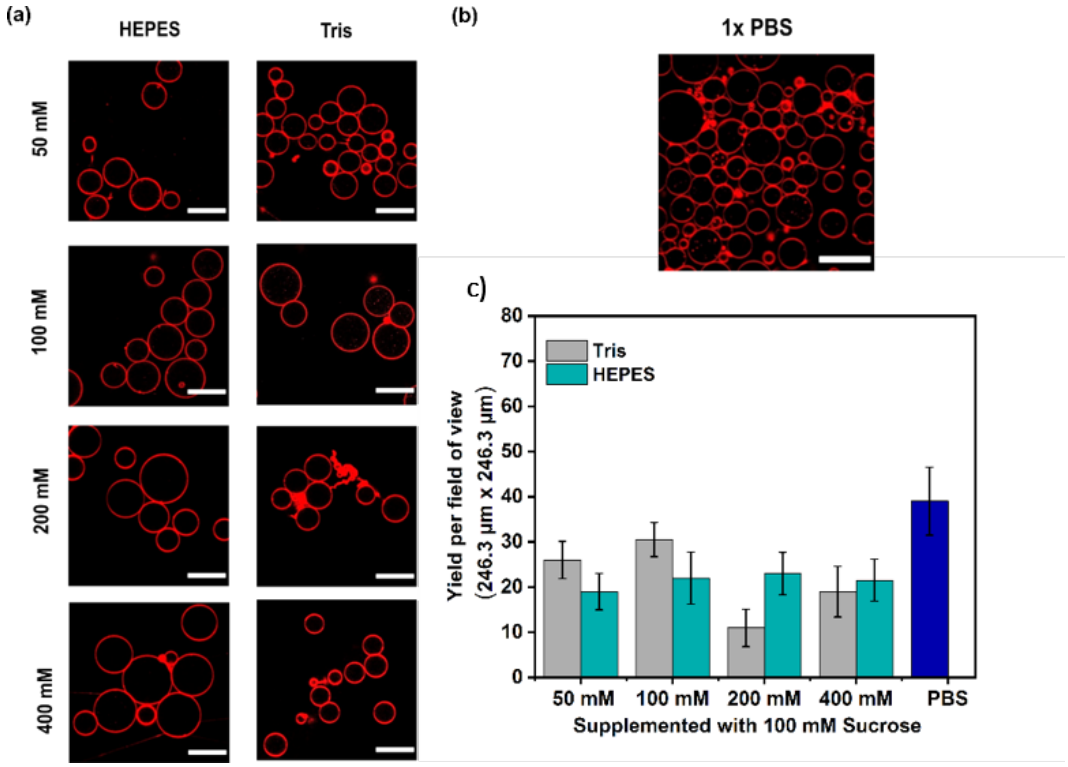

Figure 42. Physiological buffers using the emulsion-based method.
Confocal images of exemplary GUVs produced using buffer with varied concentrations of (a) HEPES and Tris buffers or (b) 1 × PBS as the inner solution only. Scale bar: 50 µm (c) The yields graph of GUVs produced for various concentrations of HEPES or Tris and with 1 × PBS. Note that 100 mM sucrose was added to the inner solution to provide a density gradient and osmotically matched glucose was used as the outer solution. Results were obtained for fixed 100 mM sugar solutions, 200 µM lipid concentration and 30 minutes interfacial incubation at 200 x g centrifugation speed with 3 minutes at RT (n=3).

As illustrated in Figure 42, the method can produce GUVs containing these widely distributed buffers that were not always feasible with conventional methods such as electroformation, especially in the case of salt-containing PBS solutions. The plot shown in Figure 42 represents the yield distribution to be less polydisperse with the buffer supplemented with Tris, PBS and HEPES with 100 mM sucrose, from three respectively reproduced experiments (n=3). The inner solution was supplemented with the individual buffers in given concentrations (50 mM, 100 mM, 200 mM, 400 mM), and 1X PBS while the outer solution was iso-osmatic with glucose only. However, the average GUV diameter was observed within the same range in all the tested condition (therefore, the data not shown).

Next towards the reconstitution study is the encapsulation of molecules, such as calcein dye, and eGFP, to assure the general stability of the GUVs (as oppose to either leakage or bursting). In this encapsulation study, a chemically synthesised stable intermediate from the pathway was encapsulated and studied over time to confirm the compatibility of the planned Moco pathway within GUVs, towards the central aim of the thesis. The GUVs are known as liposome-based protocell in the field, where these model membranes are utilised as an enclosed biomimetic entity. Hence, the method was tested to avoid permeation and loss of material through the synthetic cell membranes for a successful *in vitro* biosynthesis.

4.1.7.2 Encapsulation of Calcein Dye

To test the stability of the model membranes, a well-studied fluorescent dye was used. Calcein is very commonly used fluorescent dye in the field of membrane biophysics. It has been used to study the membrane properties while present in either the inner or the outer environment of the liposomes. Since it is a small molecule which is normally membrane impermeable.[137] This property can be utilised to investigate the instability arise due to any transient pore within the GUV population using this method. Therefore, the above-optimised method was investigated for the membrane stability by encapsulating the calcein dye inside the GUVs.

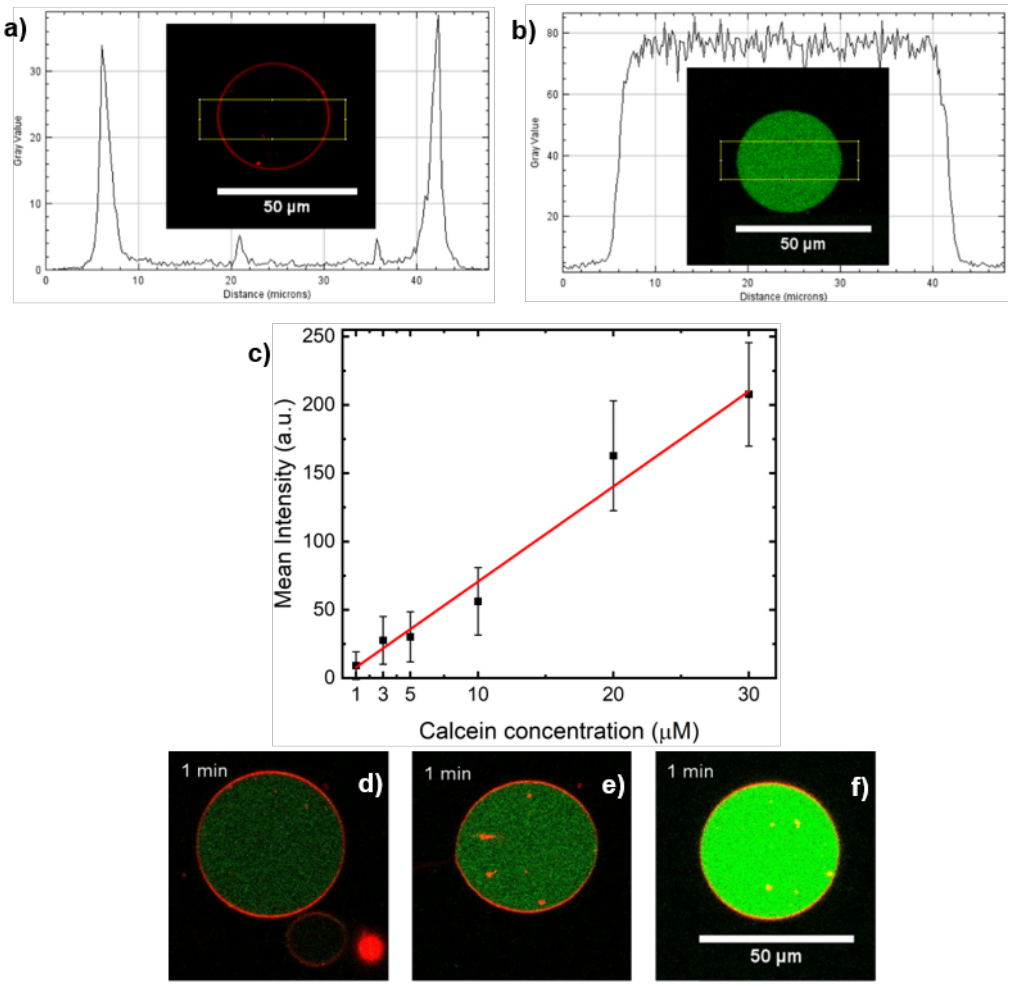

Figure 43. Encapsulation study of calcein at various concentration.
(a) The marked area is the selected profile of the membrane, labelled with membrane dye DiIC18, overlapped with fluorescence intensity graph that shows the two peaks in the plot for the fluorescence intensity of the selected profile. (b) Likewise, the selected area showing the distribution of calcein (ex 488nm, em 525nm; in green) inside the GUV that is represented using the overlapped intensity graph. c) A calibration curve plotted using multiple calcein concentrations with the mean fluorescence intensity under SP8 confocal detection, (n=3). (d-f) Representative confocal images of increasing calcein concentration (5 µM, 10 µM and 25 µM) with 500 mM sugar gradient. The data was reproduced 3 time.

The stability of GUVs was tested using the fluorescence intensity of the encapsulated calcein by using varying concentrations. For the study, varying calcein concentration with 500 mM sucrose at pH 7, was encapsulated in the inner environment. The inner environment of the GUVs was osmotically balanced with glucose in the outer environment. The encapsulated calcein inside GUVs was measured using the confocal detection (ex 488nm, em 525nm). Figure 43 a and b show the line profiles of a spherical POPC GUV, labelled with DiIC18 (red) and containing the calcein dye (green), together with their respective fluorescence confocal images. In Figure 43 a, the plot representing the fluorescence intensity of the membrane with two peaks on the vertical axis, whereas microns distance on the horizontal axis represents the diameter of the GUV. Likewise, the calcein signals from the inner environment of the same GUV are shown in Figure 43 b with the line profile measurement. The confocal images did not show any visible calcein signal from the outer environment of the GUVs. Further, a standard curve, also known as a calibration curve, was plotted to estimate the different calcein concentration with the difference in calcein fluorescence intensity. The calibration curve was a plot with varying calcein concentration to account the different calcein intensities inside the GUVs later. As expected, the curve shows a linear increase with the increase in calcein concentration in bulk. Likewise, when encapsulated in the varying concentrations inside the GUVs, using the emulsion-based method, the dye shows a linear increase in the fluorescence intensity, seen in Figure 43 c. This observation supports the linear increase in the representative confocal images with Figure 43 (d-f). Hence, confirming the efficiency of the emulsion-based method and its potential application in macromolecules encapsulation for the later application in the thesis.

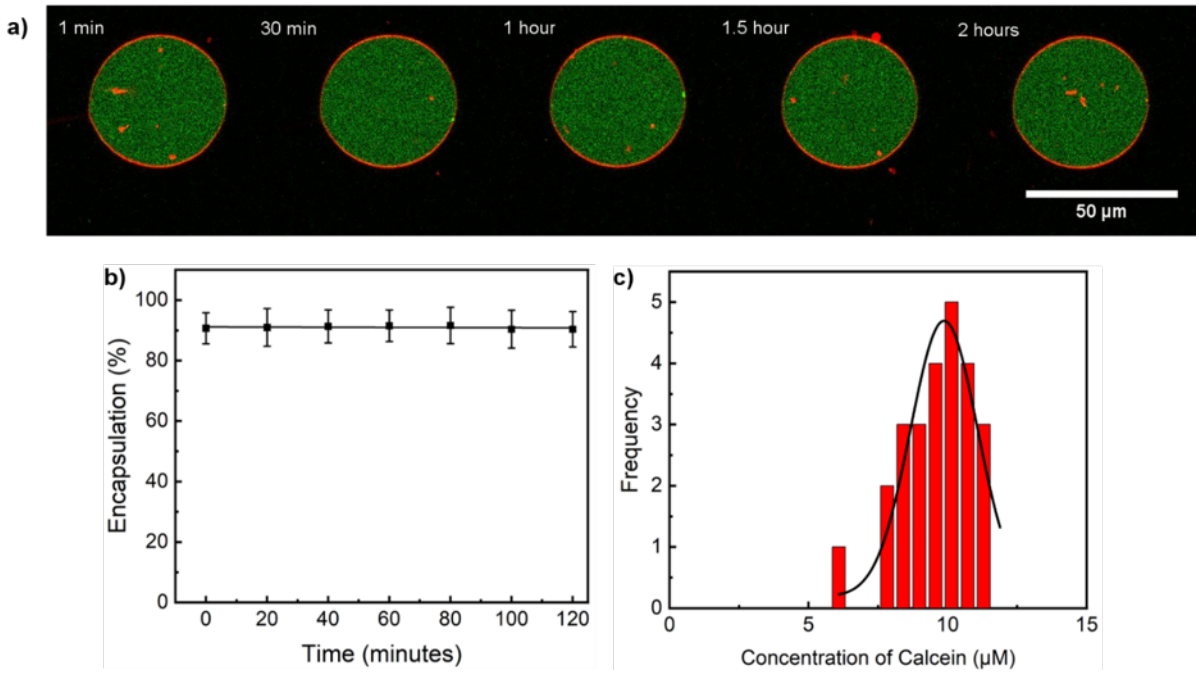

Figure 44. Time-lapse measurement of the encapsulated calcein.
a) Representative confocal images showing of the GUVs with 10 µM calcein (green) reconstituted with 500 mM sugar gradient (in/out). The measurements were acquired for 2 hours, here the snapshots are shown from each timeframe. Scale 50 µm (b) The graph showing the encapsulation over 2 hours, where every point represents the average intensity of 50 GUVs (n=3). (c) The histogram showing the encapsulation variation among the population with encapsulated calcein.

Further, the stability of the GUVs was analysed by testing GUV morphology over time with time-lapse measurements. The time-lapse acquisition was collected every 30 minutes for a total of 2 hours to examine any leakage (i.e. through unwanted pores). As observed from Figure 44 a, the GUVs showed a consistent fluorescence distribution over-time. Additional to the confocal observation where no visible bursting was found after 2 hours, the fluorescence plot from Figure 44 b, measured for 50 GUVs shows the average intensity from the inner GUVs environment. Here, the calcein fluorescence was normalised to the value of the calcein fluorescence in bulk (bulk data not shown here). The fluorescence intensity remained consistent over 2 hours which confirms the confined environment provided by GUVs. This over-time encapsulation efficiency was examined using a fluorescent intensity assay, based on the calibration seen in Figure 43 c. For the assay, the calcein intensity from GUVs has normalised to the calcein fluorescence in bulk as 100 % for the given concentration. In this study, 10 μM calcein was utilised for time-lapse measurement, hence the fluorescence from 10 μM calcein from Figure 43 c, was normalised to 100%.

As a result, the time-lapse measurement shows ~83 % overall encapsulation distributed among 50 GUVs. Further, the GUV population was plotted on a frequency histogram, which also confirms that the method can encapsulate calcein with 83 % efficiency. In the histogram Figure 44 c, for 10 μM of the encapsulated calcein, only 9.43 ± 1.69 μM was resulted inside the GUVs, while the rest lost during the production. As seen earlier, the emulsion-based method requires the number of steps, which can potentially generate this loss of inner concentration. Nevertheless, the time-lapse measurement was further taken up to 4 hours, to test the stability and encapsulation efficiency once the GUVs were formed. The trend followed a similar pattern with no detectable calcein leakage and encapsulation efficiency (therefore, data not shown here). Furthermore, this fluorescent intensity assay was further employed in the encapsulation of related substrates from the pathway (discussed later in 4.2.2.2).

4.1.7.3 Synthetic Form A inside the GUVs

The Moco biosynthesis has never studied in any minimal liposomal-based *in vitro* system. Hence, establishing the biosynthesis inside the liposomes requires the possible understanding of the Moco biosynthesis within GUVs. Since the fluorescent-based detection was utilised for the study, a fluorescent molecule from the biosynthesis was a preferred choice. However, the pathway has not yet encountered for a fluorescence-based detection. One molecule that can potentially be used is an oxidised-form of a stable intermediate from the pathway, the oxidised-form of MPT also known as its fluorescent counterpart named form A.

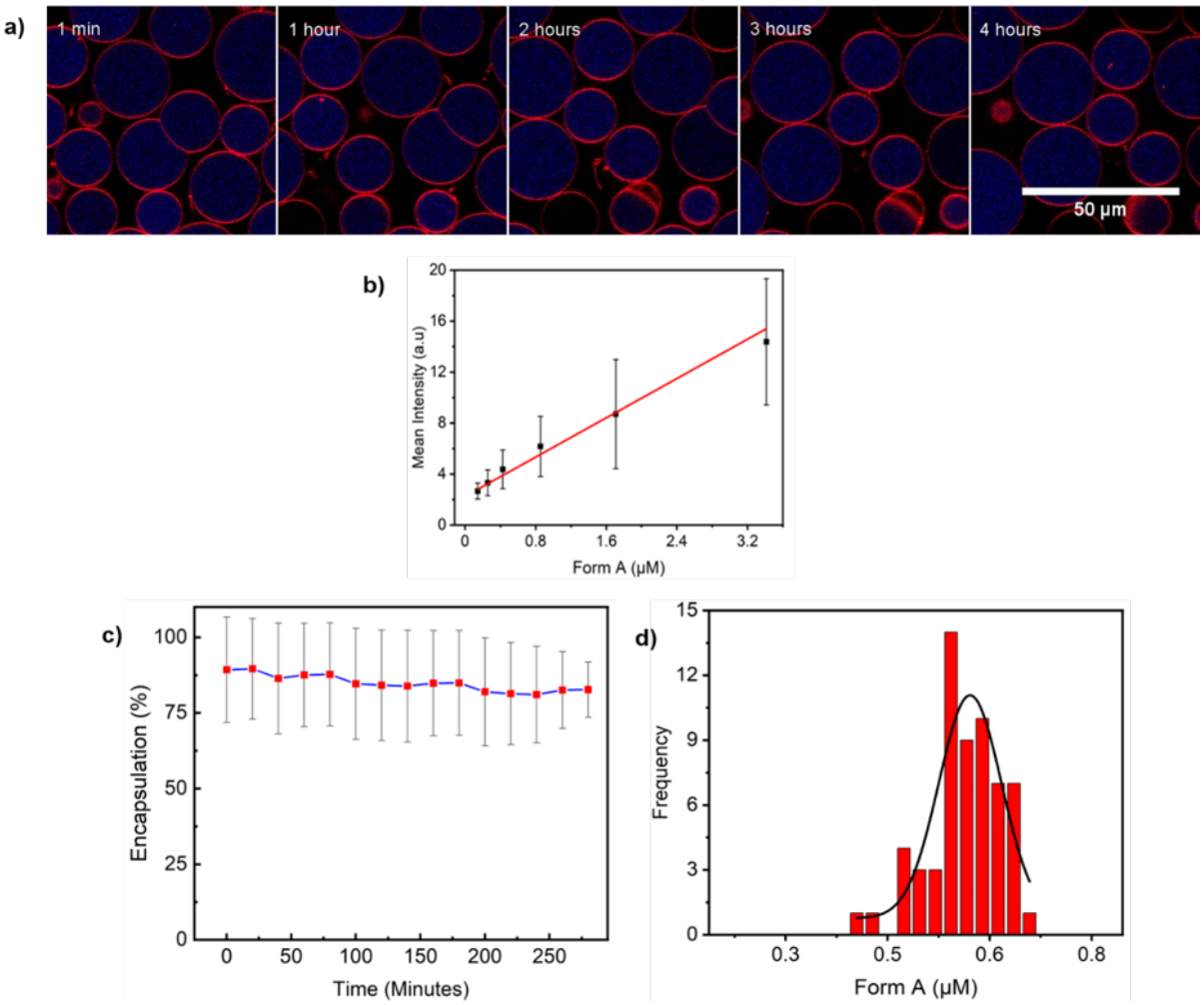

Figure 45. Encapsulation study of form A, 1 µM.
a) Represented confocal images from the time-lapse measurements, GUVs labelled with DiIC18(red), each showing the reconstituted form A (blue) on the given time points with 500 mM sugar gradient. (b)The calibration curve obtained with different encapsulated form A concentration. (c) The normalised intensity graph of the form A encapsulation studied over 4 hours, where the individual point represents the average intensity of 50 GUVs. (n=3) (d) The histogram with the distributed variation among GUVs after 10 minutes.

The fluorescent counterpart was the first choice for this compatibility study for the two systems. A chemically synthesised form A, provided by Prof. Dr Lindel, TU Braunschweig,[138] was encapsulated in the GUVs using the emulsion-based method and examined for any permeation. Here in Figure 45 a, DMSO dissolved form A (1 μM) in 500 mM sucrose makes the inner environment of the GUV, osmotically balanced with glucose solution in the external environment. The confocal fluorescence images (merged) of POPC GUVs labelled with DiIC18 (red) and containing form A (blue) over time is shown in Figure 45 a. The encapsulated form A inside GUVs was measured using 405 nm excitation and 425 nm emission with no noticeable background signals.

The fluorescence signals of form A taken from time-lapse acquisitions every 30 minutes for 4 hours show a negligible decrease indicating an enclosed and leakage-free environment for potential biochemical reactions. In Figure 45 c, time-lapse of 50 GUVs were averaged for the above-mentioned stability assay with calcein, section 4.1.7.2. This over-time measurement shows that the method can encapsulate form A with the efficiency of ~85 % with a big variation of ~32 %. Figure 45 b shows the calibration curve obtained with different encapsulated form A concentration, where the variation notably increases with the increase in concentration. This calibration curve was applied to translate fluorescence intensity to the form A concentration in the later application. Additional to the encapsulation efficiency test, a histogram based on the frequency of GUVs with different fluorescence intensity was also plotted Figure 45 d. In this test, the concentration of the inner solution conforming the internal environment was calculated $0.59 \pm .26$ μM of the 1 μM. The assay shows that the method can encapsulate the DMSO dissolved form A with 74 % efficiency with a variation of ~25 %. Where the rest was lost during the production (i.e., droplet bursting or partitioning into the oil phase). Unlike calcein, encapsulation study of form A shows notable variations and discrepancy between the two fluorescence-based assays. Therefore, to eliminate these secondary effects, possibly due to the presence of DMSO, a different system was tested inside the GUVs, e.g., a protein from the pathways supplemented with a physiological buffer condition.

4.1.7.4 Encapsulation of MOCS2A tagged with eGFP

Towards a successful *in vitro* biosynthesis inside the GUVs, an effective encapsulation of the enzymes responsible for the biosynthesis was required. Preferably, an encapsulation without any enzymatic degradation or loss of other necessary factors in the biosynthesis. The eGFP-MOCS2A complex was heterologously expressed using the *E.coli* expression system, followed by the purification using IMAC technique described in section 3.1.11.2 and visualised using the SDS-gel, Figure 46.

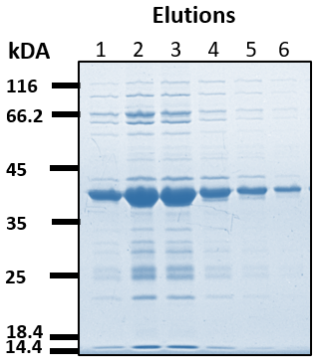

Figure 46. Analysis of the recombinant protein eGFP-MOCS2A on SDS-PAGE.
The elution fractions were separated on 15% SDS-PAGE gel of eGFP-MOCS2A (36.20 kDa) and stained with Coomassie brilliant blue. The image shows the elution profile (1-6) after Ni-NTA purification, and the different lanes represent the fractions.

However, there are several enzymes involved in the Moco Biosynthesis; here we chose a human cytosolic enzyme (MOCS2A) for this encapsulation study for the following reasons.

1) MOCS2A is a smaller and stable protein while other enzymes such as MOCS1A/MoaA are oxygen-sensitive and has 2[4Fe-4S] clusters which are challenging to handle at first glance.
2) It is a cytosolic enzyme responsible for the transformation of cPMP into Moco, makes it a crucial molecule in later studies.
3) The initial handling of this stable enzyme will help us proceed with more complex enzymes in the later applications, e.g. MOCS1A/MoaA, MoaC etc.
4) Finally, the enzyme could be fused with eGFP, a factor most convenient for the fluorescent-based detection system.

The eGFP-MOCS2A protein complex was easily observed with the confocal microscopy, hereby, the encapsulation efficiency was further tested. The complex was reconstituted inside the inner environment of the GUV at 20 µM concentration in 500 mM sucrose supplemented with 100 mM Tris. Figure 47 a, shows confocal images of POPC GUVs labelled with DiIC18 (red) containing eGFP-MOCS2A (in green) over time. As thoroughly described in the optimisation studies (section 4.1.7.1), every step in the experiment was optimised to maintain the physiological conditions for the enzymes. For example, an optimal temperature of 4°C could be maintained throughout the sample preparation, while imaging could be performed only at room temperature.

Upon the successful encapsulation, fluorescence signals of the encapsulated enzyme were seen to be constant in the time-lapse acquisitions (Figure 47 a). The images were taken every 30 minutes for 4 hours where no degradation was observed, indicating an enclosed environment for potential biochemical reactions.

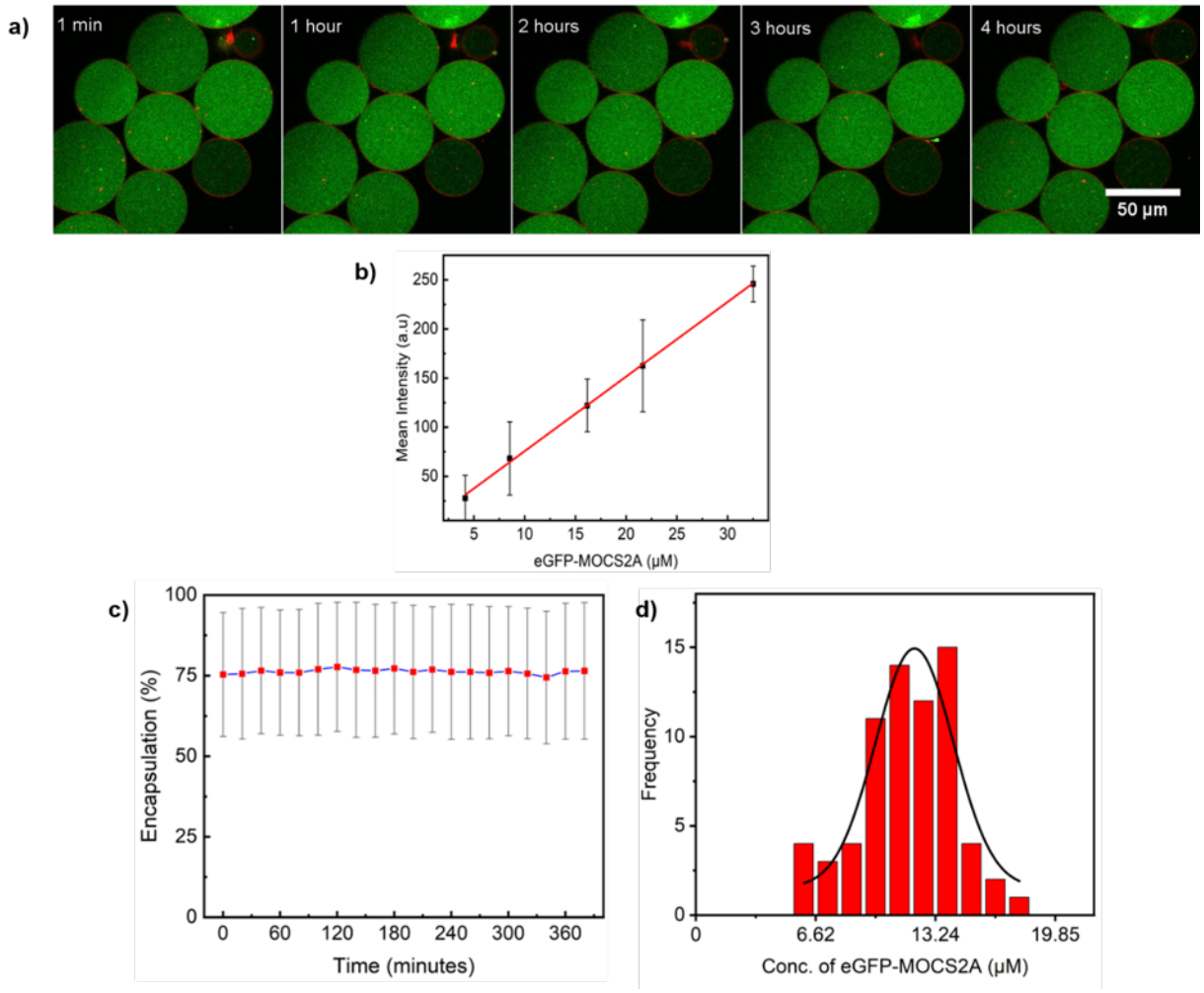

Figure 47. Encapsulation study of eGFP-MOCS2A.
a) The confocal images of GUVs, labelled with DiIC18 (red), with homogenous reconstituted eGFP-MOCS2A (green) with 500 mM sugar gradient in 100 mM Tris buffer. The snapshots were taken from the time-lapse measurement. (b) A calibration standard plotted with the given increasing eGFP-MOCS2A concentration. Each data points represent an average of three independent data set. (c) The intensity of eGFP-MOCS2A over 4 hours, where each point represents the average intensity of 50 GUVs. (n=3). (d) The histogram from the same set, showing the encapsulation variation among the GUV population after 10 minutes

Figure 47 c confirms the stability (i.e., no bursting or leakage) over 4 hours quantitatively. Additionally, the GUVs were found stable up to 12-15 hours in the provided conditions (data not shown). Figure 47 b shows the calibration curve of the encapsulated protein, where the increase in concentration shows increased intensity. The frequency histogram in Figure 47 d shows that 20 µM of the encapsulated eGFP-MOCS2A resulted in 13.18±3.46 µM inside the GUVs. The absolute concentration of the protein inside the GUVs shows the variation in the encapsulation, which indicate the loss of protein. In

conclusion, of the optimisation and encapsulation study of this emulsion-based method, optimal production of GUVs was performed at 18 minutes by reducing the incubation time from 30 to 15 minutes. Throughout this thesis, 200 µM lipid concentration, the centrifugation speed and time was mainly 200 x g for 3 minutes, whereas in some case 140 x g was utilised. Thereafter, understanding the encapsulation efficiency and stability with varying biomolecules opens the range for potential application of the method in the field. In this thesis, now that the method was well optimised, the Moco biosynthesis was further investigated.

4.2 *In vitro* Molybdenum cofactor Biosynthesis

In nature, molybdenum is found coordinated with a pterin molecule called molybdopterin (MPT) which forms molybdenum cofactor (Moco). The biosynthetic pathway of Moco has been intensively studied in recent decades, leading many discoveries on the reaction mechanism, structural characterisation of the stable intermediates and various essential catalytic complexes.[98,104] This well-known *in vivo* system was our choice for the reconstitution study in the thesis because it is also spatially separated in the eukaryotic cell. The biosynthesis involves complex enzymatic cascades, to simplify reconstitution, the pathway was divided into two intermediate steps. The steps are as follows, step 1; the generation of cPMP with a characteristic pyranopterin ring under anaerobic conditions. And step 2; is the transformation of cPMP to MPT by adding two sulphurs on the pyranopterin ring, both discussed in section 1.5.2. Further, the respective enzymes involved in these two steps were purified and analysed. Note that both reaction steps require different physiological pH and salts concentrations for their optimal conditions, therefore separating the steps would be beneficial at this point.

4.2.1 Step 1: Generation of cyclic Pyranopterin Monophosphate

Two enzymes MoaA/MoaC are responsible for GTP conversion into the first stable intermediate cPMP. MoaA is a radical S'adenosyl-L-methionine (SAM) dependent enzyme with 2[4Fe-4S] clusters as cofactors and requires a closed anaerobic environment to maintain the catalytic subunit. An active MoaA enzyme confined with 2[4Fe-4S] and MoaC was heterologously expressed in *E. coli* BL21 (DE3), described in 3.1.10. The protein was analysed conventionally over SDS-PAGE stained with Coomassie blue, Figure 48.

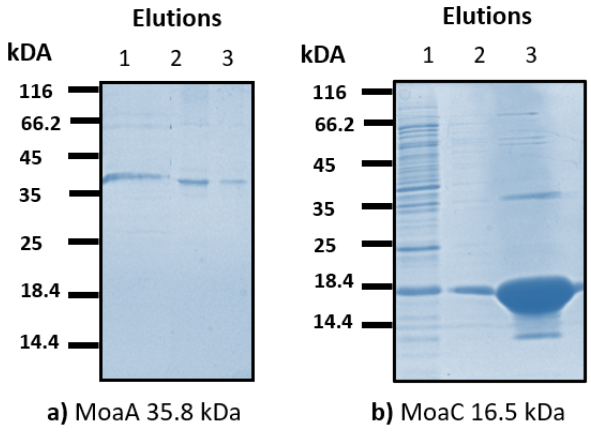

Figure 48. Protein analysis using SDS gel stained with Coomassie-Brilliant Blue. Three elution were collected and analysed (a) on 15% SDS-PAGE MoaA (35.8 kDa), and (b) on 12 % SDS-PAGE for MoaC (16.5 kDa) respectively, with fractions from the IMAC.

The MoaA/MoaC form a complex with S-adenosyl-methionine and GTP, as the main substrate to produce cPMP. The *in vitro* cPMP production in this thesis was adapted from Johnson & Rajagopalan,1989, Hover & Yokoyama, 2015,[127,139] whereas, the intermediate products were analysed by NMR/MS revealing the transformation of GTP to 3',8-cH_2GTP and subsequently convert 3',8-cH_2GTP, a substrate for MoaC, to synthesize a tetrahydropyranopterin cPMP.[91,98] From these characterisation studies, its well understood that the cPMP is not a stable molecule, meaning that it quickly oxidises to an

additional stable fluorescent product. This stable fluorescent product is known as compound Z, a molecule that has been adapted to assay the cPMP content in the past. Likewise, in this thesis compound Z was assayed to investigate the cPMP production.

4.2.1.1 Compound Z based assay for cPMP Quantification

The cPMP molecule was assayed with its stable residual product compound Z. For the reaction in this thesis, MoaA 200 µM, and MoaC 100 µM was first incubated, in 100 mM Tris-HCl buffers supplemented with 300 mM NaCl, pH 9, to form a complex. The reaction was followed by addition in a sequence of GTP/SAM (250 µM), $MgCl_2$ (500 µM) and DTT/Na-dithionite (1 mM). The reaction mixture was incubated for 1 hour at room temperature, under anaerobic conditions, and further oxidised overnight. In parallel, for positive control *in vitro* purified cPMP was oxidised into compound Z and similarly analysed through a reversed-phase C18 column at HPLC. The chromatography was conducted by isocratic elution with 0.1% methanol and 10 mM Potassium phosphate pH 3, with a flow rate of 1 mL/min and monitored by fluorescence (ex 383nm, em 450nm). The retention time of the reaction was expected around 6 sec as shown in Figure 49.

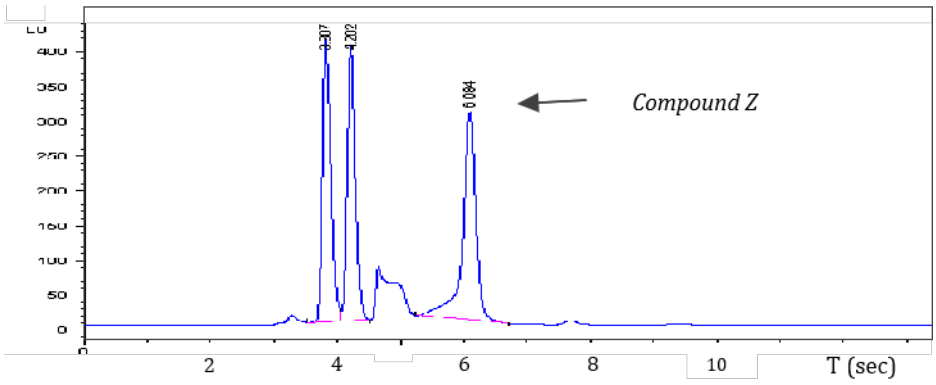

Figure 49. HPLC elution profile of cPMP content, over a reversed-phase C18 column. The elution profile of compound Z produced from the reaction mix (MoaA 200 µM, and MoaC 100 µM, GTP/SAM 250 µM, $MgCl_2$ 500 µM, and DTT/Na-dithionite 1 mM), was overnight oxidation with acidic iodine and separated on a reversed-phase C18 column using 10 mM potassium phosphate pH 3. The elution was observed with an Agilent 1100 series fluorescence detector with excitation 383 nm and emission 450 nm. The retention time around 6 sec indicates the presence of compound Z in the reaction mixture.

There have many characterisation investigations on the pathway, yet no literature was found on varying physiological conditions such as incubation temperature, pH range or duration for the assay. However, there are pH-dependent studies suggesting a chemical shift in pterins, for instance, at low pH nitrogen atoms N1 and N5 are positively charged that result in a more soluble and stable cPMP.[96] The information on the varying physiological conditions could be beneficial for the later reconstitution steps. Therefore, two different conditions such as the pH ranged from pH 6 – pH 10. Additionally, by eliminating one substrate at a time the reaction was examined to account for unspecific peaks.

In this direction, the experiments were performed first by eliminating a given substrate, such as the enzymes, GTP, SAM, DTT, and Na-dithionate, as seen in Figure 50 a. The graph was normalised to the initial concentration of GTP and further quantified as ~62 %

product formation (in the reaction mixture) with a variation of ~18%. Where the product formation in the absence of the given reactants was below 5 %. Experiments on the pH study (Figure 50 b) surprisingly suggests that pH 7 works better than pH 9 because the current literature suggests an alkaline environment for the reaction is more suitable.[111]

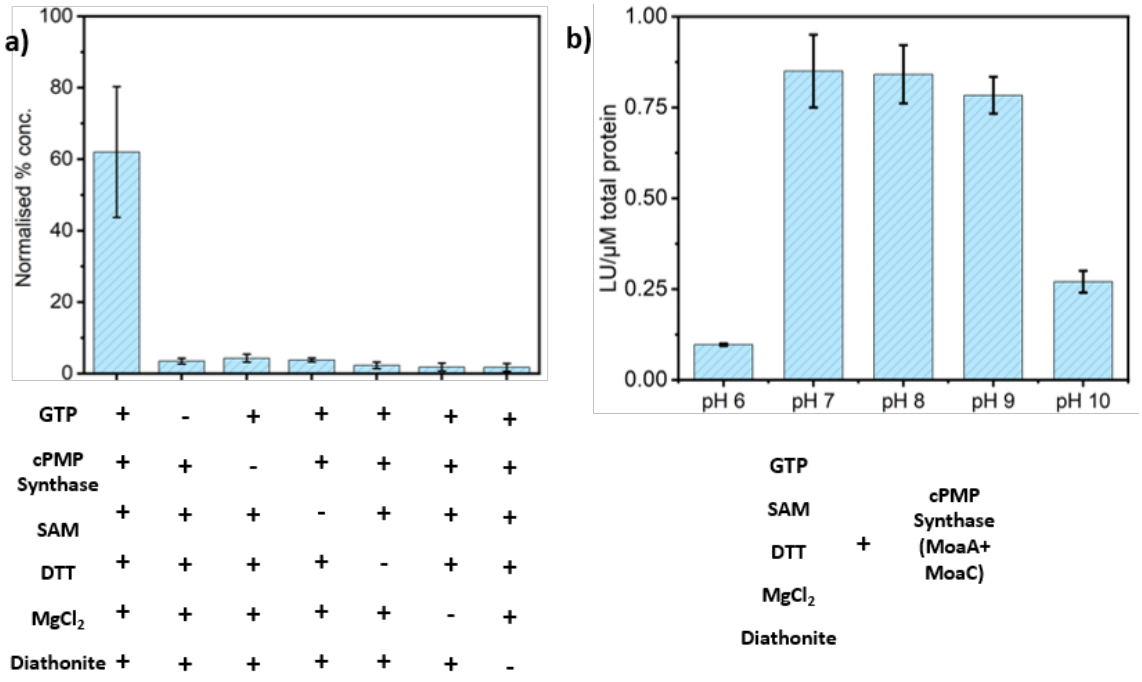

Figure 50. cPMP was oxidised to compound Z using KI/I_2.
(a) Compound Z analysed upon overnight oxidation of the reaction mixture, MoaA 200 µM, MoaC 100 µM, GTP/SAM 250 µM $MgCl_2$ 500 µM, and DTT/Na-dithionite 1 mM, with acidic iodine and separated on a reversed-phase C18 column using 10 mM Potassium phosphate pH 3. The compound Z concentration was normalised values obtained from pure cPMP run while estimated with GTP initial concentrations, n=3. (b) Whereas the LU/µM of total protein content was applied to illustrate cPMP formation per µM of protein in the reaction, over the given pH range from pH 6 to pH 10, this data was acquired at 25°C for 1 hour reaction time. (n=2)

However, this study provides insight into the reaction mechanism; there have been discrepancies within each set of experiments. Understanding the changing pH in this reaction mechanism was not an aim for this thesis, therefore, a separate investigation must be performed addressing this observation. Furthermore, this method could be also utilised for in-house cPMP purification.

4.2.1.2 cPMP Detection via released Pyrophosphate

The compound Z was only faintly detected under the confocal detection system, as the fluorescence of compound Z (ex 367nm, em 450nm) was under the detection limit. Hence, an alternative fluorescent-based detection was utilised for the confocal-based experiments. Since the formation of every cPMP molecule involves a pyrophosphate (PPi) cleavage from GTP backbone, upon providing a cyclic phosphate group to the cPMP. Hence, upon the release of PPi molecule, it can be assayed as a marker for the produced cPMP. In this study, a detection assay from Sigma-Aldrich was employed that gives stronger fluorescence signals in the presence of PPi molecule, Figure 51.

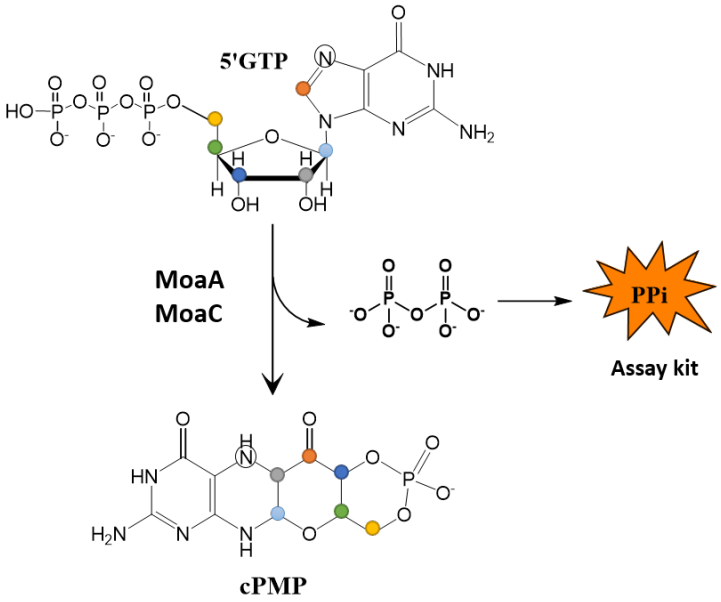

Figure 51. Pyrophosphate released with the production of cPMP.
In the reaction, for GTP transformation, the carbon and nitrogen atoms are labelled in different colours, which transfer to cPMP. In addition, where every cPMP formation results in the release of one PPi in the solution. A pyrophosphate assay was employed to detect the amount of pyrophosphate, which is directly proportional to the amount of cPMP formed.

The initial experiments were performed to plot a calibration curve under the confocal detection. The calibration curve helps to determine the correlation between the fluorescence intensity and the PPi concentration. Therefore, the fluorescence intensity from microscope images could be converted to a PPi concentration and thus to a cPMP concentration. To assay the cPMP production via PPi released in the solution, similar calibration curves were plotted as discussed previously in section 4.1.7. This time, the plots of the varying pyrophosphate concentrations using standard-PPi provided with the commercial assay-kit. The plot of the PPi concentration on the x-axis with respective fluorescence (in airy units) on the y- axis. Figure 52 a, shows the standard from the plate-reader as prescribed with the assay-kit, which was further adapted to the confocal, shown in Figure 52 b. A same range of the PPi concentrations was chosen in both cases, where the expected concentration was only in few microliter ranges. In all the plotted standard curves, a straight-line can be plotted using the linear fitting, as the straight-line was essential to adapt these calibration curves into the study. Essentially to correctly translate the fluorescence intensity from confocal images to a PPi concentration, and consequently to the cPMP concentrations.

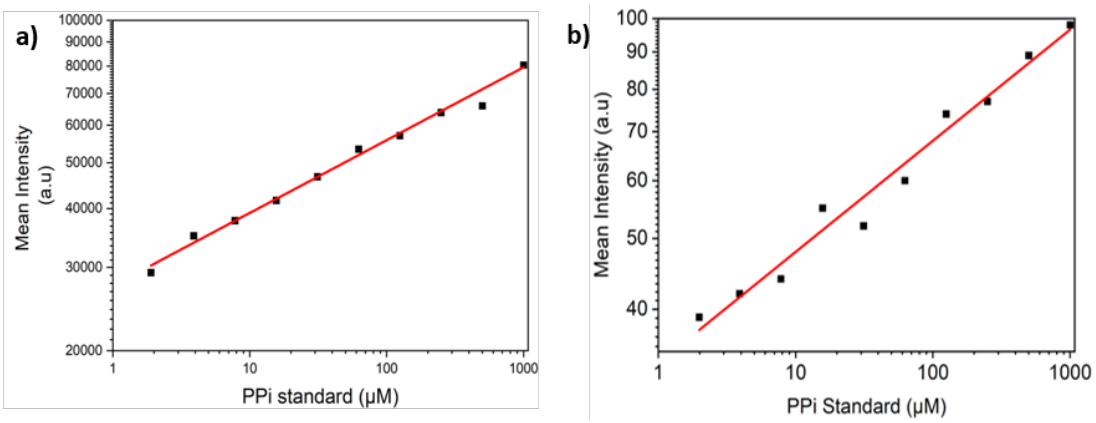

Figure 52. cPMP detection via PPi assay-kit.
(a) A bulk calibration curve for the PPi plotted with the given increasing concentrations on a plate reader, and (b) repeated under the confocal fluorescence measurements, where each point indicates average of 10 data points.

4.2.1.3 cPMP inside GUVs detected via PPi assay

Further, the PPi standard was plotted inside the GUVs mainly as a control for the later application. The PPi standard of 25 μM was measured inside the GUVs for over 4 hours, where the representative confocal images confirm a homogenous distribution over 4 hours, as shown in Figure 53 a. The time-lapse measurements were taken from an average of 50 GUVs. The bulk PPi fluorescence was normalised to 100 % that was utilised to estimate the reconstituted PPi fluorescence. The normalised percentage graph shows the percentage of PPi inside the GUVs, Figure 53 b.

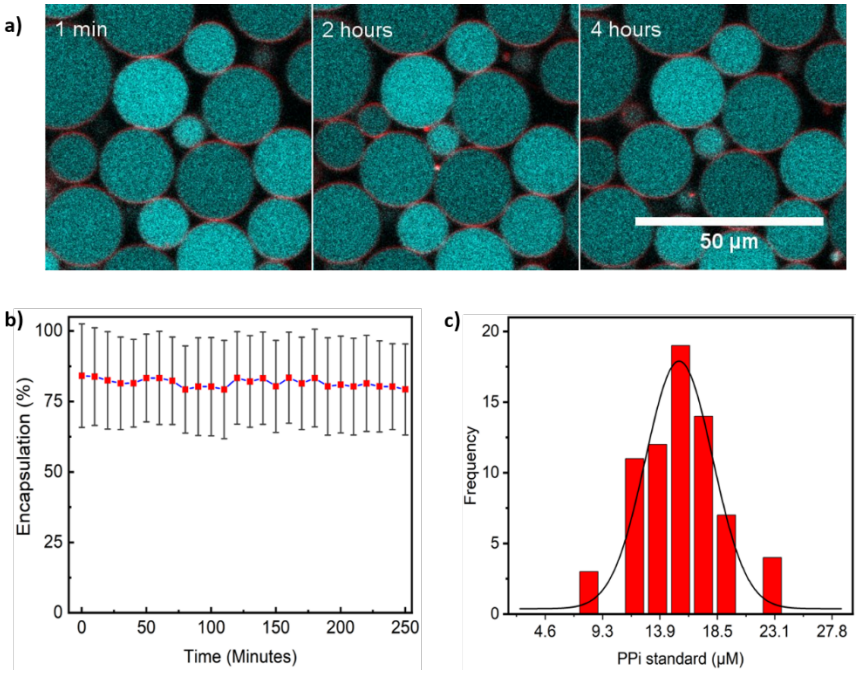

Figure 53. Encapsulation study of PPi, 25 μM.
a) Confocal images of the GUVs, labelled with DiIC18 (red), in the presence of the PPi standard (cyan), 25 μM with 500 mM sugars. The represented snapshots were taken from 4 hours time-lapse measurements. (b) The normalised plot of the PPi standard over time, where the individual point represents the average intensity of 50 GUVs, (n=3). (c) Histogram showing the encapsulation variation among the population after 10 minutes.

The reconstituted values show a very variation distribution with about ~80 % efficiency. Next, the population of 50 GUV was distributed on the histogram based on the fluorescence intensity. The investigation was made inside POPC-based GUVs and measured after 1 hour for the end-point measurements. The histogram distribution confirms the encapsulation efficiency to the PPi concentration inside GUVs. The histogram demonstrates a concentration 14.52± 4.7 µM for PPi after one hour inside the GUVs. This observation provides insight into the stability of the GUVs in the presence of PPi detection assay.

Finally, the reaction step of cPMP formation in the presence of all the essential components (enzymes, GTP, SAM, $MgCl_2$, and DTT) was reconstituted inside the GUVs. Figure 54 b, shows the amount of produced cPMP (plotted on the y-axis, with translated PPi concentrations) to the respective reaction mixture (plotted on the x-axis). The active reaction implies to the reaction mixture of the essential component such as MoaA (200 µM), MoaC (100 µM), GTP/SAM (100 µM), $MgCl_2$ (400 µM), DTT/ Na-dithionate (800 µM), where the other mixtures were plotted in the absence of these individual components, as negative controls. The plot was taken after 1-hour incubation time of the reaction mixture inside the GUVs as the synthetic *in vitro* systems. The fluorescence signals from the inner environment of GUVs were converted to cPMP concentration using the PPi calibration curve. Subsequently, the cPMP production was successfully quantified from the reaction mix, whereas the negative controls showed significantly lower values as expected.

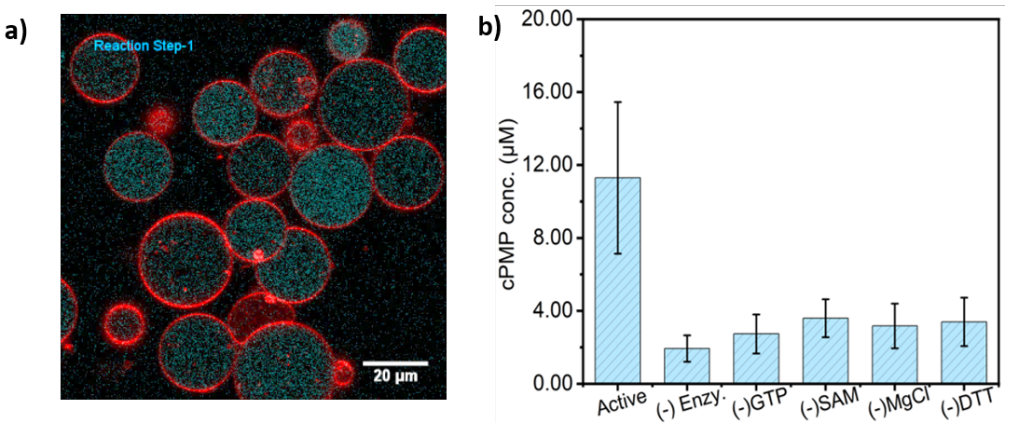

Figure 54. PPi Assay to detect the cPMP formation in GUVs.
(a) Representative confocal image from the step-1 reconstitution. The GUVs were labelled with DiIC18 (red), and the inner GUV environment shows PPi (cyan). (b) The end point measurements after one hour from the active reaction mixture i.e., all the substrate present. The other data-points were as named, without individual components in the reaction such as, enzymes MoaA (200 µM), MoaC (100 µM), GTP (100 µM), SAM (100 µM), $MgCl_2$ (400 µM), and DTT (800 µM). (n=3)

The fluorescence intensity of this PPi release was also studied over time through time-lapse acquisitions in the GUVs starting from relative time zero (t_0). The relative t_0 is referred to the time at which the first image was obtained, which was after ~30 minutes of the reaction mixture incubation. This delay results from the inherent time required for the sample preparation, followed by time spent on transporting from the anaerobic chamber to confocal microscopic set-up.

As the increase in fluorescence intensity was expected in case of the active reaction, the GUVs showed the PPi release, whereas the reaction faintly but linearly increased until 2 hours. As observed in Figure 55, the data shows very little increase in cPMP concentration with over ~3.2 µM variations.

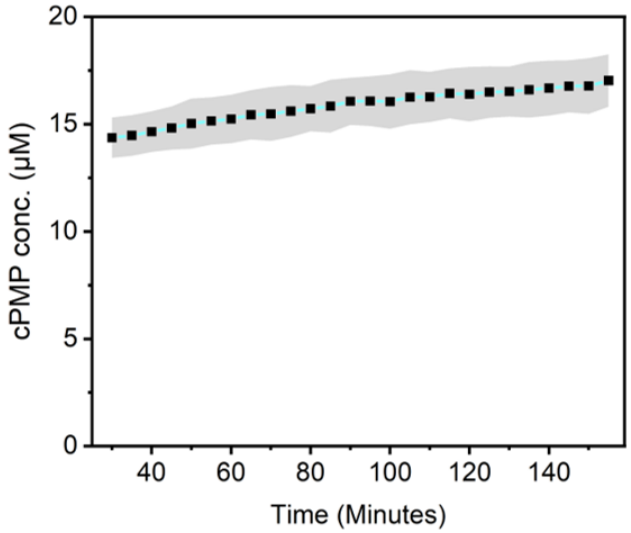

Figure 55. Formation of cPMP from GTP.
Time-lapse measurements of the GTP to cPMP formation (MoaA 200 µM, MoaC 100 µM, GTP/SAM 100 µM, $MgCl_2$ 400 µM, and DTT/Na-diathionate 800 µM), over 150 minutes (2.5 hours). Individual data point represents an average from 20 GUVs. (n=3)

Nevertheless, the PPi release was measured with longer exposure of 2.5 hours was planned as an end-point measurement, and also to assure unspecified lags due to the presence of sugars in both the solutions. The slight increase in the cPMP concentration, perhaps, was an indication of photobleaching of the assay-kit fluorophores. To test any photobleaching of the unknown fluorophores provided in the assay-kit, control tests were performed previously. The control test was supplied only with PPi standard inside the GUVs and likewise measured the GUVs over-time. As shown in Figure 53, no such increase was observed with only PPi standard. Additionally, there were considerable chances that the sample transportation, before imaging, had exposed the reaction mixture to the oxygen that results in instant termination. In this direction, the samples were closely sealed using parafilm for transporting to the microscope. In conclusion, although the reaction was actively reconstituted and detected under the PPi based fluorescence assay. The system lacks an explanation for the limited production rate, either due to unknown interference of the detection assay, oxygen breaching or other unspecific contaminations such as sugars or lipids.

4.2.2 Step 2: Formation of Molybdopterin

This cytosolic reaction step in eukaryotic Moco biosynthesis is the cPMP conversion to MPT. The simple reaction step involves the introduction of two sulphur atoms which are catalysed by MPT synthase. An active MPT synthase was obtained by heterologous expression of *E.coli* BL21 (DE3), as described in section 3.1.11.5. The enzyme complex was purified using ammonium precipitation method with ammonium sulphate. Upon the dialysing of ammonium from the precipitation method, a second purification with gel filtration was applied, and the elution was tracked on the SDS-PAGE gel images as shown in Figure 56. MPT synthase is a heterodimer constituted with two MoaD (8760 kDa) and two MoaE (16.981 kDa) subunits in bacteria, including the central dimer of the complex, is composed of two MoaE subunits carrying one MoaD on each end. MoaE subunits bind cPMP molecules, whereas MoaD subunits introduce the sulfur atoms.

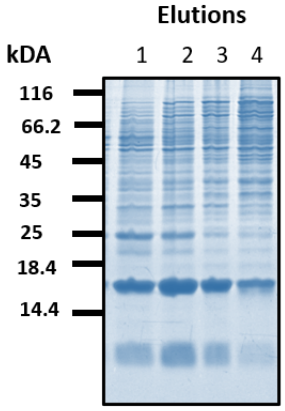

Figure 56. SDS-PAGE analysis using 15 % gel stained with Coomassie-Brilliant-Blue. The SDS gel image with three elution fractions of MPT synthase (16.981+8760 kDa), taken after size exclusion chromatography. The different lanes represent the fractions collected from the elution profile.

4.2.2.1 Form A based assay for MPT Quantification

For MPT formation, the reaction mixture of 100 µM cPMP was incubated with MPT synthase 40 µM, in a Tris-HCl buffer at pH 7.2 for 10 minutes. The conventional assay was performed under the closed anaerobic environment to protect cPMP form any unwanted oxidative degradation. The analysis of the produced MPT was performed using form A, for this reaction mixture was oxidised overnight in the dark as explained in 3.1.14.

The expected retention time of form A peak from the reaction was around 9 sec, Figure 57, the elution confirms that MPT being successfully produced in the reaction. There has been evidence from the literature that the reaction takes about 10 minutes to complete.[97,99] Thus to confirm this time-range, different time points for MPT production were further quantified. To observe the time dependence on the MPT formation would be helpful for the later reconstitution study.

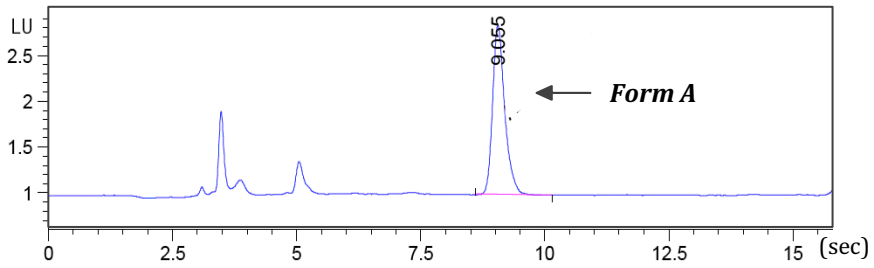

Figure 57. HPLC profile of form A, over a reversed-phase C18 column at HPLC.
The elution profile of form A produced from the reaction mixture with pure cPMP (100 µM) and MPT Synthase (40 µM) was overnight oxidation with acidic iodine and separated on a reversed-phase C18 column using 5 mM ammonium acetate. The elution was observed with an Agilent 1100 series fluorescence detector with excitation 383 nm and emission 450 nm. The retention time of 9.055 sec indicates the presence of form A in the reaction mixture.

As stated above, MPT was detected through into form A over HPLC on the reversed-phase C18 column, results are shown in Figure 58 a. According to this observation, the reaction reaches a plateau within 10 minutes, whereas, the literature studies suggest it take only up to 5 minutes,[98,108] Figure 58 b. It could well be possible that this shift in the product formation was limited to the *in vitro* experiments in this thesis. This observation was repeated several times, which indicated reproducible results with some variation, thereby, this reaction was always performed for 10 minutes in the thesis.

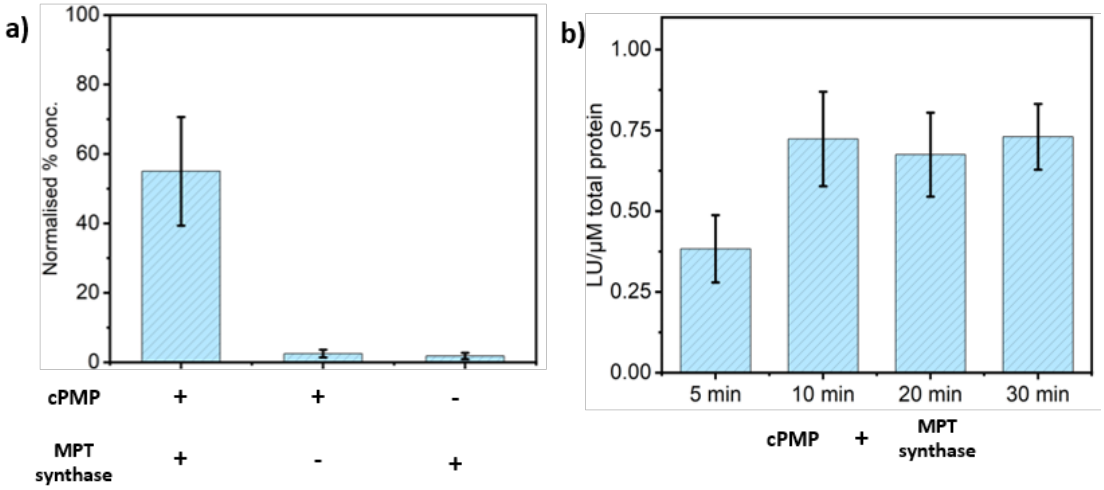

Figure 58. MPT quantification using oxidation with KI/I_2.
(a) Form A analysed upon overnight oxidation of cPMP (100 µM) and MPT synthase (40 µM) with acidic iodine and separated on a reversed-phase C18 column using 5 mM ammonium acetate. The elution was observed at excitation 383 nm and emission 450 nm with an Agilent 1100 series fluorescence detector. Here, the form A production was normalised to pure cPMP run. (b) The LU/µM of total protein content was applied to illustrate the produced form A over a different time range, from 5 min to 30 min, for cPMP (100 µM) and MPT synthase (40 µM), n=3.

However, this *in vitro* produced form A fluoresces under the confocal detection limit, thus an alternative fluorescent molecule was required for further MPT detection. The fluorescence molecule with a possible fluorescence emission within the confocal detection range, suitable for the GUV reconstitution study.

4.2.2.2 Calcein based MPT Detection Assay

As discussed above, the conventional fluorescent product of MPT (form A) was under the limit of detection of the confocal set-up. Hence, a calcein based detection assay was planned,[80,131,137] as the calcein (ex 495nm, em 515nm) is strongly quenched in the presence of divalent cation such as copper, cobalt and nickel.[140] An ion relevant to the Moco biosynthesis is molybdenum, as it binds to MPT and forms Moco (MPT-Molybdate).[94] Nonetheless, this is highly unlikely that molybdate, (being anion) will quench the calcein. Therefore, an obvious alternative was copper cation that has properties to quench the calcein, Figure 59.

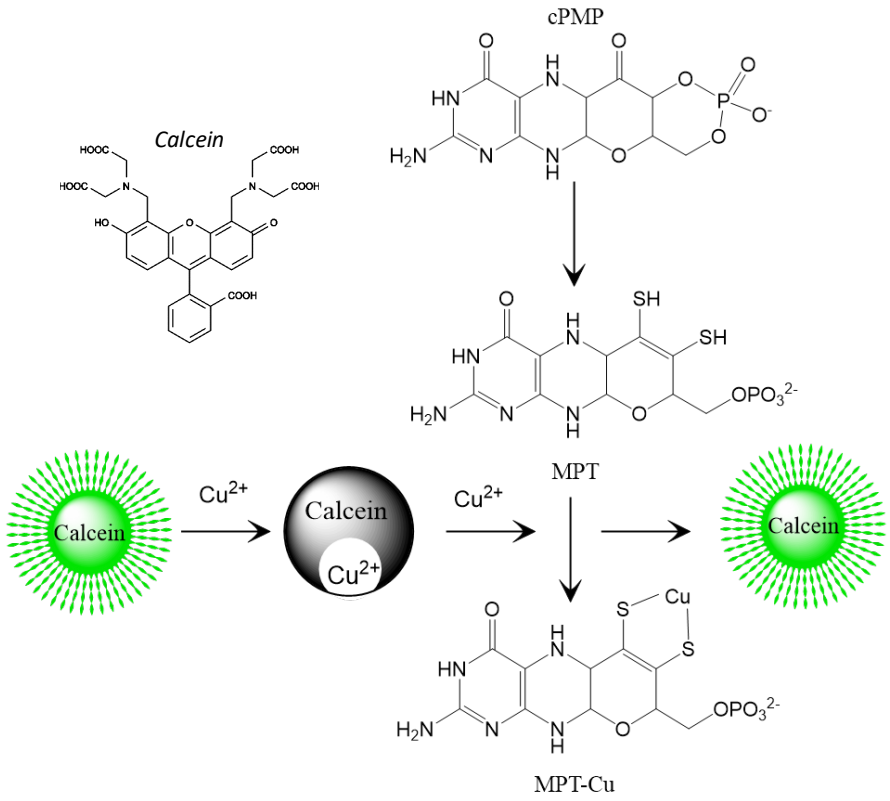

Figure 59. Schematic of the Calcein-quenching assay for MPT detection.
Calcein fluorescence is quenched in the presence of Cu^{2+} while MPT shows a higher affinity towards Cu^{2+} and acts as a chelator in the solution. In this assay, calcein fluorescence recovers in the presence of MPT, which was detected over confocal fluorescence set-up, essential for detection in the GUVs.

This was proven experimentally, as shown in Figure 60 a & b, where molybdenum does not show a linear decrease in calcein fluorescence or any quenching. The solutions were measured under confocal detection for calcein fluorescence (ex 495nm, em 515nm). As seen in Figure 60 a, the molybdate was capable of quenching the calcein with a concentration of 500 mM. The trend overall has poor correlation, with only up to a decrease in the calcein fluorescence by 40%. Since the physiological concentration of molybdenum/molybdate would be expected between 10 and 150 µM. The later experiments were repeated using the molybdate concentrations in the micromolar range. Likewise, a lower calcein concentration was used to test the difference in the quenching graphs (1 µM & 500 nM).

Upon decreasing the calcein concentration (1 µM), an increase in calcein fluorescence with increasing molybdate concentration was seen. The graphs on this range of molybdate concentration show a very poor correlation, Figure 60 b. The quenching was not seen from the millimolar to the micromolar range of molybdate with 1 µM calcein concentration (verified that all the samples were within pH 7 supplemented with 100 mM Tris-HCl solution). Therefore, the alternative approach with known calcein quencher was implemented, with copper. The MPT produced *in vitro* is extremely unstable, as discussed in section 3.1.14, unlike the *in vivo* production, where MPT is tightly bound to synthase enzyme.[93] Additionally, MPT binds to copper which prevent the thiol group from further Mo insertion and blocks the Moco formation. Copper is not physiologically relevant for Moco biosynthesis, as it protects the dithiolene sulfurs from molybdenum insertion and inhibits Moco formation.[114,117] However, this property was beneficial for the fluorescent-based detection of MPT since the copper can quench the calcein, concurrently competing to bind with MPT.

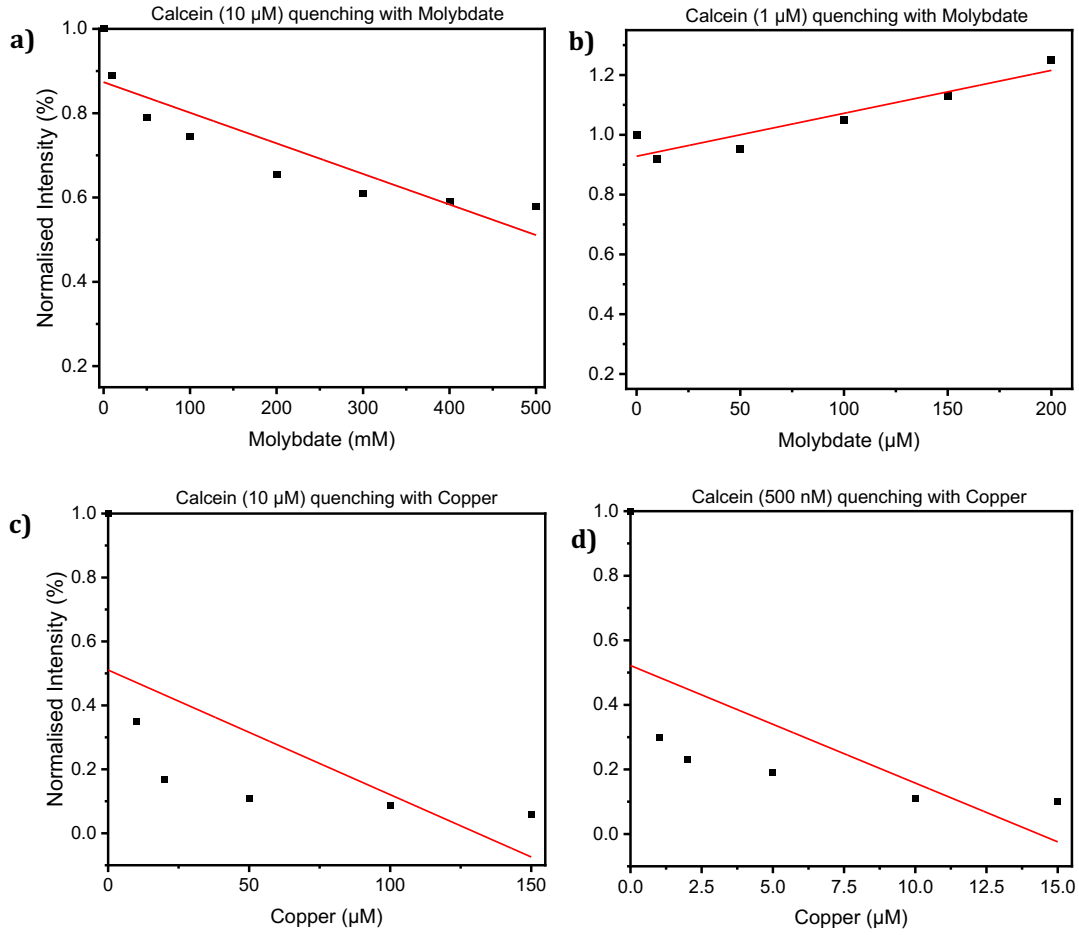

Figure 60. Development of calcein-quenching assay.
Calibration or standard curves, taken on the confocal microscope at ex 495nm, em 515nm with a) 10 µM, and b) 1 µM calcein with varying amounts of molybdate in the millimolar range supplemented to 100 mM Tris-HCl pH 7.2 solution. Molybdate appears to quench 10 µM calcein, but the trend overall has poor correlation and hence an alternative quencher copper was used. Thus, c-d) shows quenching curves for two calcein concentrations (10 µM & 500 nM) with varying amount of copper in the micromolar range, as given.

Nevertheless, it is noteworthy that for this quenching to occur, MPT must have a higher affinity for copper rather than calcein. A calcein-copper complex, with an increasing copper to the calcein molecules, was plotted to understand the quenching phenomenon. The complex mainly based on the concentration ratios of the calcein to that of copper, seen in Figure 60 c & d. Initially, the experiments involved obtaining a standard curve for 10 µM calcein concentration with varying copper concentration (millimolar range, data not shown). As expected, the copper was a suitable candidate for calcein quenching, and further micromolar concentration was plotted. As shown in Figure 60 c, a copper concentration of 10 µM reduces the calcein fluorescence to 40%, whereas 50 µM copper reduces the fluorescence to 10%. Since the practical concentration of MPT in the assay would range in a few micromolar. The data was reproduced with a few micromolar range of calcein with corresponding micromolar ranges of copper. According to Figure 60 c, the copper was able to quench the calcein in <150 µM and within few µM, as seen in Figure 60 d. Moreover, the µM concentration range was suitable for the concentration of the active reaction product. Observing these findings, a final and lower calcein concentration was chosen for the quenching assay was 500 nM - 5 µM that followed the similar quenching trend (data not shown). Further, as a final working calcein concentration, 500 nM was chosen to adapt the calcein quenching assay. The calcein-copper assay was further verified to determine the copper concentration required to quench 500 mM calcein. A standard plot of varying copper concentration with 500 nM calcein as shown in Figure 60 d.

Following the concentration curve of the increasing copper concentration from 0.5 to 15 µM, the copper sufficiently quenched the 500 nM calcein. The calcein fluorescence was reduced about approximately 22 % with 2.5 µM and about 18 % with 5 µM. Therefore, the suitable copper concentration for future investigations could be selected between 2.5 µM to 5 µM. Further, these concentrations were re-plotted (data not shown), where the 4 µM copper and 500 µM calcein was the concluding concentrations for the calcein quenching assay. Now that the quenching assay has been finalised, the ultimate application of this assay was to investigate whether the MPT show a preferred binding with copper.

Moreover, a preferential MPT-copper binding, where the complex should release calcein. Henceforth, the MPT will recover the quenched calcein fluorescence from copper. However, it is noteworthy that this quenching assay would only work only if the MPT itself shows no binding to calcein. The basic principle of the assay follows as the MPT binds to the copper, and the calcein fluorescence releases. This release in calcein fluorescence instantly confirms the presence of MPT in an active reaction. Henceforth, the MPT production can be additionally quantified, by knowing the amount of quenched calcein prior to the MPT production and by determining the fluorescence after MPT production. Consequently, the hypothesis was that the preferential binding of copper to MPT releases calcein and results in the recovery of calcein fluorescence.

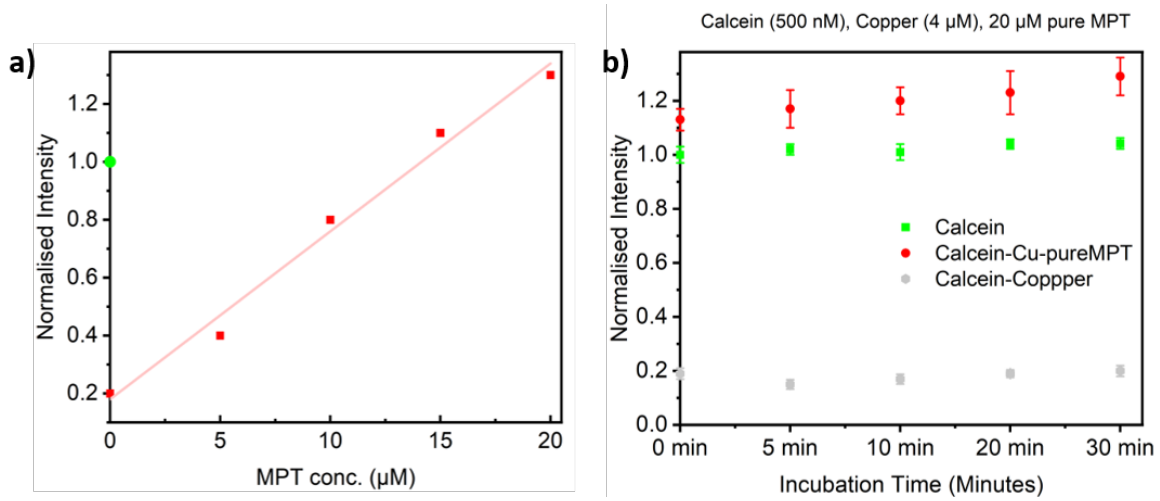

Figure 61. Pure MPT with the calcein assay, and time-lapse.
(a) MPT standard plotted on confocal microscope at ex 495nm and em 515 nm, with varying concentrations (0-20 µM) of the pure MPT in 100 mM Tris-HCl pH 7.2. Here, the pure calcein fluorescence was average and normalised to 1, represented in green. (b) The time-lapse measurement from the different solutions, for calcein, calcein-copper and calcein-copper-MPT from time 0 to 30 minutes. (n=3)

To quantify the MPT detection with the aid of calcein quenching as explained above. Additional standard curves were plotted with an increasing MPT concentration from 5 µM to 20 µM, including the calcein and copper (with above-concluded concentrations, 500 nM calcein and 4 µM copper). Figure 61 a, shows a linear calcein recovery with the increase in the MPT concentration. However, some recovery values increase above that of the calcein fluorescence (represented in green on the graph). Therefore, there was a need for an additional investigation to find out whether MPT hinders with the calcein fluorescence. Figure 61 b, shows a plot of three independent observations over-time, i.e. the calcein, the calcein in solution with copper, and the calcein in solution with copper and pure MPT. At first time-point, the fluorescent-based plot shows that the MPT does have some effect on the calcein. Surprisingly, the fluorescence continues to gradually recover over the 30 minutes of measurement. These graphs were interpreted by normalising the calcein signal as 1, while the other solutions were calculated accordingly. In parallel, the measurements acquired to trace the development in the calcein fluorescence shows no significant increase, Figure 61 b. Whereas, the calcein signal in the presence of MPT increases even more at 30 minutes (compared to 10 min in Figure 61 a).

One explanation can be that the study was performed in bulk and oxygen influenced MPT stability. Another reason being the possibility of the contamination that chelates the calcein. Nevertheless, the over-time increase above the calcein fluorescence, suggests a notable sensitivity of the quenching assay. Thus, the MPT solution must be thoroughly analysed for any additional contamination that interferes with the assay. Since the MPT applied in the assay was purified from in-house produced human sulfite oxidase (SO). There are suspected impurities either from the SO enzyme or from the supplemented buffer. Considering that the components of the elution buffer for the SO enzyme include traces of EDTA. Possibly the EDTA supplemented buffer in our standard SO production protocols were the interfering the assay since EDTA acts as a chelator to calcein.

Therefore, to eliminate this chelating factor, human SO was re-expressed and purified in the buffer without EDTA. The fresh stock of human SO was further utilised to re-plot the MPT standard curve from 1 µM to 40 µM range (within the physiological concentrations). Here, Figure 62 shows the MPT where 1 µM MPT recover 55 % and 40 µM shows up to ~80 % recovery in the calcein intensity. In this new plot, the calcein recovery in the given MPT range does not exceed the calcein fluorescence, comparing with Figure 61 b. Therefore, the graph suggests the feasibility of the quenching assay be subsequently applied for the MPT production in the pathway. Finally, to conclude the quenching assay inside GUVs, the assay was reconstituted in the GUVs for the optimisation studies for the final reaction reconstitution.

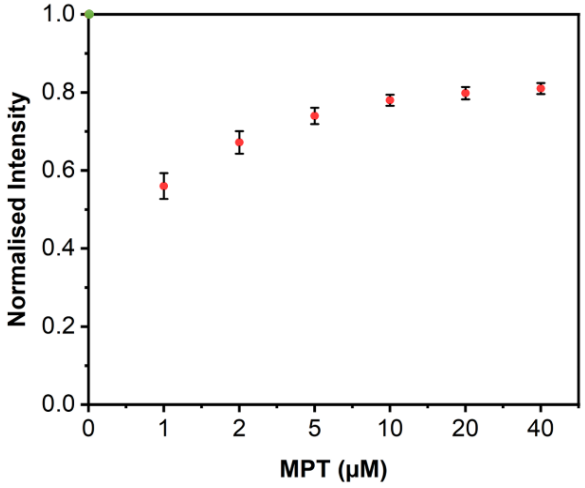

Figure 62. Pure MPT calibration re-plotted from EDTA-free sulfite oxidase.
MPT calibration (without EDTA) was re-plotted in varying MPT concentrations (1 to 40 µM) with calcein 500 nM, copper 4 µM, in 100 mM Tris-HCl pH 7. The pure calcein fluorescence is normalised to 1, represented in green, where the recovery data points are represented in red. The plots were taken on confocal at ex 495nm and em 515 nm, immediately upon the mixing of the solution components. (n=3)

4.2.2.3 To Estimate MPT Production inside GUVs

The MPT inside the GUVs was so far described with normalised calcein intensity. A calibration curve was needed to convert these normalised values to the MPT concentration. The curve co-relating the fluorescence intensity of the calcein-copper complex with varying MPT was plotted. This curve was repeated in GUVs to validate the results from bulk studies and to ensure the normalised fluorescence intensities from the sample. Initially, the calcein-copper calibration was reconstituted in the GUVs. The fluorescence intensities of the encapsulated calcein-copper complex show a discrepancy with bulk studies. Here, Figure 63 shows that the ratio of copper required per calcein molecule has increased inside the GUVs. This could be only possible when the copper molecules are partitioning to the lipids, which has been also reported in previous studies.[141] As seen in Figure 63 b, the encapsulated calibration standard was generated using the copper concentration (1 µM - 15 µM) with fixed calcein 500 nM.

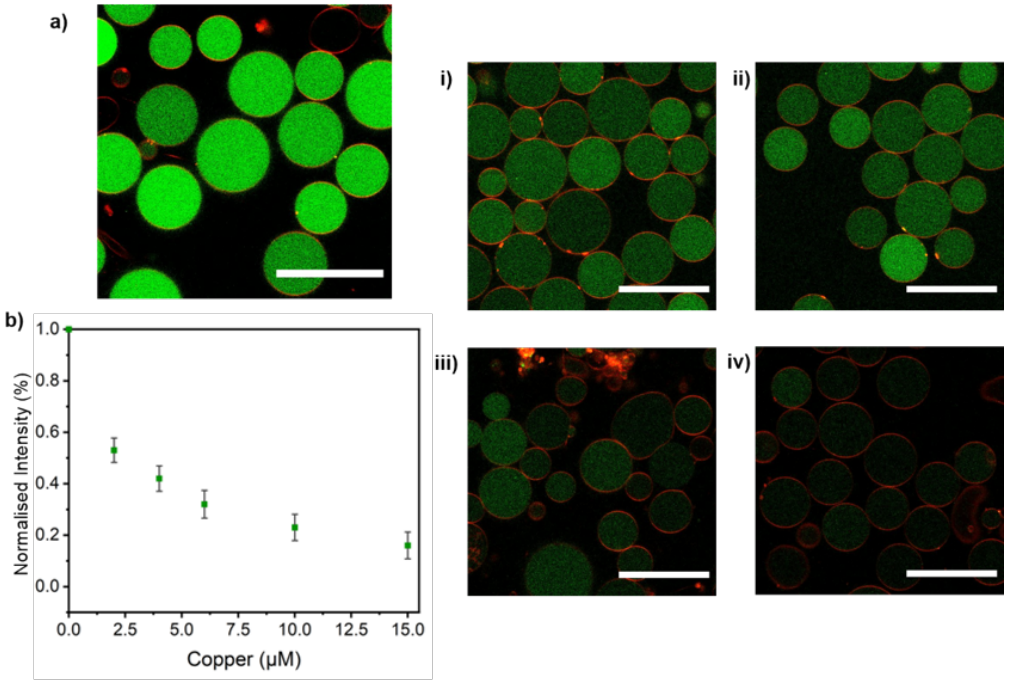

Figure 63. Calcein-quenching re-calibration in GUVs.
Measurement of different copper concentrations with 500 nM calcein encapsulated inside the GUVs to ensure the normalised fluorescence intensities. (a) Representative confocal image of calcein (500 nM) encapsulated, (i) 500 nM calcein in solution with 2 µM copper, (ii) calcein in solution with 4 µM copper, (iii) calcein in solution with 6 µM copper, (iv) calcein in solution with 10 µM copper. Scale bar 50 µm (b) The standard curve re-plotted inside the GUVs for calcein quenching, (n=3).

This shift in the quenching percentage suggests a higher copper concentration for the assay inside GUVs, which is 6 µM. This background information on the quenching concentration was essential for further optimisation inside GUVs. Additionally, a standard curve indicating varying MPT concentration reconstituted in the GUVs will help conclude the MPT concentration from the reaction. Therefore, upon obtaining the calibration standards inside GUV, the active reaction product (MPT) could easily be calculated.

Hence, the MPT calibration curve within the micromolar concentration range, from 5 µM to 25 µM, should be plotted. Keeping in mind that the pure MPT is known as a sensitive molecule, with a half-life of 20 minutes, upon exposure to an oxygen-rich environment. This characteristic feature brings a time constraint as an essential factor when plotting this calibration curve. However, the 20 minutes duration appears as a good fit with the GUV production using the emulsion-based method. However, the encapsulation of the pure MPT calcein-quenching complex leads to a puzzling observation, i.e., calcein recovery in every sample reached about the same value, Figure 64 (i-iii) and plot a.

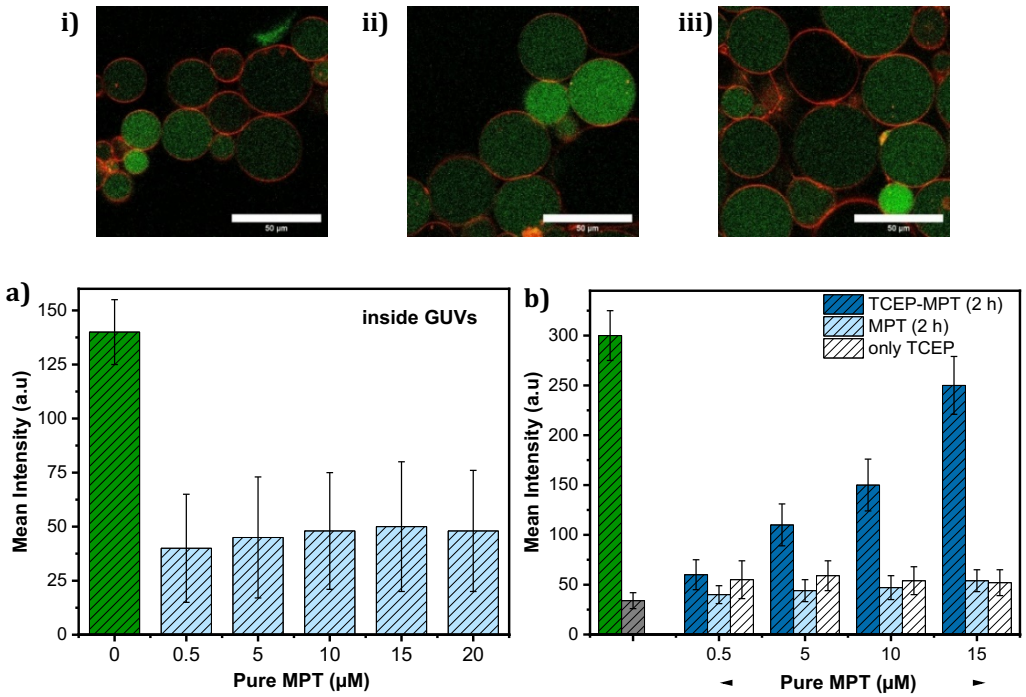

Figure 64. MPT detection using calcein-quenching assay.
(i-iii) Representative confocal images of pure MPT (5 µM, 10 µM and 20 µM resp.) with calcein-quenching assay (500 nM calcein & copper 6 µM), encapsulated in POPC-based GUVs (in red). Scale 50 µm. a) The pure MPT in different concentrations (0.5 µM, 5 µM, 10 µM, and 15 µM), assayed with the calcein-quenching, data from average of 50 GUVs. b) The fluorescence intensity from solution of MPT calibration with and without TCEP (2x MPT each). (n=3)

This unwanted effect could be the result of following speculations: 1) pure MPT bring some contaminations from the source enzyme SO, 2) MPT-copper complex interacts with lipid molecules because calcein does not seem to show any interaction with the membranes. 3) The sugar solution supplemented for the density gradient affects the stability of the pure MPT molecules. And 4) or the pure MPT has degraded before binding with copper, resulting in termination of the complex formation. Hence, the calcein recovery shows an unrelated distribution among all the concentrations, Figure 60 (i-iii). An effort to stabilise the purified MPT using a reducing agent i.e., TCEP was performed, a stabilised MPT here simply refers to prevent the two-thiol groups in a reduced state. Though MPT instability has been a limiting factor for various other *in vitro* investigations, there has never been any attempt on stabilising the molecule. Hence, this stabilising study sought to involve a careful examination of the catalytic role of a stable MPT on a molecular level.

However, before executing the detailed investigation on stable MPT, the effect of TCEP on MPT as a chelator must be tested under fluorescence detection. For the complete reduction of the two-thiol groups present on MPT two TCEP molecules per MPT should be considered. As TCEP as a reducing agent was another additional factor to the assay. Attempts to validate the TCEP interference on the calcein-quenching were necessary, essentially to avoid any artefacts in the final quantification. For this, an additional calibration curve with different MPT concentrations, with and without TCEP was plotted. The solution needs an incubation time from 2 to 14-hour for a complete reduction, according to background study on the reducing properties of TCEP. Hence, the initial experiments were conducted on different time-points i.e. 2 hours, 4 hours, and overnight TCEP incubation with the pure MPT. Figure 64 b, shows four different concentrations of the pure MPT (0.5 µM, 5 µM, 10 µM, and 15 µM) incubated with TCEP (1 µM, 10 µM, 20 µM and 30 µM) for 2 hours. The plot shows a linear increase in the calcein recovery with the increased MPT concentration. Although TCEP blank produces a false positive calcein signal, shown in Figure 64 b, this can easily be substrate from the principal data points and correct the given values.

From this study, it was clear that the 2 hours incubation provides a suitable reducing environment. While the results from 4 hours and an extended overnight incubation do not follow this linear increase (data not shown). Hence, 2 hours of incubation was further utilised in the assay. Subsequently, the TCEP reduction was a possible option for stabilizing the MPT in the assay. Hence, MPT supplemented with TCEP would be reconstituted in the GUVs for future investigations. However, there was no literature available on the MPT stability upon the TCEP treatment. Therefore, to validate whether TCEP affects MPT on the molecular level, a well-defined protocol on the SO activity was planned. The SO is a Moco dependent homodimer enzyme that essentially requires a stable Moco (MPT-Mo) centre for catalytic oxidation of sulfite. The SO was characterized enzymatically with UV-Visible spectrum that shows a typical spectrum for heme-containing enzymes. The activity of the SO can be measured spectroscopically by a reduction spectrum with the reduction of Cyt c at 550 nm. The reaction batch prepared with 50 µL Cyt c (13 mg/ml), 4 µL of 100 mM Na sulfite, 10 µM active SO, for the total volume of 1 ml filled with 50 mM phosphate buffer, 0.1 mM EDTA, pH 8.5. The UV-Vis spectrum for the reduction of Cyt c at 550 nm was taken every 5 minutes to confirm the trend, and the activity was calculated. The trend on the SO activity in the presence of the provided pure MPT that was treated with TCEP. However, the UV-Vis spectrum of the reduced Cyt c did not show any activity when the TCEP was present in the assay (data not shown). Therefore, the TCEP treatment on MPT could not be positively concluded on the molecular level.

4.2.2.4 MPT Production inside the GUVs

For the second step in Moco biosynthesis, the reaction of MPT formation from cPMP in the presence of MPT synthase was performed. The pure cPMP 40 µM was incubated, in 100 mM Tris buffer, pH 7.2 with MPT synthase, 40 µM, supplemented with the above established calcein-quenching assay. The MPT produces in the reaction and binds to copper, which releases the quenched calcein. The released calcein will simultaneously recover the fluorescence intensity, thus indicating the MPT formation.

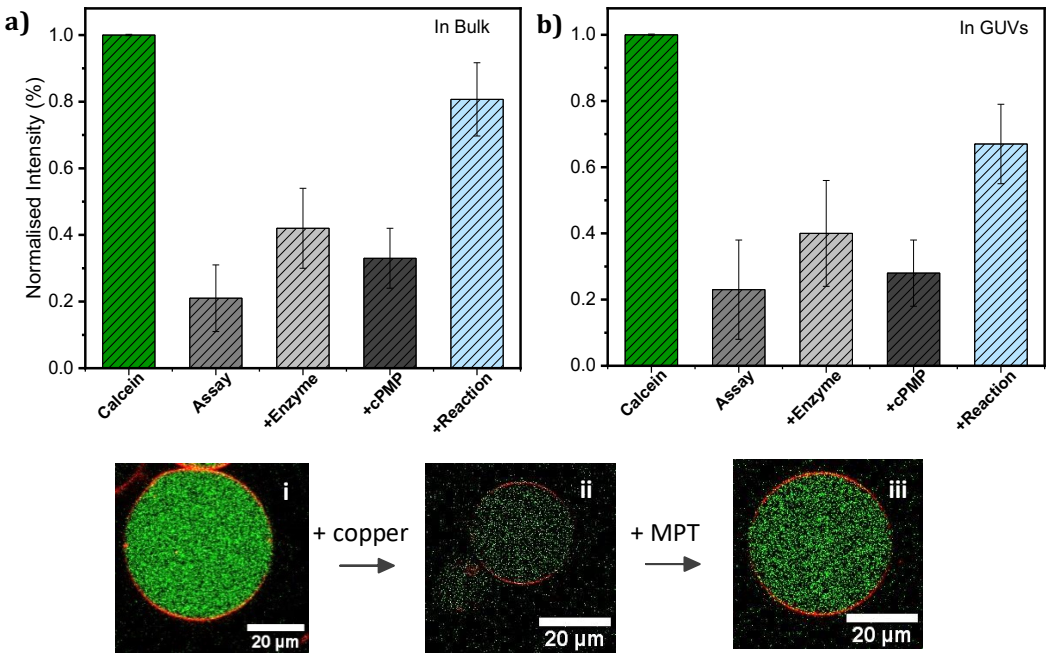

Figure 65. Reaction step 2 detection via calcein quenching assay.
To graphs of the MPT production through MPT synthase (40 µM) from cPMP (40 µM) plotted in (a) bulk and (b) inside 20 GUVs. The graphs represent intensities normalised to 1 for calcein, where each point such as assay (calcein 500 nM, and copper 6 µM), assay with enzymes, assay with cPMP and finally the assay with full reaction components in 100 mM Tris-HCl pH 7.2. Images (i & ii) are represented confocal snapshot of the GUVs with calcein and quenched calcein. (iii) The recovered calcein observed in the GUV taken after 10 minutes. The data was acquired at ex 488nm, em 520nm for the quenching assay, and GUV labelled with DiIC18 at ex 550nm, em 570nm. (n=3)

The above standard curves of the pure MPT will be an advantage in translating the fluorescence intensity of the encapsulates into MPT concentration. Alternatively, the fluorescence intensity could be normalised to calcein intensity to trace the difference. As represented with Figure 65 a, the active reaction of cPMP conversion to MPT was detected in bulk, with the respective controls. Individual sample in the graphs were named as calcein, where the intensity normalised to 1 for the later estimation. The assay was shown for calcein and copper solution, as the established quenching assay itself. Further the quenching assay with enzyme MPT synthase, the quenching assay with cPMP, were named on the graph accordingly. And lastly, the quenching assay with full reaction components with cPMP, MPT synthase was shown as the reaction. Where the fluorescence recovery was averaged 40 % more in the active reaction, compared to that of the controls. Likewise, the reaction was encapsulated in the GUVs and measured for the calcein recovery, as represented with Figure 65 b. To investigate the active reaction, the normalised calcein values were utilised, where the plot shows ~65 % recovery in the calcein signal inside the GUVs.

These were endpoint measurements i.e. taken after 10 minutes of addition of cPMP to MPT synthase, confocal images in Figure 65 i-iii. The measurements were taken immediately on the 96-well plate upon the GUV formation. Where the reaction mixture was reconstituted in the inner environment of the GUVs using the emulsion-based method. Further, time-lapse could be a final approach towards mimicking an active

reaction. However, it is a time-sensitive reaction, and time zero inside the GUVs could be only implemented when the reaction was triggered only after the encapsulation. In this case, one approach can be temperature control, to cool-down the sample until measured.[9,142] The reaction would be triggered upon exposing to room temperature while being immediately measured under the confocal. In this study, the reaction mix preparation and the GUV production were simultaneously kept on 4°C and also incubated on ice while transporting to the confocal imaging. Although it takes 20-25 minutes to produce an optimal number of GUVs using the emulsion-based method, the sample preparation was performed within 15 minutes.

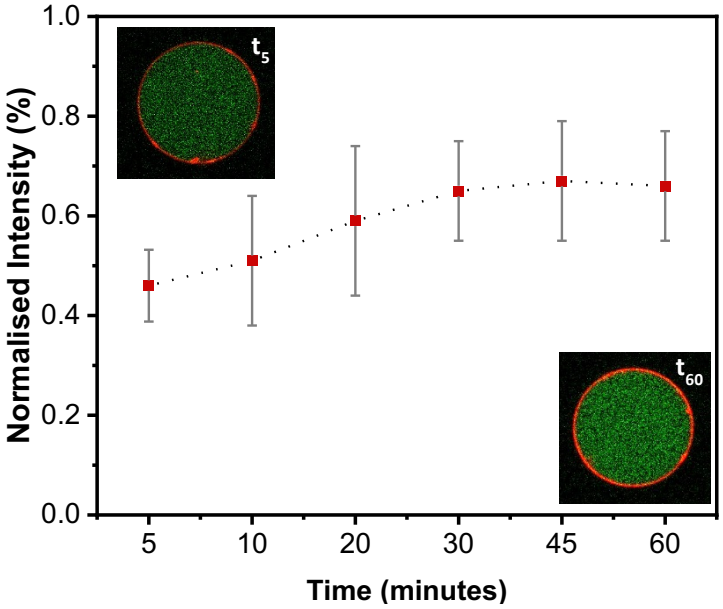

Figure 66. Time-lapse measurements of step 2 with calcein-quenching assay. The graph representing the normalised calcein intensity over 1 hour from the quenching assay with cPMP (40 µM) and MPT synthase (40 µM) in 100 mM Tris-HCl pH7.2. Each point represents the average intensity of 50 GUVs with standard error for the given time. The representative confocal images from t_5 and t_{60} shows the GUVs (red) with calcein (green) from the individual time points. (n=3)

Nevertheless, the measurement could be only started after 20 minutes of reaction mixing (although incubated at 4°C), the calcein had already begun to recover, seen in Figure 66. As described previously, that reaction takes 5-10 minutes to complete, and it is perhaps impossible to detect this reaction from time-zero. However, the time-lapse measurements were indeed taken up to 1 hour at room temperature, with a modest increase in calcein recovery was measured, reaching the plateau at about 30 minutes. The calcein recovery was observed from 5 to 30 minutes, while the sucrose in the enzymatic buffer expected to create some lag. After 30 minutes, there was no visible recovery quantified under the confocal detection. All these normalised values can be further translated to MPT concentration, once provided the standard curve, and this will be discussed in the later discussion.

4.3 Investigation on the cPMP Transport

In eukaryotes, this first stable intermediate (cPMP) transports from the mitochondrial matrix to the cytosol. However, this phenomenon has not been well understood in the literature.[103] Therefore, this chapter investigates the cPMP membrane permeation using the above defined synthetic cells system. For the study, a lipid bilayer with mitochondria-like composition was designed, as a typical mitochondrion has two bilayer membranes, inner and outer membrane (discussed in 1.2.2), both enriched with PC, PE, SM, cardiolipin etc. The cPMP formation occurs in the mitochondrial matrix, the first contact site is the inner leaflet of the inner mitochondrial membrane. Hence, the inner membrane provides the first barrier in traversing the cPMP molecules to the lumen and later the outer membrane to the outside. Therefore, it is reasonable to work with the inner mitochondria-like membrane system. The GUVs, due to their cell-sized similarities and composition tunability, have been well used to study the membrane permeation. Therefore, a GUV model was constructed from the lipid composition of the inner mitochondrial bilayers, and further utilised as a membrane system in this study. Although, the cPMP molecules being a partial negatively charged, should not permeate simply via diffusion across a bilayer without pores (explained in the section 1.3.1.2 with Figure 9). However, we aimed to test this assumption with various experimental setup in this chapter.

Table 6. The lipid composition utilised in the construction of mitochondrial GUV.

Lipids	Charge	%
POPC (phosphatidylcholine)	+/-	**42.7**
POPE (phosphatidylethanolamine)	+/-	**30.5**
POPI (phosphatidylinositol)	-	**5.39**
SM (Sphingomyelin)	+/-	**2**
Cardiolipin	--	**18.4**
POPS (phosphatidylserine)	-	**1**

4.3.1.1 Production of Mitochondria-like GUV

The lipid composition utilised for the construction of the membrane is listed in Table 6. The table indicates overall a highly charged mitochondria-like GUV model (named as mito-GUV, in this thesis). The preliminary experiments towards the preparation of the model mito-GUVs were performed using the emulsion-based method. As explained in section 3.1, the emulsion-based method comprises many factors that lead to the number of variations in the production process. Moreover, the production with this heterogeneous composition was challenging due to different lipid and their chemical properties. Hence, the initial effort required a thorough investigation using the varying buffers composition, pH, and temperature. The heterogeneous lipid mixture was gradually built on an initial simplified GUV, to a complete mitochondrial-like complex composition. There are inherent challenges in GUV preparation with the emulsion-based method, as shown in section 4.1. Thus, the initial focus was to maintain the yield of produced GUVs throughout the optimisation of different pH and centrifugation speed.

In nature, the overall pH inside a mitochondrion is 7.8 but varies between pH 7 to pH 7.2 on the membrane. Whereas the *in vitro* cPMP production takes place at pH 3 in this thesis. Thus, the mito-GUV production was tested within the range of pH 3 to pH 8. The preliminary experiment from the simplified composition shows a varying yield with different pH and centrifugation. Figure 67 shows the representative images with neutral lipids of the mitochondrial membrane prepared on pH 5 and pH 7 with 140 x g centrifugation.

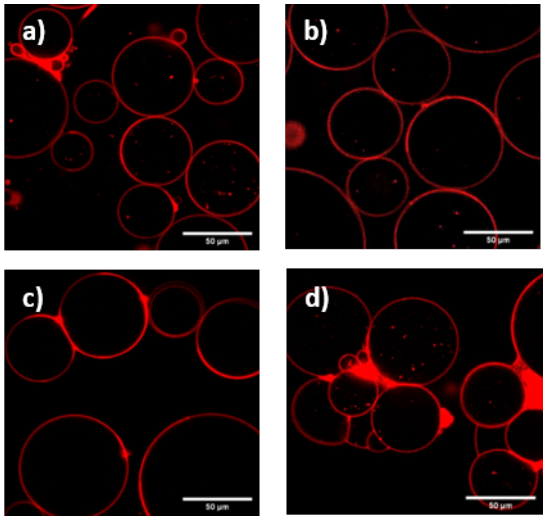

Figure 67. Representative images of mitochondrial GUVs (only neutral and positive lipids).
Confocal images (a) & (b), of the GUVs prepared with 600 mM sugars solution adjusted pH 5 at 140 g centrifugation. The confocal images (c) & (d) were prepared with solutions of 600 mM sugars, pH 7 at 140 g centrifugation. The GUVs were labelled with dye DiIC18, represented in red. Scale bar 50 µm

The other samples with lower pH did not produce an optimal number of GUV population. Upon similar optimisation with different centrifugation speeds, sugar concentrations, and pH, as stated in 4.1 (data not shown). The final working conditions to produce mito-GUVs were 140 g centrifugation, 500-600 mM sugars and solution pH 7. However, the initial results from the complete mito-GUVs illustrate an aggregated GUV population. These artefacts might have occurred due to charged lipid and oil interaction, used in the emulsion-based method. This unwanted interaction creates instability of the GUVs that result in clustering, clumping, and bursting. To circumvent these artefacts, GUVs could be prepared with different lipids in the inner and outer leaflet of a bilayer. Additionally, implying different approach such as the one leaflet to have neutral, and the other charged lipids or vice-versa.

The representative images, shown in Figure 68 a, of the GUVs produced using mineral oil, with inner leftlet was labelled with DiIC18, and outer with NBD-PE, in the emulsion-based method. Although, the representative image shows lipid debris, mainly due to the ionising effect induced by charged lipids. This illustration could be helpful in the gradual development of the mito-GUV formation. The 3-D plot shown in Figure 68 b, confirms the unwanted lipid clustering with a colour map and layering in the GUV population. As demonstrated, the production with the complete mitochondrial lipids was challenging, we further investigated alternative oils for a better lipid solubility, interface monolayer and good w/o droplet formation.

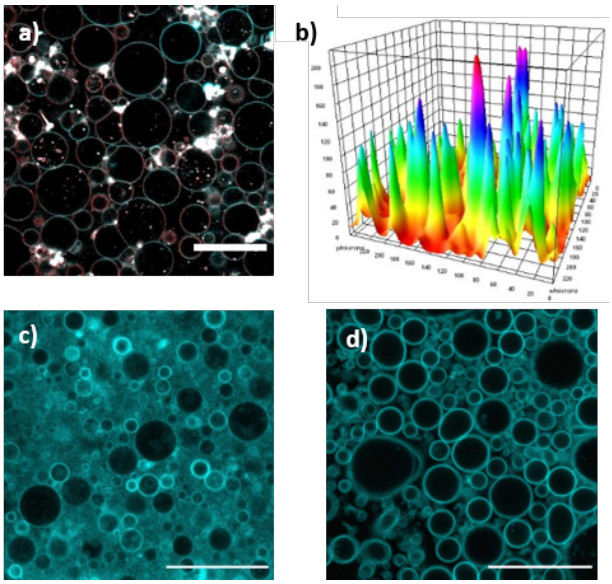

Figure 68. Representative confocal images of complete lipid GUVs.
(a) GUVs produced using mineral oil with DIlC18 labelled (in red) in the inner leaflet, and NBD-PE labelled lipid in the outer leaflet of the mitochondrial membrane. (b) The 3-D plot represents the lipid clustering and layering in GUVs. (c) Representative image of GUVs produced using carbonate-based oil for the lipid-oil mixture (d) representative image of the GUVs prepared with olive oil. In all cases the GUVs were supplemented with 600 mM sugared buffer with adjusted pH 7, at 140 g centrifugation. Scale bar 50 µm

Figure 68 c, d, shows the representative image of GUVs prepared using carbonate-based oil and with olive oil, buffers supplemented with 600 mM sugared buffer and adjusted pH 7, at 140 g centrifugation. However, there were no clumps on the lipid bilayer, moreover, the yield was better, the dye seems to be dissolving in both oils. Therefore, the mineral oil was further utilised with the above-mentioned optimised conditions i.e., pH 5 and 600 mM sugars solutions in the outer environment fo the GUVs. Additionally, the experiments performed in this section were performed using the above mito-GUV concentration from Table 6, otherwise mentioned.

4.3.1.2 Methods to detect cPMP under Confocal

Once the production of the mito-GUV was finalised using an optimal condition for the cPMP reconstitution, a fluorescent-based detection method for the cPMP was further required. However, according to its aerobic degradation properties, cPMP transforms into compound Z, which is a fluorescent molecule. Therefore, compound Z was the immediate choice as its fluorescent analogue for this reconstitution. Considering that the compounds Z can be detected using the confocal microscope under UV range (ex 405nm, em 420nm). The first approach was to overnight oxidise the cPMP solution to achieve a complete aerobic degradation. The oxidised cPMP was now expected to contain a concentrated compound Z, upon the evaporations of the aqueous solution. Thus, the solution was further planned to encapsulate inside the GUVs. Hence, providing the first proof of concept for the cPMP detection inside the mito-GUV. The preliminary results on the GUVs carrying compound Z show a promising results of its reconstitution and compatibility of the two systems.

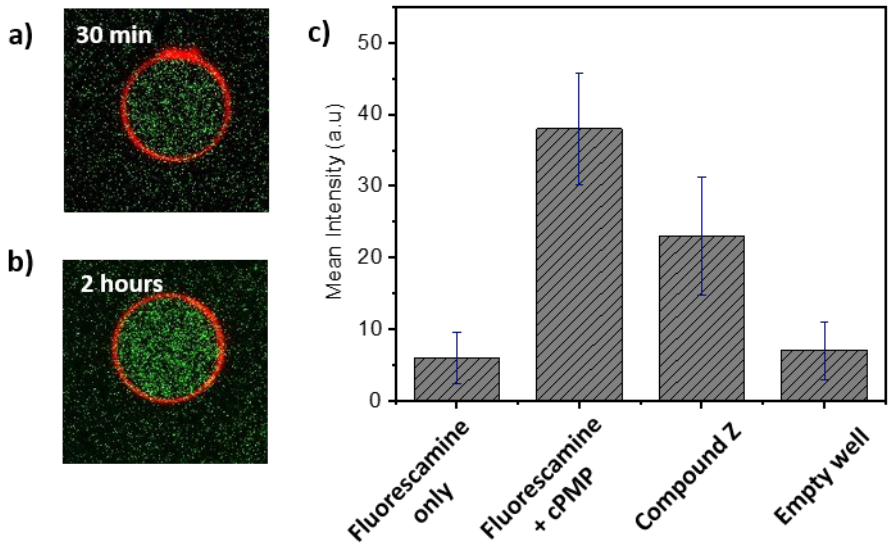

Figure 69. Different fluorescence detection for cPMP.
(a) Representative confocal images of cPMP being inside a DiIC18 labelled GUV (shown in red) at 30 minutes and (b) at 2 hours. The cPMP was detected under UV range at ex 405nm and em 420nm in all the measurements. The graph showing mean fluorescence value from samples containing only fluorescamine (40 µM), cPMP (20 µM) in solution with fluorescamine (40 µM), compound Z (40 µM), and an empty well.

As seen in Figure 69 a & b, GUVs carrying compound Z, shown in snapshots of two different time points (30 minutes, and 2 hours). The time-lapse was taken up to a few hours, but the signals did not increase after 2 hours. Additionally, the cPMP oxidation was performed up to 2 days, by simply exposing to the natural environment. However, this fluorescence intensity of the compound Z was not good enough to the quantify the permeation phenomenon. Therefore, a fluorescent label named fluorescamine was implemented to fully comprehend the fluorescence of the cPMP molecule, Figure 70. The fluorescamine dye does not emit fluorescence of its own, but rapidly reacts with the primary amine present on the molecule and produces high fluorescence (ex 405nm, em 470nm). Figure 69 c, shows a plot of the two cPMP detection techniques, where the fluorescamine, fluorescamine in solution with cPMP, compound Z solution and am empty well, were measured with the confocal microscope.

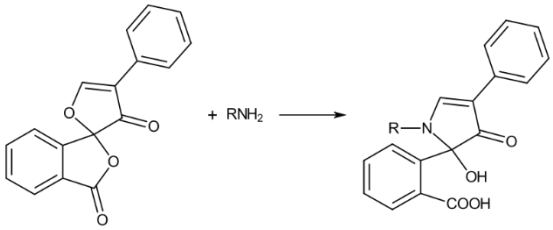

Figure 70. Structure of Fluorescamine with a primary amine.
Fluorescamine is not fluorescent itself until it binds with primary amines. The complex of both forms highly fluorescent products. *Image from Wikipedia-Fluorescamine*

The fluorescence emission spectrum from the fluorescamine was very close to the fluorescence from the empty well. Likewise, the fluorescamine-cPMP solution shows higher-intensity values then compound Z. Considering that the fluorescamine would be a new component to the emulsion-based method, an addition of the calcein dye was also

employed in the cPMP detection systems. As observed in the previous experiments, the cPMP did not show any effect on the calcein fluorescence. Therefore, the addition of the calcein would only provide a negative control in the later permeation study

4.3.1.3 cPMP permeation using Fluorescamine inside mito-GUVs

The fluorescamine dye shows promising fluorescence detection for cPMP molecules, Figure 69 c. Thus, the encapsulation of cPMP with fluorescamine dye was performed using the emulsion-based method. The encapsulated cPMP- fluorescamine inside the GUVs was imaged using 405 nm excitation and 470 emissions with no detectable background signals. These acquisitions on the encapsulation study confirmed the efficiency of the emulsion-based method to encapsulate the solution. However, to study the transport, the fluorescamine molecule (278 Da) and cPMP (345 Da) should be introduced in two separate compartments.

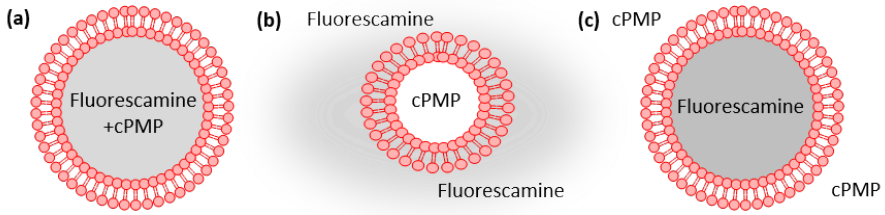

Figure 71. Schematic representation of the experimental set-up.
The fluorescamine-based experiments set-up, (a) is a control set with cPMP and fluorescamine both inside GUVs, where the fluorescence was expected. However, (b) the GUVs with fluorescamine in the outer environment, and cPMP reconstituted inside. And (c) the opposite when the fluorescamine reconstituted inside and cPMP into the outer environment. If cPMP permeates the membrane, there would be an obvious fluorescence generation due to the fluorescamine-cPMP interaction.

Therefore, the experiments were further performed with cPMP inside the GUVs while supplementing the outer solution with fluorescamine and vice-versa (schematic representation in Figure 71 a-c). The concentrations of the cPMP (20 µM) and fluorescamine (40 µM), were kept constant throughout. The osmolarity was maintained at 600 mOsm with glucose and sucrose, as explained in the encapsulation study, section 3.3.1. However, the experiments based on the schematic seen in Figure 71 a-c, with representative images, showing contradicting results. In a condition with the fluorescamine and cPMP together, fluorescence signals were detected, possiviely supporting our hypothesis. Whereas, the later conditions exhibit contrarily results in the hypothesis, Figure 72. In the investigation, where cPMP encapsulated inside GUVs with fluorescamine in the outer solution, the signals were detected from the inner environment of the GUVs, as opposed to what was expected. Likewise, the study of the GUVs encapsulating fluorescamine inside and cPMP being in the outer environment, the signals were detected from the outer environment, shown in Figure 72 (1-3).

This finding does not indicate any cPMP permeation, rather indicate that the fluorescamine dye across the bilayer instead. Perhaps the observation from these experimental findings were merely the artefact of the emulsion-based method that might arise due to droplet opening on the interface during GUV formation.

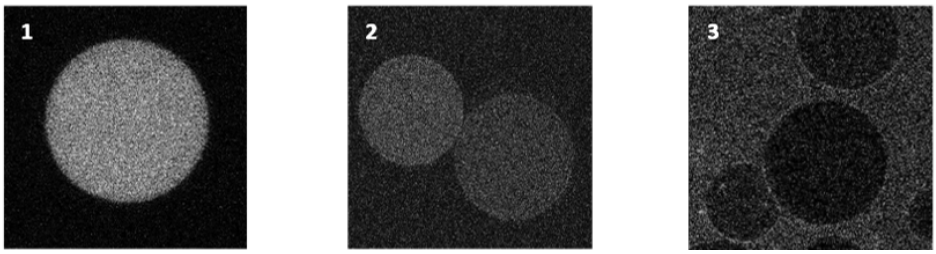

Figure 72. Representative images from the fluorescamine-cPMP measurement. Confocal images, 1) indicating the fluorescamine (40 μM) and cPMP (20 μM) signals from the GUVs, where both were reconstituted inside. 2) Image was the result from cPMP reconstitution inside, and the fluorescamine was outside and 3) The condition of fluorescamine reconstitution inside where the cPMP was in the outer environment.

Therefore, further time-lapse experiments were performed on these GUV populations to observe a development on these unexpected flow across the membrane under two study cases as follows. In the time-lapse study of the first case (Figure 71 b), where the cPMP (20 μM) inside and fluorescamine (40 μM) outside the GUVs. This GUV population was followed under the same experimental set-up as explained above with time-lapse. The GUVs was formed via the emulsion-based method with cPMP inside (20 μM) and fluorescamine (40 μM) outside, where the fluorescence from the cPMP channel that did not change significantly over-time. Additionally, the signal on the membrane does not show any significant change with time (therefore, data not shown). In contrast, the time-lapse study of the second case (Figure 71 c), where the cPMP (20 μM) was outside and the fluorescamine (40 μM) reconstituted inside the GUVs demonstrates signals on the bilayer from cPMP channel, Figure 72 c. The signal on the membrane shows a significant increase with time. However the quantified data was not produced, the representative images are shown in Figure 73. These unexpected observations could be only explained as the artefacts around the emulsion-based method at this point, such as, uncertainties with the opening of emulsion-droplet on the interfaces, and partitioning of the molecules to the oil, or the possibility of oil contamination on the membrane. Therefore, further experimental approaches must be applied that has widespread acceptance for the membrane study, and one such approach could be electroformation.

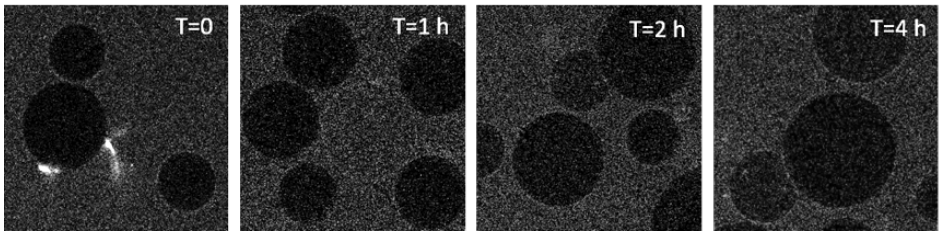

Figure 73. Time-lapse of study case 2, in the cPMP and fluorescamine interaction study. Confocal images of UV channel imaging the cPMP from the outer environment of GUV (not shown), and the fluorescamine inside. These representative images are shown only from the UV channel (for cPMP/fluorescamine).

Therefore, an alternative experimental approach with electroformation was swiftly adapted to verify these preliminary observations. The next experiments were planned with electroformed GUVs using mitochondrial lipid composition. Additionally, the microfluidic chips were utilised to trap these GUVs for the later end-point measurements on single GUVs.

4.3.1.4 cPMP and Fluorescamine within a Microfluidic Chip

The microfluidic techniques are advantageous for trapping the GUVs for a certain amount of time, with the possibility of changing the outer solution while keeping the GUVs trapped. The microfluidic trapping would allow to separate the production process of GUVs from their eventual contact with cPMP. Therefore, we first produced GUVs with electroformation, recorded their morphology under the microscope, and later implemented to the chip. The electroformed mito-GUV were trapped in microfluidic chips to study the time-dependent effect of cPMP on the pre-formed GUV. Besides, the electroformation does not require a high concentration of the sugars in the solution. The mito-GUV produced using electroformation with 350-400 mM sucrose buffered with fluorescamine was produced as discussed in 3.3.1. The GUVs were stored at 4°C until trapped into the microfluidic chip, as discussed in section 3.4.2. A schematic representation of this experimental set-up is described in Figure 74.

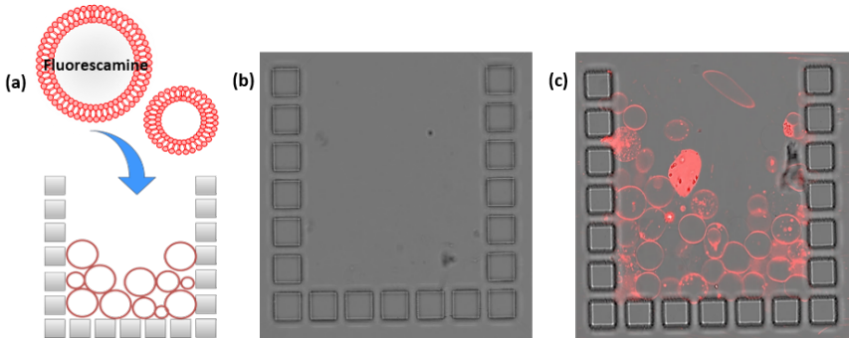

Figure 74. Transport study using microfluidic chip.
(a) Schematics of the experimental set-up, where the GUVs carrying fluorescamine inside are flushed on to the chip. Further, a buffer supplemented cPMP could be flushed onto the chip. This would help us understand the previous observations on the mito-GUV. Whether the cPMP partition again on the lipid membrane. (b) Bright-field image of a casein coated microchannel (bucket) with all visibly featured PDMS posts. (c) Representative image (fluorescence and bright field) of the electroformed GUVs (label DiIC18) were flushed into the buckets with 10 µL/min flow rate gradually with 100 µL GUV suspension each time for 400 µL.

The schematics seen in Figure 74 a represents fluorescamine reconstituted GUVs that were trapped in the microfluidic chip. Prior to the loading of the GUVs on to the chips, the microfluidic chips were always coated. Figure 74 b, shows a microfluidic chip coated with β-casein protein, sedimented via centrifugation, to avoid any unwanted surface adhesion of GUVs on the chips. The chip was further washed with glucose solution of the same osmolarities as GUV, followed by filling the chip with GUV suspension. The chip was filled via an inlet on the reverse flow with 10 µL/min flow rate, Figure 74 c. Similarly, in the main experiment of the GUVs containing fluorescamine, the GUVs upon entering the inlet, first passes through the filter to separate any lipid contamination present in the sample, and finally enters the traps. Further, an iso-osmatic solution was flushed to wash the

excess fluorescamine from the GUV suspension (at least 4 times). Followed by citrate supplemented solution (5 mM Sodium citrate) with adjusted pH as a negative control to cPMP was transferred onto the chips with 5 µL/min flow rate. Finally, 50 µL of the cPMP solution was transferred to the chip under 5 µL/min flow rate. Images from every step were simultaneously acquired, as shown in Figure 75 a; the empty trap and Figure 75 b filled with GUVs. As soon as the cPMP enters the microchannel around the trapped GUVs, the GUVs instantly started bursting, as seen in Figure 75 c. This instant bursting was unexpected as all the supplied buffers were maintained at pH 7. Besides, there were no additional supplements to change the pH during buffer exchange.

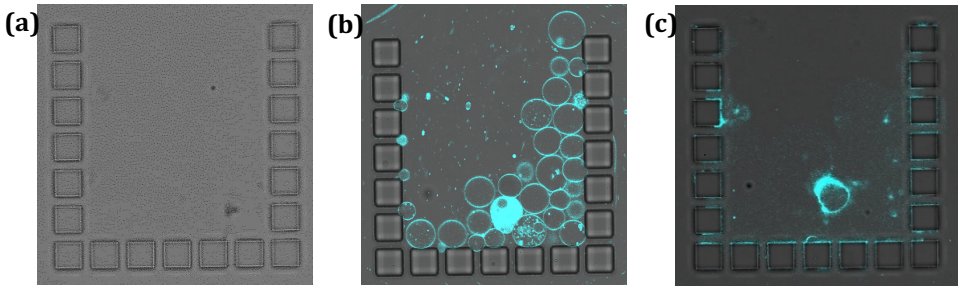

Figure 75. Representative images of the microchannel in the microfluidic chip.
a) Bright-field image of a casein coated microchannel (bucket) with all visibly featured PDMS posts. b) Representative fluorescence and bright-field image of the electroformed GUVs (label NBD-PE) were flushed into the buckets with 10 µL/min flow rate gradually with 100 µL GUV suspension each time and washed with sodium citrate buffer (5 mM). c) The buffer was exchanged with 5 µL/min flow rate, and cPMP was introduced supplemented in an iso-osmotically balanced sucrose buffer, as seen the GUVs ruptured as soon as the cPMP enters.

Furthermore, the density gradient in the solutions and the flow was also maintained at a very low flow rate. Nevertheless, the results were reproducible with three different experimental set-ups on independent experiment days. Following these observations, a set of control experiments was further implemented without the fluorescamine encapsulated mito-GUV under similar experimental manipulation. Repeatedly, the GUVs followed the same results i.e., busting upon the addition of the 20 µM cPMP solutions. Furthermore, another control experiment involving 99.99 % POPC GUV, first washed with citrate buffer and then with cPMP solution on the chip. In this case, the GUVs could withstand the cPMP solution for up to 30 minutes before gradually rupturing. This could indicate the specificity of cPMP partitioning to the mitochondrial membrane but not to the POPC membrane. Nevertheless, in parallel comparable investigations were made with calcein as discussed in the next section.

4.3.1.5 cPMP and Calcein in GUVs

As an alternative to the fluorescamine-based study, a calcein-based fluorescent system was utilised for this permeation study, as calcein has been thoroughly applied in the literature in the membrane-based investigation.[143] The emulsion-based method has previously shown a promising calcein encapsulation. Hence, it would be interesting observation if the presence of the cPMP leads to the bursting of GUVs with calcein in the solution. However, for this study, the calcein fluorescent graph was re-plotted, but this time in the solution with cPMP. These graphs were plotted to test if the presence of cPMP in the solution affects calcein's fluorescence. As represented in Figure 76, a minor increase in the calcein intensity was observed with cPMP, possibly due to a pH shift in the solution.

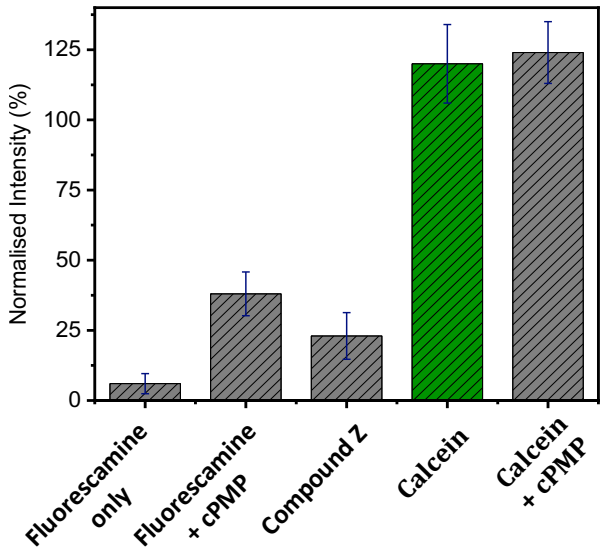

Figure 76. Graph for the fluorescence detection for cPMP in different solutions. The graph showing normalised fluorescence value from different samples. Starting from, first only fluorescamine (40 µM), cPMP (20 µM) in solution with fluorescamine (40 µM), compound Z (40 µM), calcein (500 nM) and calcein (500 mM) in solution with cPMP.

The plot in parallel also represents the normalised fluorescence intensity from fluorescamine with or without cPMP and compound Z. As expected, the fluorescence intensities in the calcein sample are higher, which can be an advantage for the later quantification. The experimental set-up was planned as previously performed with fluorescamine encapsulated using the emulsion-based method. The study included three following samples, 1) the calcein solution supplemented with cPMP together inside the GUVs. 2) Encapsulation of cPMP with the calcein surrounding the outer aqueous solution, and 3) the encapsulation of calcein while cPMP supplemented in the outer aqueous solution. The initial experiment was performed using the encapsulation of 20 µM cPMP supplemented 500 nM calcein solution. The calcein was encapsulated with upto 75 % efficiency which also co-insides the previous findings in 4.1.7.2 section. However, these GUVs resulted with the calcein partitioning to the membrane, which was yet another unknown phenomenon in this study. As demonstrated in a scheme with Figure 77 a and b, illustrating the experimental set-up. The observation in Figure 77, from (i) where the GUVs reconstitute calcein (500 mM), to (ii) where the GUVs reconstitute calcein and cPMP

(20 µM) together. This observation on the calcein being detected in the membrane the calcein-cPMP reconstituted inside the GUVs was again somewhat unique.

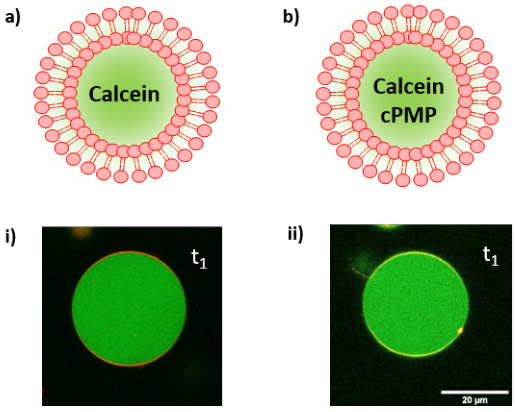

Figure 77. Intensity of cPMP with calcein molecules in GUVs.
Schematic (a-b) representation of experiment set-up for calcein-cPMP encapsulation using emulsion-based method. a) Calcein (500 nM) in sodium citrate buffer (5 mM) and b) calcein with cPMP (20 µM), with the respective confocal images (i, ii) at 5 minutes after production ($t_{1= 5\ min}$).

Further observed with a time-lapse measurement, the images were taken every 5 minutes for 1 hour, Figure 78. On average 50 GUVs chosen from the sample, the calcein fluorescence was detected to increase, including unusual morphological changes with time. Consequently, the GUVs appear to produce aggregation and thread-like nanotubes on the membrane within 2 hours. In contrast, the control study of calcein encapsulation with the citrate supplemented buffer (1 mM concentration) did not illustrate any membrane partitioning of calcein dye.

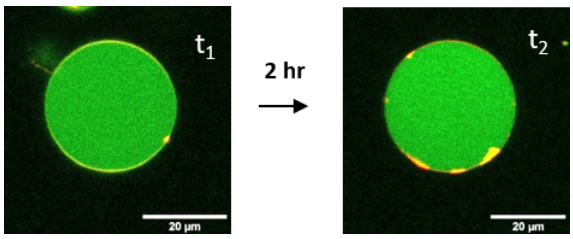

Figure 78. Time-lapse measurement of mito-GUV containing cPMP and calcein.
The representative images from over-time measurements, the images were taken up to 2 hours from first time frame ($t_{1=5\ min}$), where various defects were observed on the membrane as represented at $t_{2=2\ hour}$).

4.3.1.6 Single GUV Measurements to test the cPMP permeation

As discussed previously in the fluorescamine study, microfluidic quantification was an alternative approach for membrane study using electroformed GUVs. The electroformed mito-GUVs were planned to trap in the microfluidics chips to study the effect of cPMP on the pre-formed GUV. This approach aims, likewise, to separate the production process of GUV from their eventual contact with cPMP, and to trace the single GUV overtime. Therefore, the electroformed GUVs were imaged for their morphology under the

microscope, where a glucose supplemented buffer was applied to the outer environment. To test this calcein-based cPMP permeation approach, the mito-GUVs were incubated in glucose solution supplemented with 20 µM cPMP. The samples were imaged after 10 minutes of incubation time, represented in Figure 79. The measurement was started after 10 minutes and the calcein had already leaked in Figure 79 a. To trace the further leakage effect, the single GUV measurements were acquired for 40 minutes. The plot of normalised intensity shows a gradual leakage of the calcein from 10 to 40 minutes. In a parallel experiment, the calcein solution supplemented with only sodium citrate buffer (5 mM) and glucose (without cPMP) was flushed into the GUV population. The sample was likewise incubated for 10 minutes and imaged for a further 40 minutes with no trace of any permeation, Figure 79 b. These findings indicate that the cPMP creates a transient pore in the membrane and that make the membranes leaky. Subsequently, these results confirm the effect of cPMP on the mitochondrial membrane. Further, these experiments on the microfluidic chip could be repeated to provide more collectable data points and end-point measurement, moreover, further investigation must be performed on the pore size.

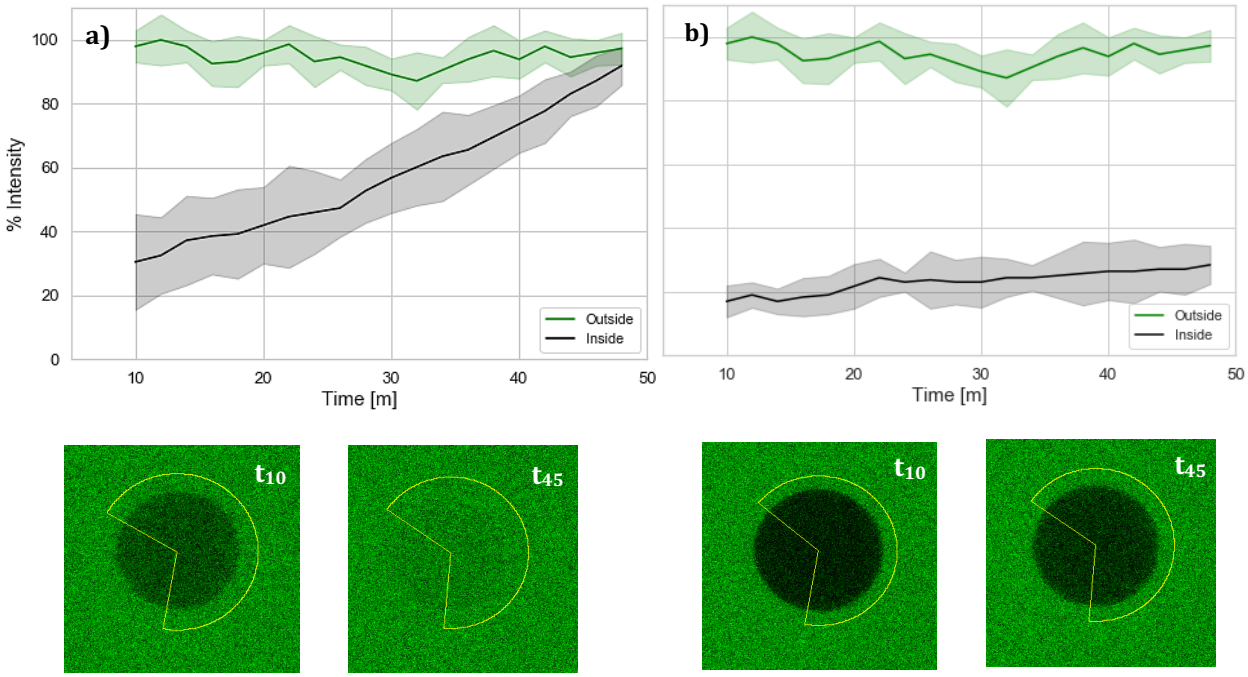

Figure 79. Leaky GUV in presence of cPMP.
a) cPMP (20 µM) supplemented solution results in leaky GUVs at different time (t_{10}=10 min) to (t_{45}=45 min). Likewise, b) control-set where only 5 mM citrate was supplemented in the outer solution, shows no sign of leakage. The data was collected for 10 GUVs each and the measurements were reproduced three times.

5 Discussion

In this section, the results are discussed individually in separate sections. In the first section, the results from the optimisation study of the emulsion-based method are discussed, followed by the encapsulation study. In the second section, the reconstituted pathway of Moco has been intensively discussed. The pathway was divided into two intermediate steps, 1) the generation of cPMP, and 2) the transformation of cPMP to MPT. The two systems are discussed separately in the reconstitution study under the two-fluorescence detection system. Finally, in the third section cPMP, permeation through the model membrane is discussed.

5.1 Production of GUVs using Emulsion Method

The emulsion-based method is relatively a new technique for producing giant vesicles when compared to electroformation or gentle hydration.[76,144] This particular method of producing giant vesicles, leaflet-by-leaflet, has a series of advantages. The major benefit is the possibility to encapsulate large (bio) molecules inside the GUVs under physiological conditions (as presented in the thesis with Moco biosynthesis), complex lipid composition (as observed with the mitochondrial membrane) and even membrane asymmetry.[77,145] The standard emulsion-based method involves multiple steps, as seen in chapter 4.1, which can result in unseen errors and affects the number of GUVs produced. Therefore, the optimisation of the method was performed to explore the GUV size and production rate generated via the emulsion-based method. Moreover, the method was optimised to produce GUVs with minimum preparation times and for high-throughput analyses. The essential parameters to mainly affect the GUV production was determined to (1) density gradients of the aqueous solutions, and (2) the centrifugation speed. It is so because gravity is needed for the movement of emulsion droplets from the oil phase to the aqueous phase through the interfacial phospholipid monolayer. In the absence of a density gradient, the droplets end put staying along with the interface without resulting in GUVs. For this reason, having a density gradient is crucial for the formation of GUVs using the emulsion-based method. Furthermore, a few studies have explored the role of pH on the vesicles in the presence of the alkaline solution and temperature during the formation of the GUVs.[18,72,146] In the present thesis, however, instead of addressing a single parameter, all these parameters including lipid concentration (only POPC lipids), the incubation time for the formation of lipid monolayer at the interface, type of the inner solutions, and different pH values in the GUV production were investigated.

5.1.1 Initial Emulsion Preparation

Beside these given parameters, another important factor in emulsion-based method was found in the preparation technique for the initial emulsion. Therefore, the emulsion production was evaluated using four different methods: 1) pipetting, 2) vortexing, 3) sonication and 4) mechanical agitation as described in 4.1.1. To evaluate these emulsion preparation techniques, the emulsion-droplets were first examined by taking bright-field images. It is found that the sonication technique did not provide a suitable emulsion droplet compared to mechanical agitation, whereas the water-in-oil droplets formed using vortex and pipetting were more polydisperse. To verify the assumption that the sizes of emulsion droplets directly translate into the GUVs size, the size distributions of

GUVs to droplets were compared. As a result, among all the four emulsion preparation techniques, mechanical agitation yields the narrowest size distribution compared to vortexing and pipetting. Moreover, these techniques would cause degradation of the macromolecules (such as proteins, cells etc.,) in the inner solution.

The GUV yield from these techniques could be further improved merely by increasing the time such as in the case of sonication and vortexing, the solution could have been incubated longer. Yet, agitating the biological samples might result in unwanted disruptions and loss of biological function, the reason for which the agitation should remain as gentle as possible. For example, sonication or solutions vortexing can cause protein degradation in the reaction mixture of the Moco biosynthesis. Although, the mechanical agitation does not include these accelerated disruptions, there always some human influence on the emulsion formation that could lead to some unwanted degradation. However, the mechanical agitation provides widespread feasibility on the molecule that can be used for emulsion formation in a short time. Therefore, mechanical agitation was used throughout this thesis due to the easier, gentler, and faster implication in the GUV preparation. Additionally, the possibility of utilising different oils for solubilising the lipids was explored, as previously utilised in different literature,[50,65,147,148] and the results were reproduced three times (n=3) with the given oil in Table 7.

Table 7. Effect of oil type on GUV preparation.
Showing that the choice of oil for solubilising the lipids is a crucial step in the emulsion-based method. In this thesis, mineral oil provided the best results compared to any other oil tested. Results were obtained for a fixed 200 µM lipid concentration, 30 minutes interfacial incubation time, and 3 min centrifugation time at RT.

Osmolarity of sugar solution (mOsm)	**Oil** / **Speed**	**Octanol** (0. 83 g/cm³)	**Oleic acid** (0.87 g/cm³)	**Anisole** (0.99 g/cm³)	**Silicon oil** (0.97 g/cm³)	**Squalene** (0.85 g/cm³)	**Mineral oil** (0.87 g/cm³)
10							
100							
400							
900	**50 × g**						
10							
100							
400							
900	**100 × g**						
10							
100							
400							
900	**200 × g**						
10							
100							
400							
900	**300 × g**						
10							
100							
400							
900	**400 × g**						

No GUVs | Few GUVs | Good number and size

The oils seen in Table 7, with density gradient closer to that of the water, were the preferred choice for this study. The selection of suitable oils was also necessary to the later optimising of the size and yield of GUV produced. A homogenous lipid solution in the carrier-oil, free from aggregation was essential for the formation of the interfacial lipid monolayer. From the findings, it is evident that mineral oil was the most suitable amongst all the tested oils, hence, used throughout this thesis.

5.1.2 Density gradient in GUV preparation

The density gradient of the aqueous solutions is an essential parameter for the water-in-oil droplets to transverse from the oil phase to the aqueous phase and become GUVs. In the past, the density gradients have been extensively utilised in the preparation of GUVs.[43,74] To maintain the iso-osmotic conditions across the membrane, sugars are used not only for their inertness towards the lipid bilayer but also as they provide a different reflective index of the GUV inner and outer environment. The different reflective index is essential for GUV visualisation using phase-contrast microscopy.

However, for GUV production, not just one, but two essential density gradients are to be taken into consideration: 1) between the oil and aqueous solutions (hence, the mineral oil with a density lower than water (ρ= 0.87 g/cm^3) was primarily utilised), and 2) the density gradient between the inner and outer aqueous solutions for two main reasons. The first reason being 1) so that the GUVs settle down on the bottom to instantly visualise the samples and 2) to avoid the sample aggregation on the interface. Hence, sugars that provide a relatively higher density than oil and maintain iso-osmotic conditions across the membrane were required. Sugars, mainly glucose (ρ= 1.56 g/cm^3) in the outer solution and sucrose (ρ= 1.59 g/cm^3) in the inner solution were mainly used in this thesis.

On the other side, different oils for the oil phase and for solubilising the lipids have been explored. As stated, the published work from this optimisation, the results indicated that mineral oil is most suitable for this application and has therefore been utilised throughout this thesis. In principle, the sedimentation phenomenon of the water-in-oil droplets traversing from the oil phase through the interface to the aqueous phase should occur naturally with time. However, this natural sedimentation phenomenon might take up to a few days for GUV formation. Thus, the process of GUV formation was assisted with a combination of centrifugal forces with different centrifugation time durations to speed-up the process. The optimisation with varying centrifugation speeds to time and different iso-osmolar sugar concentration was illustrated to find out the optimal sugar concentration for producing a good yield (clumping of lipids or clustering of GUVs). This study could be interesting, to find out whether a higher centrifugation than needed can lead to the bursting of the GUVs, in the cases where any applied centrifugation speed to the sample would be fatal.

Perhaps an alternative approach in optimising the process without centrifugation or natural sedimentation would be a future goal. A healthy natural cell contains about 5.5-100 mM sugars,[149] whereas the emulsion-based methods have been previously used with high sugar concentrations as 900-1500 mM, which do not represent the realistic osmotic conditions within a living cell. In this thesis, 400-600 mM sugar concentrations were utilised, as a good compromise between natural concentration and this liposomal

protocell. In needed, the preparation condition with 50-100 mM sugar is still approachable with the calculation on the force (in form of the centrifugation speed).

5.1.3 Centrifugation in GUV production Inner solution volume

Initially, this method was first adapted from the combination of published methods, where different solution densities and centrifugation forces (varying from 300 to 1100 x *g*) were applied.[74,76,133,150] Whereas a lower centrifugal speed was preferred in this thesis due to the planned enzyme encapsulation. As observed from the results with sugar concentrations, the emulsion-method was highly dependent on the density of the solutions. While higher centrifugal speeds for a short period might be enough to force all the droplets to pass through the lipid interface, the data suggest that it will also result in bursting and aggregation of the GUVs along the walls of the microtiter plate. Therefore, achieving a good yield at lower speeds but with a longer time duration was optimised. When applied forces in the order of 400 x *g*, 600 x *g*, 1200 x *g,* (Figure 38), the GUV yield remained stable, suggesting that most of the droplets had passed through the interface (for this specific volume of emulsion droplets and solution density gradient).

However, the plateau seen in the yield could also be a result of (i) bursting of large vesicles at the glass well bottom due to higher forces and (ii) the interfacial monolayer not having enough time to re-seal before the next droplet arrives. Even though the yield and size of the GUVs were better at 600 x *g* and for all durations, but less clustering occurred at 200 x *g* for 3 minutes. Perhaps the GUVs upon forming quickly at higher speed and start to push the formed population thus clustering, hence, the 200 x *g* was applied for further experiments. The emulsion volume should directly translate into the number of droplets in the emulsion. As it was unknown whether the number of emulsion droplet played a role or not, it was investigated if the increasing volumes of inner solution to the increased GUV yield. For this, the inner solution volumes relative to the amount of oil were varied. As the results show in Figure 39, the yield increased with volumes between 5 µL and 10 µL, while the size of the vesicles, peaked at 25 µL inner solution volume. Although it is reasonable to assume that the yield decreases with smaller volumes of the inner solution, it was unexpected that it decreases again at higher volumes. This phenomenon can be attributed to the fact that a higher volume of inner solution produces more droplets with increasing proximities to each other. That could result in a higher probability of spontaneous droplet fusion leading to larger but a lower overall number. Indeed, this was true in the case of 10 µL and 25 µL conditions whose average diameter is 1.5-fold more than the other conditions. Therefore, the subsequent experiments were performed with 7 µL of the inner solution with a 250 µL lipid-oil mixture.

5.1.4 Incubation time and Lipid concentration

For the next parameter in the optimisation study, a time-limiting factor was explored i.e., the incubation time to form a complete lipid monolayer interface. An incomplete monolayer at the interface will result in reduced yields of the GUV produced. For example, the droplets' aqueous interior can directly face the aqueous outer solution instead of the lipid monolayer at the interface resulting in the unwanted release of internal contents and reduction in the overall yield. Therefore, it was crucial to have a sufficiently assembled interfacial lipid monolayer prior to the addition of the emulsion. However, another factor to this parameter is the concentration of solubilised lipids in the oil phase.

The concentration of solubilised lipids required to form this monolayer is inversely proportional to the incubation time, to a certain extent.

For example, the lipid-oil mixture needs to have sufficient concentration of lipids, and high lipid concentrations might take lesser time than the low lipid concentration to assemble. Therefore, various lipid concentrations were tested, resulting in a GUV yield increase with increasing lipid concentration independently of the tested incubation period. As expected, the interface formation with low lipid concentrations (<200 μM) required longer incubation time and hence the time required for the overall GUV production, Figure 40. Therefore, for a time-efficient GUV production, the interfacial lipid monolayer incubation time at 30 minutes and the lipid concentrations at 200 μM was fixed. This time efficacy would be crucial for time-dependent experiments and assays in the later applications.

5.1.5 The pH of the supplemented buffers and Temperature

Another important parameter in GUV production when encapsulating a biochemical reaction is pH. Since it is crucial for the functionality of various biological reactions including Moco biosynthesis as proteins' structure and function is pH dependent. As model membranes for biological cells membranes, giant vesicles, were shown to be robust at various physiologically relevant pH and temperature ranges.[44] This is especially critical for the Moco biosynthesis reconstitution, as the two major steps of the pathway require pH 9 and pH 7.2 *in vivo* respectively, moreover, the cells maintain wide range of pH. Thus, the GUVs need to show robustness to this pH change in the surrounding. Therefore, GUVs were prepared at various pH (inside and outside) to test the yield and size of the GUVs. As a result, a moderate but gradual increase in the yield was observed from pH 4 to 9 while there was a significant decrease for pH 10 and 12. Larger GUVs ~80 μm diameter, clustering and aggregation were seen at high pH value, which might have led the significant decrease in yield. This was most likely due to the ionising effect induced by hydroxide ions and possible degradation of the lipids at such high pH environments.[151]

This gain in yield with pH increase can be attributed to the changing charged state of the lipid head groups to a more neutral zwitterionic state. It is known that charged lipids in monolayers repel each other, which may affect the formation of GUVs. pH and temperature are two factors that are essential and hence we tested the effect of temperature alongside the pH. The temperature is as well an essential factor for the biological reaction. However, the working temperature in this thesis was set to 25°C, to account for the catalytic activity of the enzymatic complex. Although the tested temperatures, seen in Figure 41, did not show any drastic effect on the yield, higher temperature resulted in aggregations and large size variations among GUV population. Consequently, the results obtained, it was possible to say that the emulsion-based method can be successfully used to produce biomimetic GUVs at different pH and temperature conditions.

Overall, the results demonstrate that density gradients using sugars are vitally important in manipulating the overall yield of the GUVs. In this thesis, a thorough enzymatic manipulation was performed and thus required to maintain a lower sugar in the buffer. Finally, we implement the emulsion-based method in microtiter plates, where all the investigations were performed on 96-well microtiter plates for parallel preparations which is an advantage for the quantification, Figure 80. This work found that the

following conditions can be used for optimal GUV yields: 20 µL of mineral oil with 200 µm lipids to form the interface over 600 mM outer glucose solution for 30 minutes. This is followed by 7 µL inner sucrose solution at 600 mM mixed with 250 µL lipid mineral oil to form the emulsion. Then 50 µL emulsion is added on top of the interface and subjected to centrifugation at 200 *g* for 3 minutes. The total time taken for the optimal production of GUVs is 35 minutes; whereas the minimum time needed to produce GUVs was estimated 18 minutes.

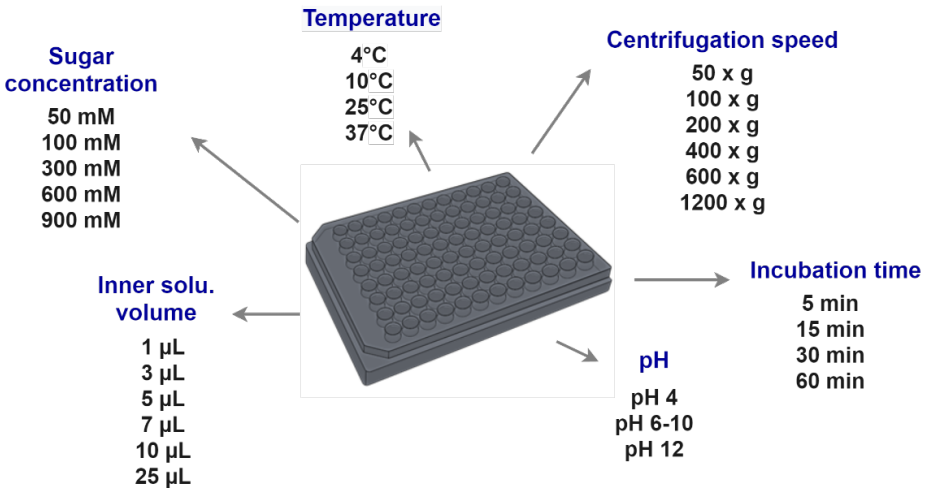

Figure 80. Overview of the optimised parameters on the 96-well plate.
The tested parameters in this thesis, namely centrifugation speed/time, incubation time, emulsion volume, sugars, temperature, and pH.

5.1.6 Encapsulation Study

The emulsion-based method was thoroughly optimised in this thesis for GUV yield and size, as discussed in the above section. This method is advantageous for the efficient and rapid encapsulation of variously charged macromolecules in varying salt buffers, starting from a low sample volume (µL-ml), and thus requiring a low amount of reagents. The main goal of the encapsulation study was a high encapsulation for the proteins that were essential for the *in vitro* Moco biosynthesis. Yet, conventional GUV preparation techniques do not easily accommodate the encapsulation of large biomolecules inside giant vesicles, especially in low volumes.[53,72] Besides, the encapsulation benefits the other biophysical studies, of the substrate or the encapsulate interacting with the inner leaflet of the plasma membranes.[152,153] Moreover, maintaining biomolecules such as structural proteins (e.g. actin filaments network, etc.), or active enzymes inside of lipid vesicles is a necessity for the bottom-up development of the artificial cells.[13,65,154] On these lines, the emulsion-based method has shown great promise in encapsulating macromolecules such as polymers, DNA, enzymes, cells and even micron-sized particles.[22,58,62,148,155,156]

However, the macromolecules are not always maintained under one defined physiological condition, but rather requires a different range of pH, buffered with varied salts and temperature.[44,134] As suggested from the results presented in this thesis, different pH and temperature did not significantly affect the production rate using this emulsion-based method. This presents an advantage towards the future reconstitution of the Moco biosynthesis, because the two steps of the Moco biosynthesis require a different buffering agent for achieving optimal reaction rate. For example, step 1 requires Tris 100

mM, 300 NaCl pH 9 buffers, whereas the step 2, 100 mM Tris pH 7.2. Therefore, the first parameter in the encapsulation optimisation was to adapt the emulsion-based method for the different buffering agents. In this case, first, only 100 mM sucrose was applied to the solutions, and the buffering salts were the main component to match the physiological cell. It should be noted that this condition only resulted in a sub-optimal number of GUVs, where 600 mM sucrose would be preferred as seen above. The lower sucrose might be necessary to maintain the biosynthetic activity, as learned from the GUV preparation using different buffers, varying salts negatively affects the GUV production.[72]

The development of a functional synthetic cell also requires the possibility of encapsulating various aqueous solutions, cargoes, and subsequently advancing into mimicking the cellular processes. In this method, the water-in-oil droplets carry the inner environment of final GUVs, where only a small volume of inner solution was required. Nevertheless, towards the applications in mimicking cellular processes, the method had to be optimised to account for permeation through the membrane and maximise the method's encapsulation efficiency. Therefore, this optimisation of the encapsulation efficiency was investigated in the thesis, using biomolecules such as fluorescent dyes, proteins, and the essential compounds of the Moco pathway.

As the lipid bilayer is permeable to water molecules, but the water flux going in and out will be equal, with net balance zero. Due to lipid membranes' impermeability to it, a hydrophilic fluorescent dye dissolved in aqueous solution was the first choice to test the encapsulation efficiency using the emulsion-based method. Hence, one preferred candidate was calcein, a fluorescein derivative whose fluorescence is virtually independent of pH within the pH range 6.5-12 and has been traditionally used as a fluorescent dye in the GUV production. Therefore, calcein was used to validate the encapsulation efficiency and the stability of the produced GUVs, as leaky GUVs will lose their fluorescence. Additionally, the calcein was later utilised in the reconstitution of the fluorescent-based detection of MPT using the calcein quenching assay. Therefore, a thorough investigation of calcein encapsulation directly contributed to the central aim of this thesis. The encapsulation was performed using increasing calcein concentrations (5 μM, 10 μM and 25 μM) which showed a linear increase in relative fluorescence intensity in the lumen of the GUVs. The observation confirmed that 1) the successful encapsulation of the small cargoes using the emulsion-based method, and that 2) the increase in the reconstituted calcein concentrations indicates the efficiency of the method to encapsulate the small biomolecule. This increasing calcein concentration inside the GUVs was further plotted as a calibration standard to understand the confocal detection limit of the assay, which allowed to quantify the fluorescence intensity in each concentration. As previously seen, the calcein is known to be non-intrusive to the enzymes, bilayer[141,157,158] (also confirmed in this thesis), and proven to be compatible with the emulsion-based method. Thus, complementing the feasibility of its application towards the central aim of this thesis. Nevertheless, the detection limit of the microscope could limit this fluorescent assay if highly fluorescence intensity becomes excessive for the detection range; for this reason, the measurements were performed within the linear range of microscope.

Further, an approximation of the encapsulation efficiency was quantified using the calibration curve. The measurements on the encapsulation efficiency of the method, demonstrated a successful efficiency of ~70%, where the histogram showed variations among GUV population for the same concentration, indicating that the encapsulate might

be lost in the production process. Furthermore, to validate whether this loss of calcein emerged during the production process or arose due to leakage in the encapsulated GUVs. A time-lapse measurement was implemented in the thesis to verify their stability, time resolved images were taken, Figure 81. The time-lapse acquisitions would reveal any unwanted pores that might be formed in the preparation process which would cause GUVs to leak the encapsulates outside. These experiments were performed over 2-4 hours where an image was collected every 10-30 minutes. This time interval was chosen to avoid any photobleaching to the system, which was additionally examined with the applied confocal system. In general, the fluorescence inside the GUVs remained consistent over the whole time confirming the stability (i.e., no leakage), thus confirming the prepared GUVs as a stable platform to study Moco biosynthesis.

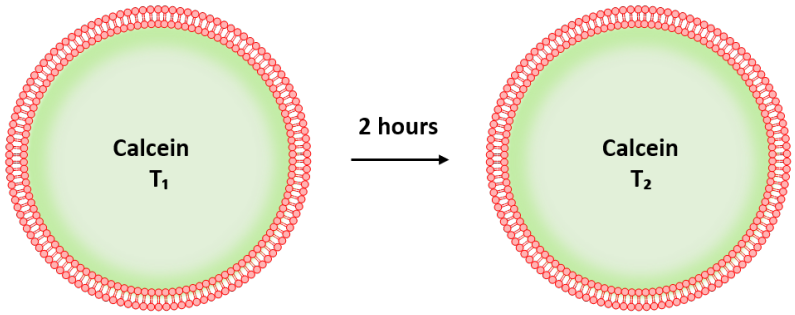

Figure 81. Summarising the time-lapse observation using emulsion-based method. Diagram based on the time-lapse observation of the calcein reconstitution for 2 hours.

However, to successfully establish the Moco biosynthesis inside the GUV-based model, further investigation to confirm the compatibility of the Moco biosynthesis, and emulsion-based GUVs must be made. In this direction, the preliminary experiments were designed to examine the two systems i.e., components from the biosynthetic pathway inside the GUVs. Hence, a likewise encapsulation study using Form A, eGFP-MOCS2A, and PPi standard was performed. Yet, different molecules in the pathway maintained on a specific buffering condition for their optimal activity. For example, form A was DMSO-dissolved, whether eGFP-MOCS2A dissolved in 100 mM Tris buffer, and PPi assay controls in commercially provided unspecific buffer. Therefore, these individual buffers and molecules were reconstituted inside the GUVs for further studies. The encapsulation study shows that enclosed liposomal environment using this method was impermeable to most of the biomolecules, yet some remain questionable. As well-known fact that the mechanical properties of lipid bilayer membrane alter in response to DMSO, which can affect the membrane permeability, hence the stability.[159] Many other high salts containing buffers still holds limitations in the wide-spread acceptance of the liposome towards the synthetic cell systems.[12,45,72] Nevertheless, the positive reconstitution on a wide range of physiological buffering conditions (such as Tris, PBS, HEPES) indicates the ability of the emulsion-based method towards creating a bottom-up model that can be potentially used as a bioreactor. Thus, the method was implemented for studying the Moco biosynthesis pathway inside the GUVs in this thesis.

5.2 Reconstitution of *In vitro* Molybdenum cofactor Biosynthesis

There have been many existing bottom-up reconstitutions of the biological pathways in recent years. In a paper by Elani *et al*., that describes a three-step glucose oxidation cascade reaction in a multicompartment liposome. Their model includes a three-step reaction, 1) formation of glucose from lactose using the enzyme lactase, and 2) the glucose oxidation by glucose oxidase, which results in the formation of hydrogen peroxide. These two steps take place in the same compartment, where the hydrogen peroxide permeates through the bilayer to an adjacent compartment. Thus causing 3) oxidisation of Amplex Red in the presence of horseradish peroxidase (HRP) which results in the formation of resorufin. In this study, only the resorufin, being a fluorescent molecule, was detected using fluorescence microscopy at the end whereas the compartment with the lactose and glucose did not show any fluorescence.[34] The multicompartment vesicle system spatially segregates the three-stepped enzymatic cascade. The system communicates via transmembrane protein pore of alpha-hemolysin (α-HL) that enables the transport of the product from each step. Further, this model was transformed into a fully communicative model system with a three-step chemical reaction pathway separated into three compartments.

In another study, protein expression incorporated within a two-compartment vesicle was engineered where the reaction mixture of *in vitro* transcription-translation (IVTT) could be reconstituted separately in two compartments. Each compartment demonstrated the biochemical synthesis, one with green fluorescent protein (GFP) expression, and another with a red fluorescent protein (RFP) expression. The expression was monitored for 50 minutes, where successful IVTT for two independent proteins was detected under a fluorescence system.[160] These studies emphasise that emulsion-based methods can be certainly applied to produce the liposomes as bioreactors to mimic cellular pathways or mechanisms.[34,39,42] Hence, supporting the idea of encapsulating Moco biosynthetic pathway in GUVs, and even in a multicompartment system to mimic a eukaryotic cell.

5.2.1 Fluorescent residues in the Moco biosynthesis

The Moco biosynthesis is conserved among all the life forms, except in some bacteria, where an additional molybdenum nitrogenase enzyme with iron-sulphur (Fe-S) based iron-molybdenum cofactor (FeMoco) is also found.[117,161] However, the common component of all molybdenum cofactors is the formation of MPT. MPT is a pterin molecule with a unique dithiolene group that binds to a molybdenum atom. The cells produce this cofactor *de novo*, and in the thesis via two intermediate steps of the pathway.[93,162]

In this thesis, both the intermediate steps were measured under well-defined catalytic assays using their respective fluorescent products, Figure 82 i.e., compound Z (for cPMP) and form A (for MPT).[96,127] The fluorescent products analysis has been well established over the past decades and led to the partial understanding of the pathway, where it has been under active investigation.[102,112,115,163–165]

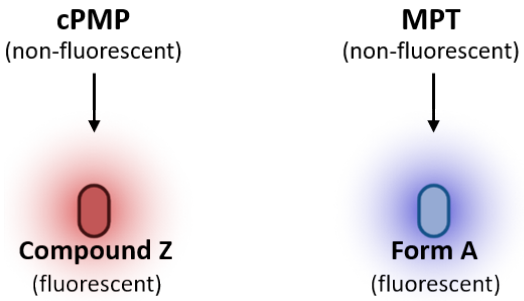

Figure 82. Fluorescent products, Compound Z and Form A.
The two main intermediate in the biosynthesis cPMP and MPT with their respective residual products for fluorescence-based detection.

As described previously, step-1 was always performed at pH 9, as another pH can lead to causing a chemical shift in pterins molecules, which would disrupt the pathway.[127] However, despite its importance, no investigation on the role of pH in the cPMP formation was performed in previous literature.[94,100] The pH study performed in this thesis was solely to question the possibility of varying pH for the later one-pot reconstitution where we concluded that pH 7 could be more optimal for high production rates, close to physiological pH conditions. However, no interpretation can be made from the reactions performed on a different pH. To better understand the effect of varying pH, a thorough study based on the structural characterisation must be applied.[85,110,139] Nevertheless, according to our findings, the pH range only for the reconstitution of the full reaction in one GUV could vary from pH 7 to pH 9 for the cPMP formation. One estimation on pH 7 for the reaction step, possibly the substrates (such as GTP, $MgCl_2$ and SAM) are more stable and less charged at this pH unlike at alkaline or acidic conditions. Overall, this analysis was applied in the thesis to validate the product (cPMP) formation. Further validations were made by eliminating substrates from the reaction to check the specificity of cPMP production. Understandably, the reaction mixture with the eliminated substrates could not result in the cPMP formation, supporting the description of GTP being the first specific substrate for MoaA activity, followed by other substrates in the intermediate steps.[110,139]

In the case of step 2, the MPT quantification was performed with the conventional form A assay as discussed previously. This reaction includes a more stable enzyme than that of step 1 reaction. The rapid conversion of cPMP to MPT with MPT synthase (~5 minutes),[97] indicates a time sensitive experimental set-up. Therefore, the first approach for the future reconstitution was to determine the time-sensitivity of the reaction mechanism. Thus, the reaction was performed with different time points, simply by terminating the reaction on different time-sets in parallel reaction samples. As observed from this study, the described *in vitro* experiment saturates within 10 minutes, putting a time limit on the study. This observation adds another challenge to the later reconstitution of the reaction. However, this time constraint was not fully addressed in the previous studies since it was never studied in such a minimal system. Using this method, the entire GUV preparation process takes a minimum of 20 minutes and the GUV transfer to the confocal setup takes approximately 5 minutes upon the formation. Therefore, the reconstitution application on the confocal-based detection will be discussed thoroughly later in the section.

5.2.1.1 cPMP production in the reaction

To reconstitute the reaction pathway into the GUV and to detect the cPMP production via a fluorescence-based detection using confocal microscopy was required. The fluorescent equivalent of cPMP i.e., compound Z (ex 383nm, em 450nm) could not be implemented in the present assay as its excitation and emission detection range was below the confocal detection set-up. Therefore, a 'higher-intensity' (>ex 383nm) fluorescence detection assay within the confocal range was needed. One approach in this direction was the detection of the reaction by-product i.e., PPi, as the conversion of GTP to cPMP results in one PPi release with every cPMP molecule. The PPi detection technique is known from two well-studied phenomena in the cell: the PPi released during ATP hydrolysis, and DNA synthesis by DNA polymerase. In two separate works, the PPi as by-product has been used as a detection technique to assay the main reaction, the ATP hydrolysis,[166] and the DNA synthesis.[167] Likewise, this thesis employed, the PPi-based assay that fluorescently probe the free PPi in the solution, Figure 83. This thesis introduces the first fluorescence detection attempt of the reaction of the cPMP formation catalysed by cPMP synthase. Thus, a careful investigation of the systems including the reaction mechanism, confocal, and GUV-based was needed.

First, the PPi detection was confirmed under confocal detection (ex 405nm, em 470nm) based on the bulk experiments, where the fluorescence values observed were within the confocal detection range. The PPi fluorescence intensity from the reaction mixture directly translates to the cPMP formation: one PPi released per cPMP formation, Figure 83. The PPi-based assay comes with a PPi standard that is an additional advantage to the study. Here by reconstituting the PPi standard inside GUVs, a preliminary understanding of the PPi detection inside GUVs was developed. Hence, upon reconstituting only PPi standard inside the GUVs, 1) it was evident that PPi signals in varying concentrations could be detected. 2) There has not been any leakage over time were stable, and thus 3) the GUV population was not affected in the presence of PPi detection system. Thus, confirming its application in the reaction detection, upon the reconstitution of the reaction mixture with this PPi detection system. Therefore, fluorescence detection of the PPi molecules released from the reaction could be performed under confocal microscopy.

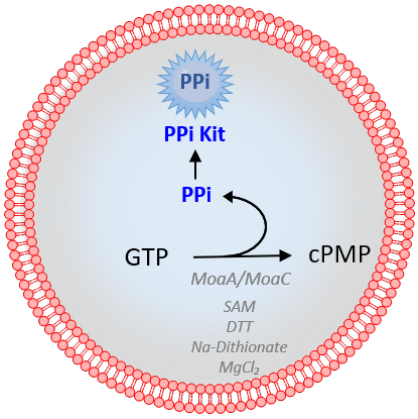

Figure 83. PPi Fluorescence detection scheme.
The detection scheme of cPMP formation from GTP in the presence of the reaction components, using PPi detection. The PPi released with the formation of every cPMP molecule was actively assayed using the PPi detection assay.

Further, for its application in the reaction detection, upon the reconstitution of the reaction mixture with the PPi detection system, fluorescence detection of the PPi molecules released could be performed under confocal microscopy. However, the reconstituted reaction in the presence of PPi detection system demonstrated relatively low values compared to that of the PPi standard. Even though, the reconstituted concentrations of the reaction mixture were kept the same as the bulk system. This observation indicates that the reaction process has been inadequate in the GUVs. Perhaps due to lower amount of substrate to the enzymes available in the GUVs i.e., decreased reaction volume inside GUV chamber, surface interaction.[168]

Though the provided minimal reaction condition, eliminated cellular complexity around the pathway, the Moco biosynthesis had not been studied previously inside GUV-based model. Explaining the reaction mechanism especially in the GUV model is challenging for the following reasons:

- First, this reaction step includes oxygen-sensitive enzymes where maintaining the oxygen-free environment throughout the experimental set-up has been possible but difficult.
- Second, the composition PPi detection kit includes unknown components that could affect the conversion rate or enzymatic stability.
- The third could be the sugar-supplemented buffer that is necessary to maintain the density gradient to form the GUVs.

Therefore, these points were further addressed, and the first essential examinations being made on the PPi assay were sugar-supplemented buffers. 1) The sugar supplements remain in the assay, as they are necessary for the formation of GUVs using inverted emulsion method and could not be eliminated. 2) The individual components from the reaction were separately encapsulated and measured under the confocal detection with PPi assay. The averaged measurements were negative for the unspecific PPi detection inside the GUVs. However, there were inconsistencies among different measurements, where the negative controls had leaky fluorescence. This may indicate free phosphate contamination in the sample buffers. Thus, a background correction was applied by subtracting the negative controls. 3) Finally, an anaerobic encapsulation of the reaction mixture containing the PPi assay as performed to avoid the oxygen contamination. This anaerobic encapsulation ensured a stable reconstitution of the substrate and the enzymes. Yet, this delayed the measurements due to the time consumed in the sample transport from anaerobic facilities to the confocal set-up. Nevertheless, the encapsulation was successful, and the fluorescence was successfully measured. The fluorescence intensity from the images could be easily converted to a pyrophosphate (PPi) concentration using the standard curve and subsequently to the cPMP concentration. It was estimated that the cPMP concentration of 13.58 µM (from 100 µM GTP) was produced inside the GUVs, with an additional lower GUV yield than those without the reaction. The production rate in this reconstitution has significantly decreased than those of the bulk studies. Further, to test the reaction kinetics under confocal detection, the time-lapse measurements were recorded up to 1 hour. These measurements indicated that the reconstituted GTP to cPMP reached a plateau within 1 hour. However, a significant concentration increases up to 16.5 µM from 13.58 µM was measured in 2.5 hours.

As previously described in literature, the overall reaction varies from 45 minutes to one hour.[112,169] Whereas, in this thesis, the reproduced results show a high standard variation between the different set of experiments. The continuous and gradual increase in the fluorescence with high variation was measured from 50 GUVs. This extended reaction time could be explained as the high sucrose effect on the reaction mixture. The high sugar supplements to the buffer interfere with enzyme activity (e.g., slow it down). Yet, another obvious factor could be the reaction volumes in the GUVs. Since the reaction chamber now confined the size to ~20 µm diameter bioreactors. The reaction down-scaling should have a measurable effect on the production rate. Since the data on the comparable reaction chamber was not yet available, the production rate could not be downsized this time.[168] Moreover, the GUV formation has been also affected by the reaction components with either microdroplet instability or higher salts components. Overall, the reaction rate could not be improved in the reconstituted condition, which indicates limited flexibility of the reaction mechanism under the given minimal conditions at this point.

5.2.1.2 cPMP to MPT conversion and further detection

Like compound Z for cPMP, the conventional fluorescent version of MPT, form A, has the fluorescence emission under the limits of confocal detection.[96] Since there is no existing fluorescence assay to detect the MPT in the pathway, this required to establish the MPT detection technique within the detectable range of the confocal set-up. Interestingly, this reaction step does not include many co-substrates or by-products, thus establishing a new detection system was suspected to be less sensitive. Towards the development of an assay for the *in vitro* produced MPT, a novel calcein-quenching technique was approached, Figure 84. In a similar work previously, the calcein-quenching was applied with cobalt externally through pores. In the study, the encapsulated calcein (10 µM) inside the GUV was supplied with AmB molecules that create pores. The pores lead cobalt ions in from the outer environment and quenched the calcein, learning from this, the calcein would be stably reconstituted inside the GUVs and would provide a strong quenching system.[137] Thus, the quenching assay was thoroughly analysed with the standard graphs with a few quenching candidates such as molybdate and various copper salts. Assuming the study, the calcein fluorescence should quench in the presence of several quenching ions. To observe a release of calcein fluorescence in the presence of MPT, the MPT should have an affinity to these quenching ions (either molybdate or copper ions). Therefore, the above-described quenching candidates molybdate and copper were examined over the standard curve. The suitable quenching ion(copper) was further analysed step-by-step, first by estimating their required concentrations to fully quench calcein, and second, by supplementing the solution with physiological buffers according to the condition of the reaction step.

Molybdate being biological relevant for the pathway would be a preferred fit for the thesis,[170] however, it could not quench the calcein molecules due to its anionic nature. The fluorescence of the calcein has been previously quenched with copper ions and shown to have recovered based on a redox reaction.[140] From the chemical structure of the calcein molecule, it was obvious that copper will strongly quench the calcein than that of molybdate. The standard curve with pure MPT solution to provide a similar standard graph as that of PPi standard was measured. The idea behind plotting the MPT standard was the following: 1) to check the recovery curve for calcein, and 2) to indicate unspecific interference arising due to the calcein fluorescence. And preferably the calcein recovery

would have a linear trend that 3) translates the released calcein fluorescence to MPT concentration. Though the standard curves plotted in bulk showed a linear trend, the reconstituted standard showed discrepancies, especially, the standard curve of the pure MPT in the quenched calcein solution. In case of reconstituted curves only calcein-copper showed a linear trend with increasing calcein concentrations. Whereas the reconstituted MPT calcein-copper calibration did not show a linear trend with the increased MPT concentrations. The reason being that the pure MPT is a sensitive molecule, could not remain stable during the measurements.[93] Therefore, the pure MPT standard could not be utilised in the thesis. The MPT production was demonstrated in the normalised percentage with the calcein throughout the thesis. Besides, the normalised fluorescence intensity has been widely accepted and utilised in previous literature.[9,34,46,67,76,171]

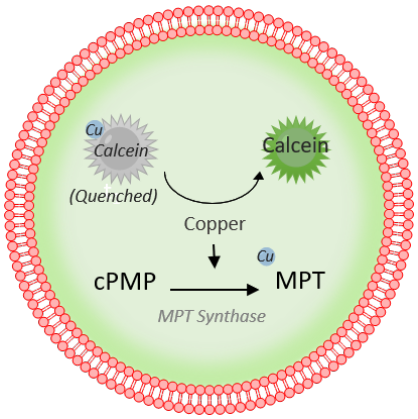

Figure 84. Calcein quenching assay for MPT detection.
The detection scheme of MPT formation using the calcein quenching assay. The assay works when the MPT, being produced from cPMP, attracts the copper from the quenched calcein and forms MPT-copper complex. This release of the copper from calcein will return the calcein fluorescence in the solution, and thus measured.

Upon the successful verification of MPT production from the cPMP in bulk, the reaction was reconstituted inside the GUVs. The fact that GUV production takes at least ~5 minutes from the emulsion to actual GUV production, the reconstituted reaction was measured immediately upon the GUV formation. The calcein recovery was measured and normalised to pure calcein fluorescence, to estimate the MPT produced. However, to observe an active development in the reaction under the confocal microscope, the catalytic activity must be measured immediately. For this, either the reaction should be slowed down, or the GUV production should be speeded-up. The later could not be possible with the optimised emulsion-based method. Hence, an approach to reduce enzymatic activity by decreasing the optimal temperature of the reaction was adapted. The temperature trigger technique has been published within two different approaches, first, where the liposomes were produced with temperature-sensitive lipids. The liposomal membrane with a defined phase transition temperature was destabilised above their threshold that demonstrated an *in situ* release of chemicals.[172] Secondly, a minimal cell that responds to temperature stimuli was demonstrated. In this work, a temperature-sensitive protein expression was reconstituted in the liposomes. The temperature-sensitive non-coding RNA sequences control the translation by blocking the ribose binding site (RBS) at low temperature. Thus, by exceeding a defined threshold temperature, the RBS was released that resulted in the gene expression.[171]

In our case, the optimal reaction temperature for most of the enzyme lies between 25-30°C. If the enzymes were kept on a temperature below 25-30°C, it would slow down the reaction. For this purpose, the working temperature was changed to 4°C, where the enzymatic activity would be minimum. To be able to trace the fluorescence from time zero, this cooling-down approach was applied. Therefore, the reaction mixture was kept on ice during sample preparation, while exposing to the room temperature once on the confocal microscope. The GUVs (at room temperature) demonstrated active reaction on the endpoint measurements. Here, the room temperature triggers the reaction during the measurement. The GUVs are the microchambers that showed a significant increase in the calcein recovery until 20 minutes and did not show any further increase. Hereby, the time-lapse observation confirms an active biosynthesis of MPT *de novo* from cPMP in the presence of MPT synthase.

However, even with the lower temperature, it was not possible to trace the reaction from time zero. On the contrary, this extended reaction delay when compared to bulk experiments could be possible for reasons, such as, the sugar supplemented solution or perhaps the pure cPMP was not sufficiently stable. Nevertheless, the reconstitution of the Moco biosynthesis was shown to be achievable and could be detected under two different fluorescence techniques. Both detection techniques are novel to the Moco biosynthesis and thus open for further improvement. Therefore, the reconstitution model could be improved in future where thorough optimisations should be applied with the enzyme or substrate concentrations.

5.2.1.3 Improving the reconstituted pathway

Many previously established bottom-up models engineered different synthetic cell-like systems with reconstituted cell-free protein expression,[67,173] defined chemical reactions,[63,174] and structural protein formation, etc.[9,13] As the previously described bottom-up model where the formation of resorufin from lactose was monitored,[34] such work represents the first synthetic cell-like system with reconstituted enzymes and their substrates. The model describes three steps table-top chemical signalling cascade, where the compartments are fully communicative. The advantage of this chemical reaction has been its well-established nature which provides a defined system.[34] Likewise, in a recent report on an advanced light-switchable photosynthetic synthetic organelles system. The light-switchable organelles with ATP synthase and two photoconverters (plant-derived photosystem II and bacteria-derived proteorhodopsin) allowed ATP synthesis. This light-switch enabled the ATP-dependent actin polymerization inside the GUVs. This system provides a highly advanced synthetic cell-like systems that demonstrate a switchable actin formation.[13] Whereas, the Moco biosynthesis includes sensitive substrates and enzymatic cascade, which requires yet, a better understanding of the pathway within the GUV system. In contrast, the previously described enzymatic cascades are more robust inside the reconstituted GUV. As the emulsion-based method has been thoroughly applied in the thesis to produce GUVs, and the method could sustain the physiological conditions of Moco Biosynthesis.

However, the method introduces factors that might have a significant effect on the reaction mechanism and vice-versa. To improve the reconstitution of the reaction steps, the effect of varying sugars concentration must be measured using the conventional analysis via compound Z and form A over HPLC. Followed by the effect of varying lipids

and oils on the reaction rate under similar product analysis. This study will be essential to understand the decreased reaction rate seen in this thesis, once understood, standards graphs for both steps should be plotted in bulk under likewise conditions. For example, to quantify the MPT production rate, a GUV-based calibration to translate the fluorescence intensity into the MPT concentration. Additionally, an incubator chamber would allow more robust temperature control on the confocal system. Nevertheless, the two intermediate steps were successfully encapsulated in two separate GUVs, which laid the foundation for the subsequent significant aim of this thesis. To encapsulate both the intermediate steps in a single GUV, where MPT could be formed from GTP, Figure 85. The physiological conditions for both steps must be analysed mainly for their buffer conditions and pH.

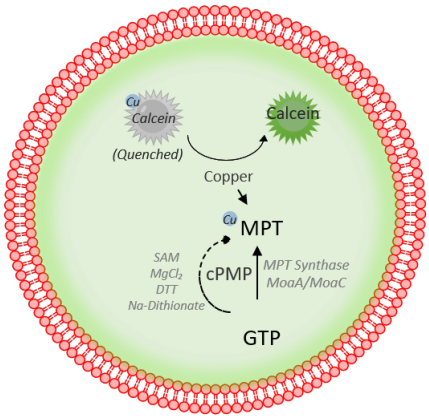

Figure 85. Diagram for the one pot Moco Biosynthesis.
Potential *in vitro* synthesis scheme of MPT from GTP in the presence of all the essential components. The MPT formation will be assayed with the calcein quenching assay as described in the main text.

The pH difference between the two steps was estimated very close, the step-1 was found to be possible at pH 7, whereas pH 7.2 is natural for the step-2. Thus, the one-pot reconstitution is a potentially possible yet a daunting task, Figure 85, because of the substrate specificity in the two reactions. The two reaction intermediates have never been studied together towards the MPT formation. The GTP conversion requires numbers of specific substrate for the reaction, which might hinder the activity of the MPT synthase, or vice-versa. Establishing the MPT formation from GTP would require a careful examination of the reaction mechanism itself, for example, the conventional form A analysis should be made carefully. Further, towards the reconstitution of this one-pot system, a fluorescence detection technique had to be considered. The developed calcein quenching assay in this thesis has not yet addressed the presence of the addition substrates from the step-1. The individual component must be discussed to test their effect on the calcein fluorescence. Furthermore, any inherent change in the osmolarities during the reactions has to be accounted for the one-pot reconstitution of the Moco biosynthesis. Finally, the reaction must be considered for the volumes of the reaction chambers while analysing the down-sized production rate.

5.3 cPMP Permeation through the Model Membrane

As described in 4.3, permeation of the cPMP from mitochondria to the cytosol during the Moco biosynthesis, the permeation across the mitochondrial membranes is not well understood yet and reviewed in this thesis. According to the observations made on the different experimental approaches, this thesis suggests that the cPMP interacts with the membrane. This study based on a model membrane, built upon the bottom approach, providing novelty to the permeation study and contributes to future bottom-up applications. This investigation on the minimal membrane with the pure cPMP in the surrounding environment leans towards the hypothesis that cPMP could be permeating the membrane. However, there has been a contradictory hypothesis of cPMP transport through an ATP-binding cassette (ABC) transporter. The ABC transporters are present across all the biological kingdoms and transport different biomolecules via active transport. The transfer of sulfur-containing molecules is one related feature to the Moco biosynthesis,[116,175] such as Atm1 and ATM3 from the inner mitochondrial membrane, of yeast and plants respectively, suspected to be involved as iron-sulfur (Fe-S) cluster transporter.[107,176,177]

The Fe-S clusters directly needed in the GTP conversion into the cPMP for the activity of MoaA enzymes.[109,111] Whereas, in the absence of Fe-S, the cPMP cannot be produced in the cell. Additionally, after many contradictory hypotheses on the molybdate transport, a highly specific ModABC was proved to be involved. Thus it has well known that the ModABC is needed to transport molybdate to the cell for the Moco formation.[92,178] Another speculation on the ABC transporters in the biosynthesis introduced a hypothesis of its involvement in the cPMP transport. Previous work, on *Arabidopsis thaliana* ATM3 mutant, indicated that ABC half-transporter ATM3 could be responsible for the cPMP transfer from mitochondria into the cytosol. The study first demonstrated the increased cPMP levels (cPMP accumulation) in the ATM3-deficient plants (ABC half-transporter), followed by the decreased levels of MPT/Moco, and a reduced Mo enzyme activity in the cells. The observation indicates the deficiency of the ATM3 in the plants would terminate the cPMP transport for the further steps in the pathway. Whereas, indicating the impaired cPMP transport across the mitochondrial membranes accumulated cPMP in the cytosol but retain its ability to transform to MPT and Moco. Following by another contradictory observation on the MPT production in the same work, where the MPT was also detected upon the reconstitution of the pure cPMP onto the protoplasts of the ATM3-deficient plants.[103] This observation suggested that cPMP diffuses through the biological membrane, that made cPMP available for the conversion.

Additionally, in a separate work from the same group, the proposed model was updated on the *Arabidopsis thaliana* ATM3 mutants indicating that ATM3 does not assist the cPMP transport, Figure 86,[105] since the exact role of ATM3 in the cPMP transport was not clearly understood previously. Likewise, the exact function of the ATM3 human orthologue ABCB7 in the transport on the cellular level has not yet demonstrated. However, it is well understood that cPMP due to its hydrophobic nature is capable of traversing the membranes.[96] Many studies support the hypothesis of its transport without a transporter. Hereby, this thesis addresses the permeation study that suggests that cPMP interacts with the membrane, and perhaps passively permeate in nature.

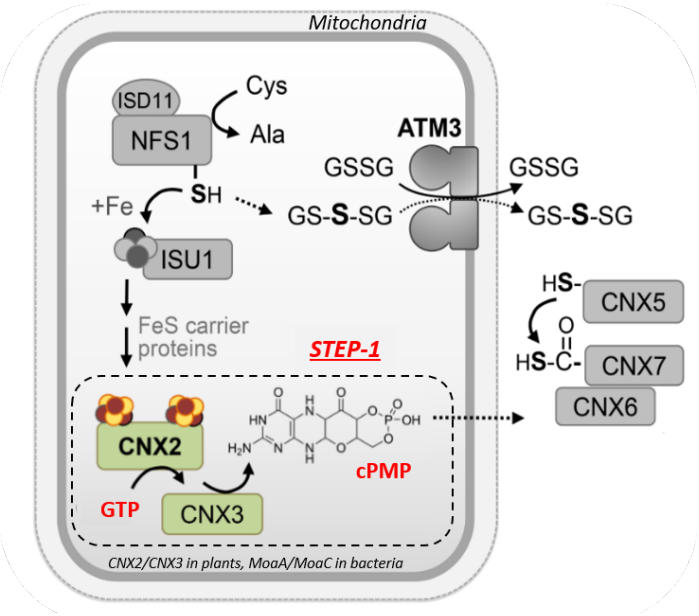

Figure 86. Moco biosynthesis (green) and FeS cluster assembly (grey) in Arabidopsis. The schematic was updated with solid arrows indicating the pathways based on experimental evidence and dashed arrows indicating speculative steps. In plants, GTP converts to cPMP in the presence of CNX2/3 (MoaA/MoaC in bacteria, as discussed in the thesis throughout). The cPMP permeates through the mitochondria (under speculations), where it enters the cytosol and further modifies in the presence of CNX6/7. The FeS clusters transport through ISU1 via NFS1/ISD11 to CNX2, where it is speculated that ATM3 transports glutathione disulfides, which was not discussed in the thesis. *Images adapted from Kruse et al., 2018.*[105]

The model membrane provides a minimal environment for this study, farther from the complex cellular functioning. For this reaction, the minimal system that focuses only on the cPMP and the model membrane without the unspecific interactions. This permeation phenomenon was introduced to the model membranes for the first time with this thesis. Therefore, a thorough investigation of the cPMP molecule on the membrane had to be performed. On the contrary with the membrane permeability section 1.3.1.2, cPMP being a negatively charged molecule, so is supposedly impermeable across the simple bilayer through diffusion like many other charged molecules. Hence, to understand the cPMP transport, it was essential to mimic the mitochondrial membrane.[8,15] The GUVs have been widely used as model system in the membrane biophysics.[14,52,179] In this direction, the emulsion-based method was initially applied to produce mito-GUVs while optimising different parameters in the production technique. The final mito-GUVs (based on PC, PE, PI, SM, PS and cardiolipin) were produced with 500 mM sugars, pH 5 at 140 x g centrifugation, which resulted on a sub-optimal yield. The yield was still quantifiable, hence, the observation on the decreased yield did not affect the measurement, yet this could be optimised in the future.

The GUVs were labelled with DiIC18 fluorescent dye, whereas the fluorescence-based assay was needed for the cPMP. Since the cPMP itself does not possess a strong fluorescence under confocal detection, it's fluorescence product compound Z was used.[96,110] The fluorescence from the compound Z was detected under the confocal limit. Thus, additional dyes were applied to assay the cPMP presence inside the GUVs. Here, two independent approaches were adapted to detect the cPMP across the GUV bilayer: 1) fluorescamine, that produces fluorescence only in the presence of a primary amine, and

otherwise does not emit on its own, and 2) calcein dye. Both dyes were not yet known with cPMP studies, and thus it is also novel to this thesis.

First, upon the successful GUV investigation under the fluorescamine-supplemented solutions in the thesis, the observation suggested that the cPMP partitions onto the membrane of the mitochondrial lipid composition. This conclusion was made through the measurements on the cPMP and the fluorescamine, segregated onto the GUV population, either from outside or inside using the emulsion-based method. The emulsion-based method integrates both the cPMP and fluorescamine (as the outer and inner solution) with the steps of the GUV production, and thus the leaky fluorescence expression on the membranes could be a direct effect of the artefact from the emulsion-based method, Figure 87. The artefact, such as membrane showing signals expected from the fluorescamine, arose from the production technique could be eliminated by choosing a different method.

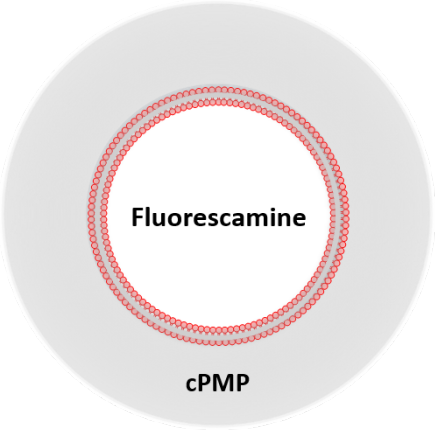

Figure 87. Summarising a fluorescamine study using emulsion-based method. Diagram based on the observation scheme of cPMP assay, the cPMP is present in the outer environment with fluorescamine reconstituted inside the GUVs. Hypothetically, if the cPMP permeates the membrane, the fluorescamine should produce fluorescence inside the GUVs.

A method that allows the segregation of the GUVs production from the final sampling and can further exchange the supplemented buffers. Thus, the trapping technique onto a microfluidic chip was applied where the outer solution could be exchanged without affecting the GUVs. Upon exchanging the outer solution with osmotically balanced 20 µM cPMP solution, the GUVs started to rupture and eventually disintegrated. Whereas the iso-osmotic solution supplemented without cPMP did not triggers such deformities in the GUV population. The observations on the trapped GUVs on the chip made it clear that cPMP influences the mito-GUVs. This was somewhat an obscure observation since all the transferred solution to the chip were kept at the same pH and osmolarities.

However, pH-sensitive measurements were not performed to confirm any possible pH change during the flow. As seen in a pH-dependent study, in microfluidic chips, there was no observable change in the morphology of the GUVs present in the trap when the external solution which was at pH-11 was replaced with the pH-5 solution.[132] The pH change would be particularly a convincing explanation for such unwanted bursting, if not cPMP interference. Nonetheless, the experiments were repeated to eliminate any chances of errors, and the results were reproducible. One alternative explanation could be that

transferring solutions past the traps with GUVs in the microfluidic chip are considered as an additive process. Considering that the surface-to-volume ratios inside the chip are very high, such an additive process might result in exponential-levels of cPMP exposure, this could explain the disintegration of the GUVs in the light of the results from other tests performed in this thesis.

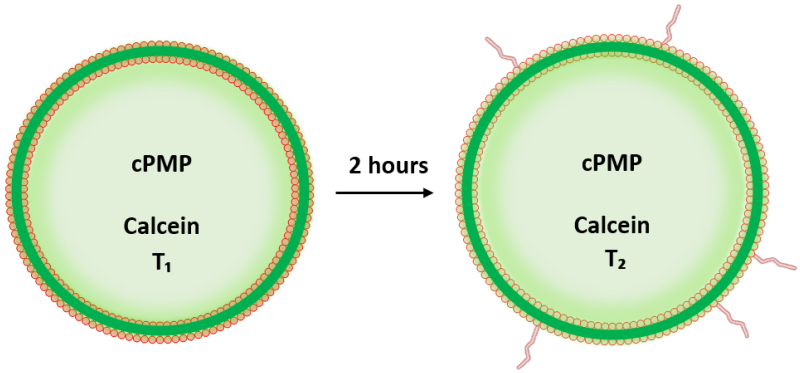

Figure 88. Summarising the observation on the calcein and the cPMP reconstitution using the emulsion-based method.
Diagram based on the pure cPMP reconstitution inside mitochondrial GUVs (from T_1) to the time-lapse observation upto 2 hours (T_2), where calcein was detected in the bilayer, which further developed different membrane patterns.

Second, in the similar illustrations for the fluorescence assay using the calcein dye, when the calcein together with cPMP was supplemented inside the GUVs, the GUVs showed strong calcein signal from the membrane, Figure 88. The calcein molecule brings four negatively charged COO− groups at the physiological pH, which could interact with the polar lipid head region.[158] However, the control GUV population (without cPMP) did not show any calcein fluorescence from the GUV bilayer. Previously, with the reconstitution of the calcein-quenching assay established in this thesis, GUVs did not show any effect in the membrane in case of pure calcein. This was also followed by an investigation based on the membrane interaction factor with a water-soluble fluorophore.[141] Further, the time-lapse measurements of these GUVs introduce more open questions with observations like varying membrane morphology such as thread-like structure formation adhering to the membrane, lipid aggregation and deformation of the GUVs, Figure 88. These effects on the GUVs are generally induced due to the asymmetry in membranes.[8,180] Perhaps, this could indicate that the GUVs are becoming asymmetric in the cPMP solution. However, to confirm any induced asymmetry upon cPMP membrane incorporation, a more thorough investigation of the cPMP-membrane interaction using techniques such as surface plasmon resonance or quartz crystal microbalance can shed light in this aspect.[181,182]

One known conventional approach which has been the gold standard for membrane study was electroformed GUVs. Thus, the electroformed mitochondrial GUVs were applied in this analysis. Surprisingly, the electroformed mito-GUVs became leaky upon contacting the cPMP-supplemented solution. As a result, the calcein present in the outer solution instantly leaks into the lumen of the GUVs, in about 40-45 minutes the mito-GUVs were completely filled with calcein solution from outside. In parallel, there was no trace of any leakage over 1 hour when the GUVs were washed without cPMP. This clearly indicates that the cPMP interfere with the membrane stability, either by partitioning to

the membrane or by creating pores. Although, the model of how the cPMP interact with the membrane could not be outlined at this point, the scheme seen in Figure 89 summaries the observations. However, the given diagram lacks insights into the membrane instability induced in the presence of cPMP. In both calcein-based cases, it was certain that the cPMP makes the calcein molecules across the membrane.

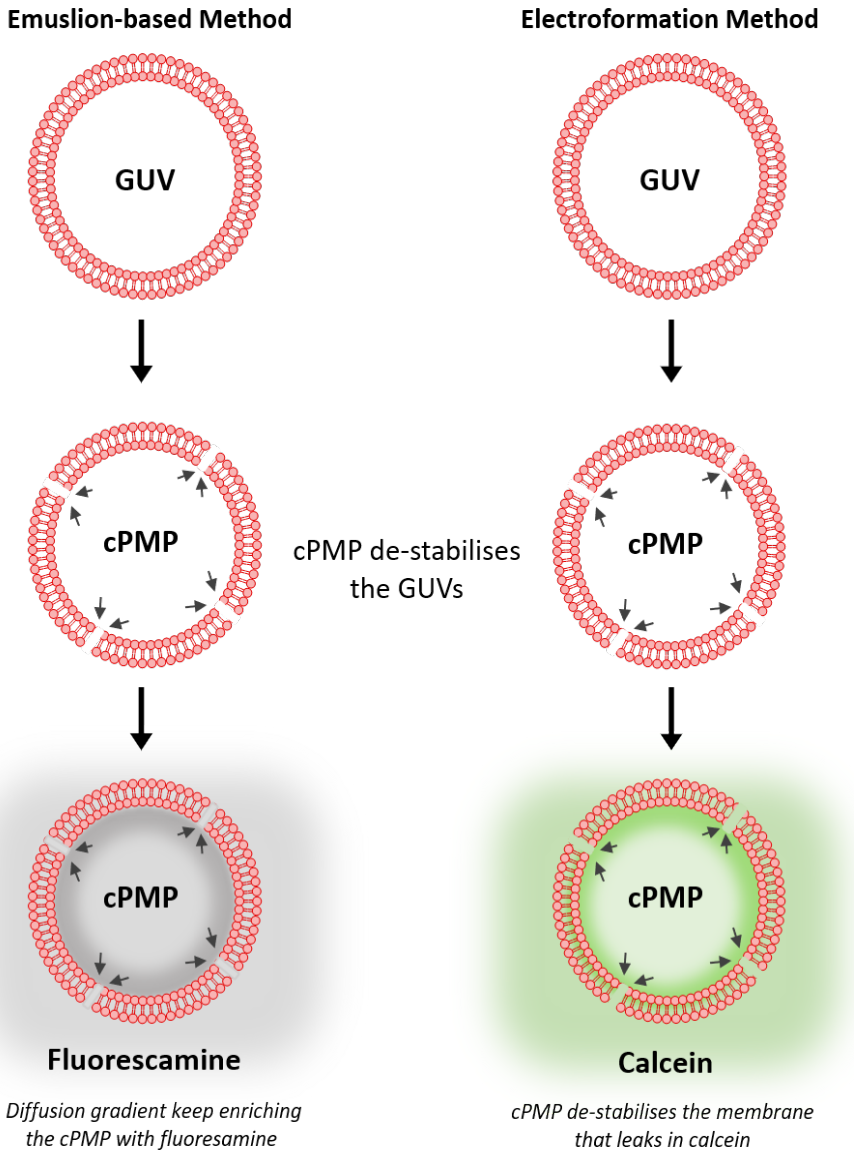

Figure 89. cPMP permeation across the membrane in two discussed systems. With two experimental i.e., the emulsion-based and electroformation utilised in the thesis. The GUVs were investigated upon cPMP treatment: with fluorescamine and calcein solutions. In both cases, the membrane was suspected to interact with the surrounding solution where leaky fluorescence was seen.

Earlier in a separate study, it was demonstrated that calcein is impermeable through the bilayer, in the absence of the membrane pores.[131,137] Supporting these observations, we also demonstrated that the calcein was impermeable through mito-GUV as well. Therefore, pore-size-based investigation should be applied in this study. Alternatively, as calcein lifetime measurements suggest that the calcein self-quenches at high concentrations, this nature could be utilised as an alternative approach for the study. In

work towards synthetic mechanosensitive signalling, a pathway was established inside multicompartment liposomes. The model built a nested vesicle-in-vesicle network, where calcium ions from outside activated the protein communication inside. The calcium-dependent activity released calcein (the self-quenched state) from the inner compartment into the outer compartment of the vesicle. The calcein release in the outer vesicle leads to the fluorescence increased through release of calcein from the self-quenched state in the outer synthetic-cell.[183]

Nevertheless, in the electroformed model, the membranes becoming leaky could indicate cPMP crossing the membrane. While in nature, the transport would be dynamic involving a continuous interaction of the surrounding environment supplemented with the essential macromolecules. The cell within the surrounding environment would go through continuous morphological changes, unlike the minimal GUV model, where the nutrition in the surrounding environment is limited will not be subjected to such changes. Hence, the main downside of this minimal model could be a temporal limitation and decreased viability with time and age. For example, the Moco biosynthesis in a natural cell is regulated by the enzymes that are continuously replenished by the other coordination enzyme.[98] On the contrary, the minimal cell had a limited supply of the substrates and enzymes. In this case, this would be the additional factors accounted for the stability of the model membrane. Since these results do not clearly indicate the cPMP permeation through the membrane, there was no direct evidence that demonstrates the cPMP transport in these experiments. However, there are separate literature supporting our observations that cPMP could be crossing across the membrane.

Moreover, as explained from the therapies on human Moco deficiency, the cPMP diffuses between the human cells: in a study where type A patient cells (unable to produce MPT from cPMP) were co-cultured with type B (able to produce MPT), the type A cells restored the cPMP level.[184] Similarly, mice models with a MOCS1 mutant, unable to form cPMP, fully recovered function upon cPMP injections.[119] This observation is indeed the fundamentals behind the current therapies for human Moco deficiency.[120] Interestingly these therapeutic investigations only demonstrate the rescued effect of cPMP in the cell. Whereas the transport of cPMP from the mitochondria to the cytoplasm is a different phenomenon. In this case, a hypothesis considering a different mitochondrial property can describe the transport. The mitochondria are dynamic and facilitate the distribution of cellular mitochondria-derived metabolites by fusion and fission events such as phospholipid, protein etc. The phospholipid transfer is also essential for the continuous repairing of the membrane composition, as well as for maintaining the exchange of metabolites and unknown molecules to and from the mitochondria in the cell. This transport of a small molecule could potentially include molecules like cPMP. Therefore, the investigation on the lipid traffic of the mitochondrial membrane could also provide insight into the cPMP transport, as represented in schematic, Figure 90. Subsequently, the investigation should be planned for the cPMP interactions and membrane pore formation properties, moreover the pore-size should be investigated. Nevertheless, in this thesis we conclude that the cPMP could passively permeate through the membrane.

5.3.1 Improving the permeation study

The current observations indicate that the cPMP partitioned to the mito-GUV making the membrane leaky. In future, first, to mimic a complete mitochondrial composition, two

independent membranes should be adapted as the inner and outer mitochondrial membrane. Membrane interaction techniques such as surface plasmon resonance-based detection could then be applied to confirm the cPMP interaction on the lipid-bilayer. Additionally, Raman spectroscopy-based measurements could be applied to detect the presence of cPMP inside or outside the GUV lumen. An advanced technique such as Coherent anti-Stokes Raman scattering spectroscopy (CARS) is a non-invasive technique that employs multiple photons to address the molecular vibrations.[86]

The CARS would be additionally beneficial because it does not demand the additional fluorescent label for the cPMP detection. In this case, the Raman emission of the cPMP molecule must be plotted, where the specified wavelengths would be further applied for CARS measurements. The CARS measurement would instantly display the presence of cPMP either inside/outside the GUV or in both.[185,186] However, these measurements would be sensitive to the substrate concentration for the detection limit.

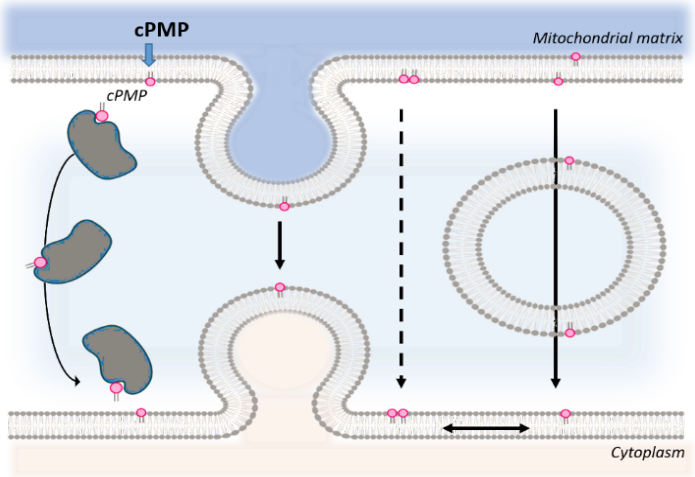

Figure 90. Translocation of phospholipids between mitochondrial membranes. Trans-bilayer movement of phospholipids in mitochondrial membranes involves translocation, coupled to modification/synthesis of a phospholipid, such as synthesis of cardiolipin and phosphatidylethanolamine in the inner mitochondrial membrane. The trans-bilayer translocation can have various modes, such as spontaneous transport, facilitated spontaneous transport, vesicles budding, close membrane contract, and lipid carrier proteins. *Image adapted from Tatsuta et al.*[15]

Further, as a localisation analysis of lipids in mitochondria suggests that transport within the outer and inner membrane is the rate-limiting factor.[15,187] The passive transport through the hydrophobic core of the phospholipid, across an aqueous phase, are comparatively slowly yet possible. The two membranes in the mitochondria assist multistep reactions to exchange or transport their lipids, and as shown in Figure 90.[15] This could also provide a mode of unspecifically cPMP transport during the phospholipid transfer between membranes. Therefore, the investigation on the lipid traffic of the mitochondrial membrane should be further planned to gain insight into the cPMP transport. Finally, computational simulations could also be employed for initial results to observe possible partitioning of the cPMP across the membrane.

5.4 Outlook

Upon better understanding the pathway, such as the labile activity of the step-1 reaction with step-2, and cPMP permeation through the mitochondrial membrane, a two-compartment system makes more sense. Hence, the proposed one-pot system could be modified with a fully compartmentalised Moco system. Thus, the two-compartment Moco system with an inner vesicle as mitochondria inside an outer GUV as the synthetic cell, Figure 91. The system would reconstitute the step-1 components in the inner vesicles, where the produced cPMP transport outside. The cPMP permeating the inner vesicle would enter the outer GUV, where MPT synthase further converts cPMP to MPT. This can give insights into the role of compartmentalisation in the pathway. However, a compartmentalised model which can perform the two previously described steps i.e., cPMP formation and MPT generation could be further developed.

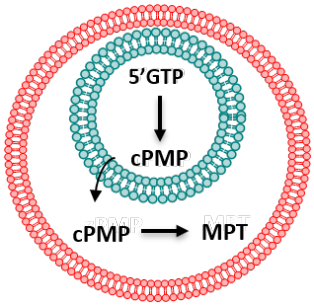

Figure 91. Next steps in the study.
A fully compartmentalised system for minimal Moco Biosynthesis, where cPMP formation takes place in the inner mito-GUV. The cPMP permeates through the membrane and transforms into MPT. The MPT molecule is then detected using the calcein-quenching assay under confocal detection.

Though the initial trial experiments did yield a compartmentalized system. In the experiments, the GUVs were produced using the emulsion-based method and further applied as the inner solution in a second emulsion-based step to form the outer GUV. A double emulsion-method resulted in the loss of inner GUVs during the process of retrieving from the microtiter plate. In addition to this, the encapsulation efficiency of inner GUVs into the lumen of GUVs was low. Hence, the compartmentalised GUVs were produced with ~25 % efficiency.

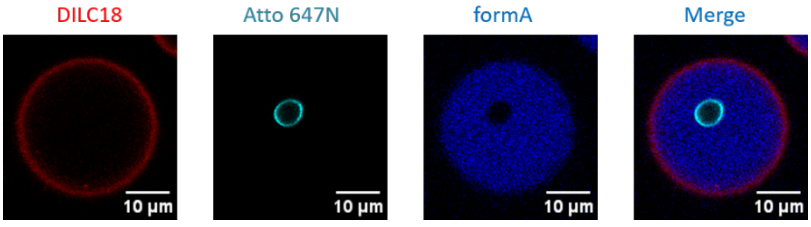

Figure 92. POPC-based compartmentalised GUV.
The representative images from the production process of the compartmentalised GUV, here the inner GUV was labelled with Atto 647 N (seen in cyan channel), outer GUV with DiIC18 (red channel) and fluorescence the product of MPT i.e., form A (blue channel).

As seen in Figure 92, the produced inner compartments during the first emulsion-based method are shown in cyan, which along with form A (blue channel) is further

encapsulated inside an outer GUV (red channel) produced using the emulsion-based method. This initial experiment concluded as a successful attempt, towards the production of compartmentalised vesicles, with no leakage of form A into the lumen of the inner GUV. The future approach in this direction could include a compartmentalised GUV with the inner compartment as mitochondrial mimic that contains the reaction mixture (GTP, SAM etc.) for the cPMP formation. Likewise, the outer compartment, would act as the cell that carries this inner compartment and the MPT synthase in the lumen for the MPT formation. The reaction is expected to start from GTP in the inner mito-GUV followed by the cPMP permeation to the outer environment, where MPT synthase catalyses the MPT formation. Further, the calcein-quenching assay would detect this active production of MPT in the outer environment.

Nevertheless, in this thesis, we reconstituted the part of Moco biosynthesis in the GUVs for the first time. The reconstituted Moco biosynthesis was detected via established fluorescence assay for cPMP and MPT production on the confocal set-up. Additionally, we investigated the cPMP permeation through the mitochondrial membranes. This work contributed to the development of the bottom-up synthetic biology as minimal cell models, as well as a potential candidate for the membrane-based phenomenon.

6 References

1. Harvey Lodish, Arnold Berk, Chris A. Kaiser, Monty Krieger, Anthony Bretscher, Hidde Ploegh, Angelika Amon KCM. *Molecular Cell Biology*. 8th. ed 20. (Harvey Lodish, Arnold Berk, Chris A. Kaiser, Monty Krieger, Anthony Bretscher, Hidde Ploegh, Angelika Amon KCM, ed.). W. H. Freeman and Company; 2016. doi:1-4641-8339-2

2. SCHOPF JW. *The Discovery of Earth ' s Earliest Fossils: Cradle of Life*. 1999th ed. Princeton University Press; 1999.

3. Walde P. Building artificial cells and protocell models: Experimental approaches with lipid vesicles. *BioEssays*. 2010;32(4):296-303. doi:10.1002/bies.200900141

4. Schrum JP, Zhu TF, Szostak JW. The origins of cellular life. *Cold Spring Harb Perspect Biol*. 2010;2(9):27-41. doi:10.1007/s10482-014-0169-5

5. Benner SA. Defining Life. 2010;10(10). doi:10.1089/ast.2010.0524

6. Alberts B. *The Cell*. 6th ed. 20. (Bruce Alberts, Alexander Johnson, Julian Lewis, David Morgan M, Raff, Keith Roberts, Peter Walter ; with problems by John Wilson TH, eds.). Garland Science, Taylor & Francis Group, LLC, an informa business; 2015.

7. Blain JC, Szostak JW. Progress Toward Synthetic Cells. *Annu Rev Biochem*. 2014;83(1):615-640. doi:10.1146/annurev-biochem-080411-124036

8. Dimova, Rumiana and Marques C. *The Giant Vesicled Book*. 2020th ed. CRC Press, Taylor & Francis Group; 2020.

9. Pontani LL, Van Der Gucht J, Salbreux G, Heuvingh J, Joanny JF, Sykes C. Reconstitution of an actin cortex inside a liposome. *Biophys J*. 2009;96(1):192-198. doi:10.1016/j.bpj.2008.09.029

10. Singer S., Nicolson GL. Fluid mosaic model of the cell membrane_Singer1972. *Science (80-)*. 1972;175:720-731.

11. Toparlak OD, Mansy SS. Progress in synthesizing protocells. *Exp Biol Med*. 2019;244(4):304-313. doi:10.1177/1535370218816657

12. Dervaux J, Noireaux V, Libchaber AJ. Growth and instability of a phospholipid vesicle in a bath of fatty acids. *Eur Phys J Plus*. 2017;132(6):1-10. doi:10.1140/epjp/i2017-11554-1

13. Lee KY, Park SJ, Lee KA, et al. Photosynthetic artificial organelles sustain and control ATP-dependent reactions in a protocellular system. *Nat Biotechnol*. 2018;36(6):530-535. doi:10.1038/nbt.4140

14. Altamura E, Milano F, Tangorra RR, et al. Highly oriented photosynthetic reaction centers generate a proton gradient in synthetic protocells. *Proc Natl Acad Sci U S A*. 2017;114(15). doi:10.1073/pnas.1617593114

15. Tatsuta T, Scharwey M, Langer T. Mitochondrial lipid trafficking. *Trends Cell Biol*.

2014;24(1):44-52. doi:10.1016/j.tcb.2013.07.011

16. Gallet PF, Zachowski A, Julien R, Fellmann P, Devaux PF, Maftah A. Transbilayer movement and distribution of spin-labelled phospholipids in the inner mitochondrial membrane. *Biochim Biophys Acta - Biomembr*. 1999;1418(1):61-70. doi:10.1016/S0005-2736(99)00022-X

17. Chen Y, Okur HI, Lütgebaucks C, Roke S. Zwitterionic and Charged Lipids Form Remarkably Different Structures on Nanoscale Oil Droplets in Aqueous Solution. *Langmuir*. 2018;34(3):1042-1050. doi:10.1021/acs.langmuir.7b02896

18. Mengistu DH, Kooijman EE, May S. Ionization properties of mixed lipid membranes: A Gouy-Chapman model of the electrostatic-hydrogen bond switch. *Biochim Biophys Acta - Biomembr*. 2011;1808(8):1985-1992. doi:10.1016/j.bbamem.2011.03.001

19. Israelachvili JN. Refinement of the fluid-mosaic model of membrane structure. *BBA - Biomembr*. 1977;469(2):221-225. doi:10.1016/0005-2736(77)90185-7

20. Schrum JP, Zhu TF, Szostak JW. The Origins of Cellular Life. *Cold Spring Harb Perspect Biol*. 2010;2(9):a002212-a002212. doi:10.1101/cshperspect.a002212

21. Lipowsky R. (CUL-ID:1486149) The conformation of membranes. *Nature*. 1991;349(6309):475-481. doi:10.1038/349475a0

22. Schwille P, Spatz J, Landfester K, et al. MaxSynBio: Avenues Towards Creating Cells from the Bottom Up. *Angew Chemie - Int Ed*. 2018. doi:10.1002/anie.201802288

23. Sun S, Li M, Dong F, Wang S, Tian L, Mann S. Chemical Signaling and Functional Activation in Colloidosome-Based Protocells. *Small*. 2016;12(14):1920-1927. doi:10.1002/smll.201600243

24. Noireaux V, Libchaber A. A vesicle bioreactor as a step toward an artificial cell assembly. *Proc Natl Acad Sci U S A*. 2004;101(51):17669-17674. doi:10.1073/pnas.0408236101

25. Walde P, Cosentino K, Engel H, Stano P. Giant Vesicles: Preparations and Applications. *ChemBioChem*. 2010;11(7):848-865. doi:10.1002/cbic.201000010

26. Lu Y. *Cell-Free Synthetic Biology*.; 2020. doi:10.1007/978-981-13-1171-0

27. Bartelt SM, Chervyachkova E, Ricken J, Wegner S V. Mimicking Adhesion in Minimal Synthetic Cells. *Adv Biosyst*. 2019. doi:10.1002/adbi.201800333

28. Leonard JN, Fritz BR, Timmerman LE, Daringer NM, Jewett MC. Biology by design: From top to bottom and back. *J Biomed Biotechnol*. 2010;2010. doi:10.1155/2010/232016

29. Koonin and M. A minimal gene set for cellular life derived by comparison of complete bacterial genomes. *Chemtracts*. 1996;11(3):234.

30. Brea RJ, Hardy MD, Devaraj NK. Towards Self-Assembled Hybrid Artificial Cells:

Novel Bottom-Up Approaches to Functional Synthetic Membranes. *Chem - A Eur J*. 2015;21(36):12564-12570. doi:10.1002/chem.201501229

31. Brea RJ, Devaraj NK. *& FunctionalS Ynthetic Membranes Towards Self-Assembled Hybrid Artificial Cells:Novel Bottom-Up Approaches to FunctionalS Ynthetic Membranes*. Vol 21.; 2015. http://devarajgroup.ucsd.edu.

32. Sung BH, Choe D, Kim SC, Cho BK. Construction of a minimal genome as a chassis for synthetic biology. *Essays Biochem*. 2016;60(4):337-346. doi:10.1042/EBC20160024

33. Pezzulo G, Levin M. Top-down models in biology: Explanation and control of complex living systems above the molecular level. *J R Soc Interface*. 2016;13(124). doi:10.1098/rsif.2016.0555

34. Elani Y, Law R V, Ces O. Vesicle-based artificial cells as chemical microreactors with spatially segregated reaction pathways. *Nat Commun*. 2014;5:5305. doi:10.1038/ncomms6305

35. Elani Y. Construction of membrane-bound artificial cells using microfluidics: A new frontier in bottom-up synthetic biology. *Biochem Soc Trans*. 2016;44(3):723-730. doi:10.1042/BST20160052

36. Patil YP, Jadhav S. Novel methods for liposome preparation. *Chem Phys Lipids*. 2014;177:8-18. doi:10.1016/j.chemphyslip.2013.10.011

37. Deng N-N, Yelleswarapu M, Zheng L, Huck WTS. Microfluidic Assembly of Monodisperse Vesosomes as Artificial Cell Models. *J Am Chem Soc*. 2016;139(2):587-590. doi:10.1021/jacs.6b10977

38. Dewey DC, Strulson CA, Cacace DN, Bevilacqua PC, Keating CD. Bioreactor droplets from liposome-stabilized all-aqueous emulsions. *Nat Commun*. 2014;5. doi:10.1038/ncomms5670

39. Pautot S, Frisken BJ, Weitz DA. Production of unilamellar vesicles using an inverted emulsion. *Langmuir*. 2003;19(7):2870-2879. doi:10.1021/la026100v

40. Trantidou T, Friddin M, Elani Y, et al. Engineering Compartmentalized Biomimetic Micro- and Nanocontainers. *ACS Nano*. 2017;11(7):6549-6565. doi:10.1021/acsnano.7b03245

41. Szoka F. AND METHODS OF PREPARATION OF LIPID VESICLES (LIPOSOMES) l. *Cancer Res*. 1980:467-508. doi:10.1073/pnas.73.11.3862

42. Elani Y, Gee A, Law R V, Ces O. Engineering multi-compartment vesicle networks. *Chem Sci*. 2013;4(8):3332-3338. doi:10.1039/C3SC51164B

43. Hadorn M, Boenzli E, Eggenberger Hotz P, Hanczyc MM. Hierarchical Unilamellar Vesicles of Controlled Compositional Heterogeneity. *PLoS One*. 2012;7(11):1-7. doi:10.1371/journal.pone.0050156

44. Okano T, Inoue K, Koseki K, Suzuki H. Deformation Modes of Giant Unilamellar

Vesicles Encapsulating Biopolymers. *ACS Synth Biol*. 2018;7(2):739-747. doi:10.1021/acssynbio.7b00460

45. Nishimura K, Suzuki H, Toyota T, Yomo T. Size control of giant unilamellar vesicles prepared from inverted emulsion droplets. *J Colloid Interface Sci*. 2012;376(1):119-125. doi:10.1016/j.jcis.2012.02.029

46. Friddin MS, Barlow NE, Elani Y, et al. Sculpting and fusing biomimetic vesicle networks using optical tweezers. *Nat Commun*. 2018;9(1):1-11. doi:10.1038/s41467-018-04282-w

47. Basu A, Maity P, Karmakar P, Karmakar S. Preparation of giant unilamellar vesicles and solid supported bilayer from large unilamellar vesicles: Model biological membranes. *J Surf Sci Technol*. 2016;32(3-4):85-92. doi:10.18311/jsst/2016/7753

48. Sobrinos-Sanguino M, Zorrilla S, Keating CD, Monterroso B, Rivas G. Encapsulation of a compartmentalized cytoplasm mimic within a lipid membrane by microfluidics. *Chem Commun*. 2017;53(35):4775-4778. doi:10.1039/c7cc01289f

49. Robinson T, Verboket PE, Eyer K, Dittrich PS. Controllable electrofusion of lipid vesicles: initiation and analysis of reactions within biomimetic containers. *Lab Chip*. 2014;14(15):2852. doi:10.1039/c4lc00460d

50. Deshpande S, Dekker C. On-chip microfluidic production of cell-sized liposomes. *Nat Protoc*. 2018;13(5). doi:10.1038/nprot.2017.160

51. Kong F, Zhang X, Hai M. Microfluidics fabrication of monodisperse biocompatible phospholipid vesicles for encapsulation and delivery of hydrophilic drug or active compound. *Langmuir*. 2014;30(13):3905-3912. doi:10.1021/la404201m

52. Girard P, Pécréaux J, Lenoir G, Falson P, Rigaud J-L, Bassereau P. A New Method for the Reconstitution of Membrane Proteins into Giant Unilamellar Vesicles. *Biophys J*. 2004;87(1):419-429. doi:10.1529/biophysj.104.040360

53. Basu A, Maity P, Karmakar P, Karmakar S. Preparation of giant unilamellar vesicles and solid supported bilayer from large unilamellar vesicles: Model biological membranes. *J Surf Sci Technol*. 2016;32(3-4):85-92. doi:10.18311/jsst/2016/7753

54. Hou J, Belardi B, Fletcher DA, Vahey MD, Wang J, Son S. Claudin-4 reconstituted in unilamellar vesicles is sufficient to form tight interfaces that partition membrane proteins. *J Cell Sci*. 2018;132(4):jcs221556. doi:10.1242/jcs.221556

55. Robinson T, Verboket PE, Eyer K, Dittrich PS. Controllable electrofusion of lipid vesicles: initiation and analysis of reactions within biomimetic containers. *Lab Chip*. 2014;14(15):2852. doi:10.1039/c4lc00460d

56. Henriksen JR, Ipsen JH. Thermal undulations of quasi-spherical vesicles stabilized by gravity. *Eur Phys J E*. 2002;9(4):365-374. doi:10.1140/epje/i2002-10091-3

57. Yandrapalli N, Robinson T. Ultra-high capacity microfluidic trapping of giant vesicles for high-throughput membrane studies. *Lab Chip*. 2019. doi:10.1039/c8lc01275j

58. Okano T, Inoue K, Koseki K, Suzuki H. Deformation Modes of Giant Unilamellar Vesicles Encapsulating Biopolymers. *ACS Synth Biol*. 2018;7(2):739-747. doi:10.1021/acssynbio.7b00460

59. Litschel T, Ganzinger KA, Movinkel T, et al. Freeze-thaw cycles induce content exchange between cell-sized lipid vesicles. *New J Phys*. 2018. doi:10.1088/1367-2630/aabb96

60. Tsugane M, Suzuki H. Reverse Transcription Polymerase Chain Reaction in Giant Unilamellar Vesicles. *Sci Rep*. 2018;8(1). doi:10.1038/s41598-018-27547-2

61. Trantidou T, Dekker L, Polizzi K, Ces O, Elani Y. Functionalizing cell-mimetic giant vesicles with encapsulated bacterial biosensors. *Interface Focus*. 2018;8(5). doi:10.1098/rsfs.2018.0024

62. Natsume Y, Wen H, Zhu T, Itoh K, Sheng L, Kurihara K. Preparation of Giant Vesicles Encapsulating Microspheres by Centrifugation of a Water-in-oil Emulsion. *J Vis Exp*. 2017;(119):1-8. doi:10.3791/55282

63. Walde P, Ichikawa S. Enzymes inside lipid vesicles: Preparation, reactivity and applications. *Biomol Eng*. 2001;18(4):143-177. doi:10.1016/S1389-0344(01)00088-0

64. Kubatta EA, Rehage H. Characterization of giant vesicles formed by phase transfer processes. *Colloid Polym Sci*. 2009;287(9):1117-1122. doi:10.1007/s00396-009-2083-3

65. Pautot S, Frisken BJ, Weitz D a. Production of Unilamellar Vesicles Usingan Inverted Emulsion. *Langmuir*. 2003;(10):2870-2879. doi:10.1021/la026100v

66. Hanczyc MM, Szostak JW, Matsushita-Ishiodori Y, Wang A, Yomo T. Using Imaging Flow Cytometry to Quantify and Optimize Giant Vesicle Production by Water-in-oil Emulsion Transfer Methods. *Langmuir*. 2019. doi:10.1021/acs.langmuir.8b03635

67. Deng NN, Yelleswarapu M, Huck WTS. Monodisperse Uni- and Multicompartment Liposomes. *J Am Chem Soc*. 2016;138(24):7584-7591. doi:10.1021/jacs.6b02107

68. Elani Y, Gee A, Law R V., Ces O. Engineering multi-compartment vesicle networks. *Chem Sci*. 2013;4(8):3332-3338. doi:10.1039/c3sc51164b

69. Liu Y, Agudo-Canalejo J, Grafmüller A, Dimova R, Lipowsky R. Patterns of flexible nanotubes formed by liquid-ordered and liquid-disordered membranes. *ACS Nano*. 2016;10(1):463-474. doi:10.1021/acsnano.5b05377

70. Peters RJRW, Marguet M, Marais S, Fraaije MW, Van Hest JCM, Lecommandoux S. Cascade reactions in multicompartmentalized polymersomes. *Angew Chemie - Int Ed*. 2014;53(1):146-150. doi:10.1002/anie.201308141

71. Dimova R. Recent developments in the field of bending rigidity measurements on membranes. *Adv Colloid Interface Sci*. 2014. doi:10.1016/j.cis.2014.03.003

72. Stein H, Spindler S, Bonakdar N, Wang C, Sandoghdar V. Production of isolated giant

unilamellar vesicles under high salt concentrations. *Front Physiol*. 2017;8(FEB). doi:10.3389/fphys.2017.00063

73. Altamura E, Stano P, Walde P, Mavelli F. Giant vesicles as micro-sized enzymatic reactors: Perspectives and recent experimental advancements. *Int J Unconv Comput*. 2015;11(1):5-21.

74. Tsumoto K, Hayashi Y, Tabata J, Tomita M. A reverse-phase method revisited: Rapid high-yield preparation of giant unilamellar vesicles (GUVs) using emulsification followed by centrifugation. *Colloids Surfaces A Physicochem Eng Asp*. 2018;546:74-82. doi:10.1016/j.colsurfa.2018.02.060

75. Liu X, Zhou P, Huang Y, Li M, Huang X, Mann S. Hierarchical Proteinosomes for Programmed Release of Multiple Components. *Angew Chemie - Int Ed*. 2016;55(25):7095-7100. doi:10.1002/anie.201601427

76. Kubatta EA, Rehage H. Characterization of giant vesicles formed by phase transfer processes. *Colloid Polym Sci*. 2009;287(9):1117-1122. doi:10.1007/s00396-009-2083-3

77. Measurements of the effect of membrane asymmetry on the mechanical properties of lipid bilay.

78. Moga A, Yandrapalli N, Dimova R, Robinson T. Optimization of the Inverted Emulsion Method for High-Yield Production of Biomimetic Giant Unilamellar Vesicles. *ChemBioChem*. 2019;20(20). doi:10.1002/cbic.201900529

79. Yandrapalli N, Seemann T, Robinson T. On-chip inverted emulsion method for fast giant vesicle production, handling, and analysis. *Micromachines*. 2020;11(3). doi:10.3390/mi11030285

80. Kamiya K, Kawano R, Osaki T, Akiyoshi K, Takeuchi S. Cell-sized asymmetric lipid vesicles facilitate the investigation of asymmetric membranes. *Nat Chem*. 2016;8(9):881-889. doi:10.1038/nchem.2537

81. Keating CD, Monterroso B, Sobrinos-Sanguino M, Rivas G, Zorrilla S. Encapsulation of a compartmentalized cytoplasm mimic within a lipid membrane by microfluidics. *Chem Commun*. 2017;53(35):4775-4778. doi:10.1039/c7cc01289f

82. Funakoshi K, Suzuki H, Takeuchi S. Formation of giant lipid vesiclelike compartments from a planar lipid membrane by a pulsed jet flow. *J Am Chem Soc*. 2007;129(42):12608-12609. doi:10.1021/ja074029f

83. Conchello J, Lichtman JW. Optical Sectioning Microscopy. *Nat Rev*. 2006;(January). doi:10.1038/nmeth815

84. Ishikawa-Ankerhold HC, Ankerhold R, Drummen GPC. Advanced fluorescence microscopy techniques-FRAP, FLIP, FLAP, FRET and FLIM. *Molecules*. 2012;17(4):4047-4132. doi:10.3390/molecules17044047

85. Sanderson MJ, Smith I, Parker I, Bootman MD. HHS Public Access. 2016;2014(10). doi:10.1101/pdb.top071795.Fluorescence

86. Pawley JB. *Handbook of Biological Confocal Microscopy: Third Edition*.; 2006. doi:10.1007/978-0-387-45524-2

87. Conchello JA, Lichtman JW. Optical sectioning microscopy. *Nat Methods*. 2005;2(12):920-931. doi:10.1038/nmeth815

88. Olympus. Olympus FluoView Resource Center: Introduction to Confocal Microscopy. http://www.olympusconfocal.com/theory/confocalintro.html. Accessed June 30, 2020.

89. Meulen H Ter. Distribuation of Molybdnum. 1932.

90. Leimkühler S, Wuebbens MM, Rajagopalan K V. The history of the discovery of the molybdenum cofactor and novel aspects of its biosynthesis in bacteria. *Coord Chem Rev*. 2011;255(9-10):1129-1144. doi:10.1016/j.ccr.2010.12.003

91. Johnson JL, Hainline BE, Rajagopalan K V, Arison BH. The Pterin Component of the Molybdenum Cofactor - Structural Characterization of 2 Fluorescent Derivatives. *J Biol Chem*. 1984;259(9):5414-5422.

92. Aguilar-Barajas E, Díaz-Pérez C, Ramírez-Díaz MI, Riveros-Rosas H, Cervantes C. Bacterial transport of sulfate, molybdate, and related oxyanions. *BioMetals*. 2011;24(4):687-707. doi:10.1007/s10534-011-9421-x

93. Leimkühler S, Rajagopalan K V. In vitro incorporation of nascent molybdenum cofactor into human sulfite oxidase. *J Biol Chem*. 2001;276(3):1837-1844. doi:10.1074/jbc.M007304200

94. Mendel RR, Leimkühler S. The biosynthesis of the molybdenum cofactors. *J Biol Inorg Chem*. 2015;20(2):337-347. doi:10.1007/s00775-014-1173-y

95. Zhu W, Winter MG, Byndloss MX, et al. Precision editing of the gut microbiota ameliorates colitis. 2018;553(7687):208-211. doi:10.1038/nature25172.Precision

96. Wuebbens MM, Rajagopalan K V. Structural characterization of a molybdopterin precursor. *J Biol Chem*. 1993;268(18):13493-13498.

97. Leimkühler S, Freuer A, Araujo JAS, Rajagopalan K V., Mendel RR. Mechanistic studies of human molybdopterin synthase reaction and characterization of mutants identified in group B patients of molybdenum cofactor deficiency. *J Biol Chem*. 2003;278(28):26127-26134. doi:10.1074/jbc.M303092200

98. Hänzelmann P, Schwarz G, Mendel RR. Functionality of alternative splice forms of the first enzymes involved in human molybdenum cofactor biosynthesis. *J Biol Chem*. 2002;277(21):18303-18312. doi:10.1074/jbc.M200947200

99. Rajagopalan K V., Johnson JL. The pterin molybdenum cofactors. *J Biol Chem*. 1992;267(15):10199-10202.

100. Iobbi-nivol C, Leimkühler S. Biochimica et Biophysica Acta Molybdenum enzymes , their maturation and molybdenum cofactor biosynthesis in Escherichia coli ☆. *BBA*

- *Bioenerg*. 2013;1827(8-9):1086-1101. doi:10.1016/j.bbabio.2012.11.007

101. Kuper J, Palmer T, Mendel RR, Schwarz G. Mutations in the molybdenum cofactor biosynthetic protein Cnx1G from Arabidopsis thaliana define functions for molybdopterin binding, molybdenum insertion, and molybdenum cofactor stabilization. *Proc Natl Acad Sci U S A*. 2000;97(12):6475-6480. doi:10.1073/pnas.110568497

102. Neukranz Y, Kotter A, Beilschmidt L, et al. Analysis of the Cellular Roles of MOCS3 Identifies a MOCS3-Independent Localization of NFS1 at the Tips of the Centrosome. *Biochemistry*. 2019;58(13):1786-1798. doi:10.1021/acs.biochem.8b01160

103. Teschner J, Lachmann N, Schulze J, et al. A Novel Role for Arabidopsis Mitochondrial ABC Transporter ATM3 in Molybdenum Cofactor Biosynthesis. *Plant Cell*. 2010;22(2):468-480. doi:10.1105/tpc.109.068478

104. Veldman A, Santamaria-Araujo JA, Sollazzo S, et al. Successful treatment of molybdenum cofactor deficiency type a with cPMP. *Pediatrics*. 2010;125(5). doi:10.1542/peds.2009-2192

105. Kruse I, Maclean AE, Hill L, Balk J. Genetic dissection of cyclic pyranopterin monophosphate biosynthesis in plant mitochondria. *Biochem J*. 2018;475(2):495-509. doi:10.1042/BCJ20170559

106. Llamas Á, Tejada-Jiménez M, Fernández E, Galván A. Molybdenum metabolism in the alga Chlamydomonas stands at the crossroad of those in Arabidopsis and humans. *Metallomics*. 2011;3(6):578-590. doi:10.1039/c1mt00032b

107. Tejada-Jiménez, Manuel, Angel Liamas, Emanuel Sanz-luque AG. A Novel Role for Arabidopsis Mitochondrial ABC Transporter ATM3 in Molybdenum Cofactor Biosynthesis. *J Biol Chem*. 2007;104(May):20126-20130. doi:10.1016/j.bbamcr.2014.09.021

108. Johnson, J. L. K V Rajagopalan LWI. Molybdenum Cofactor Biosynthesis. *Am Soc Biochem Mol Biol*. 1991;july 1991(19):12140-12145. doi:10.1039/9781782623915-00100

109. Yokoyama K, Leimkühler S. The role of FeS clusters for molybdenum cofactor biosynthesis and molybdoenzymes in bacteria. *Biochim Biophys Acta - Mol Cell Res*. 2015;1853(6):1335-1349. doi:10.1016/j.bbamcr.2014.09.021

110. Hover BM, Loksztejn A, Ribeiro AA, Yokoyama K. Identification of a Cyclic Nucleotide as a Cryptic Intermediate in Molybdenum Cofactor Biosynthesis. *JACS*. 2013:7019-7032.

111. Hänzelmann P, Schindelin H. Crystal structure of the S-adenosylmethionine-dependent enzyme MoaA and its implications for molybdenum cofactor deficiency in humans. *Proc Natl Acad Sci U S A*. 2004;101(35):12870-12875. doi:10.1073/pnas.0404624101

112. Santamaria-Araujo JA, Fischer B, Otte T, et al. The Tetrahydropyranopterin Structure of the Sulfur-free and Metal-free Molybdenum Cofactor Precursor. *J Biol Chem*. 2004;279(16):15994-15999. doi:10.1074/jbc.M311815200

113. Hover BM, Tonthat NK, Schumacher MA, Yokoyama K. Mechanism of pyranopterin ring formation in molybdenum cofactor biosynthesis. *PNAS*. 2015;112(20):6347-6352. doi:10.1073/pnas.1500697112

114. Mendel RR. The molybdenum cofactor. *J Biol Chem*. 2013;288(19):13165-13172. doi:10.1074/jbc.R113.455311

115. Daniels JN, Wuebbens MM, Rajagopalan K V., Schindelin H. Crystal structure of a molybdopterin synthase-precursor Z complex: Insight into its sulfur transfer mechanism and its role in molybdenum cofactor deficiency. *Biochemistry*. 2008;47(2):615-626. doi:10.1021/bi701734g

116. Leimkühler S. The Biosynthesis of the Molybdenum Cofactor in Escherichia coli and Its Connection to FeS Cluster Assembly and the Thiolation of tRNA. *Adv Biol*. 2014;2014(7):1-21. doi:10.1155/2014/808569

117. Mendel RR, Kruse T. Cell biology of molybdenum in plants and humans. *Biochim Biophys Acta - Mol Cell Res*. 2012;1823(9):1568-1579. doi:10.1016/j.bbamcr.2012.02.007

118. Hille R, Nishino T, Bittner F. Molybdenum enzymes in higher organisms. *Coord Chem Rev*. 2011;255(9-10):1179-1205. doi:10.1016/j.ccr.2010.11.034

119. Schwarz G, Santamaria-Araujo JA, Wolf S, et al. Rescue of lethal molybdenum cofactor deficiency by a biosynthetic precursor from Escherichia coli. *Hum Mol Genet*. 2004;13(12):1249-1255. doi:10.1093/hmg/ddh136

120. Schwahn BC, Van Spronsen FJ, Belaidi AA, et al. Efficacy and safety of cyclic pyranopterin monophosphate substitution in severe molybdenum cofactor deficiency type A: A prospective cohort study. *Lancet*. 2015;386(10007):1955-1963. doi:10.1016/S0140-6736(15)00124-5

121. Nagappa M, Bindu PS, Taly AB, Sinha S, Bharath RD. Child Neurology: Molybdenum cofactor deficiency. *Neurology*. 2015;85(23):e175-e178. doi:10.1212/WNL.0000000000002194

122. Jakubiczka-Smorag J, Santamaria-Araujo JA, Metz I, et al. Mouse model for molybdenum cofactor deficiency type B recapitulates the phenotype observed in molybdenum cofactor deficient patients. *Hum Genet*. 2016;135(7):813-826. doi:10.1007/s00439-016-1676-4

123. Hahnewald R, Wegner W, Reiss J. AAV-mediated gene therapy for metabolic diseases: Dosage and reapplication studies in the molybdenum cofactor deficiency model. *Genet Vaccines Ther*. 2009;7:1-7. doi:10.1186/1479-0556-7-9

124. Kügler S, Hahnewald R, Garrido M, Reiss J. Long-term rescue of a lethal inherited disease by adeno-associated virus-mediated gene transfer in a mouse model of

molybdenum-cofactor deficiency. *Am J Hum Genet*. 2007;80(2):291-297. doi:10.1086/511281

125. Lee HJ, Adham IM, Schwarz G, et al. Molybdenum cofactor-deficient mice resemble the phenotype of human patients. *Hum Mol Genet*. 2002;11(26):3309-3317. doi:10.1093/hmg/11.26.3309

126. Bender D, Kaczmarek AT, Santamaria-Araujo JA, et al. Impaired mitochondrial maturation of sulfite oxidase in a patient with severe sulfite oxidase deficiency. *Hum Mol Genet*. 2019;28(17):2885-2899. doi:10.1093/hmg/ddz109

127. Johnson JL, Wuebbens MM, Rajagopalan K V. The structure of a molybdopterin precursor. Characterization of a stable, oxidized derivative. *J Biol Chem*. 1989;264(23):13440-13447.

128. Garrett RM, Johnson JL, Graf TN, Feigenbaum A, Rajagopalan K V. Human sulfite oxidase R160Q: Identification of the mutation in a sulfite oxidase-deficient patient and expression and characterization of the mutant enzyme. *Proc Natl Acad Sci U S A*. 1998;95(11):6394-6398. doi:10.1073/pnas.95.11.6394

129. Van Severen MC, Andrejić M, Li J, et al. A quantum-mechanical study of the reaction mechanism of sulfite oxidase. *J Biol Inorg Chem*. 2014;19(7):1165-1179. doi:10.1007/s00775-014-1172-z

130. Hege dale, Endy Spriet M. Usermanual for Leica SP8 confocal. *Leica SP8 Man*. (1):1-29.

131. Robinson T, Kuhn P, Eyer K, Dittrich PS. Microfluidic trapping of giant unilamellar vesicles to study transport through a membrane pore. *Biomicrofluidics*. 2013;7(4). doi:10.1063/1.4816712

132. Yandrapalli N, Robinson T. Ultra-high capacity microfluidic trapping of giant vesicles for high-throughput membrane studies. *Lab Chip*. 2019;19(4):626-633. doi:10.1039/C8LC01275J

133. Pautot S, Frisken BJ, Weitz D a. Production of Unilamellar Vesicles Usingan Inverted Emulsion. *Langmuir*. 2003;19(10):2870-2879. doi:10.1021/la026100v

134. Wang Q, Li W, Hu N, et al. Ion concentration effect (Na+ and Cl−) on lipid vesicle formation. *Colloids Surfaces B Biointerfaces*. 2017;155:287-293. doi:10.1016/j.colsurfb.2017.04.030

135. Discher DE, Eisenberg A. *Polymer Vesicles*. Vol 290.; 2000. http://science.sciencemag.org/.

136. Li Y, Lipowsky R, Dimova R. Membrane nanotubes induced by aqueous phase separation and stabilized by spontaneous curvature. *Proc Natl Acad Sci U S A*. 2011;108(12):4731-4736. doi:10.1073/pnas.1015892108

137. Altamura E, Stano P, Walde P, Mavelli F. *Giant Vesicles as Micro-Sized Enzymatic Reactors: Perspectives and Recent Experimental Advancements*. Vol 0.

138. Klewe A, Kruse T, Lindel T. Aminopyrazine Pathway to the Moco Metabolite Dephospho Form A. *Chem - A Eur J*. 2017;23(47):11230-11233. doi:10.1002/chem.201702274

139. Bradley M Hover KY. Mechanistic Investigation of cPMP Synthase in Molybdenum Cofactor Biosynthesis Using an Uncleavable Substrate Analogue- HHS Public Access. *Physiol Behav*. 2015;176(1):7229-7236. doi:10.1016/j.physbeh.2017.03.040

140. Chang L, Wu T, Chen F. Determination of L-cysteine base on the reversion of fluorescence quenching of calcein by copper(II) ion. *Microchim Acta*. 2012;177(3-4):295-300. doi:10.1007/s00604-011-0759-0

141. Hughes LD, Rawle RJ, Boxer SG. Choose your label wisely: Water-soluble fluorophores often interact with lipid bilayers. *PLoS One*. 2014;9(2). doi:10.1371/journal.pone.0087649

142. Langton MJ, Scriven LM, Williams NH, Hunter CA. Triggered Release from Lipid Bilayer Vesicles by an Artificial Transmembrane Signal Transduction System. *J Am Chem Soc*. 2017;139(44):15768-15773. doi:10.1021/jacs.7b07747

143. Dutta S, Watson BG, Mattoo S, Rochet J. Calcein Release Assay to Measure Membrane Permeabilization by Recombinant Alpha-Synuclein. *HHS Public Access*. 2020;10(14). doi:10.21769/bioprotoc.3690.Calcein

144. Noireaux V, Libchaber A. A vesicle bioreactor as a step toward an artificial cell assembly. *Proc Natl Acad Sci U S A*. 2004;101(51):17669-17674. doi:10.1073/pnas.0408236101

145. Méléard P, Bagatolli LA, Pott T. Giant Unilamellar Vesicle Electroformation. From Lipid Mixtures to Native Membranes Under Physiological Conditions. *Methods Enzymol*. 2009;465(C):161-176. doi:10.1016/S0076-6879(09)65009-6

146. Bockmann, A. Hac A, Heimburg T, Grubmu H, Bo RA. Effect of Sodium Chloride on a Lipid Bilayer. *Biophys J*. 2003;85(September):1647-1655.

147. Swaay D van, deMello A. Microfluidic methods for forming liposomes. *Lab Chip*. 2013;13(5):752-767. doi:10.1039/C2LC41121K

148. Nishimura K, Suzuki H, Toyota T, Yomo T. Size control of giant unilamellar vesicles prepared from inverted emulsion droplets. *J Colloid Interface Sci*. 2012;376(1):119-125. doi:10.1016/j.jcis.2012.02.029

149. Toparlak D, Zasso J, Bridi S, et al. Artificial cells drive neural differentiation. *Sci Adv*. 2020;6(38):1-13. doi:10.1126/sciadv.abb4920

150. Kurihara K, Natsume Y, Itoh K, Wen H, Sheng L, Zhu T. Preparation of Giant Vesicles Encapsulating Microspheres by Centrifugation of a Water-in-oil Emulsion. *J Vis Exp*. 2017;(119):1-8. doi:10.3791/55282

151. Vácha R, Jurkiewicz P, Petrov M, et al. Mechanism of interaction of monovalent ions with phosphatidylcholine lipid membranes. *J Phys Chem B*. 2010;114(29):9504-

9509. doi:10.1021/jp102389k

152. McMahon HT, Boucrot E. Membrane curvature at a glance. *J Cell Sci*. 2015;128(6):1065-1070. doi:10.1242/jcs.114454

153. Kurylowicz M, Paulin H, Mogyoros J, Giuliani M, Dutcher JR. The effect of nanoscale surface curvature on the oligomerization of surface-bound proteins. *J R Soc Interface*. 2014;11(94). doi:10.1098/rsif.2013.0818

154. Elani Y, Law R V, Ces O. Vesicle-based artificial cells as chemical microreactors with spatially segregated reaction pathways. *Nat Commun*. 2014;5:5305. doi:10.1038/ncomms6305

155. Tsumoto K, Hayashi Y, Tabata J, Tomita M. A reverse-phase method revisited: Rapid high-yield preparation of giant unilamellar vesicles (GUVs) using emulsification followed by centrifugation. *Colloids Surfaces A Physicochem Eng Asp*. 2018;546(January):74-82. doi:10.1016/j.colsurfa.2018.02.060

156. Karamdad K, Hindley JW, Bolognesi G, et al. Engineering thermoresponsive phase separated vesicles formed: Via emulsion phase transfer as a content-release platform. *Chem Sci*. 2018. doi:10.1039/c7sc04309k

157. Salassi S, Simonelli F, Bartocci A, Rossi G. A Martini coarse-grained model of the calcein fluorescent dye. *arXiv*. 2019.

158. Maherani B, Arab-Tehrany E, Kheirolomoom A, Geny D, Linder M. Calcein release behavior from liposomal bilayer; Influence of physicochemical/mechanical/structural properties of lipids. *Biochimie*. 2013;95(11):2018-2033. doi:10.1016/j.biochi.2013.07.006

159. Gironi B, Kahveci Z, Mcgill B, et al. Effect of DMSO on the Mechanical and Structural Properties of Model and Biological Membranes. *Biophys Soc*. 2020;119(2):274-286. doi:10.1016/j.bpj.2020.05.037

160. Elani Y, Law R V, Ces O. Protein synthesis in artificial cells: using compartmentalisation for spatial organisation in vesicle bioreactors. *Phys Chem Chem Phys*. 2015;17(24):15534-15537. doi:10.1039/c4cp05933f

161. Rubio LM, Ludden PW. Biosynthesis of the iron-molybdenum cofactor of nitrogenase. *Annu Rev Microbiol*. 2008;62:93-111. doi:10.1146/annurev.micro.62.081307.162737

162. Kaufmann P, Iobbi-Nivol C, Leimkühler S. Reconstitution of molybdoenzymes with bis-molybdopterin guanine dinucleotide cofactors. *Methods Mol Biol*. 2019;1876:141-152. doi:10.1007/978-1-4939-8864-8_9

163. Plate J, Sassen WA, Hassan AH, Lehne F, Köster RW, Kruse T. S-sulfocysteine induces seizure-like behaviors in zebrafish. *Front Pharmacol*. 2019;10(APR):1-6. doi:10.3389/fphar.2019.00122

164. Hilken S, Kaletta F, Heinsch A, Neudörfl JM, Berkessel A. Synthesis of an oxidation-stable analogue of cyclic pyranopterin monophosphate (cPMP). *European J Org*

Chem. 2014;2014(11):2231-2241. doi:10.1002/ejoc.201301784

165. Hercher TW, Krausze J, Hoffmeister S, et al. Insights into the Cnx1E catalyzed MPT-AMP hydrolysis. *Biosci Rep*. 2020;40(1):1-12. doi:10.1042/BSR20191806

166. Yi YJ, Sutovsky M, Kennedy C, Sutovsky P. Identification of the inorganic pyrophosphate metabolizing, atp substituting pathway in mammalian spermatozoa. *PLoS One*. 2012;7(4). doi:10.1371/journal.pone.0034524

167. Kottur J, Nair DT. Pyrophosphate hydrolysis is an intrinsic and critical step of the DNA synthesis reaction. *Nucleic Acids Res*. 2018;46(12):5875-5885. doi:10.1093/nar/gky402

168. Jo SM, Wurm FR, Landfester K. Biomimetic Cascade Network between Interactive Multicompartments Organized by Enzyme-Loaded Silica Nanoreactors. *ACS Appl Mater Interfaces*. 2018;10(40):34230-34237. doi:10.1021/acsami.8b11198

169. Clinch K, Watt DK, Dixon RA, et al. Synthesis of cyclic pyranopterin monophosphate, a biosynthetic intermediate in the molybdenum cofactor pathway. *J Med Chem*. 2013;56(4):1730-1738. doi:10.1021/jm301855r

170. Arkadiusz Zupok,a Michal Gorka,b Beata Siemiatkowska,b Aleksandra Skirycz b SL. Biosynthesis Genes in Escherichia coli. *J Bacteriol*. 2019;201(17):1-15.

171. Jia H, Heymann M, Härtel T, Kai L, Schwille P. Temperature-sensitive protein expression in protocells. *Chem Commun*. 2019;55(45):6421-6424. doi:10.1039/c9cc02734c

172. Villar G, Bayley H. Formation of droplet networks that function in aqueous environments. *NIH*. 2012;6(12):803-808. doi:10.1038/nnano.2011.183.Formation

173. Machida K, Kanzawa K, Shigeta T, Yamamoto Y, Tsumoto K, Imataka H. Huntingtin Polyglutamine-Dependent Protein Aggregation in Reconstituted Cells. *ACS Synth Biol*. 2018;7(2):377-383. doi:10.1021/acssynbio.7b00372

174. Elani Y, Solvas XCI, Edel JB, Law R V, Ces O. Microfluidic generation of encapsulated droplet interface bilayer networks (multisomes) and their use as cell-like reactors. *Chem Commun Chem Commun*. 2016;52(52):5961-5964. doi:10.1039/c6cc01434h

175. Radon C, Enzymologie M. *The Link between the Biosynthesis of the Molybdenum Cofactor, FeS Cluster Biosynthesis and the Thiolation of TRNA in Humans*.

176. Bernard DG, Cheng Y, Zhao Y, Balk J. An allelic mutant series of ATM3 reveals its key role in the biogenesis of cytosolic iron-sulfur proteins in Arabidopsis. *Plant Physiol*. 2009;151(2):590-602. doi:10.1104/pp.109.143651

177. Riedel S, Siemiatkowska B, Watanabe M, et al. The ABCB7-Like Transporter PexA in Rhodobacter capsulatus Is Involved in the Translocation of Reactive Sulfur Species. *Front Microbiol*. 2019;10(MAR):1-19. doi:10.3389/fmicb.2019.00406

178. Tejada-Jiménez M, Llamas A, Sanz-Luque E, Galván A, Fernández E. A high-affinity molybdate transporter in eukaryotes. *Proc Natl Acad Sci U S A*.

2007;104(50):20126-20130. doi:10.1073/pnas.0704646104

179. Prévost C, Zhao H, Manzi J, et al. IRSp53 senses negative membrane curvature and phase separates along membrane tubules. *Nat Commun*. 2015;6. doi:10.1038/ncomms9529

180. Elani Y, Purushothaman S, Booth PJ, et al. Measurements of the effect of membrane asymmetry on the mechanical properties of lipid bilayers. *Chem Commun (Camb)*. 2015;51(32):6976-6979. doi:10.1039/c5cc00712g

181. Dimova R. Giant Vesicles and Their Use in Assays for Assessing Membrane Phase State, Curvature, Mechanics, and Electrical Properties. *Annu Rev Biophys*. 2019;48(1):93-119. doi:10.1146/annurev-biophys-052118-115342

182. Dimova R, Aranda S, Bezlyepkina N, Nikolov V, Riske KA, Lipowsky R. A practical guide to giant vesicles. Probing the membrane nanoregime via optical microscopy. *J Phys Condens Matter*. 2006;18(28):S1151-76. doi:10.1088/0953-8984/18/28/S04

183. Hindley JW, Zheleva DG, Elani Y, et al. Building a synthetic mechanosensitive signaling pathway in compartmentalized artificial cells. *Proc Natl Acad Sci U S A*. 2019;116(34):16711-16716. doi:10.1073/pnas.1903500116

184. Johnson JL, Wuebbens MM, Mandell R, Shih VE. Molybdenum cofactor biosynthesis in humans. Identification of two complementation groups of cofactor-deficient patients and preliminary characterization of a diffusible molybdopterin precursor. *J Clin Invest*. 1989;83(3):897-903. doi:10.1172/JCI113974

185. Paul A, Wang Y, Brännmark C, Kumar S, Bonn M, Parekh SH. Quantitative Mapping of Triacylglycerol Chain Length and Saturation Using Broadband CARS Microscopy. *Biophys J*. 2019;116(12):2346-2355. doi:10.1016/j.bpj.2019.04.036

186. Syed A, Smith EA. Raman imaging in cell membranes, lipid-rich organelles, and lipid bilayers. *Annu Rev Anal Chem*. 2017;10(March):271-291. doi:10.1146/annurev-anchem-061516-045317

187. David C. Chan. Fusion and Fission: Interlinked Processes Critical for Mitochondrial Health. *Annu Rev Genet*. 2012;46(1):265-287. doi:10.1146/annurev-genet-110410-132529

7 Acknowledgment

I am very grateful for the financial support from the “International Max Planck Research School (IMPRS) on Multiscale Bio-systems” at the Max Planck Institute of Colloids and Interfaces, as well as to Prof Dr. Reinhard Lipowsky for giving me this opportunity. Most importantly I want to thank my supervisors, Prof. Dr. Silke Leimkühler for her immense scientific support, and financial aid towards the last days, and Dr. Tom Robinson for the opportunity to pursue my PhD in his lab, for the guidance and support throughout my project. Thank you, I am sincerely grateful for the time you both invested in me.

Thank you Dr. habil. PD Rumina Dimova, Dr. Angelo Valleriani and my mentor Dr. Ana Vila Verde from the Max Planck Institute of Colloids and Interfaces for the various good advice. A special thanks goes to all the group members of Molecular Enzymology and Biomicrofluidic Systems, in particular, Angelika, Jasmine, Yannika, Abrar, Tina, Elisa and Naresh for the amazing advice and help throughout my project.

During my time at the Max Planck Institute and University, I have received a great deal of support from IT-people, Library staff, people at the International Welcome Center. Many thanks to Ms Susan Weber and Ms Jeanette Ziegler for helping through the comprehensive world of documentation.

My family, I can never thank you enough, and Hjörtur for always believing in me. I am sincerely thankful for all my friends Tobi, Csilla, Isabell, Mereike, Tabea, Valentino, Pallavi with whom I have laughed, cried, and played board games. Not to mention all the up-hill biking tours, walks, the running habits in this difficult year of covid. Without you, I would have struggled to find the motivation needed to complete this dissertation